Synthesis and Optimization of Mechanical Properties of Aluminium Composite Reinforced with High Entropy Alloy

A Thesis

Submitted in partial fulfillment of the

requirements for the award of the degree

of

Doctor of Philosophy

in

Department of Mechanical Engineering

by

Akshay Kumar

(183116009)

MAULANA AZAD

NATIONAL INSTITUTE OF TECHNOLOGY

BHOPAL - 462003 (INDIA)

September, 2023

© MAULANA AZAD NATIONAL INSTITUTE OF TECHNOLOGY, BHOPAL-462003

ALL RIGHTS RESERVED

MAULANA AZAD NATIONAL INSTITUTE OF TECHNOLOGY, BHOPAL

CANDIDATE'S DECLARATION

I hereby certify that the work which is being presented in the thesis entitled "**Synthesis and Optimization of Mechanical Properties of Aluminium Composite Reinforced with High Entropy Alloy**" in partial fulfillment of the requirements for the award of the Degree of **Doctor of Philosophy** and submitted in the **Department of Mechanical Engineering of the Maulana Azad National Institute of Technology, Bhopal** is an authentic record of my own work carried out during the period from **December 2018** to **Sep 2023** under the supervision of **Dr. Alok Singh**, and **Dr. Amit Suhane**, Assistant Professor, Department of Mechanical Engineering, Maulana Azad National Institute of Technology, Bhopal.

The matter presented in this thesis has not been submitted by me for the award of any other degree of this or any other Institution.

AKSHAY KUMAR
Scholar No. 183116009

This is to certify that the above statement made by the candidate is correct to the best of my knowledge.

Date: 06/09/2023

Dr. ALOK SINGH
Assistant Professor
Mechanical Engineering
MANIT, Bhopal

Dr. AMIT SUHANE
Assistant Professor
Mechanical Engineering
MANIT, Bhopal

The Ph.D. Viva-Voce Examination of **Mr. Akshay Kumar**, Research Scholar, has been held on **06/09/2023** and is recommended for award of the Ph.D. Degree.

Signature of Supervisor

Signature of External Examiner

Dedicated To

My Beloved Mother

And Father

ABSTRACT

Aluminium Matrix Composites (AMCs) are finding a wide range of applications in automobile, aerospace, defense, and general engineering sectors, because of their higher specific strength and stiffness, good wear and seizure resistance, and improved high-temperature properties as compared to the base alloy. Potential uses of these materials in automobile sectors are found in making the components like brake drums, pistons, cylinder heads, drive shafts, etc. Most of these components are subjected to abrasive and sliding types of wear during operations and are presently either made of cast iron and steels or aluminum alloys. AMCs are lighter than cast iron or steel and the former has a better specific strength and wear resistance as compared to the latter one. Thus, considerable efforts are being made to replace these components with AMCs. It will not only improve the life of components but also reduce the weight and improve fuel efficiency.

An Mg-Si-based Aluminium 6082 alloy with varying concentrations of CoCrFeMnNi high entropy alloy (HEA) reinforced composites were fabricated through stir squeeze casting assisted with an ultrasonic transducer probe. The composites were heat treated to examine the age-hardening effect (T6) on microstructural changes, fracture mechanism, and an interface between HEA particles and aluminium matrix. The evolution of microstructure and topography of HEA particles, alloy, and composite at as cast and heat-treated conditions, was investigated through field emission scanning electron microscope (FESEM) with energy dispersive X-Ray Spectroscopy (EDS) and transmission electron microscope (TEM). X-ray diffraction (XRD) is used to characterize the phase evolution of HEA particles, alloys, and composites at the as-cast condition, and heat-treated condition. In this study, the mechanical behavior of alloy and composite was investigated and the cause of failure was studied through tensile fractured surface. Under the T6 condition, composites exhibit superior mechanical properties such as improved hardness, yield strength, and ultimate tensile strength, however, the ductility of composites is less as compared to the as-cast condition which might be due to the formation of precipitates. The performance of industrial tribo-systems depends on advanced composites with superior tribological characteristics. The effect of HEA particles on the dry sliding wear performance of HEA reinforced Aluminium metal matrix composites was examined in as-cast conditions using a pin-on-disc wear tester at varying pressure and constant sliding

speed, special emphasis is centered on response factors such as wear rate, and seizure resistance. The composite showed an ability to withstand higher temperatures and better seizure and wear resistance over the alloy. The topography of the worn-out surface was examined through an optical profilometer and FESEM. In all the wear conditions, the wear rate of 8 wt.% HEA/AA (T6) composite shows maximum resilience against wear, the inclusion of HEA particles also influences the extent of the subsurface at the seizure condition. Whereas, at higher applied pressures, the wear surface was depicted as a series of parallel transverse as well as longitudinal cracks and damaged portions. The propagation of longitudinal and transverse cracks resulted in the formation of flaky shape debris. Furthermore, FESEM of the subsurface of alloy shows a mechanically mixed layer (MML), a thin plastically deformed and bulk undeformed zones. With increased applied pressure, the extent of subsurface deformation was increased. The flow of Al dendrite was noted in a less deformed region. It depicted a highly plastically deformed region, which was formed due to void formation and shear deformation of the alloy. During the sliding action, this void joined together and formed subsurface cracks, which were in due course joined together forming wear debris.

ACKNOWLEDGEMENT

I express my deep sense of gratitude and indebtedness to my thesis supervisors, Dr. Alok Singh and Dr. Amit Suhane, for providing valuable supervision throughout this work. Their help and conscientious effort made it possible to present the work contained in this thesis. Also, Dr. P.M. Mishra and Dr. Bharat Modhera, both members of SRPC have given me valuable suggestions which have always been useful for my Ph.D. work. I would also like to thank Ph.D. inmates, especially Dr. Ashish Kumar Singh, Mr. Kashish Kumar, Mr. Pradip Kumar Verma, and all those who have guided and supported me in any way during my Ph.D. career.

I thank the Department of Mechanical Engineering, in general, and all its HODs, in particular, for facilitating the current research work that lasted from 2018 to 2023. I am grateful to all faculty and staff members of the department and the current Head, Dr. Rajesh Gupta, for the help rendered in carrying out this work.

I thank Dean (Academics) and Associated Dean (Academics), MANIT, Bhopal for the help and support extended.

I would like to thank the Director, Maulana Azad National Institute of Technology (MANIT), Bhopal, for creating a healthy academic environment and providing the desired research facilities.

My parents always inspired and motivated me throughout this academic journey leading to my Ph.D. degree from MANIT, Bhopal. The blessings and unconditional support of my loving Parents helped me throughout my thesis work. Their constant encouragement, inspiration, and active support made it possible for me to overcome all hurdles and complete this thesis work. I will remain indebted to them throughout my life.

At the same time, I also extend my sincere gratitude to my nephews, and friends, whose support has been invaluable to me throughout this journey.

TABLE OF CONTENT

LIST OF FIGURES

LIST OF TABLES

CHAPTER – 1

INTRODUCTION

Aluminium, the second most abundant element in the Earth's crust, has been instrumental in the advancement of human civilization. Its unique properties make it an excellent substitute for wood, copper, iron, and steel. It consumes more energy than all other nonferrous metals and alloys combined with its lightweight, low density, thermal and electrical conductivity, and excellent corrosion resistance. Its high utility index makes it an essential component in various industries such as transportation, packaging, electrical, chemical, food, and architecture.

The aircraft industry was the first to demand aluminium alloys due to their excellent combination of properties, including lightweight, high specific strength, stiffness, exceptional corrosion resistance, and increased ductility. Although its poor mechanical properties, including yield and tensile strength, have limited its wider use, significant efforts are being made to increase the mechanical strength of aluminium to meet the demands of various industries.

Aluminium is alloyed with various elements, including Cu, Zn, Mg, Si, and Mn, to increase its mechanical strength and modulus. Al Zn-Mg alloys have demonstrated a significant increase in mechanical strength and are widely used in structural parts for aircraft and automobiles. Aluminium alloys can be categorized into two groups: cast and wrought alloys. The primary method of property improvement for each group is further divided into alloys that can and cannot be heated. Many alloys react to thermal treatment based on phase solubility. Quenching, precipitation, age hardening, and solution heat treatment are examples of these processes. Different wrought compositions can be work-hardened through mechanical reduction, frequently in conjunction with various annealing techniques for property improvement. These alloys are also known as work-hardening and non-heat treatable alloys.

The wrought aluminium alloys that respond to heat treatment strengthening, primarily by aging, are classified into three main series: 2XXX (Al-Cu, Al-Cu-Mg), 6XXX (Al-Mg-Si), and 7XXX (Al-Zn-Mg, Al-Zn-Mg-Cu). These alloys can be further divided into two categories based on their weldability and strength. The first category comprises medium-strength and easily weldable alloys, such as Al-Mg-Si and Al-Zn-Mg. The second category includes high-

strength alloys, such as Al-Cu, Al-Cu-Mg, and Al-Zn-Mg-Cu, which have limited weldability. Alloys that cannot be heat-treated are hardened through cold working instead of heating, typically from the 1XXX, 3XXX, 4XXX, and 5XXX series. These alloys obtain their initial strength from the hardening effect of their alloying elements, and cold working can provide additional strengthening.

The majority of wrought compositions that do not respond to strengthening by heat treatment consist of various grades of aluminium and alloys with manganese (Mn) or magnesium (Mg) as the main additions. However, due to their low strength and stiffness at low and high temperatures, low wear resistance, and low seizure resistance, aluminium alloys have a limited range of applications. To address these limitations, Aluminium Matrix Composites (AMCs) have been developed by reinforcing aluminium with a wide range of materials, including continuous or discontinuous fibers, whiskers, and particles. AMCs have become a significant class of materials in industries such as automotive, aerospace, defense, and general engineering, where there is a growing demand for lighter-weight and more durable components. They have the potential to replace conventional materials currently in use.

There are various categories of processing techniques used for the production of AMCs, depending on the primary treatment made for the matrix. These techniques include the liquid phase technique, solid-phase technique, and semi-solid (mixed) phase technique

Solid-phase processing techniques, such as powder metallurgy, are capable of producing high-quality products with a uniform dispersion of reinforcing phases. Spark plasma sintering offers superior features such as high heating rates, shorter sintering times, full and uniform densification, and reduced porosity compared to conventional sintering methods such as pressure-less sintering, hot press, and hot isostatic sintering. Vacuum sintering is more appropriate for larger-scale production with enhanced mechanical properties. Additionally, microwave sintering can be used, which reduces energy consumption while improving product properties. These techniques offer controlled porosity, minimizing machining by producing components with superior dimensional accuracy. However, these methods are limited to simple-shaped products, unlike liquid-state casting techniques.

Squeeze casting is a technique that allows for greater wettability between the elements, uniform distribution of reinforcing phases, and limited porosity. Liquid phase techniques such

as stir casting can produce products with both simple and intricate shapes and are being widely adopted due to their simplicity and cost-effectiveness [1]. However, issues such as wettability between constituents, porosity, and particle distribution arise in the stir-casting technique, which can be resolved by incorporating appropriate modifications [2].

Furthermore, in addition to solid and liquid-phase processing techniques, other techniques such as semi-solid phase techniques (composting, rheocasting, and thixocasting), in-situ techniques, and spray deposition techniques are also adopted. Composting offers greater dispersion of reinforcing particles, extremely reduced porosity, and improved wettability of the matrix with reinforcement, resulting in superior mechanical properties such as yield strength, hardness, and wear resistance compared to conventional stir casting. The in-situ technique enables a clean, unoxidized interface between the matrix and reinforcement, greater interfacial strength, more homogeneous reinforcement distribution, and superior wettability over ex-situ methods

Several studies have investigated the dry sliding wear behavior of aluminium matrix composites (AMCs) against steels and found that the composites exhibit significantly higher wear resistance than unreinforced aluminium alloys. Ceramic reinforcing particles typically support the contact stresses under low contact loads and sliding speeds, minimizing the consequences of frictional heating. The reinforcing phases restrain the matrix alloy, thereby preventing subsurface plastic deformation and shear, and improving the ability to withstand seizures due to higher temperature strength. The wear behavior of AMCs is significantly impacted by microstructural features, such as the shape, size, distribution, and volume percentage of the reinforcing phase, interface properties, and matrix microstructure. The wear mechanism also varies between alloys and composites.

The impact of the aforementioned parameters on the sliding wear behavior of AMCs has not been thoroughly studied. Identifying the wear mechanism offers a better understanding of designing and developing improved wear and seizure-resistant components that are subjected to sliding wear conditions. In constructing wear mechanism maps for Al alloys, Liu et al. [3] proposed oxidation, delamination, severely plastic-deformed zone, and melt wear regimes. Bembalge et al. [4] found abrasive wear modes, along with adhesive wear marks at lower loads and speeds, which transformed into oxidational wear modes when undergoing higher limits of applied pressure and sliding velocity. Wilson et al. [5] observed that incorporating 20% SiCp

to A356 Al alloy significantly extended the mild wear regime to a higher extent of applied load and sliding speeds, hence inhibiting severe wear. Beyond a critical load, Zhang et al. [6] observed a severe wear regime resulting in considerable surface degradation and material transfer to the counter disc.

James et al. [7] observed that the wear behavior of AA6061 composite containing 5% ZrO_2 was mild and smooth under static conditions. However, with an increase in the concentration of ZrO_2 to 15%, agglomerated sites were evident, leading to severe wear in the form of deep ploughing, grooving, and delamination. Ramchandra et al. [8] identified oxidation, micro-cutting, and thermal softening as the dominant wear mechanisms. The development of the mechanically mixed layer (MML) on the worn surface of metallic alloys was found to strongly influence wear response [9]. Rosenberger et al. [10] characterized the MML as consisting of the matrix material, counter surface, matrix oxides, and cracked ceramics reinforcement. Basavarajappa et al. [11] observed an increase in microhardness near the worn end of the subsurface due to the formation of a thicker MML. They also noted that the addition of graphite reinforcement reduced subsurface deformation. Venkataraman et al. [12] established a correlation between the transitional load and material hardness based on variations in the MML's nature, subsurface cracking, and other microstructural changes. They found that the transition load increased with the hardness of the MML. Wear residues, material displacement (transfer) from the counter disc, a coalition of mating surfaces under higher normal loads, and greater heating due to friction were the main factors responsible for the evolution of the MML. Uthayakumar et al. [13] reported that debris formation was significantly influenced by the thickness of the tribo-layer and subsurface deformation. Lesser subsurface deformation led to smaller wear debris with equiaxed dimensions. The effect of applied load and sliding distance on the production and stability of the MML or oxide layer has not been fully established. In the case of composites, the hard ceramic dispersoid on the surface of the composite could have an abrasive effect on the counter surface. Material transfer between contacting surfaces is likely to occur during sliding wear, and in composites, these particles may increase the amount of counter-surface material on the specimen surface. Therefore, the amount of counter-surface material transfer to the specimen surface may vary between alloys and composites

Furthermore, the characteristics of MML in composites are distinct from those in alloys. In addition, previous studies have only investigated the dry sliding wear behavior of AMCs with single solid lubricant particle reinforcement, while the influence of hybrid particles composed of strong ceramic and soft, brittle, and self-lubricating particles on the wear behavior of Al alloy requires further investigation. The objective of the present study is to investigate how two different types of reinforcing particles and heat treatment impact the mechanical and tribological properties of the AA 6082 alloy and its composites. The wear experiments include various extrinsic and intrinsic experimental variables such as applied pressure/load, sliding distance, nature and weight fraction of reinforcements, and matrix microstructures. Heat treatment is utilized to modify the matrix microstructure. The temperature and frictional force during sliding wear are examined as a function of the applied pressure and sliding distance for different materials. In order to achieve a better understanding of the sliding wear mechanism in composites as opposed to alloys, future research is recommended to conduct a systematic study of the MML characteristics and stability as a function of speed and applied load. X-ray diffraction and SEM-EDX analysis of worn surfaces can be utilized to analyze the wear mechanism maps for alloys and composites, showing the transition of wear regions based on wear rate, temperature data, as well as wear surface and subsurface analysis.

CHAPTER - 2

LITERATURE REVIEW

2.1 INTRODUCTION

This chapter summarizes the available information pertaining to the effects of alloying elements on the physical and mechanical properties of aluminium, the equilibrium diagram of the AlMg, and AlSi phase, Metal Matrix Composites (MMCs), and their processing techniques with special emphasis on Aluminium Matrix Composites (AMCs), microstructures, mechanical and tribological properties of AMCs as compared to the virgin alloy, types of wear, the effect of experimental variables and microstructural characteristics on sliding wear behavior of AMCs, and wear mechanisms. This literature survey was made to update my knowledge and understanding of the present status of AMCs with special reference to the mechanical and tribological behavior of these materials. Based on the literature survey, the problem for the present investigation has been identified.

2.2 ALUMINIUM ALLOYS

Various combination of different alloying elements results in different kinds of alloys. Aluminium alloys are broadly classified into three groups including (i) age-hardening alloys, (ii) casting alloys and (iii) work-hardening alloys. All age-hardening alloys contain alloying elements that can be dissolved at elevated temperatures (solution heat treated) and precipitated at lower temperatures (aged) to produce a significant increase in strength. In most casting alloys, silicon (Si) is used as the major alloying element because Al-Si alloys can fill the mold completely and are not sensitive to hot cracking. Silicon in shape casting produces a modest increase in strength because of the large volume fraction of hard Si particles formed during solidification. The work-hardening alloys are of two basic types; the Al-Mn-based alloys, which form a fine dispersion of inter-metallic phase particles give a modest increase in strength, and the Al-Mg-based alloys in which the Mg remains in solid solution, produces a larger increase in strength, particularly after cold working. A combination of Al-Mg-Mn is widely used in Al alloy beverage containers. All alloying elements will increase work hardening, but the above two systems are extensively used because both of them remain stable

during processing and have excellent corrosion resistance. Al-Mg-Si alloys represent the group that shows the medium strength but high wear resistance property among all commercially available Al alloys. They are being widely used in the automobile and aerospace sectors. These alloys are heat-treatable and the binary phase diagram of Al-Mg-Si alloy is illustrated in Figure 2.1.

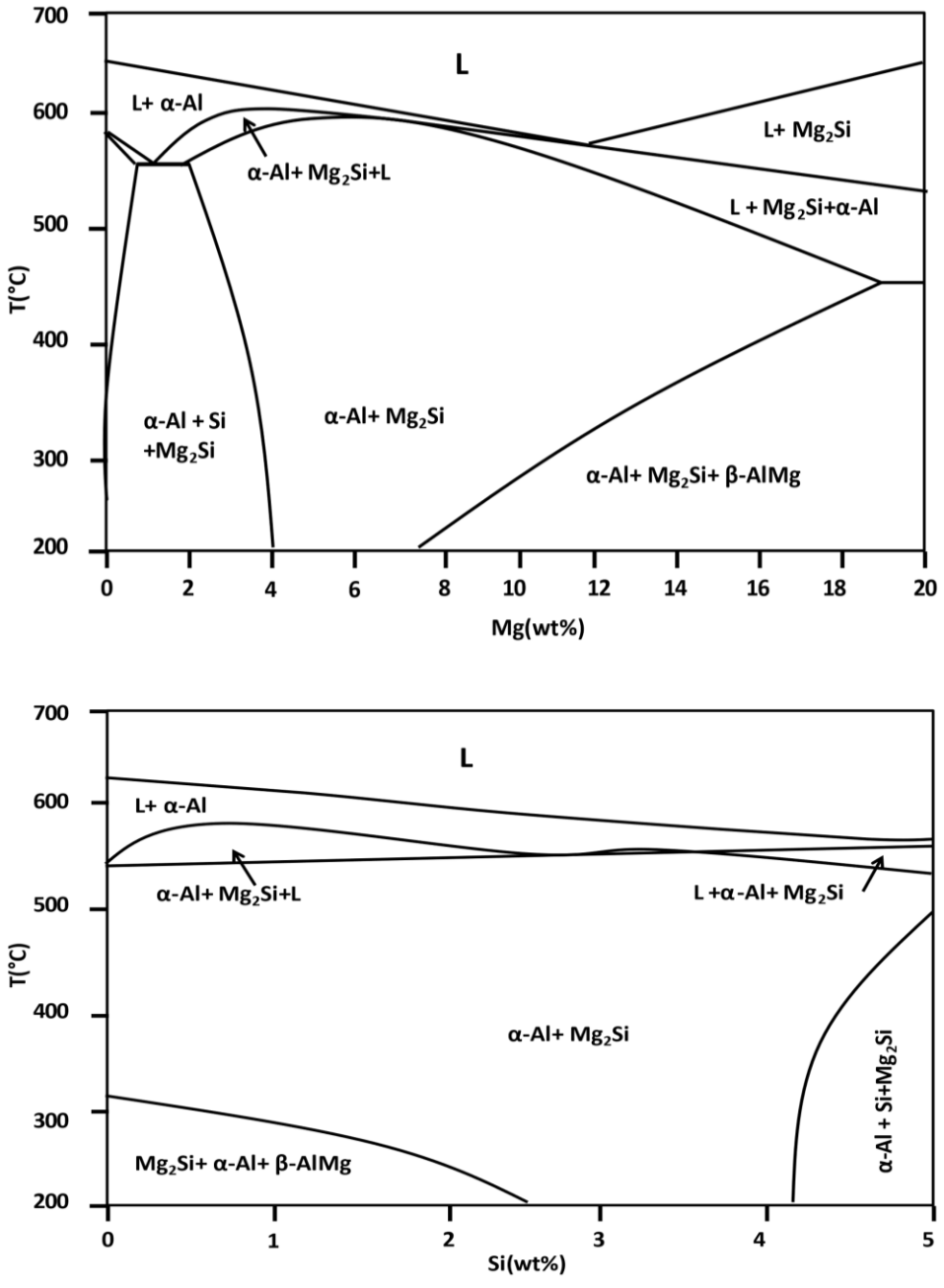

Figure 2.1: Aluminium-magnesium-Silicon Phase diagram

2.3 COMPOSITE MATERIALS

The term 'Composite' states to a combined form of material composed of a discrete 'reinforcement' distributed (dispersed/embedded) in a 'matrix' continuous phase and which extracts its distinguishing characteristics from the properties, geometries, and architectures of its constituents and the properties of the interfacial boundaries existing in the vicinity of these constituents [14]. The significant advantageous features of composites lie in the tailorability of their physical, mechanical, and tribological properties to approach the predetermined design criteria. In MMCs, light metallic alloys (or pure metals) such as Mg, Al, Cu, and Ti alloys are often used as matrix phases, and amongst all, Al or Al alloys are being broadly used owing to their excellent specific strength, resistance against abrasion and corrosion, better toughness [15]. In Polymer Matrix Composites (PMCs), matrix phases are usually cross-linked thermoset polymers (e.g., polyester, epoxy, phenolics). Thermoset polymers reinforced with glass fibers exhibit higher stiffness and strength-to-weight ratio; therefore, these polymers are mostly employed in various automobile parts. PMCs also confine thermoplastic resins (e.g. Polyvinyl Chloride, i.e. PVC, polyethylene, i.e. PE, Nylon) [16]–[18]. Ceramic Matrix Composites (CMCs), consist of ceramic matrices such as C, Al_2O_3, and SiC embedded with similar or different ceramic fibers and are being used in many sectors such as aero-engines and automotive components [19]. In some recent studies, some evidence has been found regarding the emergence of ultra-high temperature ceramics (UHTC) enabling an innovative class of CMCs, namely ultra-high temperature ceramic matrix composites (UHTCMCs). Composites, reinforced with particulates (particles) may consist of glasses, ceramics, metallic, and (or) amorphous materials, and in such composites, the modulus is higher over the matrix, while ductility and permeability are comparatively lower [20]. Thus, particulate composites provide sustainability towards higher compressive, tensile, and shear stresses. In composites reinforced with fibers (i.e. continuous fiber composites and short fiber composites), the modulus of developed composites is superior as compared to that of a matrix owing to their robust covalent bonds along the length of these fibers [21]. In such composites, the varying forms and the relative fiber orientations also play a vital role in the alternation of the mechanical and tribological properties. In addition to the aforementioned constituents of the composites (i.e. matrix and reinforcement), there is another factor that has also a significant impact on the expected properties, namely the 'interface' existing between the matrix and reinforcement [22].

A discontinuous behaviour of many factors (such as chemical potential, strength, and elastic modulus) at the interfaces appears due to the nonequilibrium thermodynamic natures of the matrix and reinforcing phases [23]. Additionally, chemical compounds are also formed at the interfaces because of the discontinuous chemical potentials of the constituents. This leads to an interacting zone influencing the expected properties to some extent. Moreover, a discontinuous coefficient of thermal expansion of the constituents may also result in thermal stresses at the interfaces leading plastic deformation, deviation in the expected properties and initiations of cracks under extreme conditions [24].

2.3.1 ALUMINIUM MATRIX COMPOSITES (AMCS)

The aluminium metal matrix composite received the attention of researchers, academia, and engineers due to their diversified application of lightweight materials including transportation, and aviation industries because of their low density, high strength-to-weight ratio, high stiffness, and better dimensional stability [25], [26]. Most of the AMCs were commonly reinforced with ceramic particles, alumina, and boride. Even though they are often utilized in the strengthening phase, a poorer bonding interaction, poor wettability, and a sizable differential in the thermal expansion coefficient between the ceramic particles are found [27], [28]. Metallic reinforcement provides a suitable substitute as they exhibit superior interface bonding between metal matrix and reinforcement. For example, Mo [29], β-Al_3Mg_2 [30], Ti [31], and metallic glass-reinforced particles with AMCs exhibited better mechanical and tribological properties. In recent, a new alloy design approach draw attention and provide completely a new dimension in a metallurgical field that was unexplored. High entropy alloy was first reported in 2004 individually by J W Yeh et.al. [32] and Cantor et. al. [33]. HEAs are defined as alloys that have five or more principal elements which are in equiatomic or nearly equiatomic ratio and the concentration of elements not exceeding 35% without any distinction between solute and solvent [34]–[36]. The HEAs reportedly derived their distinct properties through the main four core effects which are high entropy effect, severe lattice distortion, sluggish diffusion, and cocktail effect which imparted excellent properties such as high hardness, corrosion resistance, improved tribological properties, superior tensile strength, better thermal stability, and other different novel physical properties [37]–[39].

HEAs metallic powder is generally obtained through different processing techniques such as atomization [40], and mechanical alloying [41]. Whereas mechanical alloying was reported widely due to easy and better control of processing attributes such as milling atmospheric condition, milling time, processing control agent, milling RPM, the ball-to-powder weight ratio, and volume fraction of particles [42]. The desired particle size and morphology achieved can be achieved by optimizing these process parameters. The dominant key attributes are milling time and RPM followed by the ball-to-charge weight ratio and PCAs [43], [44].

In-situ reaction, powder metallurgy, spray deposition, melt infiltration, casting procedures, and others are among the fabrication techniques that are most frequently employed to develop aluminium metal matrix composites [45]. The spray depositing technique is used to simultaneously spray metal melt and reinforcing particles in an inert atmosphere environment while fabricating composite materials. The undesirable particle segregation phenomena substantially decreased, although the preparation method is complex, and a sophisticated instrument is needed [46]. Melt infiltration used capillary force to bring hot, molten metal into the preform. Although the approach provides a consistent material structure and a superior combination of traits, Its drawbacks include a difficult process and a higher interface wetting [47]. Even though the powder metallurgy technology yields better properties, production costs are higher, and making any sizable products is just not feasible given the extensive processing requirements and equipment requirements [48]. Due to its simplicity, low cost, and scalability, the casting process is the most efficient for producing matrix composites for industry sectors [49], [50].

It is widely acknowledged that mechanical properties greatly rely upon chemical composition, microstructure, size and morphology of reinforcement particles, processing technique, and also on some physical characteristics such as grain size, density, and porosity developed [49], [51], [52]. Whereas, a comprehensive study that deals with the artificial ageing of AMCs is not appropriately discussed. Thermal aging can enhance the properties such as hardness and strength by microstructural stabilization [53]. Dutta and Surappa [54] revealed that thermal aging can effectively be influenced by concentration, morphology, and distribution of reinforcement in the AMCs, ageing time, and temperature. Kurita et al. [55] stated that due to mismatch in thermal strain present in composite elements leads to dislocations and excessive

vacancies which improve the precipitation kinetics vis-à-vis ageing behavior. Sekar et al. [50] revealed that hardness and strength are influenced by ageing conditions. The composite showed a decrease in strength while exceeding peak age temperature. It was observed that composite possesses higher strength than matrix alloys at high temperatures. S.Z.Zhu et. al. [56] investigated the hardening ability of peak artificial aged Al-Mg-Si alloy and SiC_p/Al-Mg-Si. It was noticed that stronger precipitation strengthening was an exhibit for composite than the alloy owing to smaller precipitation size and larger volume fraction. In a different study, R. Perez-Bustamante et. al. [57]studied the effect of artificial ageing on mechanical properties and evolution of the microstructure of mechanically alloyed carbon nanotube/Al2024 composite. The finding of the study indicated the good distribution of Al_4C_3 and CNT_s in the Al matrix due to rapid growth in precipitation kinetics. The composite possesses higher mechanical characteristics owing to the better thermal stability of Al_4C_3 and CNT_s in the Al matrix. It is well established that AA 6082 belongs to an Al-Mg-Si aluminium alloy which is heat treatable and posse's medium strength, superior, corrosion resistance, better weldability as well as better processability [58], the alloy mainly found its application in automotive parts, rail transit parts, and ship buildings. However, the strength of AA 6082 is not enough that used for high-performance components. Therefore, the strengthening of AA 6082 is vital to improve its applicability. Hence it is important to investigate the AA 6082 metal matrix composite.

The increase in service demands, requirements for improved performance, and the need to create lighter-weight components have driven the need for innovation in cast metal and the development of new lightweight materials and which has emerged as the strong reason for the advent of lightweight metallic composites [14]. Among all available metallic matrices, Mg, Cu, and Al metals (or their alloys) are being most commonly used materials. Development of Mg metallic composites has been limited due to some disadvantageous characteristics arising in it such as lower ductility and instant reactivity (oxidation) while exposed to higher temperatures which require an inert (nonreactive) environment during fabrication [59]. Cu metallic composites are mainly used where electrical and thermal properties are the major requirements; however, the pure form of Cu metal is relatively less impressive as a matrix since it poses inferior strength [60]. AMCs overcome these shortcomings to a significant extent and are being prominently used since they offer excellent strength-to-weight ratio, resistance to abrasion and corrosion, feasibility, and ease in processing through different techniques with

relatively reduced cost [61]. Attaining expected properties through the developed AMCs, selection of appropriate matrix and reinforcement is a very vital stage. Amongst all commercially available Al alloys, A199, AA 2024, A356, AA 6061, and AA 7075 are the frequently adopted matrix materials in the production of AMCs. On the other hand, there are several categories of reinforcements such as particles (particulates), fibers, agricultural wastes (agro-wastes), and industrial wastes with varying geometry and architecture and are being significantly incorporated in the Al matrix for the development of AMCs [62]. The advantageous features of whiskers such as SiCw, Al_2O_{3p}, and $SiNO_3$, or discontinuous particulates such as mostly B_4C_p, Al_2O_{3p}, and SiC_p in the comparison of continuous fibers in the production of AMCs, can be found in the literature. However, higher cost, inferior ductility, lower fracture strength, inability against corrosion, and deficient supply in many areas have restricted the development of AMCs reinforced with discontinuous reinforcements. After going through several research studies, it has been observed that the overall performance of the developed discontinuously reinforced AMCs is a robust function of the reinforcements embedded in the matrix. Additionally, based on these surveyed articles, to improve the overall performance of AMCs, the following methodologies can be adopted; (i) first methodology while dealing with limited availability and costlier reinforcements is to choose another alternative and economical reinforcements such as derivatives of various agricultural and industrial wastes with abundant availability and cheaper cost. The research study [63] reported that the developed AMCs with these alternatives exhibited considerable enhancement over unreinforced matrices, however, some inferior behaviors have also been noted as compared to discontinuously reinforced AMCs, and (ii) in addition to these two remedies, another approach is to optimize the reinforcement sizes to nanoscales while dealing with micron (or submicron) ceramic particulates [64]. Mechanical properties such as ductility and fracture strength of discontinuously reinforced AMCs improved without any compromise in the strength. However, greater cost, scarce availability, and segregation of these nano particulates during processing have been recognized as the major challenges in the development of nanoparticulated AMCs [65]. In several research studies, AMCs containing conventional ceramic reinforcements have reported many typical defects, such as extreme brittleness, porosity, agglomeration, and detrimental interfacial reactions, that adversely restricted their applications [66]. To eliminate these defects occurred in the AMCs, many novel

reinforcements, such as Al based- (e.g. $Al_{84}Gd_6Ni_7Co_3$), Fe based- (e.g. $Fe_{74}Mo_4P_{10}C_{7.5}B_{2.5}Si_2$) [67], Ti-based- (e.g. $Ti_{55.5}Cu_{18.5}Ni_{17.5}Al_{8.5}$) [68], Zr based- (e.g. $Zr_{57}Ti_8Nb_{2.5}Cu_{13.9}Ni_{11.1}Al_{7.5}$) [69], Mg-based- (e.g. $Mg_{58}Cu_{28.5}Gd_{11}Ag_{2.5}$) [70] metallic amorphous alloy/bulk glass particles and fibers, high entropy alloy particles ($CoNiFeAl_{0.4}Ti_{0.6}Cr_{0.5}$) [71], Ti-Al-Nb-Mo-B (TNM) crystalline particles [72], and intermetallic have been incorporated significantly. The aforementioned novel reinforcements offered extremely reduced porosity [73], and greater interfacial properties (i.e. greater compatibility with the matrix material owing to their metallic nature when compared with other conventional ceramic particles [74]. Moreover, the closer coefficient of thermal expansion between the amorphous alloy reinforcement and the metallic matrix resulted in improved interfacial stability, unlike that noticed in the case of conventional ceramic reinforcements. These outcomes together significantly enabled the superior mechanical performance of AMCs [75].

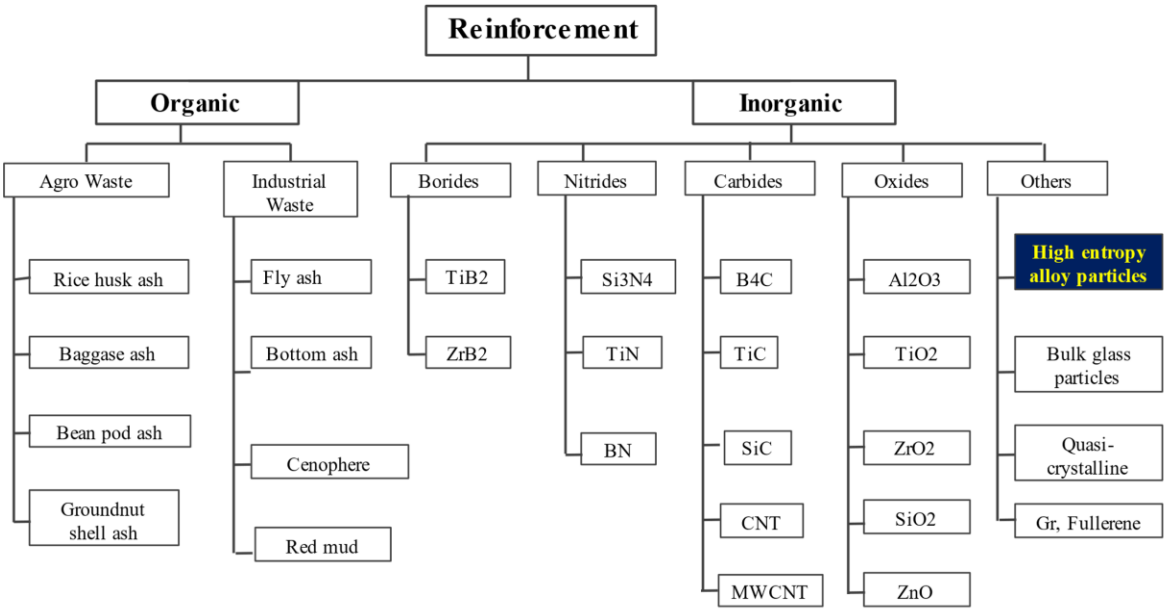

Figure 2.2: Classification of reinforcement used in the aluminium metal matrix composite

2.3.2 HIGH ENTROPY ALLOY

Over the era, metals (alloys) have played a significant role in almost all aspects of human lives. For many years, metals were used in hunting tools and agricultural equipment, and thereafter it was applied in transportation, energy, and defense sectors [76]. The periodic development of

metals and alloys is illustrated in Figure 2.3. Alloying of materials in material science and engineering for centuries has followed the same principle of using two or three elements in which one is the primary element in a larger concentration whereas the secondary element with smaller concentration[77], [78]. Considering numerous research articles [79]–[83], several alloys of iron, zinc, copper, aluminium, magnesium, and titanium have been developed and investigated for mechanical, thermal, and tribological properties. Although in recent progress the chemical composition of alloys has been extended, for example, Inconel 718 superalloy and other elements are being used with Nickel alloy[84]. HEAs have considerably gained the attention of researchers due to their superior properties over the traditionally used alloys [85], [86]. These properties are not restricted to the higher hardness [87], while, combined with greater strength, improved fatigue[88] as well as ductility [89], stability at elevated temperature, exceptional resistance against corrosion[90], wear, and oxidation [91] are also noticeable in such alloys. Thus, HEAs are familiarized as the front-most innovative class of materials having a wide range of potential applicability in several sectors from the automobile to marine [92], [93].

However, discussion on the effect of MA and its parameters on the performance of the HEAs is noticed to be very scarce. Therefore, an effort has been made to critically assess the role of MA in the processing of HEAs including various challenges and their prospects. Furthermore, recommendations regarding various process variables associated with MA are also made to assist and encourage ongoing and upcoming research.

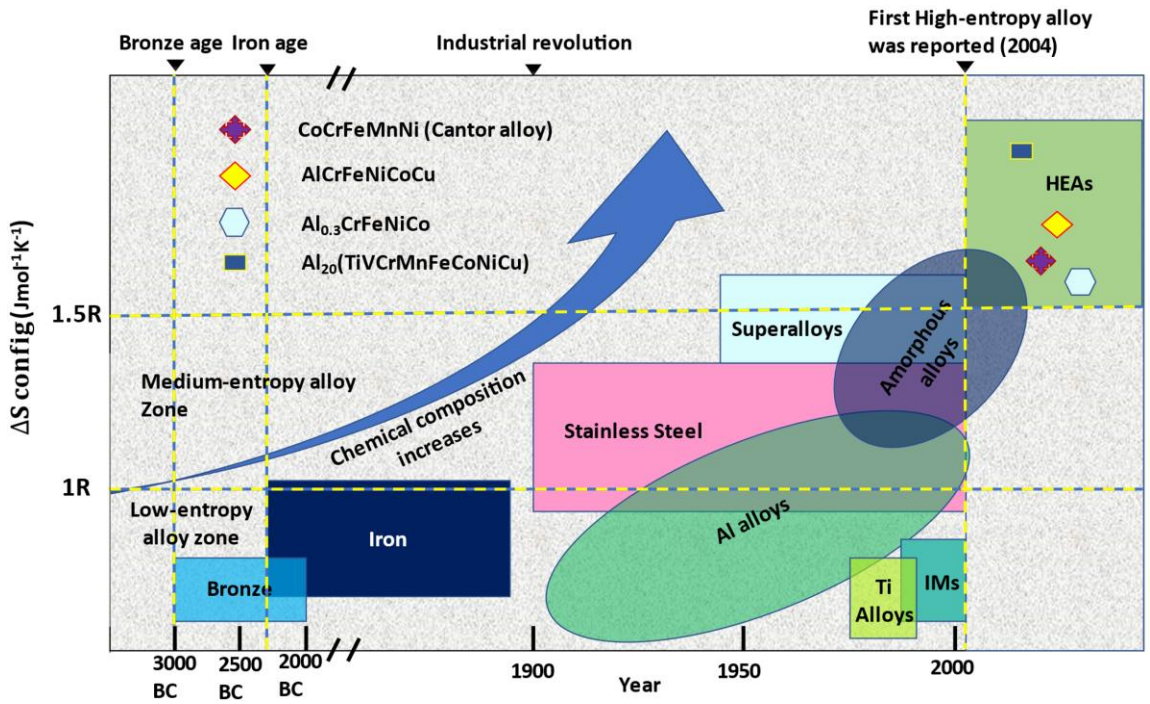

Figure 2.3: Periodic development in metals [94]

2.3.3 CONCEPT OF HIGH ENTROPY ALLOYS (HEAs)

HEAs were first investigated by cantor et al. [95] and yeh et al. [32] separately in 2004 and it was conveyed that these materials were different from the conventional alloys in terms of the design approach. In the last few decades, the alloying approach generally consists of two or three elements, whereas the HEAs consisted of five or more principal elements maximum up to thirteen in the equiatomic ratio [32], [96]. According to the binary and ternary phase diagram, several phases would evolve with the involvements of multi-elements, while yeh et al. [32] reported that configurational entropy was high enough to form stabilized single or double phases with a simple crystal structure. Several researchers termed this new class of materials as high entropy alloys (HEAs), whereas in many research articles, other terms were also coined such as multi-principal elements alloys and compositionally complex alloys [89], [97], [98]. The progressive evolution of the compositionally complex alloys is shown in Figure 2.4. In general, the concept of HEAs further broadened and categorized into three categories such as high entropy alloys (more than five elements), medium entropy alloys (three or four principal elements), and small entropy alloys (less than 3 principal elements) [99], [100] as

shown in table 2.1. Moreover, HEAs are no longer limited to the development of perfect HEAs but the focus of academia and researchers shifted to utilize the entropy and develop a specific combination to attain desired mechanical and functional properties.

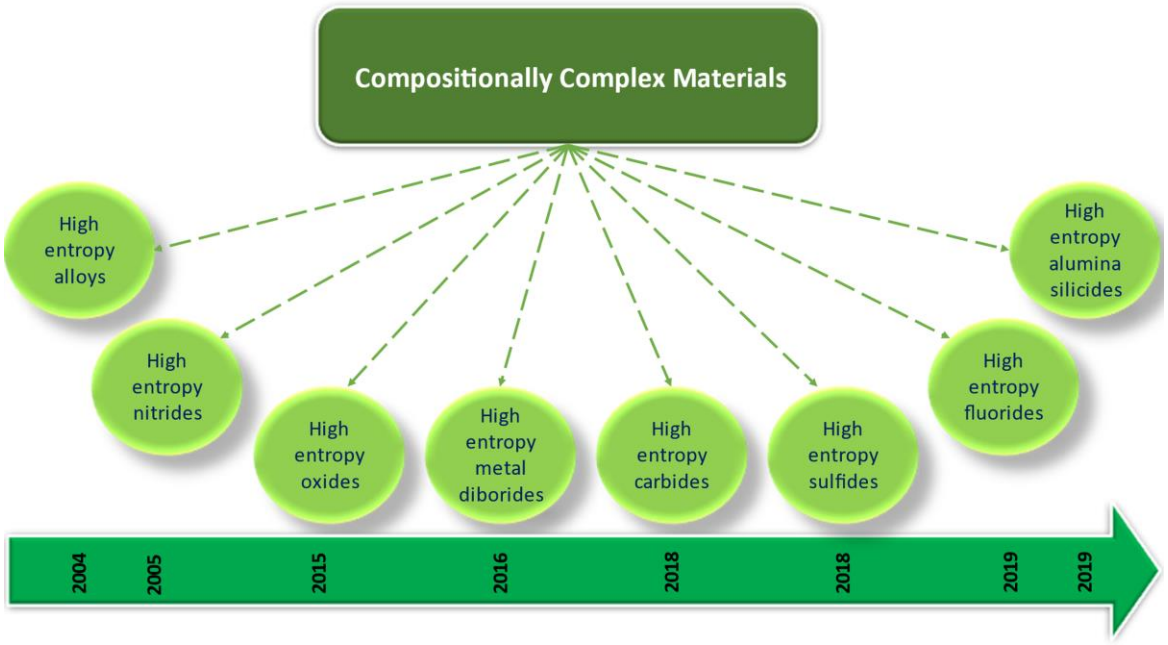

Figure 2.4: Evolution of compositionally complex materials [101]

Table 2.1. Classification of high entropy alloys based on the element range

Alloy	Elements range	Entropy	Lattice	Examples
High Entropy Alloys	$5 \leq n \leq 13$	$\Delta Sconfig > 1.5\ R$		AlCoCrFeMnNi, CoCrFeMnNi, AlCrCuFeNi, MoNbTaW

Medium Entropy Alloys	$3 \leq n < 5$	$1R \leq \Delta Sconfig \leq 1.5R$		CoCrNi, CoCrFeNi
Low Entropy Alloys	$1 \leq n < 3$	$\Delta Sconfig < 1R$	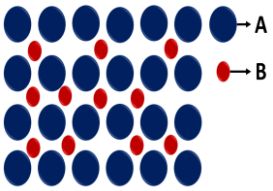	Al-Mg, Al-Cu, NiCo

Table 2.2: Difference between conventional dilute alloys and high entropy alloys considered from different aspects

S.No.	**Aspects**	**HEAs**	**Conventional dilute alloys**
1.	Compositional space	High- and hyper-dimensional	Low-dimensional
2.	Alloy design strategy	Based on multi-principal elements	Based on one or two principal elements
3.	Solid solution	undistinguishable solvent and solute atoms	Distinguishable solvent and solute atoms
4.	Composition	Limitless	restricted
5.	Concentration of secondary elements	Concentrated	Dilute
6.	Phase diagram	Central region	Edges & corner
7.	Modulus mismatch	Severe	Average

8.	Configuration entropy of mixing	Higher	Lower
9.	Lattice distortion	Severe	Mild
10.	Properties	Enormous possibilities	Limited possibilities
11.	Atomic size mismatch	Severe	Mild
12.	Microstructure	More diversified	Less diversified
13.	Solid solution strengthening	Stronger	weaker
14.	Diffusion	Sluggish	Relatively fast

In contrary to conventional alloys, the term "high entropy alloys" was coined since it was believed that random phases formed sooner than intermetallic compounds owing to the high entropy of mixing, which stabilized the phases and formed a basic crystal structure [32]. Researchers have introduced terminologies like multi-principal element alloys and compositionally complex alloys to describe this new class of materials [89], [97], [98]. Some HEAs are classified according to their compositions and microstructures, while others are classed according to their properties or a combination of properties and microstructure stated in Table 2.3.

Table 2.3: Classification of High entropy alloys

S. No.	**Based upon**	**Classification**	**Refer.**
1.	Composition	a) Equiatomic HEAs, b) non-equiatomic HEAs	[85]
2.	Composition	a) Light weight HEAs, b) 3d transition metal HEAs, c) refractory metal HEAs, d) precious metals HEAs, e) interstitial compound HEAs, f) lanthanide transition metal HEAs	

3.	Microstructure	a) Single-phase HEAs, b) dual-phase HEAs, c) multi-phase HEAs	
4.	Microstructure	a) FCC AlCoCrCuFeNi and derivatives, b) FCC CoCrFeMnNi and derivatives, c) BCC refractory HEAs, d) HCP HEAs, e) other HEAs	
5.	Microstructure	a) Random solid solutions, b) ordered solid solutions, c) intermetallic phases	[102]
6.	Microstructure	a) Terminal solutions, b) intermediate solutions, c) intermetallic compounds	
7.	Microstructure	a) Simple disordered phases, b) simple ordered phases, c) complex ordered phases	
8.	Microstructure	a) Solid solutions, b) intermetallic compounds, c) a mixture of solid solutions and intermetallic compounds	[103]
9.	Microstructure + properties	a) FCC strong and ductile HEAs, b) BCC refractory HEAs, c) HCP HEAs, d) lightweight HEAs, e) precious functional HEAs	[104]
10.	Mechanical properties	a) FCC 3d-transition metals, b) transition metals with larger-atomic-radius elements, c) BCC refractory metals, d) others	[105]
11.	Phase stability	a) Stable HEAs, b) metastable HEAs	

2.3.4 FOUR CORE EFFECTS ASSOCIATED WITH HEAs

HEAs derive their unique properties from four core effects which make them different from the rest of the alloys [106], [34]. The core effect influences the morphology as well as the intended properties of HEAs. The mechanics of the four core effects and their mutual relationship with microstructural and mechanical properties are demonstrated in Figure 2.5.

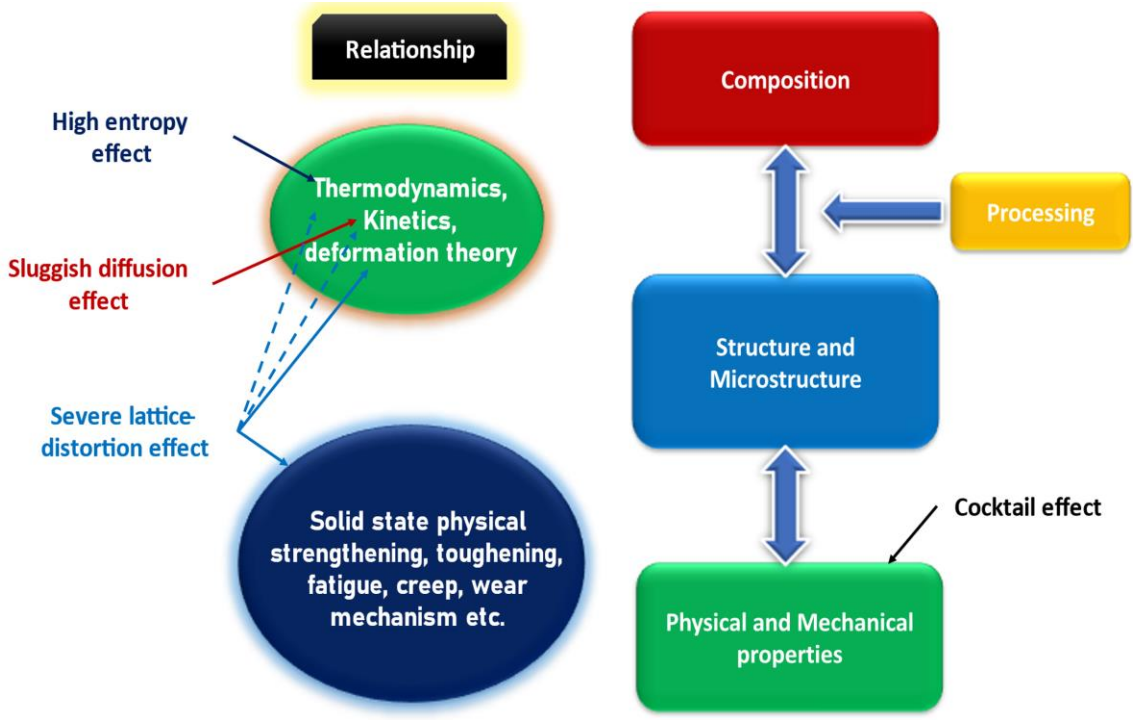

Figure 2.5: Four core effects and their relationship with microstructure and properties [107]

2.3.4.1 HIGH ENTROPY EFFECT

The high entropy effect is associated with the thermodynamic aspect of alloys and is recognized as one of the four core effects. Based on the second law of thermodynamics, the state which has the lowest Gibbs free energy is termed an equilibrium state[85], [106]. It is observed that the high entropy raises the stability of solid-solution phase evolution. The high entropy effect is crucial to inhibit the formation of intermetallic which are highly brittle and thus difficult to analyze[105].

2.3.4.2 SLUGGISH DIFFUSION

The sluggish diffusion effect prevents the atomic diffusion of the elements, restricts the phase transformation, and leads to the formation of fine precipitates, amorphous structure, slower grain growth, higher recrystallization temperature, reduced coarsening rate, and enhance creep resistance[108]. It also offers better control over the morphology and microstructure of HEAs as well as enhances their performance [109], [71].

2.3.4.3 SEVERE LATTICE DISTORTION

Severe lattice distortion causes due to the multi-principal elements in the matrix of the solid solution phase in HEAs. Each atom is surrounded by a different kind of atom of varying atomic size and is responsible for lattice stress and strain. Crystal structure and different bonding energy cause higher lattice distortion because the electronic structure and nonsymmetrical binding exist between the atoms and this non-symmetry differs from site to site in the lattice. Lattice distortion avoids the thermal effect due to the significant solution hardening in a highly deformed lattice and enables improved strength and hardness [110], [111].

2.3.4.4 COCKTAIL EFFECT

The cocktail effect is first coined by Ranganathan et al. [112] and stated that the cocktail effect is highly stressed in HEAs as at least five principal elements are used to enhance the properties of the materials. According to the composition and processing, HEAs can have single, or multiple phases [113]. The derived properties are the result of the overall contribution of phase distribution, the shape of phases, and the properties of the individual phase. Each phase is a solid solution consisting of multiple elements and these solid solutions can be described as atomic-scale composites. The obtained properties are the outcome of basic properties and mutual interaction between the elements and severe lattice distortion [114], [115]. Figure 2.6 presents a lattice arrangement that leads to different core effects in HEAs.

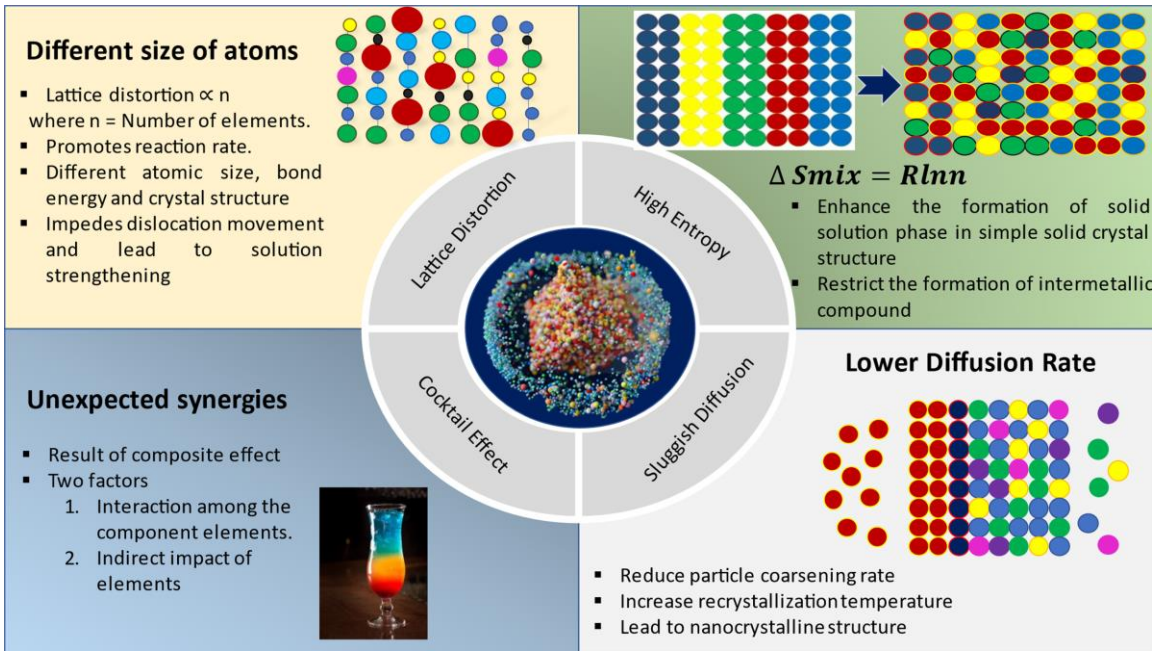

Figure 2.6: Lattice arrangement that leads to different core effects

2.4 PROCESSING METHODS FOR HEAs

The preliminary step in the processing of HEA is to obtain a fine metal powder, especially in HEAs where five or more principal elemental metallic powders contribute to the alloy. From different research articles, it is observed that mainly two routes are adopted for the processing of HEAs. By using pre-alloyed powder as the preliminary material, and another is by conventionally mixing metal powder and followed by cold isostatic pressing or spark plasma sintering to provide the desired shape [116]–[123]. In fully pre-alloyed powder basically, two methods are used i.e., atomization and MA, and other routes to obtain HEAs by melting and then powdering by high energy milling [124], [125]. Figure 2.7 encompasses the various methods including their percentage contribution in the processing of HEAs. In addition, table 2.4 significantly compares different HEAs processed through varying techniques including their key features and applicability.

The pre-alloyed HEA powder is developed generally through MA and gas atomization which is then consolidated through various consolidation techniques as shown in Figure 2.7. MA followed by spark plasma sintering is proven to be one of the best combinations for the bulk production of HEAs [126]. The most common method used for pre-alloyed powder is MA as it gives the choice to researchers to get any composition feasible with enough energy and

time duration. In SPS sintering, temperatures attain at the short interval and have low dwell time which resulted in a highly dense structure and avoiding excessive grain growth. There are some other methods such as hot pressing and hot isostatic pressing through which a highly dense structure is obtained but that requires high temperature and needs to be kept for a long duration which results in higher grain growth.

After the SPS, the next most famous consolidation technique for processing HEAs is the conventional press and sintering route for large production. Most of the work is concentrated on conventional uniaxial pressing whereas a few publications are reported where the cold isostatic press is used [127], [128]. Mostly HEAs are processed through traditional vacuum arc melting (VCM) or induction melting (IM) followed by MA and then sintering using the spark plasma method. In the melting technique [129], the casted material needs to be reheated several times to prevent the non-uniformity of the elements. The time-consuming characteristics yielded by both the techniques and some HEAs require higher cooling rates to diminish the precipitation of unwanted intermetallic compounds/phases occurring through the solid solution phase. In addition, based on the aforementioned discussion, the fabrication of some HEAs through conventional techniques leads to laborious work, especially while dealing with complex geometries [87].

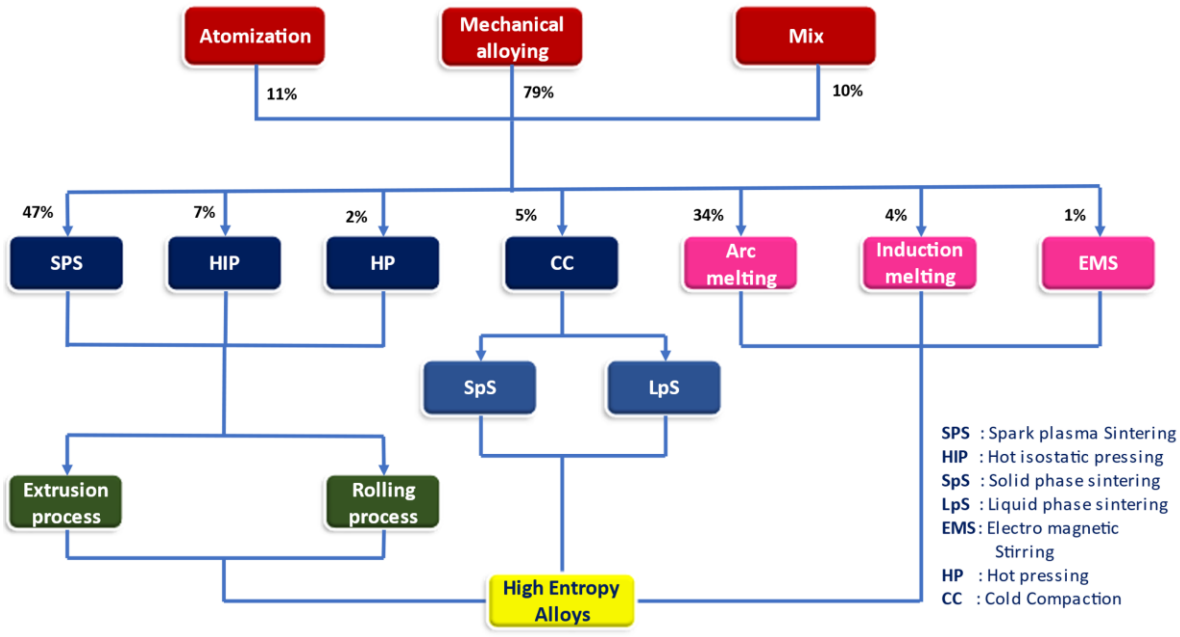

Figure 2.7: Different methods and their contribution in the processing of HEAs

Table 2.4. HEAs synthesized through different processing techniques

HEA	Processing route	Major outcome	Salient features		Applications	Ref.
			Favorable	Adverse		
$Al_{0.5}$CoCrFeNi	Arc melting	Slow diffusion rate	Highly efficient, better level of solubility	Difficulty in the complex composition	Aviation and turbine manufacturing	[340]
CoCrFeMnNi	Vacuum arc melting	Superior anti fouling properties	Lower specific energy consumption, better workability, development of high melting point HEAs	Grain refinement is limited, melting dangerous, higher electrode production cost	Marine, ship vessels	[341]
FeCoNiCrMn	Cold spraying	Lower wear rate	No phase change, no aggregation, higher bond strength, lower wear rate	Porosity issue, Limited ductility, high equipment cost	Coatings in the automobile sector	[342]
AlCOCrFeNi	Electron Beam Melting	Tensile strength 197MPa	Better purity, large ingots, lower energy consumption, superior microstructural control	Brittle product, limited alloying, material losses, higher melting cost	Tools and high-temperature applications	[343]
CrMnFeCoNi-WC	Laser melting deposition	Tensile strength 800MPa	Equiaxed grains, Homogeneous composition, complex geometry, grain refinement	Hazardous, no support structure	Coatings	[344]
MgMoNbFeTi2Yx, CuAlNiCrFe	Laser Cladding	Hardness value 1046 HV	Better surface finish, quick and effective	Poor internal performance	The lightweight structural material, automotive and electronic sector	[109], [345]

AlCoCrFeNi, CoCrFeNiTi	Mechanical alloyed followed Spark plasma sintering	Compressive yield strength 1537 MPa	In single operation compaction and sintering took place, homogeneous dispersion of particles.	Applicable only for a simple and symmetrical design.	Coatings	[346][347]
CoCrFeMnNi	MA followed by hot isostatic sintering	Compressive yield strength	Better mechanical strength, low porosity	Time-consuming, lower yield, higher energy consumption, unsuitable for nanocrystalline structure	Weldings	[242]
CoCrFeNi	Gas atomization followed spark plasma sintering	Hardness 271HV, yield strength 610MPa, Compressive strength 921 MPa	Enhanced thermal conductivity, enhanced wear characteristics, and homogeneity in the particle distribution	Suitable for the simple and symmetrical object, lower solidification rate limited to small size product	The structural component in a nuclear reactor	[348]
$FeCoNi_{1.5}CuY_{0.2}B_x$	Cold isostatic pressure followed microwave sintering	Compression strength 1546MPa, yield strength 1112MPa, hardness 367.1 HV	rapid heating rate, improved physical and mechanical performance-enhanced diffusion processes, lower energy consumption, and eco friendly	Expensive equipment, difficult for ceramics	Structural application and high load applications	[220]

2.5 MECHANICAL ALLOYING

The fabrication of HEAs via MA was first reported by S. Vara Lakshmi et al. [37] who developed nanocrystalline AlCrCuFeTiZn HEA. Afterward, an upward trend is realized in research publications that dealt with MA. At present, there are only three review articles available on mechanical alloyed HEAs [130]–[132]. Thereby, this review aims to provide the latest development in the field of mechanical alloyed HEAs and subsequently mechanical & functional properties enabling potential applications. MA is a non-equilibrium process suitable for powder processing of alloys containing low/high melting point constituents, synthesis of nanocrystalline materials with uniform microstructures and compositional homogeneity, as well as for achieving an extension of solid solubility. MA is a solid-state fabrication technique used for the development of smart and advanced materials [133], [134]. The main objective of milling is to reduce the particle size, mixing and blending, and reshaping of the particles [135], [136]. In MA, particles embedded the reinforcement phase into the matrix during the repetitive welding-fracturing-welding period [137]. During the milling, metal powder trapped between the balls or in the ball-wall surface leads to deformation, fracture, or welding that depends on the mechanical characteristics of the metallic powder [138]. A steady-state equilibrium is reached between the rate of welding and fracturing after milling for a certain time [139]–[141]. This approach requires the strengthening process to be homogeneously distributed and supersaturated solid solutions to be formed. In the next step, the particles get deformed which results in a change of their morphology from straightened to the original one. The welding process, which produces equiaxed particle formation, predominates in the following step. Oriented welding lines are observed at this stage, thereafter welding and fracturing processes achieve equilibrium, and spontaneously aligned welding lines predominate in the forming of particles. The end-stage is characterized by the phase of steady-state in which refinement of microstructure begins, but the distribution of particles and size remains roughly constant [142]–[144]. The key characteristics of MA include the development of a fine mixture of secondary phase particles, expansion of solid solubility limits, refinement of grain sizes down to the nanometer range, synthesis of novel crystalline and quasi-crystalline structures, formation of amorphous phases, and encouragement of chemical reactions at low temperatures [145], [146]. The whole mechanism of MA can be understood in Figure 2.8.

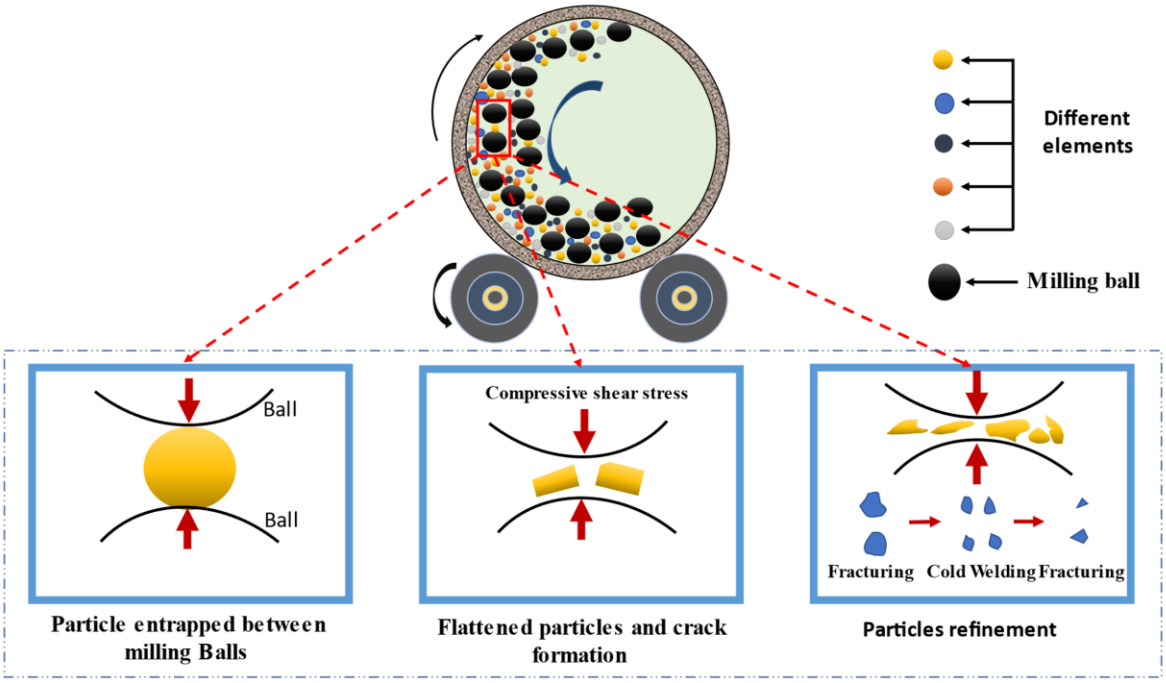

Figure 2.8: Planetary ball milling and different stages in MA [147]

MA depends on various major factors as shown in Figure 2.9, that play a vital role in the development of homogenous compounds. These factors control the end product properties such as final stoichiometry, amorphization, and the degree of disorder. Better control of these factors results in improved powder development. The current status of research articles dealing with the associated variables of MA is portrayed in Figure 2.10. Furthermore, different factors and their effects on HEAs crystal size and lattice strain are comprehensively discussed in table 2.5.

Salient Features for mechanical alloying

- MA includes shorter time, lower energy consumption, better adhesion of coatings, and favorable flexibility to form various structural coatings.
- It provides better compositional accuracy and can overcome the problem of segregation.
- Best-suited technique to produce nanostructured alloy or composites with better chemical homogeneity.

- It exhibits a higher diffusion rate.
- It is best suited to produce different classes of materials i.e. amorphous, quasi-crystalline materials and oxide dispersion strengthened, etc.[148]
- HEA alloy powder is the preferable technique for achieving nanocrystalline nature, however difficult to retain its nature for bulk material. [148]

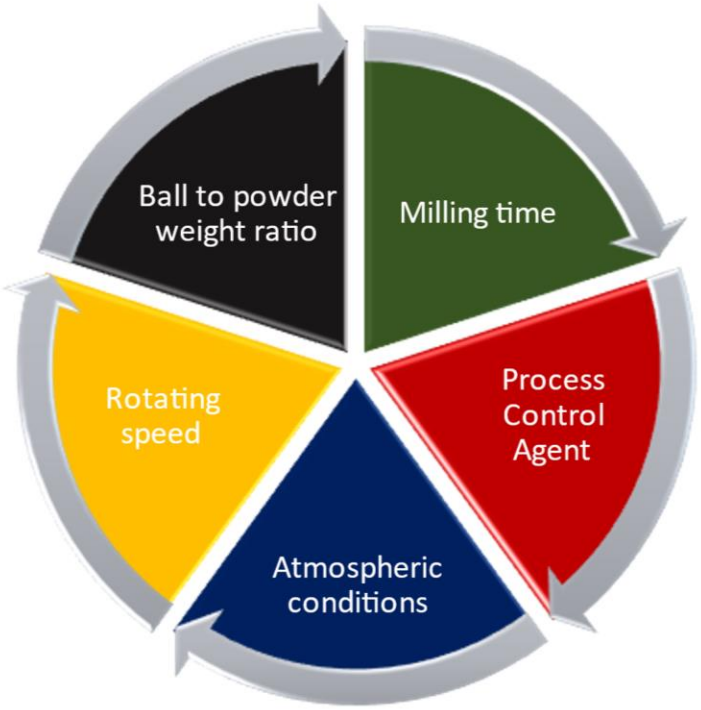

Figure 2.9: Different major factors associated with MA

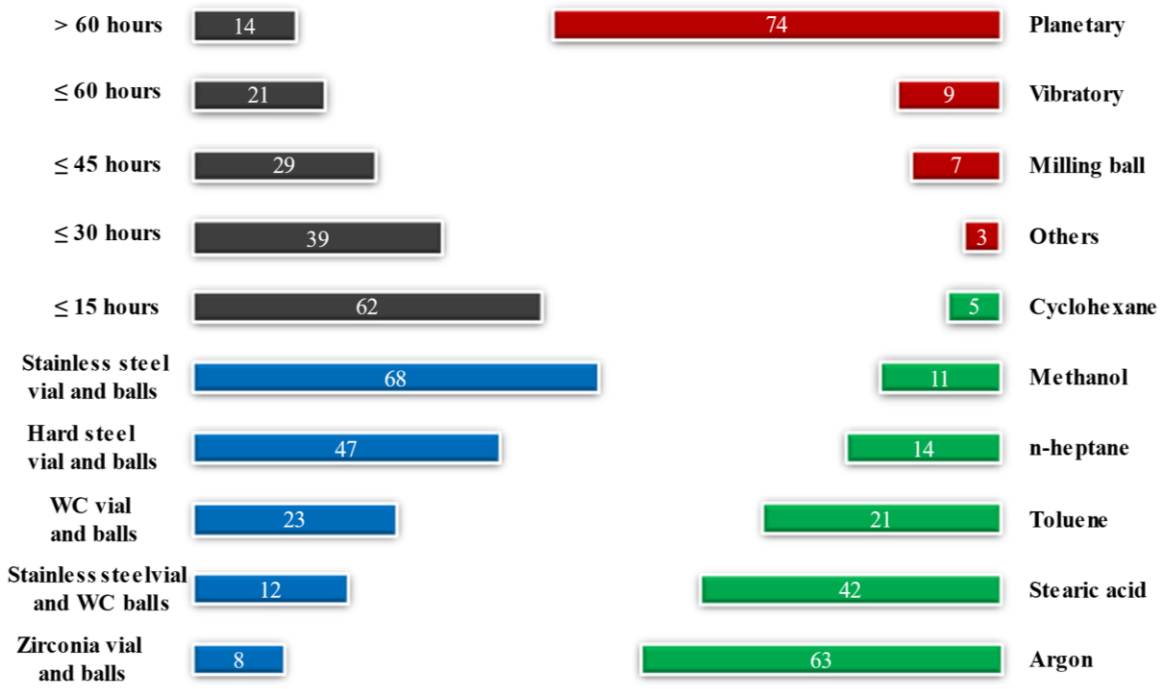

Figure 2.10: Current status of research publications on different factors associated with MA

Table 2.5. Different HEAs processed through the MA technique

HEA Powder	Feed Stock		Milling Parameters			Lattice strain (%)	Crystallin e size (nm)	Phase	Refe r.
	Purit y (%)	Particl e size (µm)	Speed (RPM)	Time (h)	Ball-to-powder ratio				
CoCrCuNi	99.5	-	300	15	10:1	-	6-10	BCC+FC C	[149]
$Al_xCoCrFeMnNi$	99	45	600	14	18:1	0.84-1.28	7.4-11.4	FCC	[150]
$Co_xCrCuFeMnNi$	99.5	75	300	50	10:1	1.05-1.84	5.6-8.9	BCC+FC C	[151]
$Al_xCoFeNi_{1.5}V_{0.5}Cu_{1-x}$	99.5	48	300	70	10:1	1.21-1.52	6.3-7.7	BCC+FC C	[152]
$CrFeMoVMn_x$	99	75	200	15	10:1	-	-	σ + BCC	[153]
$(AlCrFeMnV)_{100-x}Bi_x$	99.5	-	200	25	20:1	-	-	Bi+BCC	[154]
AlCoCrFeNiSi	75	75	300	30	10:1	0.73	11.7	BCC+FC C	[155]
$AlCo_xFeNiSiB$	99.5	75	350	140	15:1	-	-	BCC	[156]

AlCoCrFeCu	99.5	-	300	15	10:1	0.5	10	BCC+FCC	[157]
AlCoCrFeMnNi	99	45	200	40	10:1	0.24-0.70	15-20	BCC	[141]
$Al_{0.4}CoFeNiSi_{0.4}$	99	-	300	70	20:1	-	-	BCC+FCC	[158]
$AlCoCrCuFeTi_x$	-	45	300	20	10:1	0.096-0.231	13-58	BCC+FCC	[159]
$Al_{0.4}CoCr_{0.5}FeNiTi_{0.6}$	99.6	30	-	30	10:1	0.175	7	BCC+FCC	[160]
AlCrFeTiZnCu	99.5	45	300	20	10:1	1.31-1.52	9-10	BCC	[37]
CoCuFeNi	99.5	-	300	15	10:1	0.73	9	FCC	[157]
$Co_{1.5}CrFeNi_{1.5}Ti_{0.5}$	99.5	-	250	30	10:1	-	-	BCC+FCC	[161]
$CoCrFeMnNiTi_{0.3}C_{0.3}$	99.5	-	250	45	15:1	-	-	BCC+FCC	[162]
CrFeNiTi	99.9	50	400	10	25:1	1.5	6.53	FCC	[163]
AlCoFeNiCu	99	-	-	10	5:1	-	7.1	BCC+FCC	[164]
$Al_xCrFeMoV$	99.5	-	200	7	10:1	-	-	BCC	[153]
AlCoCrFeNiMo	99	-	-	10	5:1	-	8.3-16.5	BCC	[164]
CoCrFeNiTi	99.9	50	400	10	25:1	1.4	6.38	FCC	[163]
AlNiTiZrCu	99.5	70	350	-	15:1	-	-	Amorphous	[165]
NbMoWZrV	99.5	50	-	100	10:1	0.58	11	BCC+FCC	[166]
CoCrFeNi	99.5	-	-	15	10:1	-	10	BCC+FCC	[167]
$Al_{0.15}CoCrCuFeNiTi_xC$	99.5-99.9	180	500	36	15:1	-	-	BCC+FCC	[168]
AlCoCrFeNiCuTi	99	-	-	10	5:1	-	6.8	BCC+FCC	[164]
CoCrFeMnNi	99.9	-	250	45	15:1	-	-	FCC	[162]
NbMoTaW	99.9	48	300	60	10:1	0.688	11.8	BCC	[140]
CoCrCuFeNi	99.5	-	300	15	10:1	1	7	BCC+FCC	[157]
CoCrFeNi	99.5	-	300	15	10:1	0.83	6	BCC+FCC	[157]
$(CuCrFeTiZn)_{100-x}Pb_x$	99.5	-	200	44	20:1	0.0372-0.1092	-	BCC+FCC	[154]

$(CuCrFeTiZn)_{100-x}Pb_x$	99.5	-	200	25	20:1	-	-	BCC+FCC+Pb	[154]
NbMoTaWV	99.5	75	300	6	10:1	0.96	66.1	BCC	[169]
$Fe_{18}Ni_{23}Co_{25}Cr_{21}Mo_8WNb_3C_2$	99.5	70	940	24	60:1	-	-	Mo + γ	[170]
NbMoTaWVTi	99.9	-	-	40	13:1	-	-	BCC	[171]
CoCrFeMnNi	99.9	300	1100	1	10:1	-	11	FCC	[172]
FeCoNiMnV	99.9	20	350	96	10:1	-	-	BCC+FCC	[173]
AlCuNiFeCr	99.8	45	580	5	10:1	0.2893-0.2889	14	BCC	[174]
FeCoCrNiMn	99.9	45	250	45	15:1	-	11.4	FCC+BCC+σ +Cr23C6	[175]
FeCrVNbMn	99.5	45	500	10	10:1	1.06	40	FCC	[176]
MoNbTaTiV	99.9	48	350	40	10:1	0.89	12.9	BCC	[177]
WMoVCrTa	99.5		250	32	6:1	-	3.1586	BCC	[178]
CoCrNiCuZn	99.5	45	300	6	20:1	0.70	13	BCC	[179]
$AlCoCrFeNiSi_x$	99.5		300	20	10:1	0.87	32	BCC	[180]

2.5.1 PHASE EVOLUTION IN HEAs

Phase evolution and its stability are one of the pivot themes of ongoing research in HEAs [141], [181]. Configurational entropy is the main aspect that allows the formation of solid solution phases in HEAs [37]. $\Delta Sconfig$ effect is based on the second law of thermodynamics for an irreversible process that occurs only in a single direction for a low free energy state which can be represented by

$$\Delta Gmix = \Delta Hmix - T\Delta Smix \quad (1)$$

Where $\Delta Hmix$ is the enthalpy of mixing, $\Delta Gmix$ is Gibbs free energy and $\Delta Smix$ is the entropy of mixing respectively, which are discussed in the given equation;

$$\Delta Smix = \Delta Sconfig + \Delta Sthermal \quad (2)$$

By the given equation it is clear that with an increase in $\Delta Smix$, the free energy of the solid solution decreases.

According to Boltzmann's analysis, $\Delta Sconfig$ can be calculated from the given expression,

$$\Delta Sconfig = -R \sum Xi \ln Xi, \quad (3)$$

Where R is the universal gas constant and Xi is the mole fraction,

$$\Delta Sconfig(max) \; for \; Xi = 1/n \quad (4)$$

Hence,

$$\Delta Sconfig(max) = R \ln n \quad (5)$$

where n is defined as the number of components/elements. $\Delta Sconfig$ alone is not a sufficient parameter to stabilize the solid solution but other parameters also involve to find the criterion for solid solution formation. Zhang et al [182] described certain conditions that have to be fulfilled for the formation of a solid solution.

$$\Delta Sconfig > 1.5 \, R \quad (6)$$

$$-15 KJ/mol < \Delta Hmix < 5 KJ/mol \quad (7)$$

$$\delta < 6.6\% \quad (8)$$

Where δ = size factor

Prediction of phase stability (e.g., mole fraction and number of phases) of HEAs is the function of temperature and composition. Whereas, the enthalpy of mixing is another important key parameter after $\Delta Sconfig$, which is often expressed as follows [183].

$$\Delta Hmix = \sum_{i=1, i \neq j}^{n} \Omega_{ij} \, c_i c_j \quad (9)$$

$$\Omega = \frac{T_m \, \Delta S_{mix}}{|\Delta H_{mix}|} \quad (10)$$

Where c_i and c_j are the atomic percentage of i_{th} and j_{th} component respectively. $\Omega_{ij} = (4\ \Delta H_{AB}^{mix})$, ΔH_{AB}^{mix} is the enthalpy of mixing for the binary alloys AB. If ΔH_{AB}^{mix} is positive, it indicates that elements in HEAs tend to part away easily. Whereas, intermetallic compounds are formed when ΔH_{AB}^{mix} is negative [184]. The ratio omega of $T_m \Delta S_{mix}$ and $|\Delta H_{mix}|$ is used to evaluate the solid solution formation ability [185], [186].

Valence electron concentration (VEC) is the deciding factor for the formation of a solid solution,

For BCC solid solution,

$$VEC \leq 6.87 \tag{11}$$

For FCC solid solution,

$$VEC \geq 8 \tag{12}$$

If BCC and FCC coexist,

$$6.87 \leq VEC \geq 8 \tag{13}$$

Table 2.6 shows the values of melting temperature, change in mixing enthalpy and entropy, atomic size mismatch, and valence electron concentration resulting in various phases for different HEAs. Moreover, Figure 2.11 presents the phase distribution mapping of different HEAs regarding varying element numbers.

Table 2.6. High entropy alloys with their values of aforementioned variables

HEA	**Tm[k]**	**$\Delta Hmix$**	**$\Delta Smix$**	**VEC**	**δ**	**Phase**	**Ref.**
CoCrCuFeMnNi	1720	1.44	14.9	8.5	0.99	FCC	[95]
FeCoNiMnV	1528.80	-8.96	13.38	7.80	3.47	BCC	[173]
AlCuCrNiFeCr	-	-4.00	13.38	7.6	5.62	BCC	[174]
$FeCoCrNiMnAl_0$	1517.8	-4.16	13.381	8	3.48	FCC	[175]
$FeCoCrNiMnAl_{0.1}$	1500.9	-5.24	13.921	7.90	4.07	FCC+BCC	[175]
$FeCoCrNiMnAl_{0.3}$	1469.3	-7.16	14.432	7.72	4.49	FCC+BCC	[175]

$FeCoCrNiMnAl_{0.5}$	1439.8	-8.79	14.697	7.55	4.85	FCC+BCC	[175]
$FeCoCrNiMnAl_{0.7}$	1412.5	-10.18	14.834	7.39	5.16	FCC+BCC	[175]
$FeCoCrNiMnAl_{1.0}$	1374.9	-11.89	14.897	7.17	6.56	FCC+BCC	[175]
AlCrCuFeMnNi	1580.58	-5.11	14.9	7.5	4.73	BCC	[187]
CrCuFeMoNi	1985	4.64	13.38	8.2	2.92	FCC	[188]
AlCoCrFeNi	1675.10	-12.32	13.38	7.2	5.25	BCC	[189]
AlCoCrFeNi	-	-12.32	13.38	7.2	5.77	FCC+BCC	[180]
$AlCoCrFeNiSi_{0.3}$	-	-18.18	14.43	7.0	6.12	FCC+BCC	[180]
$AlCoCrFeNiSi_{0.6}$	-	-22.75	14.77	6.8	6.37	FCC+BCC	[180]
$AlCoCrFeNiSi_{0.9}$	-	-26.32	14.89	6.7	6.56	BCC	[180]
FeNi(CoCrMn)	1400	-3.87	12.80	8.33	2.65	FCC	[181]
FeMnNi(CoCrNbC)	1400	-4.83	12.70	8.22	4.60	FCC	[181]

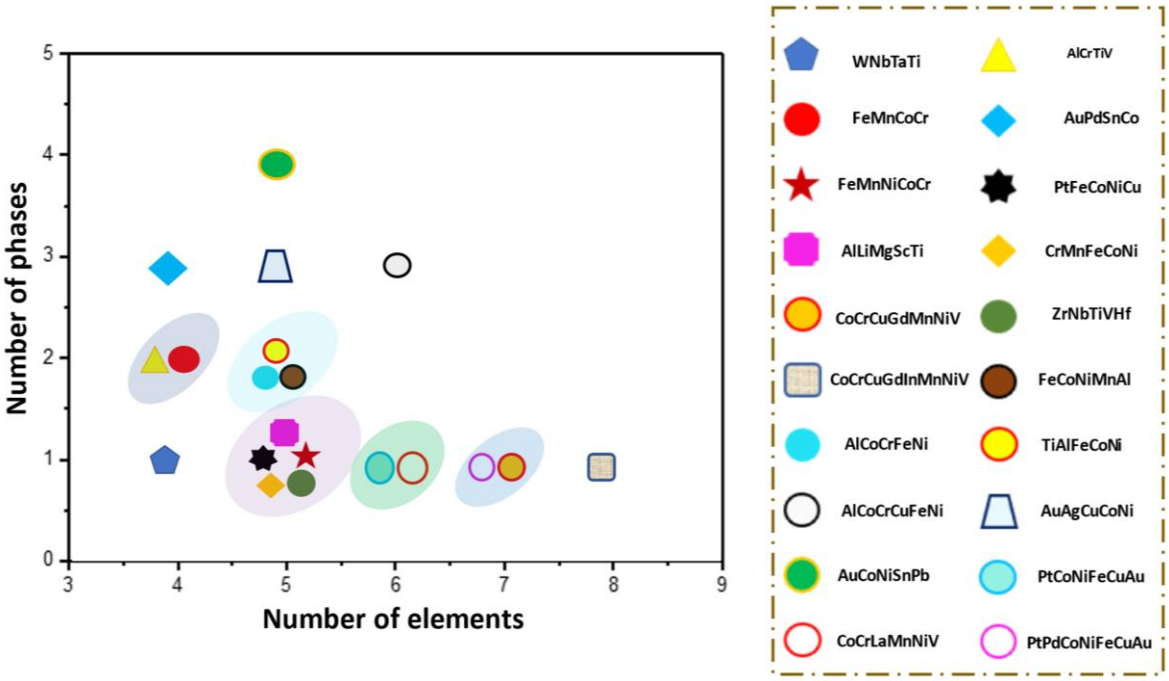

Figure 2.11: Phase distribution map of HEAs with respect to element number [98], [190]–[204].

HEAs are multicomponent alloys in which the control of configurational entropy of mixing and other parameters, already described in the literature, such as atomic size mismatch (δ), enthalpy of mixing (H), valence electron concentration (VEC), and electronegativity (χ) has allowed the formation of simple solid-solution phases rather than intermetallic compounds. The most interesting in studying HEAs is the wide range of compositions to be explored in the central regions of composition space and the consequent wide range of properties that can be achieved. The criterion, proposed by Zhang et al. [182] to predict the obtention of disordered solid-solution phases, and would also be changed by the mechanical energy. A higher value would be obtained with the introduction of tungsten (W), even when the temperature is relatively small, favoring the formation of a solid-solution phase rather than an ordered phase by using MA [42].

MA has proven as an efficient path for HEAs to accomplish superior properties by modifying microstructure and phases. It has been found that elements such as Co, Cu, Mn, and Ni promote the FCC phase while Al, Cr, V, and Ti enhance the formation of BCC phases [205]. Al plays a key role to influence the mechanical, physical, and tribological properties as well as control phase formation [206]. Chung et. al studied $Al_xCrCoCuNiFe$ (x= 0 and 0.3) HEAs and observed that with an increase in Al concentration BCC phase became more prominent which resulted in improved hardness. In another work, Al was reported as a BCC stabilizer and acting as a hardening agent in solid solutions [207]. In Milling, alloying behavior of individual elements of HEA follows systematically. In a study, Vikas Shivam et. al [141] discussed alloying behavior and phase stability of AlCoCrFeNiZn. After initial milling time, elements (Al, Zn, and Co) having lower melting points started losing their identity and formed BCC solid solution. Due to the higher diffusion rate, Al and Zn were initially affected. Co-dissolution was due to complex interaction and Fe acted as the host lattice as Cr had a higher lattice parameter than Fe. The order of elements' dissolution is represented as shown in Figure 2.12. With milling time diffraction peak broadened which attributed to a decrease in crystal size and an increase in lattice strain.

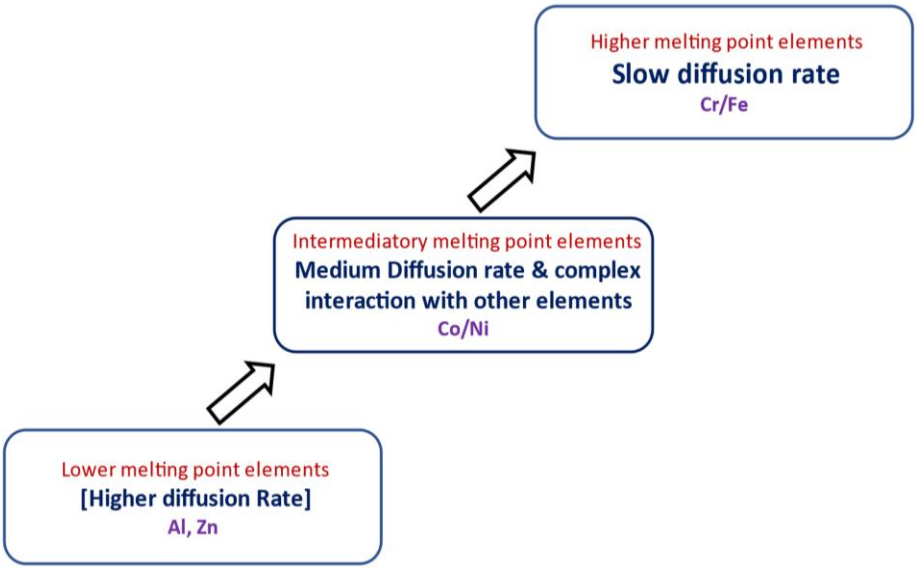

Figure 2.12: Dissolution order with milling time [141]

2.5.2 VARIOUS ATTRIBUTES OF MECHANICAL ALLOYING

It is a challenging task to achieve fine-grain particles, controlled morphology, and microstructure. It can be only achieved by optimizing the process parameters. A methodology is suggested through a flow chart shown in Figure 2.13**.** The process parameters and their effect on MA are as follows:

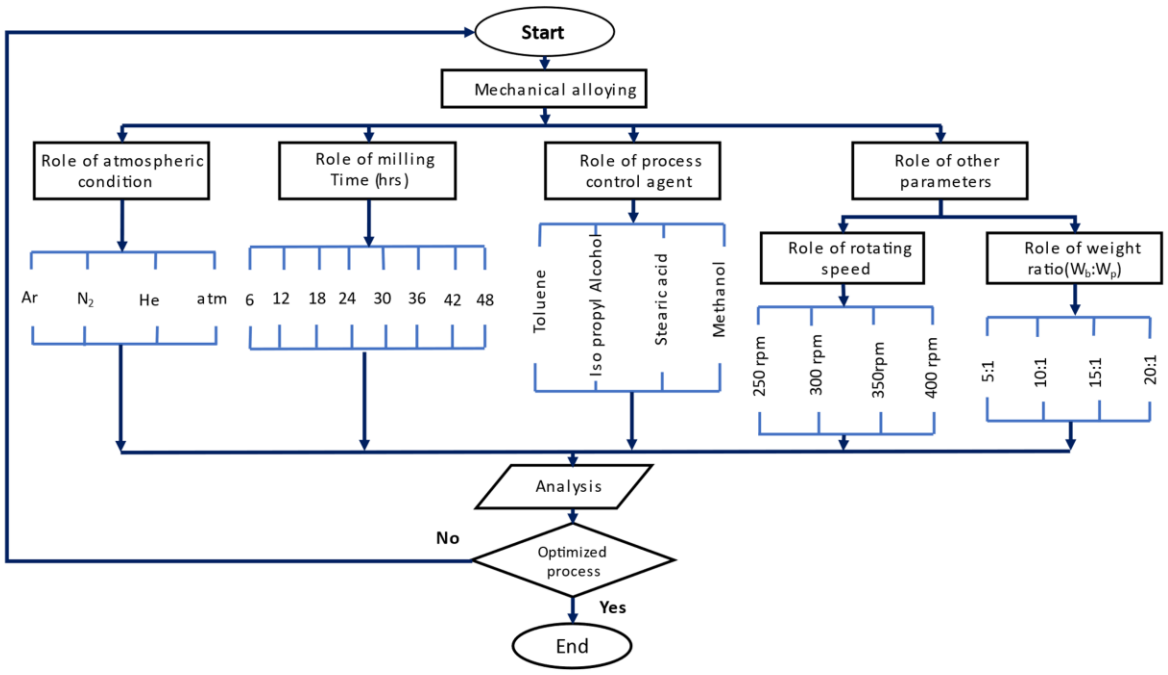

Figure 2.13: Methodology for achieving optimum process variables

2.5.2.1 BALL-TO-POWDER WEIGHT RATIO (BPR)

The amorphization rate highly depends on the kinetic energy of the ball mill charge so particles reacted and interdiffusion. The amorphization rate increases with BPR. In the early 48 h of ball milling, an amorphous phase fraction is observed, and then after when it further increases crystalline phase is observed due to the heat generation. At a higher BPR fine particles are obtained however there is a disadvantage of overusing a high weight ratio is the contamination [208]. Whereas, at lower BPR varied crystallite size indicated that differences existed in the effectiveness of the milling process and incomplete phase formation [209].

2.5.2.2 ROTATING SPEED

The morphology of the particles is also affected by rotating speed. Higher speed promotes welding as the ball hits the ball or vial surface with great intensity. It is noticed that at higher rotating speeds the particle size increased. At higher RPM the greatest impact energy is attained whereas at lower speed the efficiency of milling time was found to be low [210]. Ciprian

Alexandru Manea et al. [211] synthesized HfNbTaTiZr HEA and investigated the influence of rotational speed on HEAs. They observed while varying the RPM between 200 and 300 RPM that optimum particle size was attained at 300 RPM. My Khailo Semen'ko et al. [212] introduced the concept of high energetic milling in the synthesis of high entropy alloys. A single-phase FCC CoCrFeNi HEA is produced within 2 h while conventional milling takes around a few 10 h. In an investigation, Salemi et al. [213] even after 50 h of milling duration and rotational speed 300 RPM alloying was properly not achieved. Whereas when rotational was increased to speed 350 RPM, single-phase FCC was attained. It is reported that with an increase in rotational speed, energy transfer to the HEA powder is estimated to increase by 1.7 times (at 350 RPM). Tan et al. [214] fabricated $Al_2NbTi_3V_2Zr$ at rotating speeds of 350 RPM and 150 RPM. It was reported that high-energy milling was far more effective than low-energy milling.

2.5.2.3 MILLING DURATION

In milling, a fracturing cold-welding mechanism took place. In the early stage of milling, cold-welding predominates over fracturing, and particle size increases sharply, then particle size decrease as the fracturing mechanism dominates over cold welding. The extent of alloying can be determined through an X-ray diffraction plot at different milling durations. After a certain time, dynamic balancing occurs where cold welding comes in equilibrium with fracturing. Furthermore, the milling time should not be too large because the increased milling time weakens the diffraction peaks. This indicates a long milling time impacts adversely and phase identification of the powder becomes difficult. It is also observed that with an increase in milling time, the crystal size decreases, and lattice strain increases [139]. At a long duration of milling time, unwanted phases and contamination problems are also occurred [215]. At a lower milling duration, milling is unfavorable and unable to achieve desired properties [103]. Table 2.7 exclusively presents the effect of milling duration on the desired properties from HEAs.

Table 2.7. Effect of varying and fixed milling duration on mechanically alloyed HEAs

	HEA	Milling time	Remarks	Ref
Varying Milling Time	$CoCrFeMnNiTi_{0.1}$	10h, 15h, 20h	• Yield strength and hardness were improved by 33% and 20% respectively at 20h milling time. • Reduction in the size of produced phases as a robust function of milling time.	[216]
	AlCrCuFeZn	2.5h, 10h, 20h, 40h	• Two highly saturated and disordered solid solution phases (FeAlCr and CuZn) were observed. • The highest hardness was reported as 661 for the FeAlCr BCC.	[217]
	AlCoFeMoNiTi	10h, 20h	• The morphology of the particles got affected by MA. • MA enhanced the mechanical properties	[218]
	MoNbTaTiV	5h, 10h, 15h	• Up to 5h, cold welding, and plastic deformation dominate, 5 to 20h fracture dominates, and after 20h a dynamic balance was observed between lattice strain and grain size.	[177]
	AlCoCrFeNi	10h, 20h, 30h	• Excellent soft magnetic properties, high hardness, and yield strength.	[148]
	CoCrFeMnNi	20 Min, 60Min	• ZrO_2 peaks were observed due to the contamination of zirconia balls.	[172]
	FeCoNiMnV	0, 48h, 72h, 96h	• As Milling time reaches 72h, primary phase composition approaches stoichiometry, and phase distinction becomes more apparent.	[173]
	AlCuNiFeCr	1h, 2h, 3h, 4h & 5h	• Homogenized supersaturated solution with BCC phase attained at 5h milling.	[174]
	FeCrNiAlCo	5h, 10h, 15h, 20h	• Sequential alloying affects the corrosion behavior of HEA.	[219]
Fixed Milling Time	$FeCoNi_{1.5}CuY_{0.2}$	60h	• The addition of boron increases strength and hardness. • Compromise with plasticity and soft magnetism.	[220]
	AlCoCrFeNi	28h	• Milling and sintering control the formation of unwanted phases and impurities and shorten the duration of the process	[221]

	AlCoCrFeNi	4h	• High plastic strain and strength, good lubricity, and anti-adhesive nature were achieved.	[222]
	$FeCoNiAlCr_x$	90h	• Excellent heat resistance, corrosion resistance, and soft magnetic properties made it a promising material for microwave absorbent.	[223]

2.5.2.4 PROCESS CONTROL AGENT (PCA)

Controlling the morphology and particle size is always a critical task in which milling conditions play a crucial role [42], [224] One of the methods used to avoid severe welding is the use of surface-active compounds which are also known as process control agents [225]. These surface-active compounds are absorbed on the particle surface and minimize the surface tension [226], interfere with cold welding, and inhibit agglomeration. Various control agents such as toluene, stearic acid, methanol, propyl glycol, and ethyl propyl alcohol are often reported in MA [227]. PCA affects the intrinsic nature by reacting with material surface particles and impacting the solubility levels, refining crystal size, and consequently modifying the final mechanical properties [228].

2.5.2.5 ENVIRONMENTAL CONDITIONS

Milling atmospheric conditions are considered one of the most important factors that affect elemental powder [229]. During the milling, very fine powder is obtained which has a large surface area, thus prone to not only being highly reactive with oxygen and form oxides but also to other gases like nitrogen, sulphur or hydrogen, etc. [113].

2.5.3 RECOMMENDATIONS

To derive the best possible properties, the process variable must be optimized. The spherical morphology of elemental powder gradually transforms during MA depending on various parameters such as a low ball-to-powder ratio (10:1) and moderate speed <= 300 RPM for the optimized period that can significantly preserve the morphology of the powder [230]–[232]

Milling time should not be too large, an increase in milling time weakens the diffraction peaks. This indicates a long milling time impact adversely and phase identification of the powder becomes difficult. In the MA continuous welding-fracturing process to make an equilibrium between welding and fracturing, stearic acid is the most suitable surface-active agent. Based on the above discussion, the parameters with varying ranges and recommended values are described in the given table 2.8.

Table 2.8. Recommended values of process variables in MA

S. No.	Process variables	Range	Recommendation
1.	Particle grain size (Microns)	20-300	40
2.	Ball-to-powder weight ratio	6:1 – 60:1	10:1
3.	Rotational speed (RPM)	200-1100	300
4.	Milling duration (h)	6-90	42
5.	Process control agent (PCA)	Methanol, ethanol, n-heptane, stearic acid, toluene, ethyl glycol, ethyl propyl alcohol	Stearic acid
6.	PCA Concentration (wt.%)	1-5	1.5
7.	Environmental conditions	Ambient, argon, Nitrogen, helium, vacuum	Argon

And also, some course of preventive actions is suggested for MA

1. Instead of directly pouring metallic particles into the vial first, the different particles should be mixed properly and then pour into the vial.
2. The processing control agent must be added in a small quantity otherwise these particles settle down and milling becomes ineffective.
3. A run should be stopped after a certain period depending on various factors like materials for processing, RPM, vial, and ball materials to reduce the temperature inside the vial and wear on the motor of the jar [233].
4. A regular inspection must be made to prevent agglomeration of the powder particles permitting inferior milling.

5. After milling, the powder should be kept in a jar for a suitable time, as the powder is in a red-hot state and lead to an uninvited incidence.
6. Before the compaction and sintering stage particles should place inside the vacuum induction furnace to remove moisture and PCA from HEAs so they get free from any impurity.

2.6 PROPERTIES AND POTENTIAL APPLICATIONS OF HEAs

2.6.1 MECHANICAL PROPERTIES

Regarding the durability and quality of the material, mechanical properties are the most important deciding factor where phases play a critical role. For example, FCC-based HEAs exhibit low yield strength and excellent plasticity whereas BCC poses high yield strength and low plasticity. Mechanical alloyed HEAs exhibited microhardness ranging from 375 to 699 HV. HEAs processed through MA followed by some consolidation techniques had the advantage of nano-twin formation, multiple hardening mechanisms, and formation of precipitates which enhanced the strength of HEAs. CoCrFeNi processed through MA followed by SPS exhibits a hardness of 570 HV [41] which was nearly four times the hardness (150 HV) by as-cast alloy [234]. AlCrCoFeNi fabricated through MA followed by SPS accomplished compressive strength of 2.6 GPa [235], which was near twice the strength possessed by As-cast HEA [236]. While processing of AlCoFeNiMoTi HEA through MA nano precipitates formed which imparted higher strength than as-cast HEAs [218]. NbMoTaW HEA fabricated through MA and SPS possessed extraordinary compressive yield strength (2612MPa) and plasticity of 8.8 %. In another work, the same HEAs were synthesized through arc melting in which strength and plasticity were reported as 1246 MPa and 1.7 % respectively [237].

Non-equimolar $Co_{1.5}CrFeNi_{1.5}Ti_{0.5}$ HEA processed through MA and SPS was investigated for mechanical properties and bend-strength of 2.6GPa, the tensile strength of 1.4 GPa, hardness of 4.4 GPa, and plastic strain 4% were observed which were far better than traditionally as-cast HEAs [161]. An AlCoFeNiTi HEA fabricated by MA and SPS formed a major FCC phase with precipitates of B_2 phase and Al_3Ti particles [238]. Solid solution strengthening twin boundaries observed in the FCC phase resulted in high compression strength of 2.9 GPa and plastic strain of 5.9 % to the HEAs [238]. Because the presence of Ni_3Ti precipitates and TiO_2

particles in the FCC phase of $Co_{1.5}CrFeNi_{1.5}Ti_{0.5}$ exhibited a better combination of strength of 1460 MPa and ductility of 14.5 % [239]. $Al_{7.5}Co_{25}Cu_{17.5}Fe_{25}Ni$ HEA imparted high strength 1795 MPa and hardness of 454 HV [240]. Table 2.9 compares the major outcomes from different HEAs processed through varying techniques.

Table 2.9. Major outcomes from different HEAs developed through various processing techniques

HEAs	Processing technique	Major outcomes						Ref
		Hardness	Tensile strength		Compressive strength		Plasticity Strain	
			Yield strength (MPa)	Ultimate tensile strength (MPa)	Yield strength (MPa)	Ultimate Compressive Strength (MPa)		
CrMnFeCoNi	MA+SPS	526Hv	-	1055	-	-	6.3 $\acute{\varepsilon}_T$	[241]
CrMnFeCoNi	MA+HIP	699±14			1900	2000	0.5 $\acute{\varepsilon}_c$	[242]
CrMnFeCoNi	MA+SPS	625Hv	-	-	-	1907	11.16 $\acute{\varepsilon}_c$	[243]
$(FeCrNiCo)Al_{0.75}Cu_{0.25}$	MA+VAM	375 HV			859	2787	43.6 $\acute{\varepsilon}_c$	[244]
$(FeCrNiCo)Al_{0.75}Cu_{0.25}$ +10vol%TiC					1637	2972	31.8 $\acute{\varepsilon}_c$	
$Ni_{1.5}Co_{1.5}CrFeTi_{0.5}$	MA+SPS	442Hv	1308	1384	-	-	4.01 $\acute{\varepsilon}_T$	[161]
Al0.5CoCrCuFeNi	Arc Melting	399Hv	1292	1406	-	-	6 $\acute{\varepsilon}_T$	[245]
$Al_{0.25}CoCrFeNi$	Arc Melting	401.3 Hv	691	736	-	-	12.5 $\acute{\varepsilon}_T$	[246]
$FeNiCrCo_{0.3}Al_{0.7}$	MA+SPS	624±26 Hv	-	-	2033±41	2635±55	8.12±0.51 $\acute{\varepsilon}_c$	[247]
FeNiCrCoAl	Arc Melting	-	-	-	1250.96	2004.23	32.7 $\acute{\varepsilon}_c$	[248]
FeCoCrNi	PM	-	359	712.5	-	-	56 $\acute{\varepsilon}_T$	[249]
$CoNiFeAl_{0.4}Ti_{0.6}Cr_{0.5}$-Al	MA+HPS	15.2 GPa	336.2	362	-	-	8.4 $\acute{\varepsilon}_T$	[250]
CoCrFeMnNi-C	Arc melting	-	527	1616	-	-	1.84 $\acute{\varepsilon}_T$	[251]
$FeCoCrNiMnAl_0$	MA+HPS	415 Hv	-	-	1314	2026	20.3 $\acute{\varepsilon}_c$	[39]

$FeCoCrNiMnAl_{0.1}$		432 Hv	-	-	1631	2086	12.6 $\acute{\varepsilon}_c$	
$FeCoCrNiMnAl_{0.3}$		511 Hv	-	-	1836	2341	4.9 $\acute{\varepsilon}_c$	
$FeCoCrNiMnAl_{0.5}$		553 Hv	-	-	1932	2376	3.8 $\acute{\varepsilon}_c$	
$FeCoCrNiMnAl_{0.7}$		622 Hv	-	-	2230	2552	1.69 $\acute{\varepsilon}_c$	
$Al_{0.5}CoCrFeMo_{0.3}Ni$	Arc Melting	571 Hv	1091	2117	-	-	18 $\acute{\varepsilon}_T$	[252]
FeCoNiCrMnAl	MA+SPS	3.7 GPa	-	1011	-	-	-	[253]
$Nb_{25}Mo_{25}Ta_{25}W_{25}$	MA+SPS	7.8GPa	-	-	2460	3016	16.8 $\acute{\varepsilon}_c$	[254]
$Ti_{28}Nb_{23}Mo_{23}Ta_{23}W_{23}$	MA+SPS	7.35GPa	-	-	2377	3340	26.3 $\acute{\varepsilon}_c$	
$Nb_{25}Mo_{25}Ta_{25}W_{25}$	VAM	4.46GPa	-	-	1058	1211	2.6 $\acute{\varepsilon}_c$	

Nano crystalline HEAs has shown superior mechanical properties at elevated temperature. These HEAs exhibit higher yield strength in compression with improved ductility. In nano crystalline materials grain boundaries have more influence than their compositions on mechanical properties [255]. Nano-structured HEAs' thin film coating exhibits superior properties to their bulk counterparts. Gao et al. [256] successfully developed $CoCrFeNiAl_{0.3}$ nano metallic film and its hardness was reported approximately 4 times that of bulk material. A single-phase CoCrFeMnNi nano HEA possessed high tensile strength $\sim 1\,GPa$, extraordinary ductility, and excellent fracture toughness. Chaoqun Dang et al. [257] synthesized CoCrFeMnNi thin film coating of nano-structured HEAs that showed high hardness $\sim 6.8\,GPa$ which is far better than its bulk counterpart.S Varalakhsmi et al. [37]synthesized nanocrystalline AlFeTiCrZnCu HEAs through MA followed SPS route in which hardness is observed nearly 2 GPa that suggesting nanocrystalline HEAs solid solution have high strength. Fu et al. [258] prepared nanocrystalline $CoNiFeCrAl_{0.6}Ti_{0.4}$ HEAs in which supersaturated solid solution of metastable BCC phase and FCC phase was observed that resulted in higher hardness 5.6 GPa and compressive yield strength 2.08 GPa were noticed. Ji et al. [259] successfully synthesized and investigated the mechanical properties of nano crystalline CoCrFeNiAl that imparted high hardness and compressive yield strength of 6.1 GPa and 1.9 GPa respectively.

2.6.2 TRIBOLOGICAL CHARACTERISTICS

It is challenging to develop a high wear-resistant material without compromising mechanical properties such as compressive and tensile strength [260]. However, HEAs present a novel design approach to develop a material with exceptional tribological properties as well as good mechanical properties, a proper balancing between alloy matrix and self-solid lubricating element or hard particles must be established. The HEA solid solution achieved significant chemical disorder and topological order, overcoming the strength-ductility trade-off unconventionally [261].

The coefficient of friction (COF) and rate of wear is used to assess the tribological behavior of materials. Three configurations, namely block on block, ball on disc, and pin on the disc were employed to evaluate the tribological behavior of newly designed HEAs [262]. Various aspects such as applied load, the rotation speed of the disc, and time or total distance impact the wear rate in the methods described above. Although the majority of HEA research is focused on structural properties, tribological behavior research has lately garnered attention. Cantor alloys have been extensively studied for their tribological properties; revealing the intrinsic wear characteristics of cantor alloys is critical. Nagarjuna et al. [263] examined the wear behavior of CoCrFeMnNi HEA utilizing a ball on a disc. The surface of the HEAs was scratched with some adherent debris at the start of the wear testing, as shown in Figure 2.14. When the applied load rises, the stress at the contact surfaces increases, causing surface cracking and delamination. So, the result indicated that the transition occurred from adhesive and abrasive wear to delamination as the duration of wear continued and examined the variation of CoF with load, sliding speed, and time [264]. Dollmann et al. [265]investigated the wear behavior of CoCrFeMnNi HEAs in a separate study. A soft fcc HEA has a low hardness value for the undeformed surface, while the hardness value increases significantly to 500 HV for the deformed surface. HEAs with exceptional wear resistance qualities have received a lot of attention. Ceramics and carbides are commonly used in the strengthening phase of HEAs, but oxides are also used. Jiang et al. [266]observed in their investigation that the addition of TiC particles to CoCrFeCuAl HEA lowered the wear rate and CoF as shown in Figure 2.15. The hardness increased to 10.8 GPa with the addition of 50% TiC, resulting in a decreased wear rate of 9.6 10^{-5} mm^3/Nm. Guo et al. [267] also observed that the inclusion of Cr_3C_2 greatly

improved the wear performance of single-phase CoCrFeMnNi HEA. Cai et al [268]investigated the pinning effect of TiC particles on the strengthening of CoCrFeMnNi HEAs, which resulted in grain boundaries and grain size refinement and reduction from 76um to 26 um for a 15% TiC-CoCrFeMnNi Composite. The use of TiC improves hardness from 213 HV to 288 HV. TiC particles reduce plastic deformation and adhesive wear, increasing wear resistance. Surface hardening, namely nitriding, and boronizng, can enhance the tribological behavior of HEAs.

The thickness of the surface hardening layer protects against wear. However, researchers investigate the role of self-lubrication on the tribological behavior of HEAs. It has been found that solid lubricant plays a key role in controlling wear rate. The several kinds of solid lubricants utilized in high entropy alloys such as graphite, MoS_2, BaF_2, Cu, and Ag are reported. The soft phase Ag and Cu, which have low shear strength, are purportedly employed in CoCrFeNi HEA, which improves HEA wear resistance. Verma et al [269]evaluated the tribological properties of $CrCoFeNiCu_x$ (x=0 to 1, at 0.2 mean intervals) HEAs. Cu particle segregation at the grain boundaries of $CrCoFeNiCu_x$ HEAs reduces wear rate at room temperature and 600 C. The wear rate of $CrCoFeNiCu_x$ HEAs bearings at higher temperatures is stated to be lower than at room temperature. To achieve self-lubricating capabilities, HEAs are designed with a tailored composition that includes lubricating additives with self-lubricating properties. S. Kumar et al. [270] carried out a wear investigation of $Al_{0.4}FeCrNiCo_x$ (x=0, 0.25, 0.5, 1.0 M) HEAs under oil lubrication by varying the normal load, sliding distance, and sliding speed. The effect of varying Co was also carefully examined. It was stated that maximal wear was observed for Co=1 HEA for two reasons: (i) when cobalt concentration increases, hardness decreases, and (ii) an oil film breakdown occurs. The wear surface revealed peeling off, flow material, and cracks seen perpendicular to the sliding direction. Another work used demineralized water with and without a 3.5 % NaCl solution to conduct wear testing. The wear mode reported during the investigation were combined effect of adhesion with delamination, plastic flow, abrasive, and oxidation [271]. Furthermore, other articles on wear characteristics of HEAs are enlisted in Table 2.10.

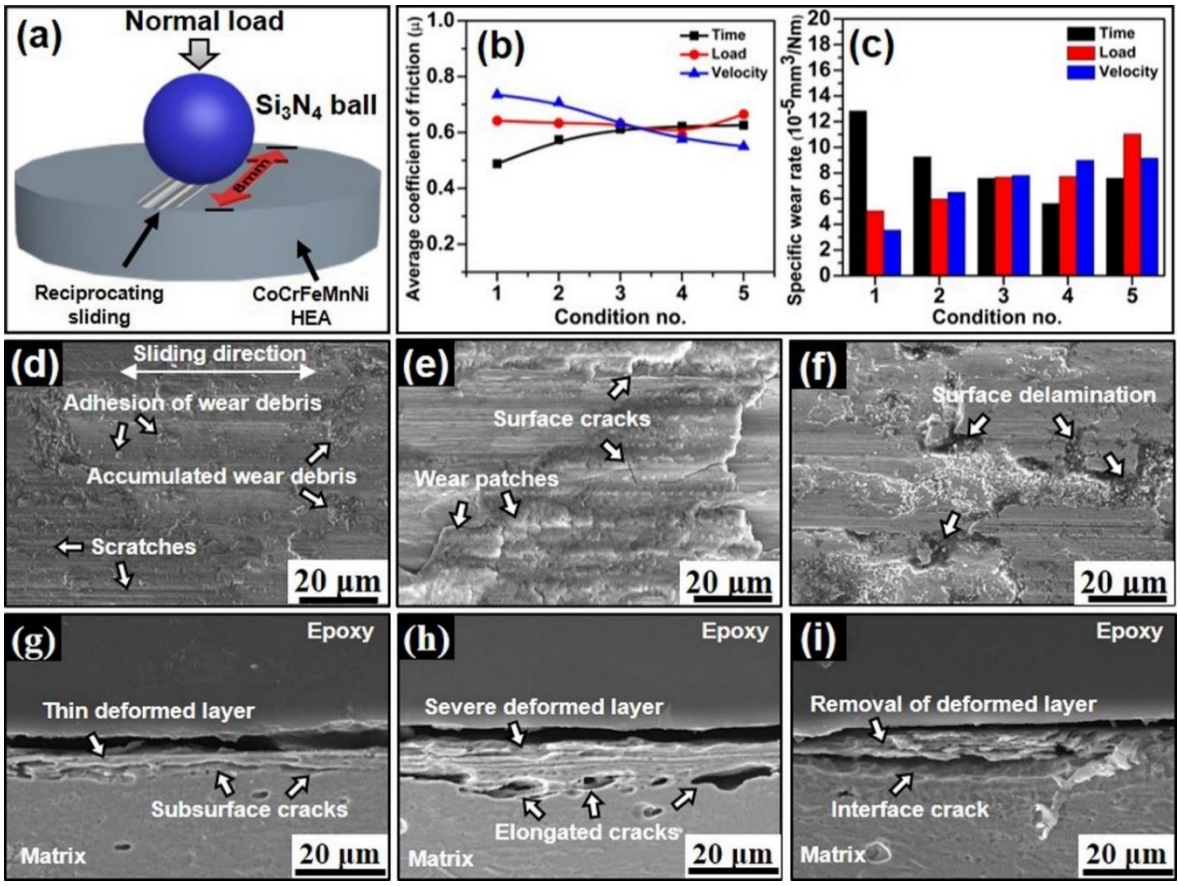

Figure 2.14: (a) shows the schematic diagram of ball-on-disc while sliding in reciprocation motion, (b) illustrates the variation of average COF, and (c) specific wear rates of CoCrFeMnNi HEA with increasing sliding time (1, 5, 10, 15, and 20 minutes.), load (2, 4, 6, 8, and 10 N) and velocities (0.02, 0.05, 0.1, 0.15, and 0.2 m/s) in dry and atmospheric conditions. SEM top view shows the wear tracks with sliding time; (d) 5 minutes, (e) 10 minutes, and (f) 20 min at a constant load of 6 N and sliding velocity of 0.1 m/s. SEM cross-sectional micrographs of wear tracks examined parallel to the sliding direction specifying the extent of subsurface plastic deformation with an increase in sliding time (g) 5 minutes, (h) 10 minutes, and (i) 20 minutes [263].

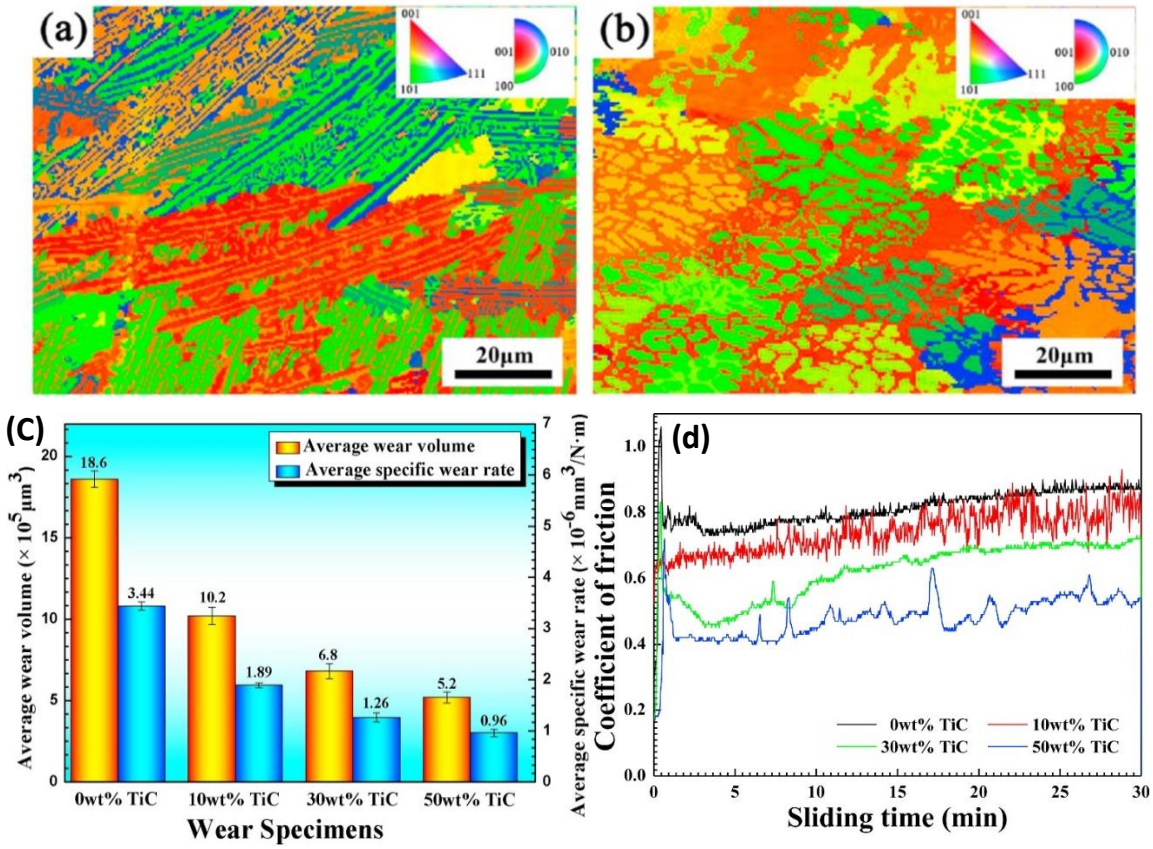

Figure 2.15: EBSD orientation plot (a) FeCoCrAlCu HEA coatings, (b) FeCoCrAlCu-50 wt.% TiC HEA, (c) the avg. specific wear rate and avg wear volume FeCoCrAlCu-xTiC, and (d) variation CoF for FeCoCrAlCu-xTiC HEA coating with sliding time [266].

Table 2.10: Summary of literature results on wear rate and friction, processed via different synthesis routes whereas the main focus is on mechanical alloying.

S.No.	HEAs	Synthesis technique	Testing method	Wear test parameters					Hardness	Wear rate	COF	Refer.
				Ball/pin dia/	Load (N)	Distance/ time	Speed	Ambient conditions				
1.	$(CuCrFeTiZn)_{100-x}Pb_x$	MA+SPS	Ball on disk	4	7	400s	0.41m/s	RT	3.5-6GPa	1.17×10^{-14}	0.28	[262]
2.	CoCrFeNiCu	MA+HPS	Ring-disk	10×17×20	1000	900s	100rpm	ET	450HV	…	0.6	[349]
3.	$Al_2Mo_{0.5}NbFeTiMn_2$	MA	Reciprocating wear tester	6	50	1800s	200rpm	RT	1098HV	…	0.41	[350]
4.	$Fe_{1.6}CoCrNi$	MA+SPS	Pin on disk	3	10	1000m	0.2m/s	RT	320-400 Vickers	0.02 % weight loss	0.65	[351]
5.	$CoCrFeNiW_{0.5}Mo+0.5$	MA+HPS	Ring on disk	10×17×20	100	900s	100rpm	ET	600HV	5mg	…	[352]
6.	$NiCoCrFeZr_{0.4}$	MA+SPS	Pin on disk	…	5	1000m	0.2m/s	RT	845HV	0.001mg/m	0.7	[353]
7.	CoCrFeMnNi	MA+SPS	Ball on disk	6	15	1000m	100mm/s	RT	640 HV	.0096	0.7	[354]
8.	CoCrFeNi(WC)	MA+HPS	Pin on disk	10×17×20	100	900s	100rpm	ET	531HV	…	0.3	[355]
9.	AlFeTiCrZnCu	MA+VHP	Pin on disk	10	30	1600m	…	RT	9.5GPa	0.01gm	…	[35]
10.	$CoCrFeNiMo_{0.2}$	MA+SPS	Ball on disk	6.35	20	36m	6mm/s	RT	460HV	…	0.629	[356]
11.	CuZrAlTiNi	MA+VHPS	Pin on disk	…	30	1200s	200rpm	RT	943HV	…	0.7	[165]

12.	AlCoCrFeNiSi	MA+APS	Ball on disk	5	5	1800s	573rpm	RT	612HV	(0.38±.08 $\times10^{-4}$)	0.57	[155]
13.	AlCoCrFeNi	MA+SPS	Pin on disk	5	5	1800s	0.19m/s	RT	630HV	1.9×10^{-5}	0.57	[222]
								200	560HV		0.53	
								400	510HV		0.61	
								600	490HV		0.54	
								800	440HV		0.86	
14.	TiNbZrMo	MA+Laser	Ball on disk	3	4	3000s	200rpm	RT	410HV	1.2mg	0.45	[357]
15.	$CoCrCuFeNiMo_{0.8}$	MA+SPS	Pin on disk	5	15	1000m	…	RT	530HV	…	0.65	[358]
16.	$FeCoNiCr_{0.8}Al_{0.2}$	Vacuum arc melting	Ball on disk	…	…	3000s	…	RT	290HV	…	0.237	[359]
17.	HfTaTiVZr	Vacuum arc melting	Pin on disk	3	50	190m	5HZ	RT	6.8GPa	3.1×10^{-4}	0.26	[360]
								423K	6.3GPa	7.1×10^{-4}	0.25	
								573K	6.3GPa	2.8×10^{-4}	0.23	
								723K	6.2GPa	2.8×10^{-4}	0.21	
18.	TaTiVWZr	Vacuum arc melting	Reciprocating wear tester					RT	8.1GPa	2.8×10^{-4}	0.23	
								423K	8.0GPa	8×10^{-4}	0.34	
								573K	7.5GPa	1.1×10^{-4}	0.32	
								723K	7.1GPa	1.1×10^{-4}	0.3	
19.	AlCrFeNiCu	Laser metal deposition technique	Ball on disk	5		480s	Operating power 2200W	RT	350HV	0.01g	0.28	[361]
							2000W			0.01g	0.27	
							1800W			0.01g	0.34	
							1600W			0.02g	0.33	

2.6.3 FUNCTIONAL PROPERTIES

HEAs are newly developed materials in which the area of research is limited to microstructure and mechanical properties. A little progress is observed on the functional properties of the HEAs. These properties include irradiation resistance, soft-magnetic properties, thermoelectric properties, and catalytic properties as described in table 2.11. These properties are affected by their unique structure feature which is a multi-principal element solid solution. The functional properties play a vital role in applications such as solar plates, electromagnetic interference shielding, and nuclear magnetic resonance.

Table 2.11. Functional properties and intended applications of HEAs

Application	HEA	Characteristics	Ref
Environmental protection	AlCrFeMn, AlCrFeNi, AlFeMnTiCr	❖ Removal of contaminants by absorbing them ❖ Low activation energy barrier ❖ Higher recyclability	[272], [273]
Gas Storage and sensing	CoFeMnTiVZr, TiZrNbMoV, HfNbTiVZr, ZrTiVCrFeNi	❖ Suitable to store hydrogen fuels ❖ Higher bulk density, better safety, and reversibility	[274]–[277]
Radiation Protection	$Al_xCoCrFeNi$, CrMNFeNi, $Ti_2ZrHfV_{0.5}Mo_{0.2}$	❖ Higher-strength and toughness ❖ Withstand harsh conditions ❖ Higher irradiation due to self-healing capabilities	[278]–[281]
Thermoelectric Materials	$Ni_2CuCrFeAl_{x,}$ $Y_xCrCoFeNi$, $Al_{0.3}CoCrFeNi$, PbSnTeSe	❖ Convert direct heat energy into electricity ❖ Improve engine efficiency by recovering waste heat	[282]–[284]
Energy storage	AlCoCrFeNi, FeNiCoMnCu, FeNiCoMnMg	❖ Ultra-high-power density, long life span, and rapid energy transfer ❖ Large storage capacity.	[154], [180]
Magnetocaloric Materials	$Gd_{20}Tb_{20}Dy_{20}Al_{20}M_{20}$ (M=Co, Fe and Ni), FeCoNiCuMn, $Mn_{27}Cr_7Ni_{33}Ge_{25}Si_8$	❖ More energy efficient than traditional refrigeration mode ❖ Economical, higher efficiency, and environment friendly.	[285]–[287]

Electromagnetic Wave absorption	FeCoNiCrAl, $FeCoNiSi_{0.4}Al_{0.4}$, FeCoNiCuZn	❖ Excellent capability to absorb electromagnetic and microwave. ❖ High conductivity and better permeability.	[139], [288]
Catalyst Materials	$Pt_{50}Fe_{11}Co_{10}Ni_{11}Cu_{10}Ag_{8,}$ $Ni_{20}Fe_{20}Mo_{10}Co_{35}Cr_{15}$, AlNiCuPtPdAu, AlNiCuPtPdAuCoFe	❖ Reduce energy consumption, and improve the rate of reaction. ❖ Improve the selectivity and even change the elementary reaction.	[289], [290]
Superconducting materials	$Ta_{34}Nb_{33}Hf_8Zr_{14}Ti_{11}$, $Hf_{21}Nb_{25}Ti_{15}V_{15}Zr_{24}$	❖ Superconductivity, Meisner effect, and strong electron-phonon coupling.	[291]–[293]
Shape memory alloy	$Ti_{16.667}Zr_{16.667}Hf_{16.667}Ni_{25}Cu_{25}$,$Ti_{16.667}Zr_{16.667}Hf_{16.667}Co_{10}Ni_{25}Cu_{15}$, TiZrHfAlNb	❖ Improve plastic deformation ability. ❖ Implant material in biomedical	[38], [294]

2.7 POTENTIAL APPLICATIONS

In science and engineering demands for functional and structural materials are increasing in several sectors such as mining, transportation [295], naval [296], and aviation over the conventionally used superalloys. Figure 2.16 displays the existing potential applications of different HEAs in various sectors.

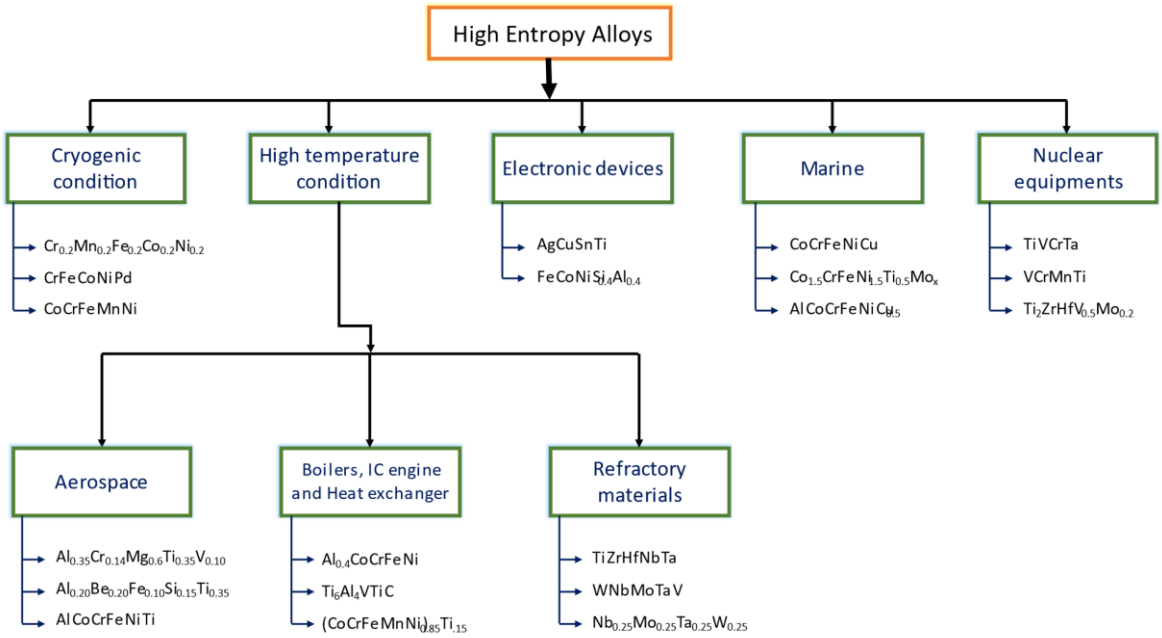

Figure 2.16: Existing applications of different HEAs in various sectors

1. HEA exhibits distinct properties such as forming simple solid solution phases of FCC and BCC with excellent thermal stability which can withstand extremely high-temperature conditions [15] and hardness nearly reported as 110 HV. Thus, it makes HEAs potential candidates for engine materials, chemical plants, steam turbine blades, boiler pipes, and tubes of heat exchangers which are subjected to high pressure and high temperature.
2. Based on the high strength-to-weight ratio and excellent cold formability, $Ti_{15}V_3Cr_3Sn_3Al$ HEA is being used as an integrated aircraft component [297]. Whereas, $Ti_3Al_8V_6Cr_4Zr_4Mo$ attains a place in the aviation industry due to its combined properties such as high strength & plasticity, maintainability of high cycle fatigue, and excellent fracture toughness [298]. Having superior ductility and lightweight ratio, $Ti_{10}V_2FAl_3Fe$ is being successfully applied in the landing gear system of Boeing 777 and A-40-500/600 [299].
3. In ultra-supercritical boilers, outstanding properties are derived with excellent mechanical properties at high temperatures, oxidation, and corrosion resistance that are required for proper operation [300], [301]. Currently, HR3C steel is frequently used for this application and can be effectively replaced by $Al_xCoCrFeNi$ HEA which can withstand the supercritical environment [302].

4. Tailoring material for a marine application is a critical task that needs a comprehensive overview of antifouling nature, tribological behavior, anti-corrosion properties, and improved mechanical properties. In a study, Yuan et al. [303] fabricated $AlCoCrFeNiCu_{0.5}$ which achieved superior antifouling properties, and better resistance to wear and corrosion. Zhou et al. [304] reported the antibacterial nature of $Al_{0.4}CoCrFeNiCu_x$. Whereas Verma et al. [305] in a separate study discussed the superior tribological behavior of $CoCrFeNiCu_x$ as the concentration of Cu increased.
5. Nanocrystalline HEAs are the most suited class of materials to develop tiny devices that are subjected to harsh environmental conditions [306]. Due to their superior properties in high-stress and high-temperature applications in civilian infrastructure, aerospace, nuclear components, and energy sectors [307].
6. In recent research, progress testified remarkable super magnetic properties, high ferromagnetic properties, and promising soft magnetic properties.
7. The higher irradiation and corrosion resistance of HEAs could make them the best suitable candidates for extremely high-pressure vessels and nuclear fuel cladding materials.
8. The high-entropy approach might be applied to nuclear reactors to simulate the fission reaction.
9. Heat or wear-resistant coatings might be made from HEAs. To make HEAs coatings more homogeneous and cohesive with substrates, new methods are required.
10. The application of refractory metallic HEAs as thermal barrier coatings should be explored.
11. The peculiar characteristics of HEAs carbides and nitrides are equally intriguing. They can have amorphous or solid solution structures, as well as excellent hardness and strength. They might be utilized as hard coatings and diffusion barriers on tool-cutting steels or high-speed steels. Recent research has also revealed that high-entropy carbides and nitrides may be used as biomedical coatings. [151].
12. The unusual physical features of the HEAs such as the near-constant resistivity of $Al_{2.08}CoCrFeNi$ make them excellent for electronic applications [308]. As a result, these types of HEAs should be investigated further.
13. Researchers develop lightweight HEAs, which may be employed in battery anode materials, as well as casings for mobile facilities and the transportation sector.

2.8 CHALLENGES AND THE OPPORTUNITIES

Figure 2.17 reveals the existing status of research articles dealing with the processing of different HEAs through MA. Herein, it is evident that MA is being prominently used in the development of HEAs, however, it has some challenges that need to be addressed appropriately. Therefore, this section effectively discusses the existing challenges and their possible prospects. Moreover, the challenges and opportunities are schematically illustrated in Figure 2.18.

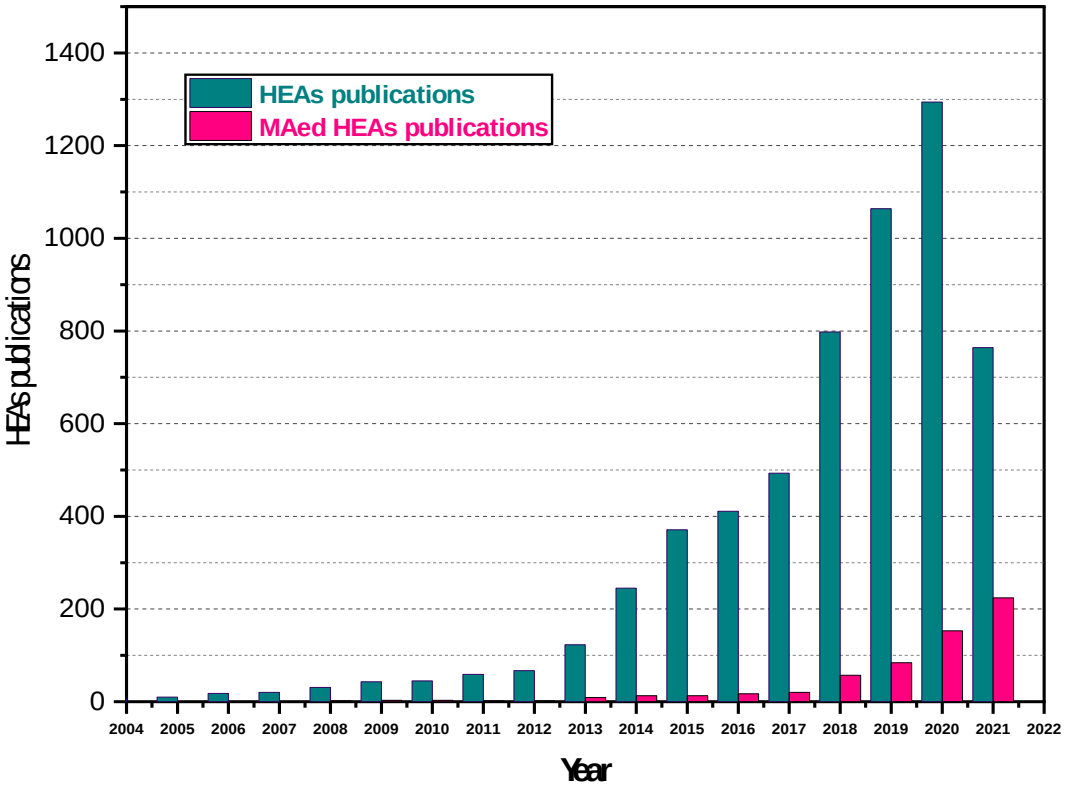

Figure 2.17: Status of research publications relating to the processing of HEAs through MA

1. Although HEA materials exhibit excellent mechanical properties such as enhanced strength at elevated temperature, improved ductility, improved hardness, and higher toughness under cryogenic conditions yet they rarely found any practical application where it replaces well-established standard alloys such as titanium, nickel-based superalloys, and steel which have well-established properties like high stiffness, strength with appropriate ductility, creep resistance, and wear resistance. Work on HEAs is mostly limited to their

microstructure and morphology, mechanical properties, and tribological behavior, So HEAs' future may not sustain while reproducing the properties which can be achieved through their predecessor class of materials.

2. HEA's future development lies in achieving superior mechanical properties along with functional properties related to better weldability, stress corrosion resistance, soft and hard magnetic material, resistance to hydrogen embrittlement, a combination of magnetic and invar response, superconductivity, shape memory effect, thermoelectric energy harvesting capabilities, anti-bacterial and anti-fouling surface oxides layers. So HEAs should be tailored for superior mechanical properties with advanced functional properties at a low overall cost.

3. A study on the role of interstitial elements in HEAs is not convincing yet, also limited work is performed on the C atom in which its effect on HEAs is investigated for mechanical properties, phase stabilization, change in microstructure, and carbide formation. While other elements like B, H, O, and N are unexplored yet need to be addressed properly.

4. In a recent development, HEAs explored morphology and microstructure, tribological behavior, and mechanical properties. The focus must be shifted more to application-based HEAs development. HEAs should be specifically designed based on the functional properties that may lead to developing new products and processes as per the future generation demand. It should be designed to create multifunction elements with exceptional properties that are difficult to attain by a single element. HEAs with superior mechanical properties remain to be explored by our metallurgy academia and materials scientists, and engineers to achieve properties like wear against oxidation and stress corrosion. These challenges pave a path to design and develop new materials according to next-generation demand for aviation, marine, energy, transportation, and structural applications.

5. As the catalyst, nanocrystalline HEAs hold great potential with a wide range of compositional space. However, the critical task is associated with the rational and controllable synthesis of these intrinsically complex materials [309]. Advancement in Computational aided rational design provides a way for rapid and effective synthesizes of HEAs at high temperatures with excellent thermal stability [310], [311].
   In prior studies, it is observed that the main focus of discussion is the bulk form of HEAs, whereas small dimension HEAs are almost neglected. However, demand for micro and nanoscale devices for high-temperature and rough environmental applications sharply increases. At elevated temperatures, in nanocrystalline materials grains drastically coarsen with the time that resulted in poor thermal stability. Therefore, the synthesis of nanocrystalline HEAs needs to be studied.

6. **Cost-effectiveness:** HEAs can only replace existing established material if it is sustainable and cost-effective (considering all aspects such as elements cost, processing cost, and handling cost). The focus is not only on pricing but also on how to use the waste scrap and recyclable material. Another area that needs to be focused on is the durability of HEAs in harsh environmental conditions so the lifespan of the material can be improved.

7. **Weldability:** There is a vast research gap in the weldability of HEA-HEA materials and HEA-non HEA materials as it is in the beginning stage. To be used in any application weldability is an important factor that cannot be ignored, thereby special emphasis should be given to exploring more about the weldability of HEAs. There is promising work carried out on CoCrFeNiMn HEA but still, there is a need for the optimization of process parameters to achieve a highly efficient joint with improved mechanical properties. From the study, it is clear that HEA can accommodate impurities which leads to unexpected phases generally in non-equilibrium solidification which resulted in improved mechanical properties of joints although impurities do not need to always improve their properties so there is a need to improve the homogeneity in the microstructure.

8. HEA alloy powder is mostly processed through MA, HEA powder prepared through other techniques such as electrolytic processing and gas atomization is rarely studied.

9. The industrial development of many industries requires new structural and tool materials with improved operational properties which can work under high temperatures, intensive wear, and dynamic mechanical loads. Improving the working capacity of such materials is an urgent and important task.

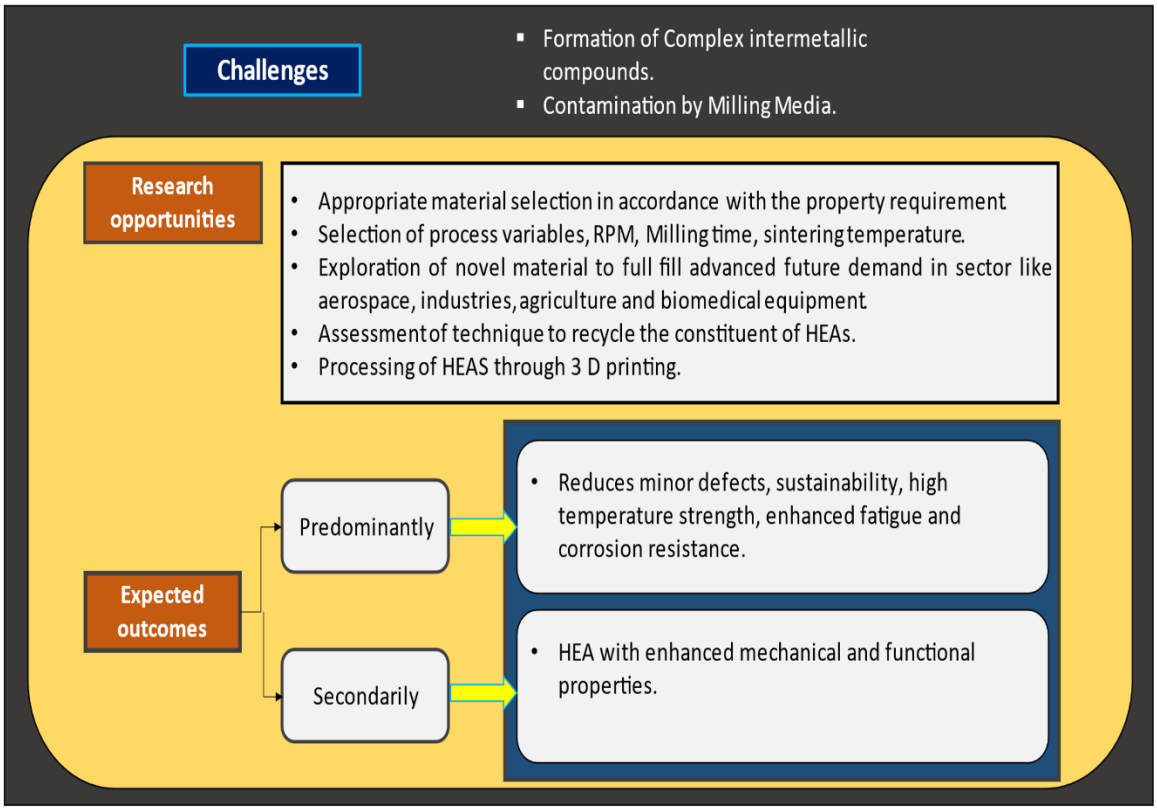

Figure 2.18: Challenges and Research opportunities associated with HEAs

CHAPTER – 3

SCOPE OF THE PRESENT WORK AND OBJECTIVES

The need for lightweight, high-performance, cost and energy-efficient materials is the prime goal for material researchers. With this goal in mind, Aluminium Matrix Composites (AMCs), a new class of material, developed by material scientists exhibit an excellent combination of physical, mechanical, electrochemical, and tribological properties and find a wide range of applications in the aerospace, defense, automobile and general engineering sectors. AMCs are tailor-made materials that can be designed and synthesized as per one's specific needs. Depending on the applications, the method of synthesis and the type of matrix alloy and reinforcements are selected. Particle-reinforced AMCs lead to significant improvement in strength, and significant improvement in wear and seizure resistance depending on the shape, size, volume fraction, distribution of particle reinforcements, and the interface between the particle and the matrix. Considerable research has been carried out on the wear behavior of AMCs in terms of sliding, abrasive, and fretting wear characteristics under different applied loads, sliding speeds, and abrasive sizes. Effects of microstructural parameters on the wear characteristics have also been studied in detail giving special emphasis on particle size, distribution, and interface characteristics. It has been reported that as long as the reinforcing particles are not fractured or fragmented and not debonded from the matrix, the composite exhibits higher wear resistance over the monolithic alloys. In the case of structural applications, there is always a need of joining and fixing the structural parts with nuts and bolts or through riveting. The materials in these areas are subjected to fretting type of wear and the effectiveness of these joints primarily depends on the fretting wear resistance of the material. Fretting wear is the wear of the contact surfaces, which are in the oscillation of lower magnitudes. Thus, the fretting wear resistance and sliding wear resistance could be interlinked with each other. Materials with higher wear and seizure resistance in sliding wear conditions could give better fretting wear resistance. Thus, there is a need of exploring the sliding wear characteristics of structural Al alloys and composites under different applied loads, sliding speeds, and sliding distances. However, inadequate studies are conducted on the sliding and fretting type of wear characteristic of the AMCs in different test conditions. The present investigation deals with the

synthesis, microstructural, mechanical, and sliding wear characteristics of wrought Al alloy-based composites reinforced with CoCrFeMnNi high entropy alloy particles. The matrix microstructure could be varied either by using alloys of different compositions or by different heat treatment cycles. The interface structure as well as the matrix microstructure away from the interface get varied due to thermal aging. Thermal aging is a precipitation phenomenon in which a super-saturated solid solution becomes unstable and the second phase precipitates nucleate and grows in the primary alloy matrix. Heating at higher temperatures accelerates thermal ageing. Aluminium alloys are generally aged from 175°C to 200°C. The heat treatment may also lead to variation in the interfacial characteristics. Precipitation at the interface may lead to mechanical locking of the particles in the matrix, which protects the particle from being scooped off from the matrix. However, during sliding, there is always frictional heating and the temperature rise may be of the order of 80° to 140°C. But the actual temperature at the contact surface may be higher than the recorded value. In addition, the surfaces are under applied pressure. Thus, the contact surfaces are under normal as well as shear stress and the localized stress may be higher than the average pressure applied on the pin surface. This leads to a situation of faster nucleation and growth of precipitates at the surface and subsurface under high temperatures and stress. This also makes one suspicious about the effect of heat treatment on the sliding wear behavior of the alloy and composites under different applied loads and sliding distances. The present investigation examines this fact for Al alloy and different composite systems under varying test conditions. The sliding wear mechanism of Al alloys against steel counter surface is studied in detail which reported that the wear mechanism in the alloy lies in two regimes depending on the applied load and sliding speed. At lower applied load and sliding speed, mainly mild oxidational wear took place; whereas at higher applied load and sliding speed, primarily localized adhesion and delaminating wear mechanisms were prevailing. During sliding, mutual transfer of material between the counter surface and pin surface took place, which strongly dictated the wear behavior of the alloy. The presence of metallic HEA reinforcement completely changes the surface characteristics of the alloy, and the HEA particles remain protruded over the matrix surface and control the effective contact between the counter surface and pin surface. Additionally, these reinforcements are considerably harder and their angular nature makes these particles as micro-machining tools. The abrasive action of these reinforcements over the counter surface may lead to a higher order

of material transfer from the counter surface and this phenomenon may be varying with the reinforcement concentration, applied load, and sliding speed. Again, the reinforcing HEA particles may get smeared out due to their fracture and fragmentation, which may cause either abrasive action over the worn surface leading to more wear, or may get mechanically mixed with the other wear debris and counter surface materials to form a mechanically mixed layer (MML). Thus, the MML in the composite may have different characteristics as compared to that of the alloy. Also, the mechanism of formation and the stability of MML in composites may be different as compared to the alloy. The present thesis also aims at a detailed study of worn surface and subsurface through FESEM-EDX analysis to understand the phenomena of formation of MML in alloy and composites and the stability of MML in the alloy and composites as a function of reinforcement content, applied load, and sliding distance. The reported literature stated that during a seizure, the worn surface of the alloy was free from MML. However, there was an indistinct detection of whether the MML was at all formed on the wear surface or not. If it was formed at all, what would be the critical applied load, and sliding distance at which MML gets destabilized. This has not been studied so far. The present thesis deals with the effect of applied load on destabilizing MML and the critical applied load at which MML gets completely destabilized.

Considering the deficiencies in the aforementioned areas for the understanding of mechanical and sliding wear behavior of aluminium alloys and composites, the present investigation has been carried out with the following objectives;

(i) Development of equiatomic CoCrFeMnNi HEA reinforcement through mechanical alloying processing technique. The concentration of HEA particles was varied as 0-2-4-6-8 wt.% while synthesizing the AMCs.

(ii) Microstructural characterization of HEA particles and composite material at as-cast and heat-treated conditions to understand HEA particle distribution and interface bonding with Aluminium matrix.

(iii) Optimization of the T6 heat treatment cycle with respect to different aging temperatures to identify the under-ageing, peak ageing, and over-ageing conditions in the AA 6082 alloy. Examination of mechanical properties e.g., hardness, impact strength, and tensile strength for different materials in as-cast and T6 HT conditions.

(iv) Field emission scanning electron microscopic (FESEM) analysis of fracture surfaces generated during tensile loading to recognize the prime causes of material failure.

(v) Study of the effect of varying concentrations of HEA_p reinforcement in AMCs on the wear response variables such as wear rate, temperature rise, coefficient of friction, and seizure pressure. Study of the effect of T6 heat treatment (artificial aging) on the sliding wear behavior of AA6082 alloy and composites

(vi) Characterization of worn surfaces through understanding the prevalent wear mechanisms in alloy and composites. Scanning electron microscopic (SEM) examination of the subsurface to understand the microstructural change and level of deformation in the sublayer under different conditions.

CHAPTER – 4

MATERIALS AND METHODS

4.0 INTRODUCTION

This chapter deals with the materials and various experimental procedures used to carry out the present investigation. These include raw material characterization, particle size analysis, synthesis of alloy and composites, specimen preparation, heat treatment, tensile testing, hardness measurement, impact testing, fracture surface study during a tensile test, microstructural characterization by scanning electron microscopy, X-ray diffraction analysis, sliding wear tests, worn (wear) surface study, subsurface study, and surface roughness measurement. The proposed methodology of the present work, in brief, can be better appreciated in light of the aforementioned objectives by referring to Figure 4.1.

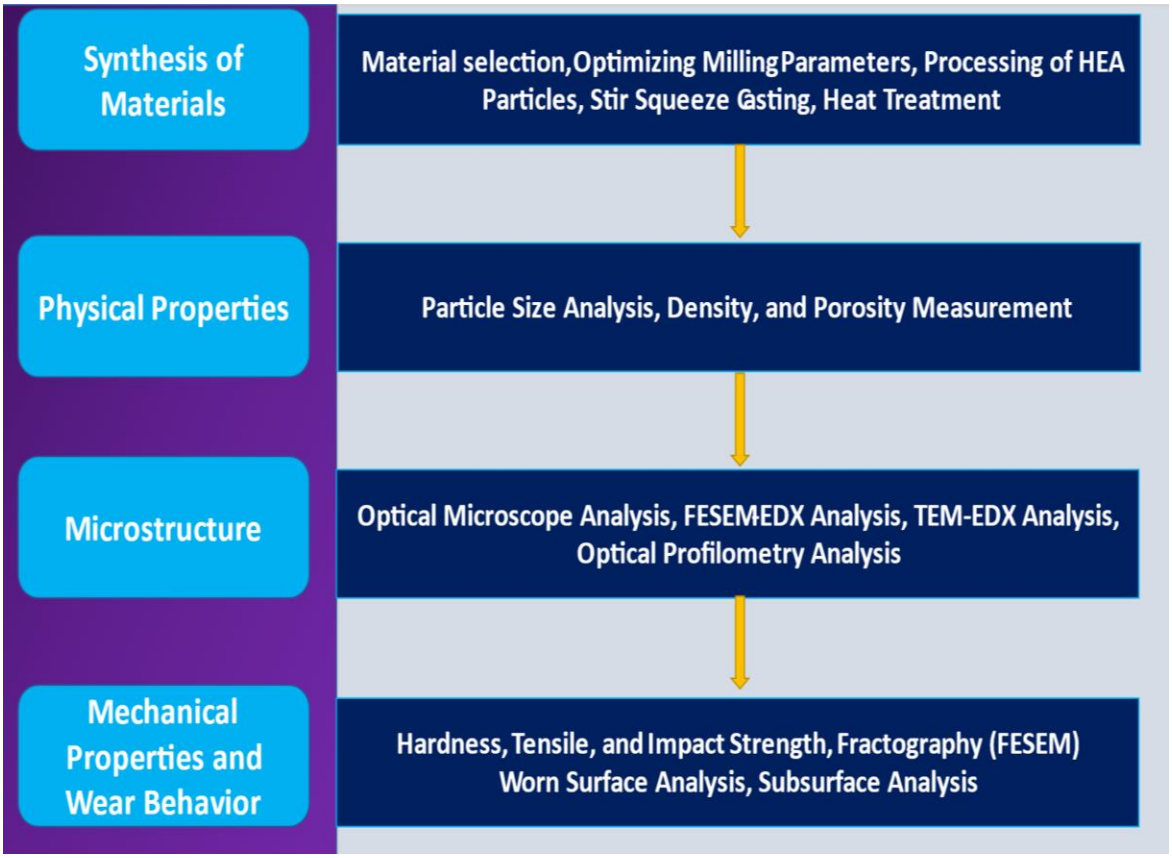

Figure 4.1: Demonstrating the proposed methodology of the present research work

4.1 SELECTION OF MATERIALS

The primary material used was Aluminium 6082 cylindrical bars and Table 4.1 presented the elemental configuration of the materials. Whereas, CoCrFeMnNi HEA opted as the reinforcement material. The compatibility and stability of the principal elements were the main criteria for their adoption. According to the thermal stability criterion HEAs Composition was selected, criteria described in Section 6.0. The CoCrFeMnNi HEA was developed by ball-milling mixtures of Co, Cr, Mn, Fe, and Ni with a purity level of more than 99.5% and an average particle size range between 60 µm and 80 µm.

Table 4.1. AA 6082 alloy chemical composition.

Materials	Mass fraction (wt.%)								
	Si	Mg	Fe	Ti	Mn	Cu	Cr	Zn	Al
AA 6082	0.7-1.3	0.6-1.2	0.5	0.1	0.4-1.0	0.1	0.25	0.2	Bal.
(AA XXXX first digit represents the principal alloying element, the second digit indicates a modification of a specific alloy, and the third and fourth digits are arbitrary numbers assigned to specific alloys.)									

4.2 METHODS

4.2.1 PREPARATION OF HIGH ENTROPY ALLOY PARTICLES THROUGH MECHANICAL ALLOYING

Ball milling was performed in an AI-VPB-2 vertical planetary ball mill with stainless steel and tungsten carbide ball vials for 42 h at 300 rev min^{-1}. Isopropyl alcohol was utilized as a processing control agent (PCA), and a powder-to-ball weight ratio of 1:10 was adopted. The milled powder is then maintained for 48 hours in a vacuum chamber to remove moisture and PCA and preserve it free of impurities.

4.2.2 SYNTHESIS OF AS-CAST ALLOY AND COMPOSITES

Stir-squeezed casting route aided with a purging attachment, ultrasonic transducer, and bottom pouring arrangement was incorporated to synthesize different HEA-reinforced composite and matrix alloys, the setup is shown in Figure 4.2. Herein, the AA 6082 matrix was melted at 720 ℃ in a bottom-pouring electrical resistance furnace. Reinforcing particles

(CoCrFeMnNi HEAs) were preheated at 450 ℃ in a muffle furnace. Preheating of milled HEA particles was to eliminate moisture and improve wettability and avert sudden temperature fall during mixing. Coverall-11 flux powder had impinged during the molten state for the removal of impurities and dross removal from the melt. Purging was carried out through dry N_2 to prevent any unwanted reactions during the casting. For the proper distribution of HEA particles in the molten matrix, stirring was carried out at 450 RPM, whereas an ultrasonic transducer was incorporated at the frequency of 20 kHz for 8 min to accomplish more significant mixing and to avert clustering of particles in the melt. The molten composite was then transferred to the squeezer through a runaway preheater maintained at 280 ℃. 150 MPa was applied onto to composite mixture using a hydraulic press. Solidification of the composite was allowed in predefined permanent molds.

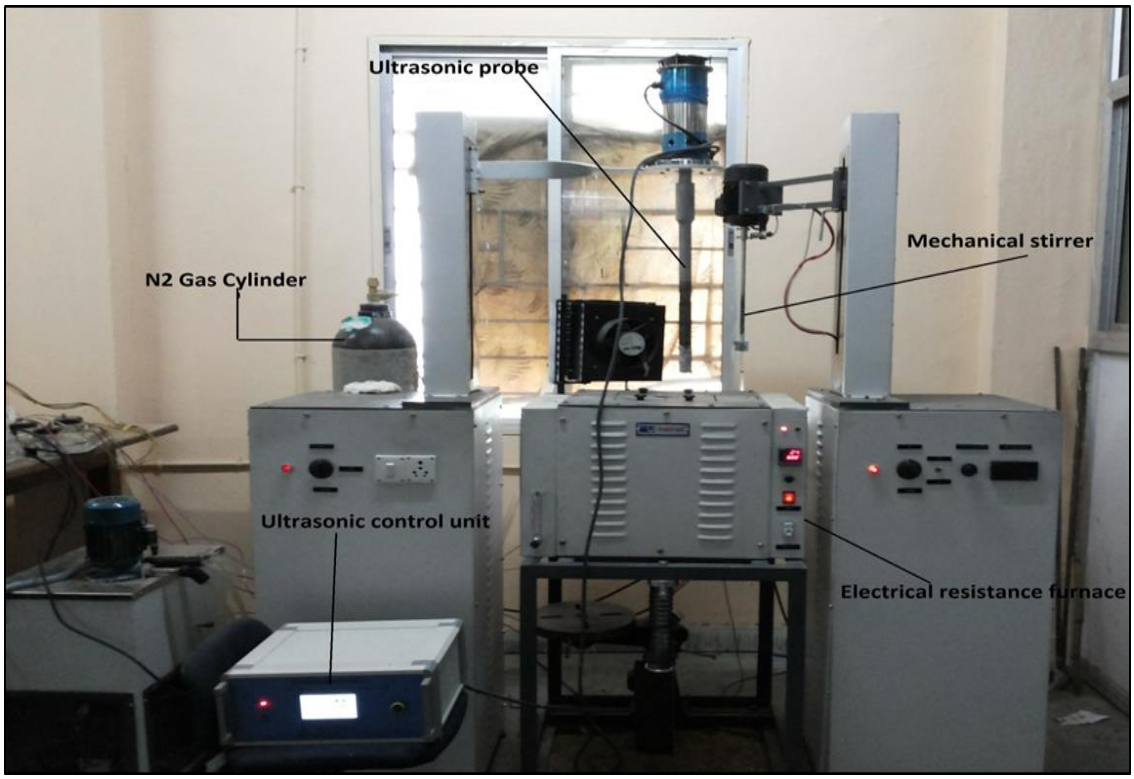

Figure 4.2: Stir Squeeze casting assisted with ultrasonic transducer

4.2.3 MICROSTRUCTURAL ANALYSIS

The phases of milled HEA powder and composite specimens were identified using the RIGAKU-JAPAN X-ray diffractometer (XRD) technique (Figure 4.3 (i)), which utilized Cu-

Ka radiation at a wavelength of 1.54 Å to identify the phases. The diffraction angle (2θ) range and scanning speeds were 20-100° and 0.02 (2θ) S^{-1} respectively. The diffracterograph was obtained given the relationship between the diffraction angle (2θ) and the relative intensity. The optical microscope AXIO imager Carl Zeiss Pvt Ltd. (Figure 4.3 (ii)) was used to study grain boundaries and different phases evolved. Whereas, the field emission scanning electron microscopy (Nova Nano FE-SEM 450 (FEI)) (Figure 4.3 (iii)) was used to examine the microstructure and morphology of the composite assisted with EDS for the elemental composition, and mapping for the distribution of elements in the specimen developed through mechanical alloying followed by squeeze stir cast technique. Keller reagent was used as the etchant containing 1% HF, 1.5% HCL, 2.5 % HNO_3, and, remaining water.

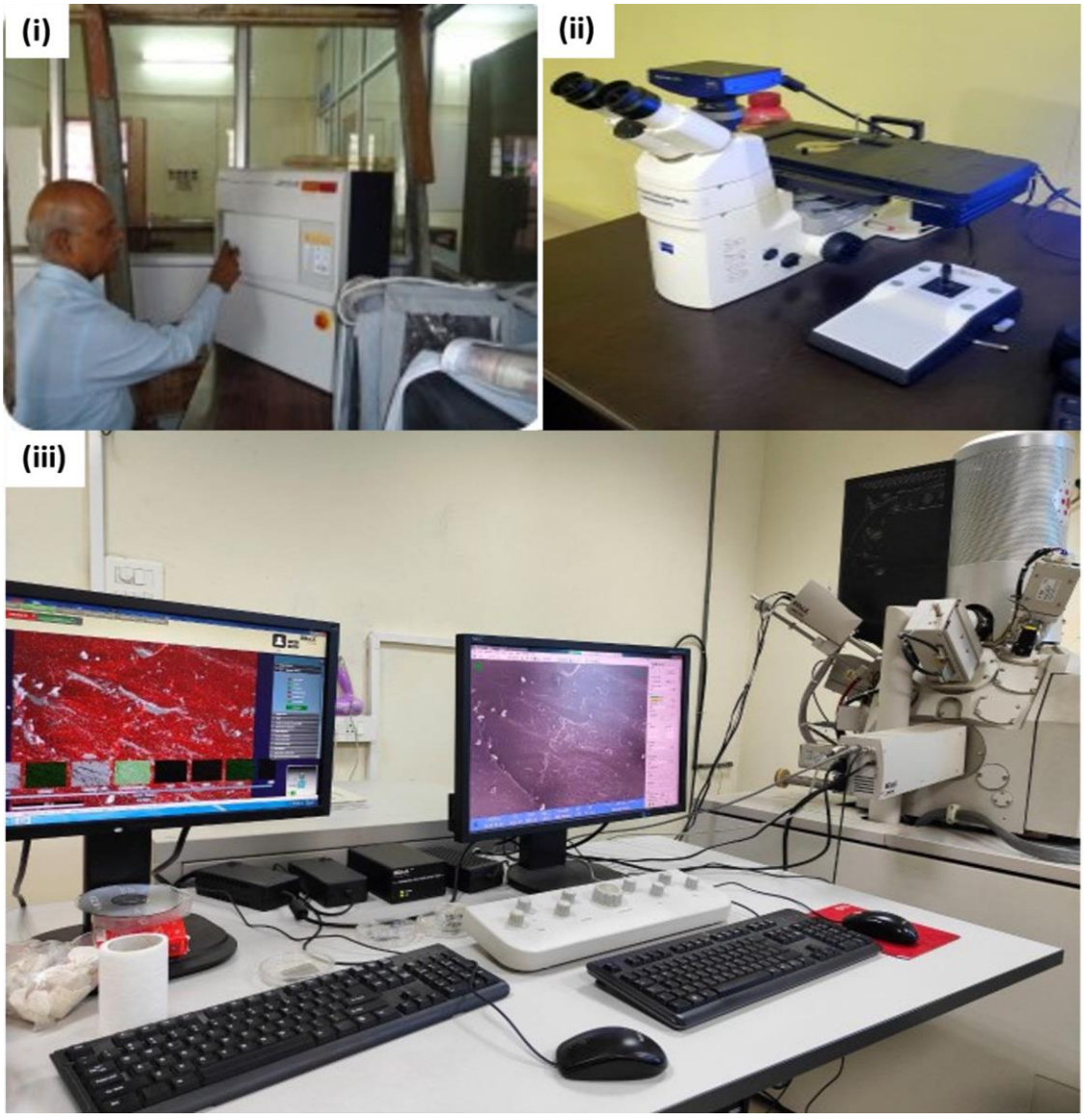

Figure 4.3: (i) X-Ray Diffractometer at MSME Department MANIT; (ii) Optical Microscope at MRC MNIT Jaipur; and (iii) FESEM Facility at Material Science and Engineering Department IIT Kanpur.

To examine the crystal structure and nanocrystalline nature of milled CoCrFeMnNi HEA powder particles JEOL JEM 300 FS (300 KV) transmission electron microscope (TEM) was used. The milled powder was kept in the ultrasonicator in ethanol for 5 minutes which prevent it from agglomeration. The HEA particles were then dried and mounted over the gold-coated grid for analysis. For the aluminium alloy and composite thin slices of 1.2-1.5 mm chip of through diamond cutter with rotating speed 80 RPM (Figure 4.4). The thin slices were then polished to 80-95 µm using different grit (800, 1200, 1500, 1800 Numbers) of emery paper as the grinding media. The scratches and deformed layers that arise during slices were removed by initial polishing. The direction of polishing changes continuously to avoid any further scratches and prevent the formation of any deformed zones. The disc punch is used to draw a 3mm diameter specimen which was followed by ultrasonication in ethanol to remove the tiny debris from the surface. The TenuPol-5 twin-jet electropolishing system (Figure 4.5) was used for the perforation of the TEM specimen. The specimen was placed in the holder which was placed in the electrolyte solution of 1200 ml CH_3OH and 300 ml HNO_3 at voltage 6V and the temperature set for the electrolyte was -30 °C at a single flow. The system turned off automatically as the perforation was completed. Finally, the post as post-ion polishing was carried out using Gatan pips II 695 ion beams milling (Figure 4.6) for 4 minutes and 30 Seconds. The specimen of alloy and composite then were examined through HRTEM (Figure 4.8). The optical profilometer (Figure 4.9) was used to study the worn surface of alloy and composites.

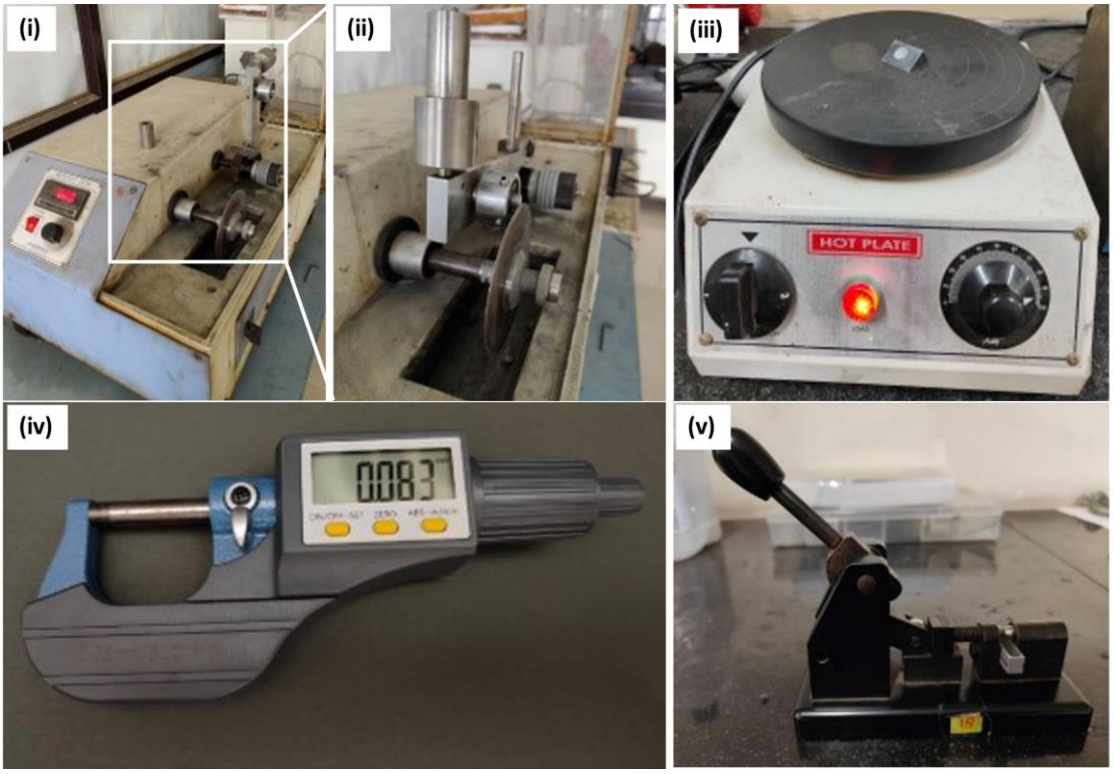

Figure 4.4: (i) and (ii) slow-speed diamond saw; (iii) Hot plate; (iv) Digital Micrometer; and (v) punch

Figure 4.5: Twin Jet Polishers (Struers)

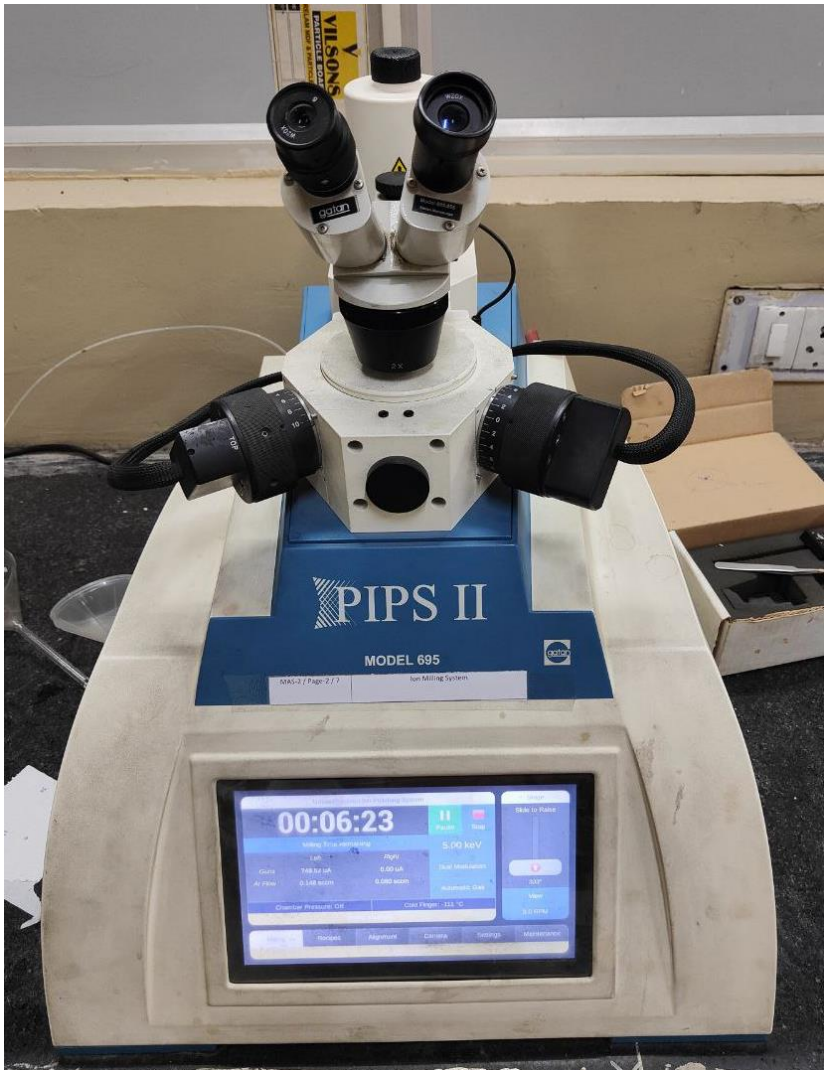

Figure 4.6: Ion Milling Setup PIPS II Model 695

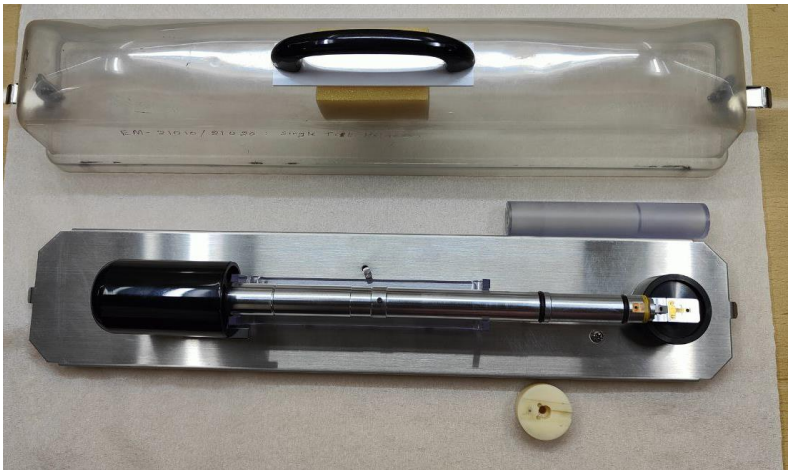

Figure 4.7: Single tilt holder

Figure 4.8: Transmission Electron Microscope Facility at the Department of Metallurgical and Materials Engineering, IIT Roorkee.

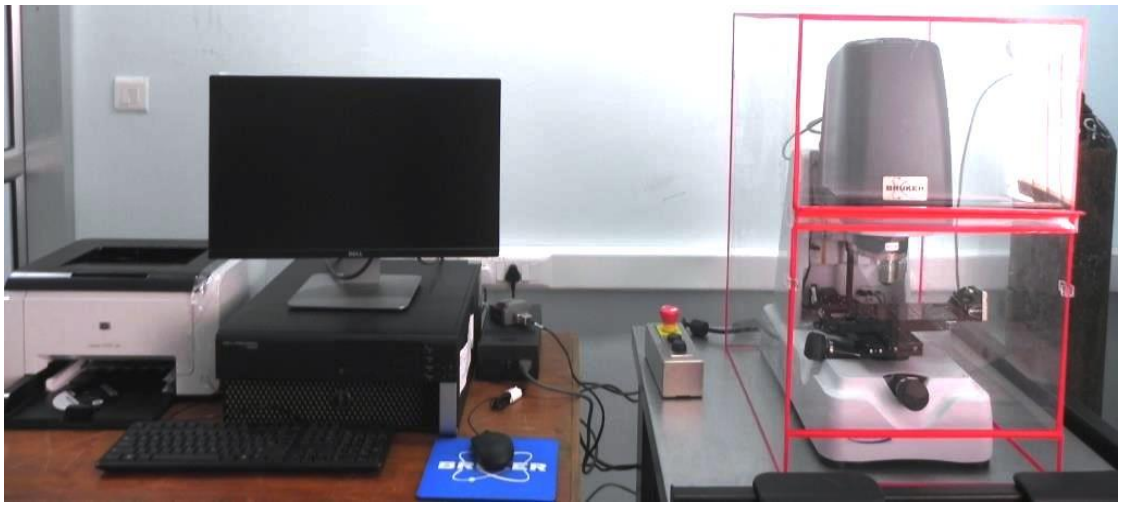

Figure 4.9: Bruker contour GT-K model setup at IIT Kanpur

4.2.4 DENSITY AND POROSITY MEASUREMENT

Following ASTM C693 standards density measurement was carried out of the casted materials in which the water displacement method was used which obeyed Archimedes principle. With the help of the following equation porosity level of the casted material was determined.

$$porosity\ \% = [\left(\frac{\rho_{th}-\rho_m}{\rho_m}\right)] \times 100 \quad (1)$$

Where, ρ_m was the measured density (actual) and $\rho_{th}$was the theoretical density. A precise measurement using the Archimedean principle revealed the actual density. The theoretical densities derived from the mixing law were evaluated by the following expression:

$$\rho_{th} = \rho_{Al} \times w_{th} + \rho_{HEA} \times w_{HEA} \quad (2)$$

Where, ρ_{th}, ρ_{Al}, and ρ_{HEA} were the theoretical density of composite, the density of matrix alloy, and the density of HEA. Here, the ρ_{Al} was 2.71 g/cm^3 and the ρ_{HEA} was 7.88 g/cm^3.

4.2.5 HARDNESS MEASUREMENT

Hardness tests were performed on the polished surfaces of alloy and composites in the as-cast condition. Digital Rockwell Tester (FIE make, model: RANSE-1) was used for examined hardness which follows the ASTM E-18 standard. The specimens were tested through a 1/16" steel ball indenter based on the B scale, whereas a 100 N load was applied for 10 seconds. The tests were performed randomly at 12 different locations which reduce any possibility of an indenter effect existing on HEAs reinforcing particles, and then the average of all twelve readings was stated.

4.2.6 TENSILE BEHAVIOR

The tension tests were performed on a universal testing machine (illustrated in Figure 4.10) that adheres to the ASTME E-8M standard, and several tensile parameters such as yield stress, ultimate tensile strength (UTS), and ductility (% elongation) were analyzed. The test was performed at the ambient condition with a constant rate of strain 0.01 S^{-1} on the specimens that were deformed to failure. For each composition, 3 specimens were tested which ensured the repeatability and reproducibility of the test result, and their mean value was reported.

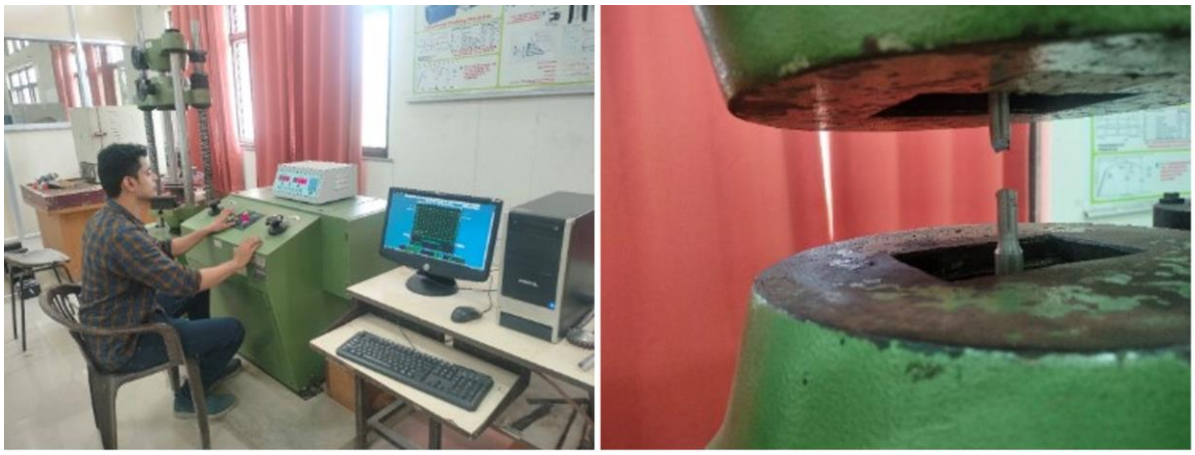

Figure 4.10: Automated Universal Testing Machine

4.2.7 ARTIFICIAL AGEING

The artificial ageing of AA 6082 was optimized to peak aged temperature. To examine the age-hardening characteristics of the alloy, hardness measured of requisite alloy as the function of ageing temperature as shown in Figure 4.11. The peak aged temperature is optimized through three distinct stages which are categorized as follows, the primary stage is solution heat treatment for 8hr at 490 ± 5 ℃ that could dissolve solute elements, the secondary stage is classified as oil bath quenching which prevents the formation of solute precipitate formation that led to attaining supersaturated solid solution (SSSS), whereas in the tertiary stage was artificial ageing (reheating) of the alloy at 9 distinct aged temperature i.e., 115 ℃, 130 ℃, 145 ℃, 160 ℃, 175 ℃, 190 ℃, 205 ℃, 220 ℃, and 235 ℃ for 6 hr to examine the overaged, peak aged, and under-aged condition. For each sample, eight readings of hardness measurements were recorded. It is worth noting that optimization of peak ageing temperature was investigated only on AA 6082 and not for composites. The Muffle furnace used for heat treatment is depicted in Figure 4.12.

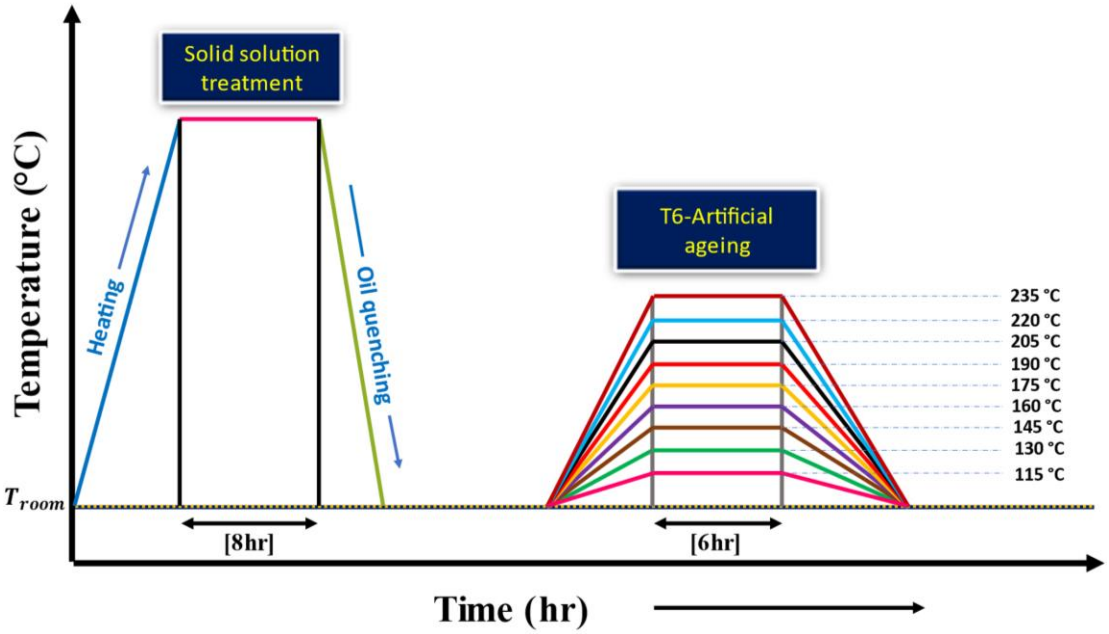

Figure 4.11: T6 Heat treatment cycle utilized to optimize peak ageing temperature of AA 6082.

Figure 4.12: Depicting actual Programmable Heat Treatment Furnace (At Nanocomposite Lab, MANIT, Bhopal, India)

4.2.8 DRY SLIDING WEAR

The tribological properties of the composites were investigated over dry sliding tests at various concentrations of HEA reinforcement, applied loads, and sliding distances. The tests were conducted on a Ducom TR-201 CL Pin on Disc Wear Apparatus (Figure 4.13), in accordance with G99-95 ASTM standard and the schematic diagram is shown in Figure 4.14. Specimens with a diameter of Ø = 10 mm and a height of h = 35 mm were fabricated from the composites for the wear tests. The sliding surfaces of the pins were carefully polished with emery paper and cleaned with ethyl alcohol before testing. To minimize measurement error, three composite samples were tested for each reinforcement condition. After each test, the track surface of the disc was thoroughly cleaned with acetone to eliminate any adhesion of wear debris. The weight loss was determined using an electronic microbalance with an accuracy of ±0.01 mg by comparing the weight of the specimen before and after the test. The test was performed for a sliding distance of 5000 m or until melting or seizure was observed, indicated by intense vibration, an unpleasant noise, and an abrupt temperature rise. The pressure and sliding distance were recorded at the moment of seizure to assess the wear response parameters. These parameters are listed in Table 2.

A weight loss approach was employed to determine the dry sliding wear rate of the fabricated alloy and composite, which was then represented as volumetric loss per unit sliding distance (mm3/m). A type K bare thermocouple tip was placed into a 2 mm diameter hole on the pin sample's lateral surface, 2 mm distant from the contact zone, to measure temperature. The pin samples were held in such a way that a 4 mm portion of it protruded from the sample holder. It is important to note that the temperature readings obtained during these tests represent the temperature at the location of the thermocouple, and the actual temperature in the contact zone may be higher than the obtained values.

Figure 4.13: Pin-on-disk wear setup (at the Material testing lab, MANIT)

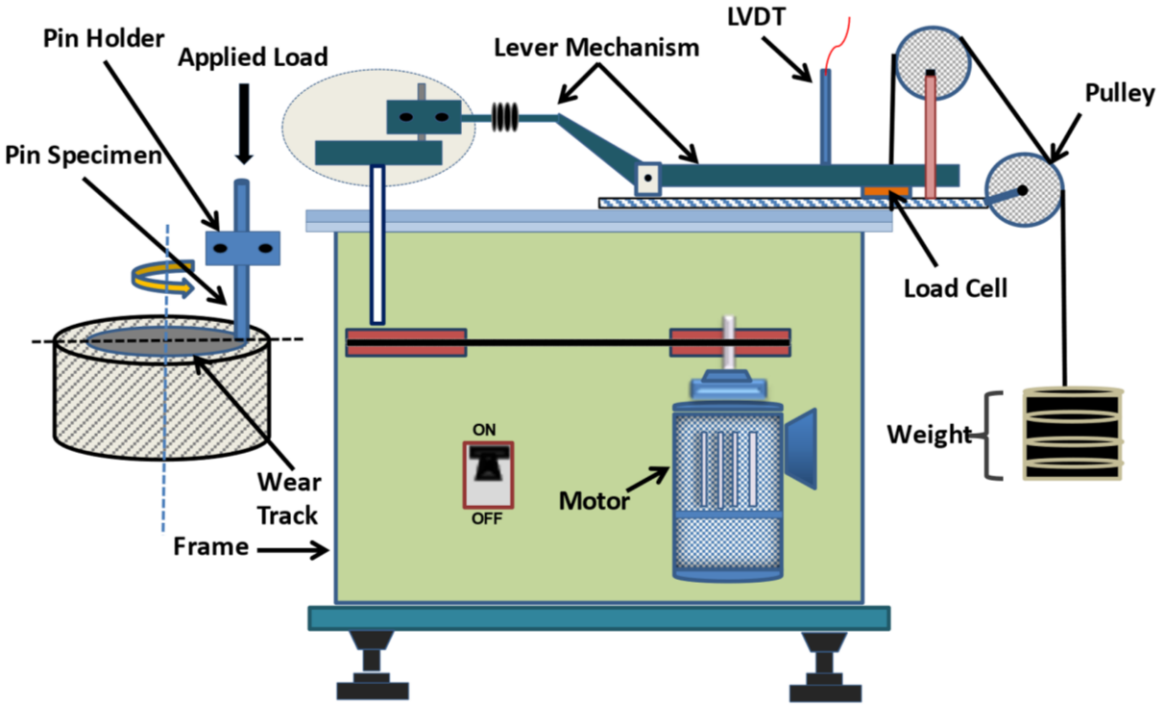

Figure 4.14: Schematic diagram of dry sliding wear machine

Table 4.2. Details of wear test parameters

S.No.	Wear test attributes	Parameter Values
1.	Ambient temperature	27-29 °C
2.	Humidity	65-70 %
3.	Cylindrical pins dimension	$\phi 10 \times 35$ mm^2
4.	Counter disk material	EN-32 Grade steel
5.	Track diameter	80 mm
6.	Sliding speed	400 RPM (fixed)
7.	Normal applied Pressure	0.25, 0.50, 0.76, 1.1, 1.27 MPa
8.	Sliding distance	5000 (fixed)

4.2.9 WORN-OUT SURFACE AND SUBSURFACE STUDIES

In these studies, the dominant wear mechanism in terms of microstructural changes and subsurface deformation was anticipated through the use of Field Emission Scanning Electron Microscopy (FESEM). The wear-affected surfaces were cross-sectioned to facilitate a detailed subsurface analysis. Subsequently, a Vickers microhardness test was performed on the polished and etched subsurface at incremental depths of 20 μm, beginning 20 μm from the worn surface. The force applied was 20 gf for 15 seconds. Microhardness measurements were repeated at 20 μm intervals until the deviation between microhardness and the bulk material hardness was no longer noticeable.

CHAPTER – 5

RESULTS

5.0 CHARACTERIZATION OF CoCrFeMnNi HEA POWDER

Figure 5.1 (a) illustrates the XRD pattern of CoCrFeMnNi HEA particles as a result of varying milling time. At 0 h, raw material peaks are noticed. The powder morphology of raw materials of Fe, Co, Cr, Mn, and Ni particles is shown in Figure 5.2. At 6 h milling, it is observed that peaks of all constituent elements start to decrease or get broadened. Whereas, due to the lesser melting point of Mn and Ni the diffraction peaks began to decrease or even disappeared completely at 6 h and 12 h respectively which is an indication of the complete dissolution of Mn and Ni. Moreover, peaks corresponding to Co are merely noticed at 18 h, whereas peaks associated with Fe are completely diminished at 24 h. Furthermore, major peaks of Cr sharply decreased after 30 h which completely vanished at 36 h. At 36 h, the presence of the FCC phase is confirmed. However, to confirm all the constituent elements completely dissociate and grain refinement and uniformity in composition milling continued for 42 h which confirmed the successful development of CoCrFeMnNi HEA powder. It is noticed that elements having a lower melting point temperature has a higher diffusion rate in the solid state to their weak bonding power of atoms as compared to higher melting point elements [312]. Therefore, it is concluded that the dissolution order of HEAs is as followed Mn → Ni → Co → Fe → Cr. After excluding the instrumental contribution, the XRD pattern is utilized to estimate the lattice strain and crystallite size which is illustrated in Figure 5.1 (b) using the Scherrer equation as given below:

$$D = \frac{K.\lambda}{\beta.cos\theta} \tag{1}$$

$$\varepsilon = \frac{\beta}{4.tan\theta} \tag{2}$$

Where D is the average crystallite size (nm), K is the Scherrer constant, λ is the X-ray wavelength, β is the line broadening at FWHM (radians) and Θ is the Bragg angle in degrees. XRD peak broadened is only due to strain i.e., crystal imperfection and distortion. Ɛ is the

micro-strain in radians, which is the ratio of peak width to the peak position. The crystallite size decreases while the lattice strain increases drastically. The lattice strain and crystallite size for 42 milling are reported to be 0.45 and 15.69 nm, respectively. Lattice strain and crystallite size are inversely i.e., lattice strain increase with decrease in crystallite size.

The average particle size distribution of CoCrFeMnNi HEA powder varied during milling. At 6h, a unimodal pattern with a larger width of 80 µm to 380 µm and an average particle size of 280.3 µm can be observed. From 6h to 24h, the average particle size declines rapidly from 280.3 µm to 34.11 µm. And at 42 h the average particle size of HEA is 0.8362 µm which can be categorized under submicron.

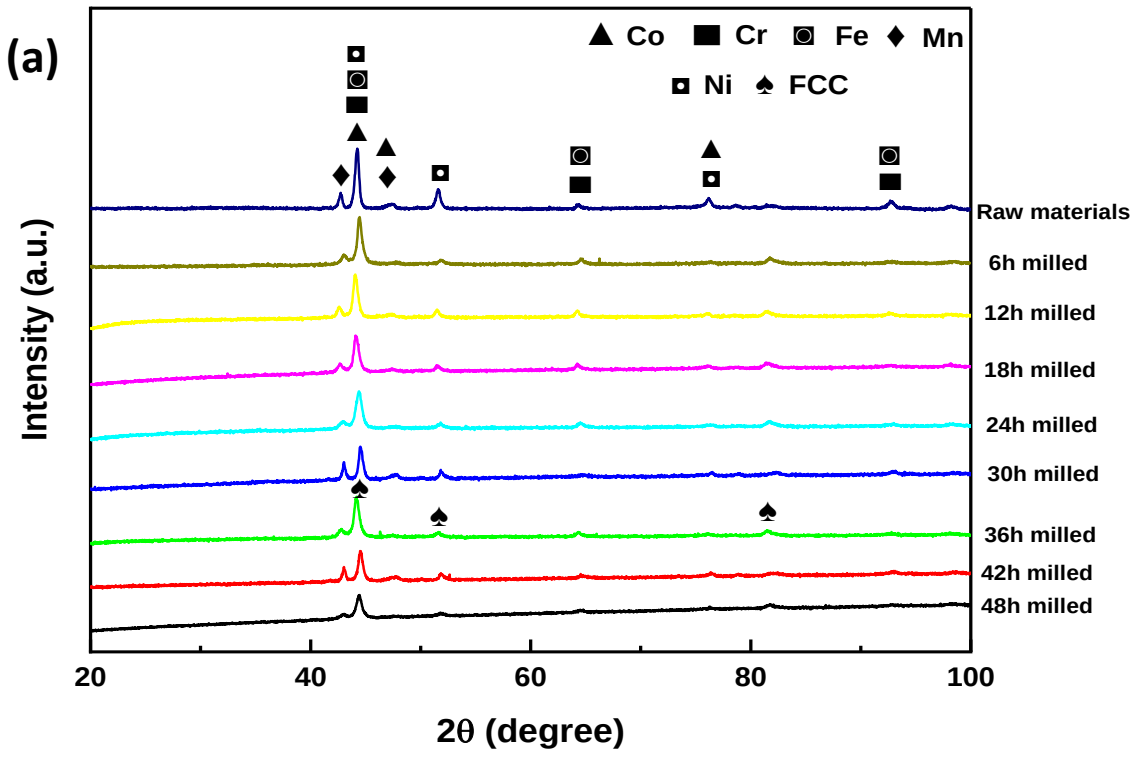

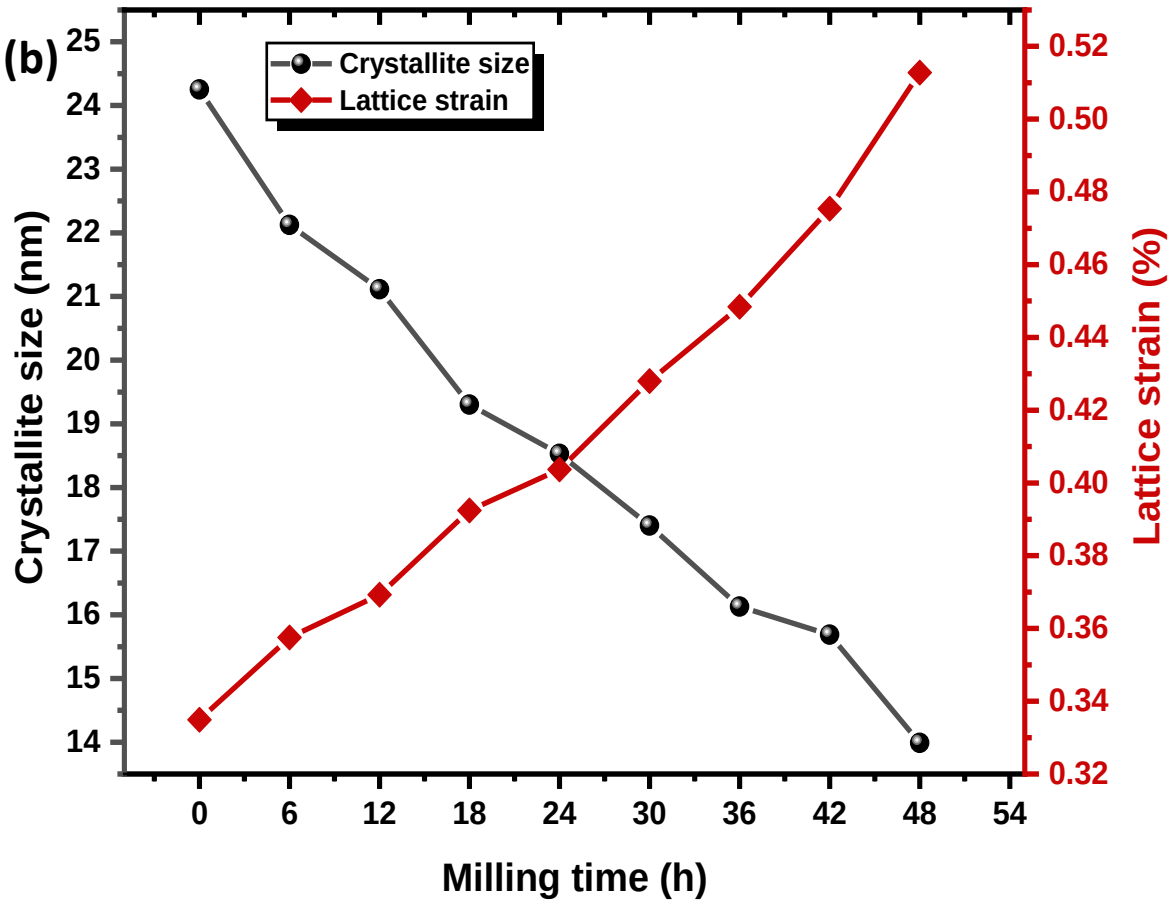

Figure 5.1: (a) XRD pattern, and (b) lattice strain and crystallite size for different milling time.

The cross-sectional morphology, microstructure evolution, and the size of the HEA particles for 6 h, 24h, and 42 h are illustrated in Figure 5.3 (a) – 5.3 (b), 5.3 (e) – 5.3 (f), and 5.3 (i) – 5.3 (j), respectively. Whereas the particle size distribution and elemental composition for the space through EDS can be visualized in Figure 5.3 (c) – 5.3 (d), Figure 5.3 (g) – 5.3 (h), and Figure 5.3 (k) – 5.3 (l). It is observed that at initial milling hours up to 6h, irregular and large-size particles are obtained. After that up to 24 h, finer particles are observed, and the average particle size decreased sharply. At 42 h, the particle is observed to be more uniform Figure 5.3 (i) – 5.3 (j) shows the spherical morphology of the particles.

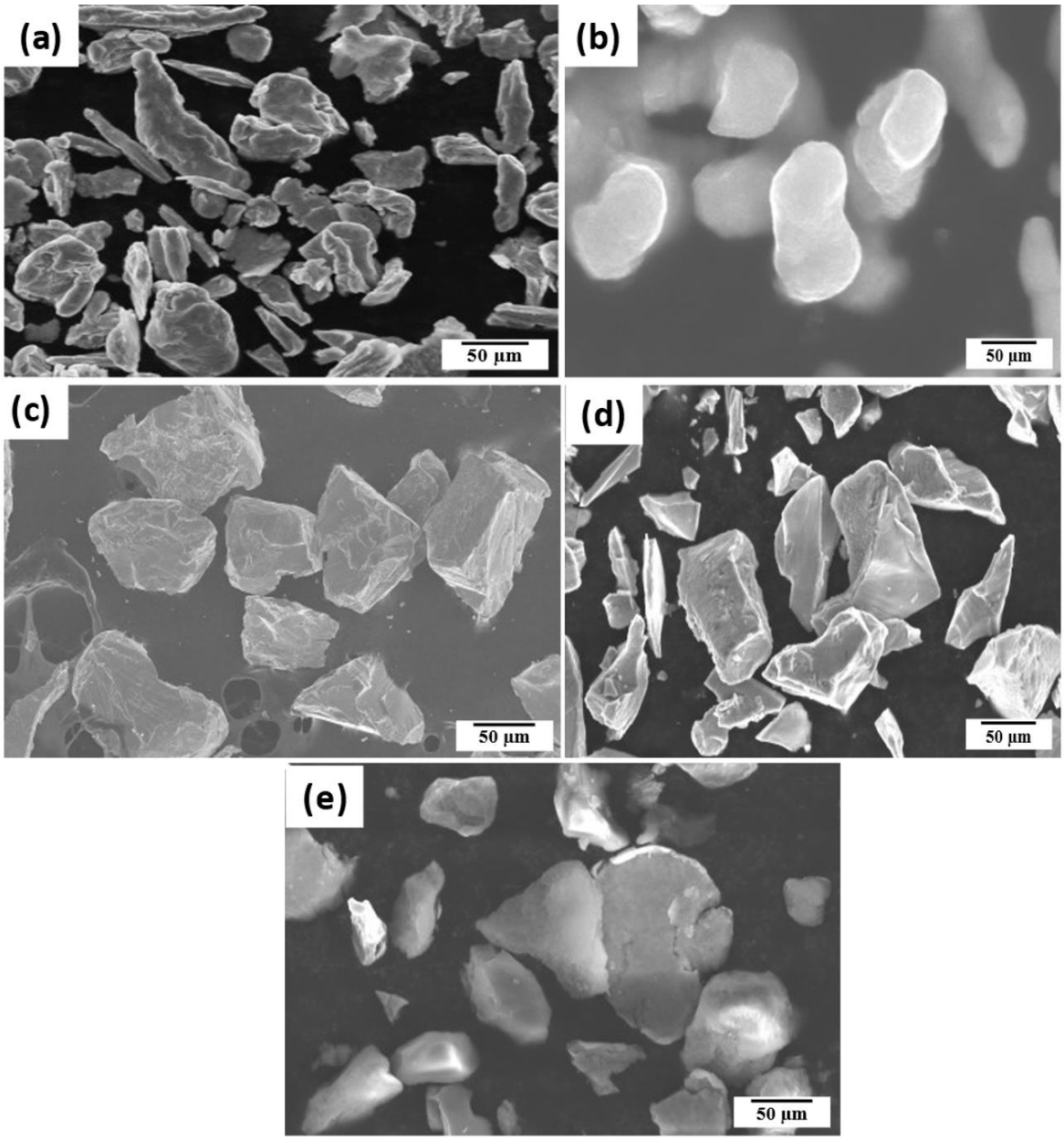

Figure 5.2: Raw material powder (a) Fe, (b) Co, (c) Cr, (d) Mn, and (e) Ni

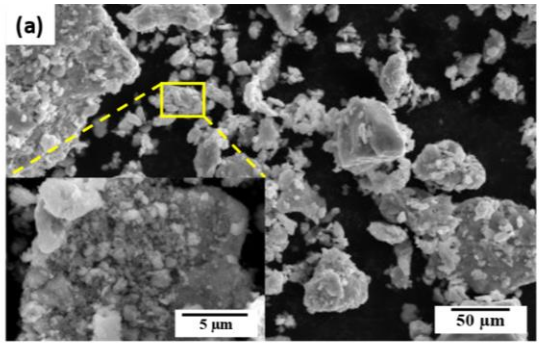

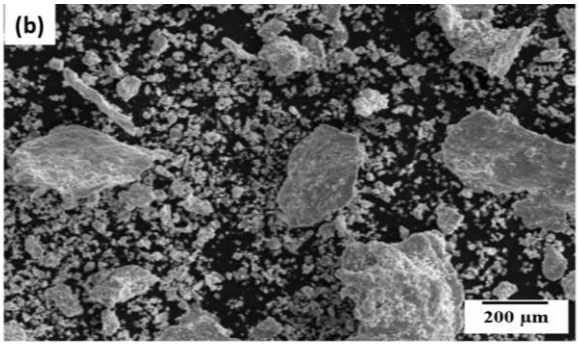

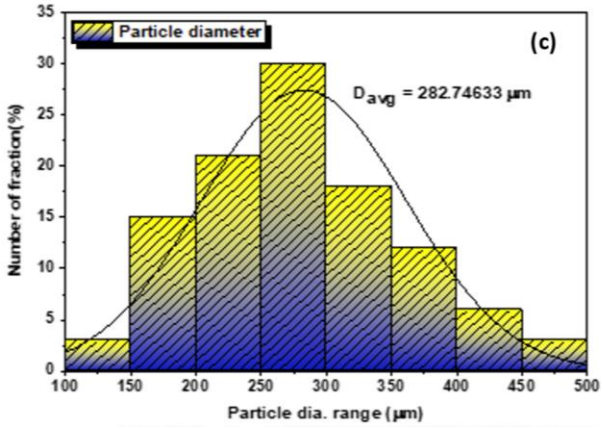

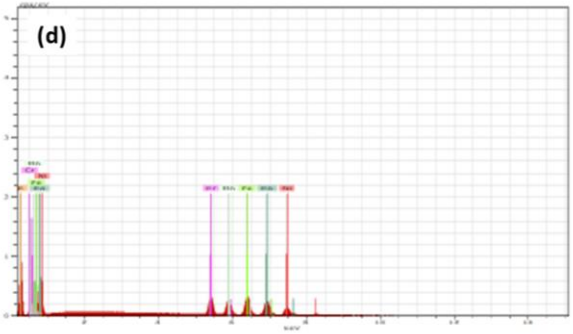

Elements	C	Co	Fe	Ni	Mn	Cr
MA-6h	30.16	19.19	17.07	12.97	10.71	9.89

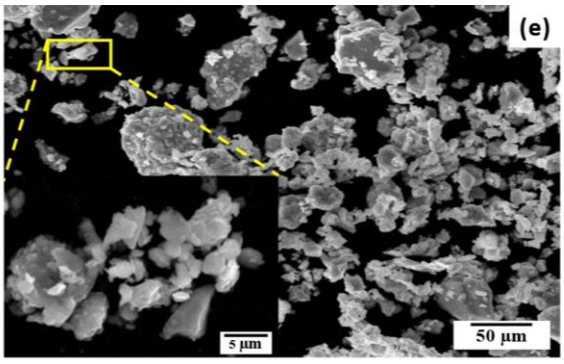

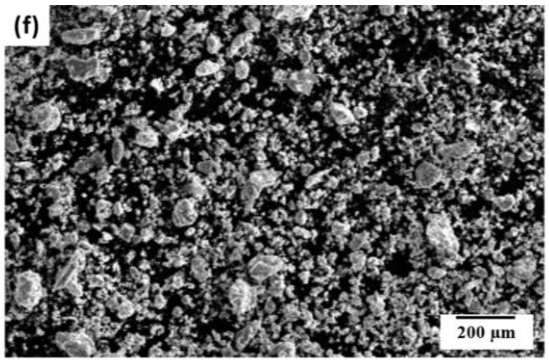

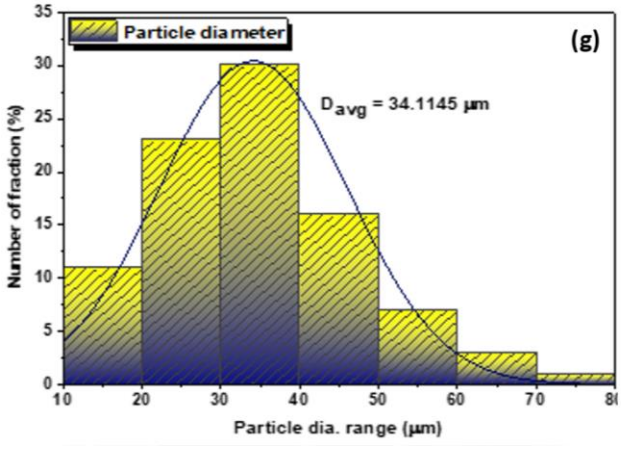

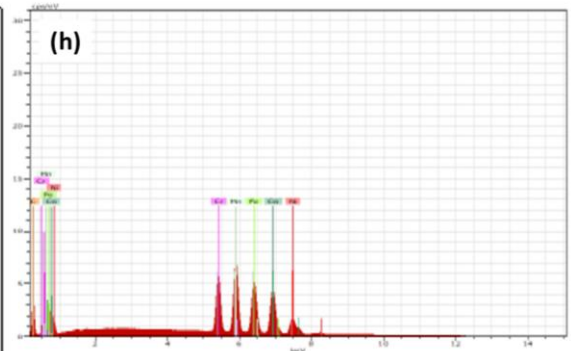

Elements	C	Co	Fe	Ni	Mn	Cr
MA-24h	25.70	20.02	19.66	12.95	12.32	9.34

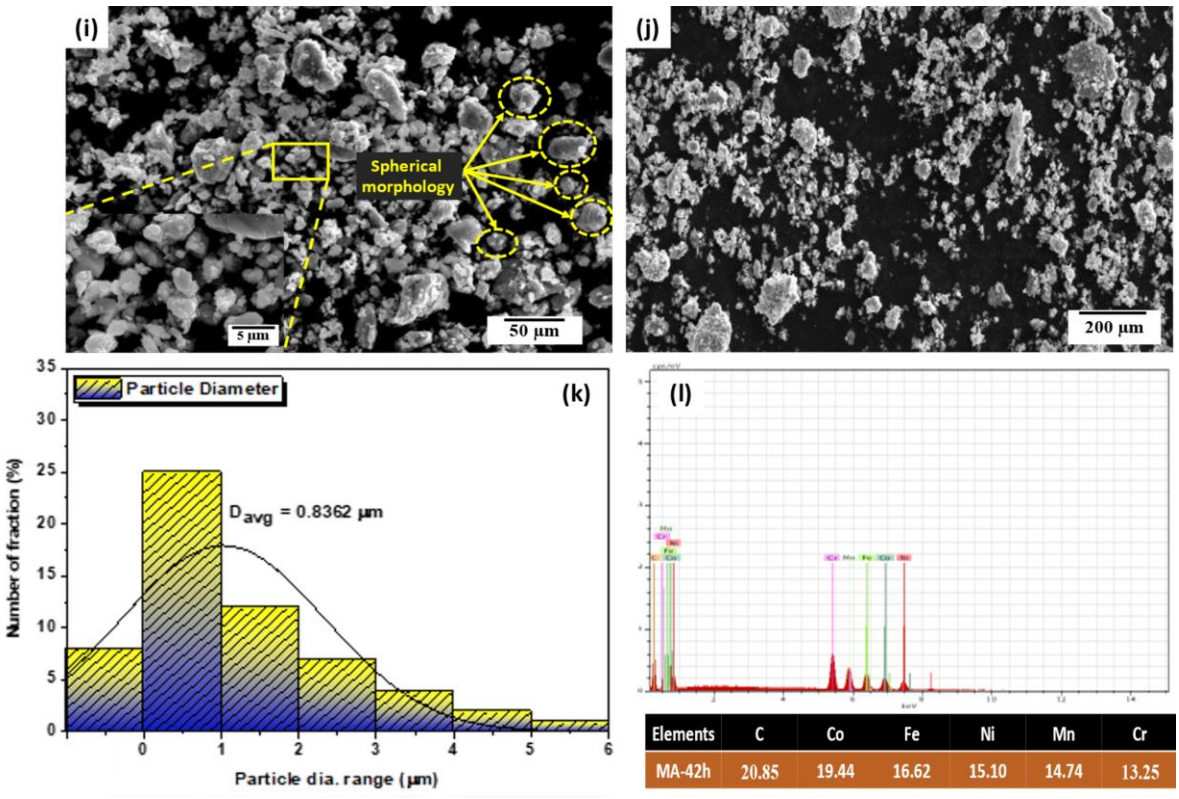

Figure 5.3: High magnification FESEM images of HEA particles (a), (e), and (i); low magnification FESEM images of HEA particles (b), (f), and (j); particle size distribution (c), (g), and (k); EDS analysis (d), (h), and (l) for 6 h, 24 h, and 42 h milling time respectively.

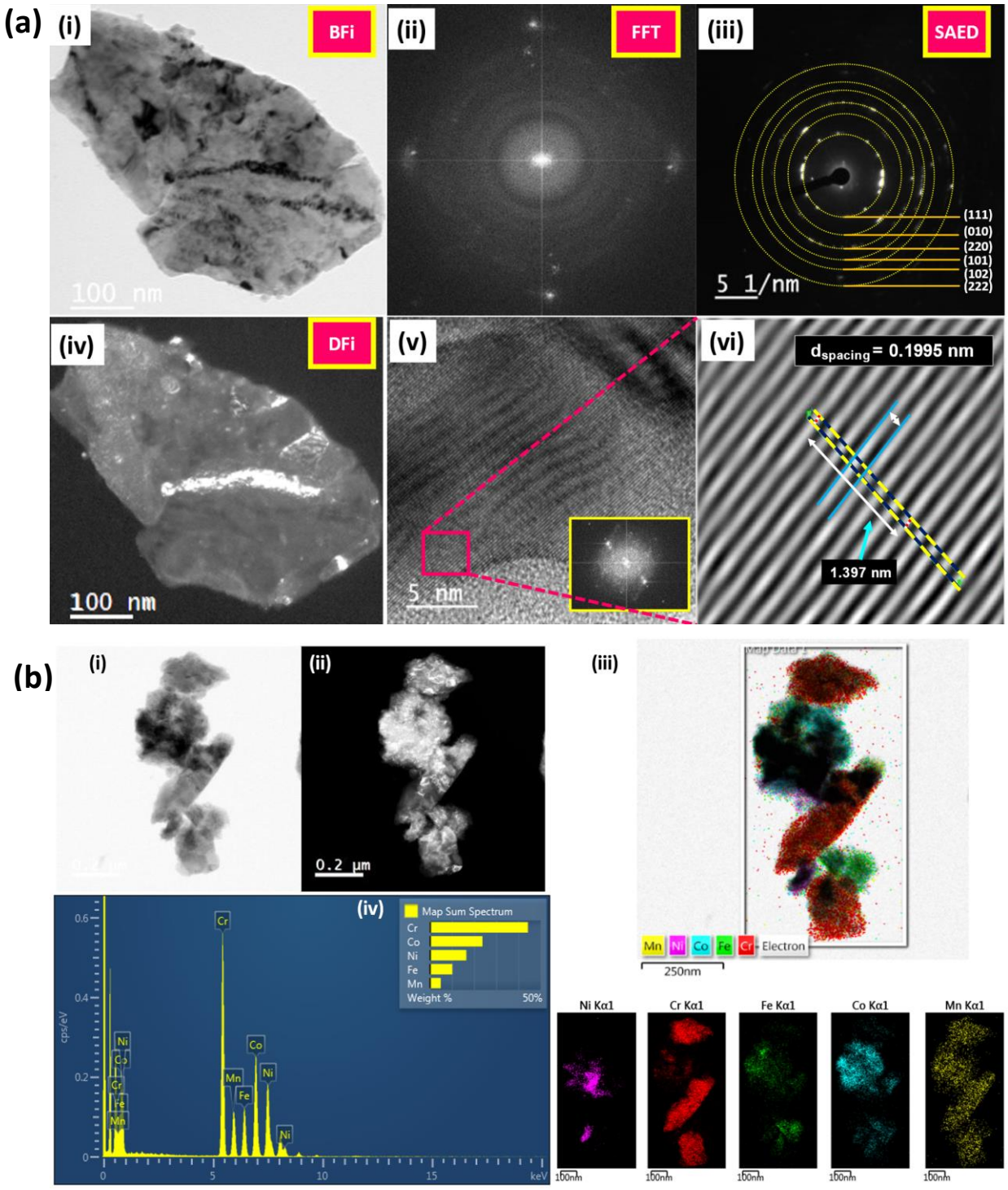

Figure 5.4: (a) TEM analysis of 42 hr CoCrFeMnNi HEA particle: (i) bright-field STEM image; (ii) FFT pattern of corresponding HEA particle; (iii) SAED pattern of HEA particle; (iv) dark field image; (v) High resolution-TEM image; (vi) Enlarge the view of pink marked

cross-section corresponding to image (v); (b) (i) Bright-field STEM of HEA particle; (ii) Dark field STEM of HEA particle; (iii) Elemental mapping; (iv) EDS analysis.

Figure 5.4 (a)(i) illustrates the bright field and dark field STEM (Scanning Transmission Electron Microscopy) image of 42 hr milled CoCrFeMnNi HEA particles with a corresponding fast Fourier transform (FFT) pattern and selected area electron diffraction (SAED) through Figure 5.4 (a)(ii) and Figure 5.4 (a)(iii) respectively. The SAED of the milled HEA particle in Figure 5.4 (a)(iii) confirms the formation of FCC phase HEA. TEM assisted with EDX was used to examine the distribution of elements in the particle for accurate study (Figure 5.4 (b)(iv)). A large particle was chosen in the TEM grid and observed that all the elements Cr, Co, Ni, Mn, and Fe were evenly distributed.TEM is good for morphology scan but it required a quite huge number of images for statistical reliability which is not an easy and cheap thing. While on the other hand, XRD can gives a crystal size distribution related to the millions of diffracted crystals illuminated by X ray during the experiment.

5.1 MICROSTRUCTURE OF THE COMPOSITES

Microstructural study of as cast AA 6082 and HEA/AA composite revealed the formation of α-Al phase and the presence of CoCrFeMnNi HEA particles additionally, different intermetallic phases are formed. The nucleated intermetallics are of different geometry such as polyhedron, round (plate form), and rod shapes. The HEA particles, α-Al phase, and intermetallics are confirmed through XRD diffractogram. The investigation of different intermetallics phases of etched specimen alloy and composites is carried out using optical microscopy along with an XRD pattern (Figure 5.5 (a)). It is observed that Keller reagents are capable to impart distinct colour to different intermetallics which are as follows: α-Al(FeMn)Si (dark phases), β-Al_5FeSi (grey phases), and Mg_2Si (black phases) which are illustrated in Figure 5.5 (b). The evolution of solute intermetallic phases evolved as a result of eutectic or/and peritectic reactions that take place during the solidification of solid solution [313][314][315]. The cluster of α-Al(FeMn)Si solute eutectic intermetallic formed near and at grain boundaries can be observed in Figure 5.5 (b) (vi). The plate form β-Al_5FeSi intermetallic phases is generally reported at the inter-dendritic zone (Figure 5.5 (b) (vii)). The Mg_2Si (black phases) intermetallics are noticeable at grain boundaries in Figure 5.5 (b) (ii), Figure 5.5 (b) (vi), and Figure 5.5 (b) (x).

$$L \rightarrow \alpha\text{-}Al + \beta\text{-}Al_5FeSi$$

$$L \rightarrow \alpha\text{-}Al + Mg_2Si$$

$$L + Al_3Fe \rightarrow \alpha\text{-}Al + \alpha\text{-}Al(MnFe)Si$$

The morphological Structures of different intermetallics phases are very intricate so along with optical microscopy FESEM with EDS is used to differentiate among different phases.

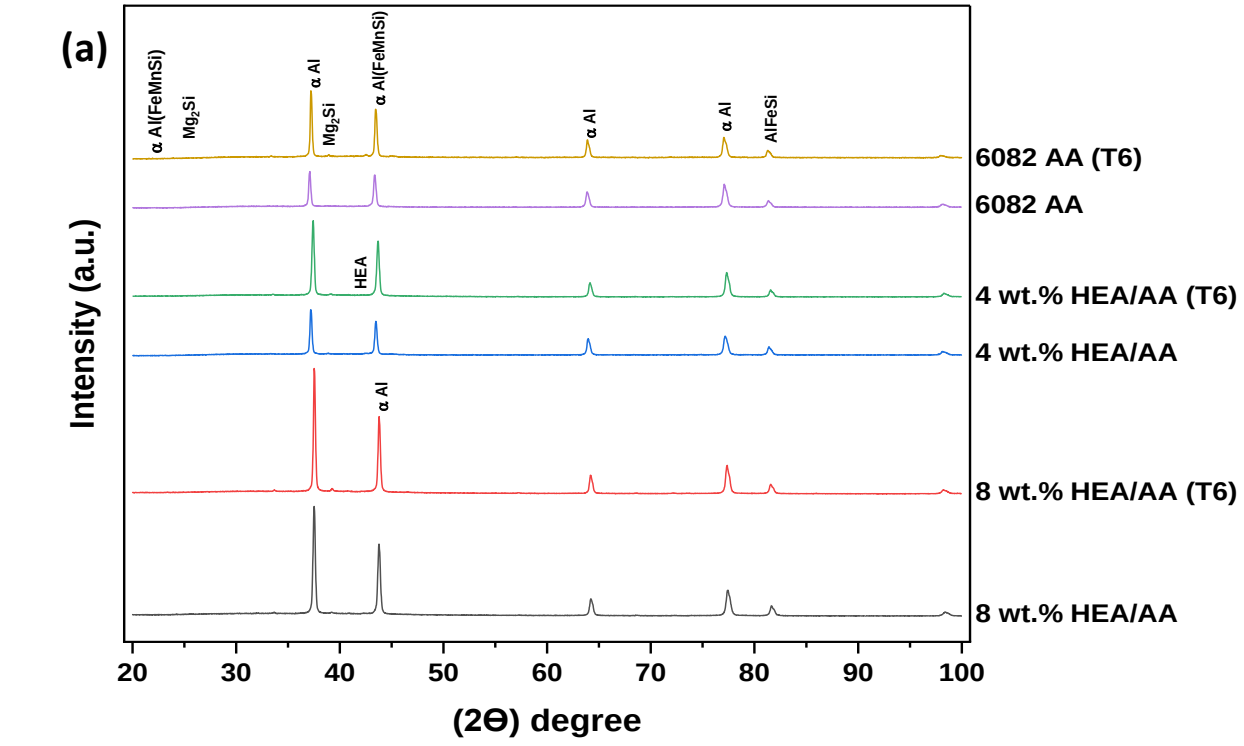

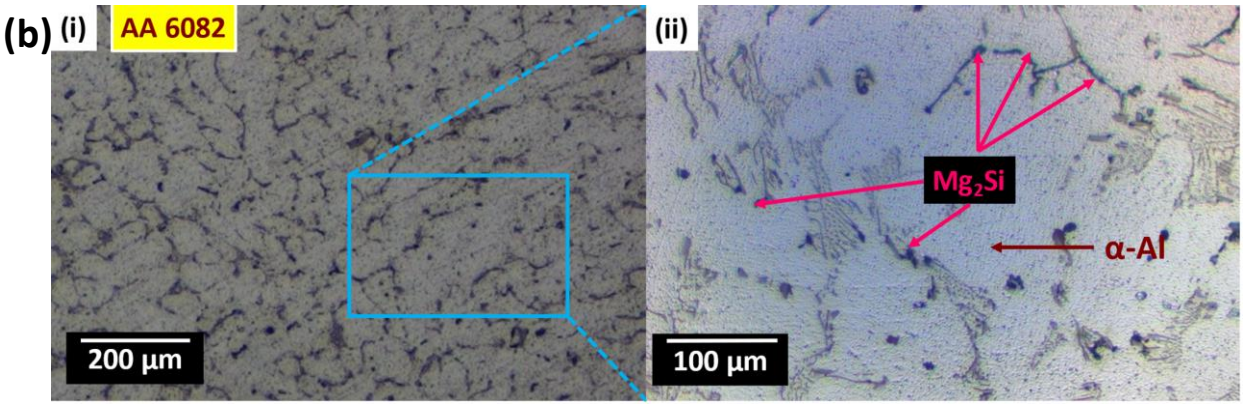

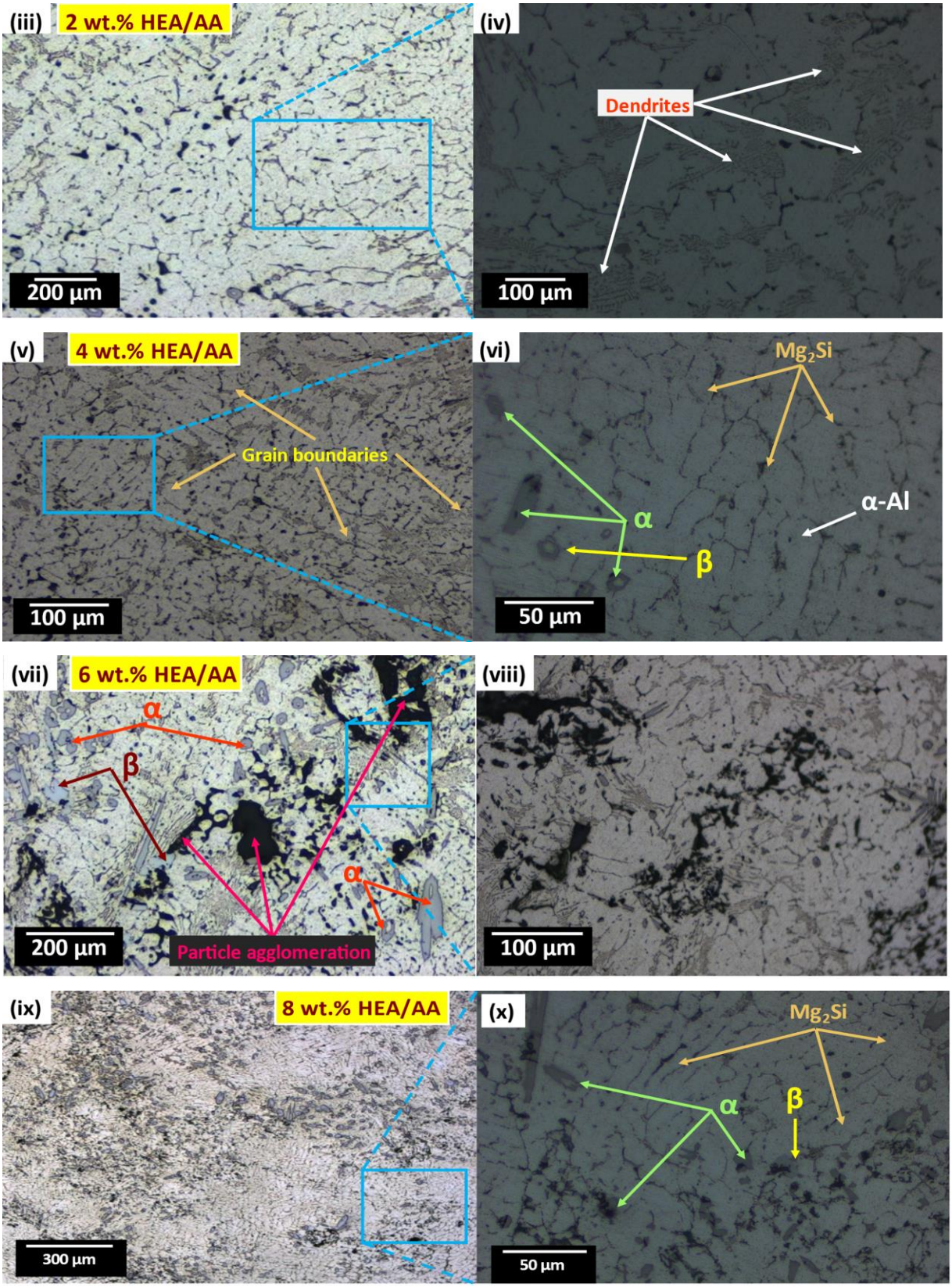
(iii)
2 wt.% HEA/AA
200 µm
(iv)
Dendrites
100 µm
(v)
4 wt.% HEA/AA
Grain boundaries
100 µm
(vi)
Mg2Si
α-Al
α
β
50 µm
(vii)
6 wt.% HEA/AA
α
β
α
200 µm
Particle agglomeration
(viii)
100 µm
(ix)
8 wt.% HEA/AA
300 µm
(x)
Mg2Si
α
β
50 µm

Figure 5.5: (a) XRD diffractogram of AA6082 and HEA/AA6082 composites; (b) Optical microscope images of AA 6082 and HEA/AA composites.

Figure 5.6 and Figure 5.7 depict the microstructure of the FESEM images of the AA 6082 alloy and HEA/AA composite with varying reinforcement content processed through a stir-squeeze casting technique assisted with the ultrasonic transducer. EDS analysis of FESEM images in Figure 5.6 and Figure 5.7 (a) shows the elemental concentration of particles in the composites given in Table 5.1. The addition of HEA particles in the Al matrix has been successfully carried out and particles are uniformly distributed as shown in Figure 5.6 (a) – 5.6 (j). The microstructure for the alloy is presented in Figure 5.6 (a) – 5.6 (b), whereas Figure 5.6 (c) – 5.6 (d), Figure 5.6 (e) – 5.6 (f), Figure 5.6 (g) – 5.6 (h), and Figure 5.6 (i) – 5.6 (j) presented microstructure of 2 wt.% HEA/AA, 4 wt.% HEA/AA, 6 wt.% HEA/AA, and 8 wt.% HEA/AA respectively. While analyzing Figure 5.6 (b), 5.6 (d), 5.6 (f), and 5.6 (h), the incorporation of HEA particles considerably refined the grain size of the AA 6082 alloy.

The grain size was calculated by the linear intercept approach using image-j software. It is witnessed that as the reinforcement concentration increased the grain size decreased. The maximum grain size is reported for as-cast AA 6082 alloy (131.089 µm), and the minimum is reported for 8wt.% HEA/AA (12.897 µm) as seen in Figure 5.6 (b) and 5.6 (j) respectively. However, the grain size of 8wt.% HEA/AA composite is higher than average grain size as compared to 4 wt.% HEA/AA. Figure 5.6 (b), 5.6 (d), 5.6 (f), 5.6 (h), and 5.6 (j) shows lower magnification microstructure whereas, Figure 5.6 (a), 5.6 (c), 5.6 (e), 5.6 (g), and 5.6 (i) shows higher magnification microstructure of HEA/AA composite. Most HEA particles are dispersed along grain boundaries, with some also found within the grains, confirming a homogeneous distribution, according to FESEM images. The smaller the particles larger will be the specific surface area and surface energy of the particles, and the greater the forces between the particles, the faster the particles agglomerate. As seen in Figure 5.7 (a), HEA particles certainly form agglomeration during the addition process. During casting, severe reactivity between the HEA particle and the Al matrix is observed under a thermodynamic scenario. Figure 5.7 (a) illustrates the homogenous distribution of HEA particles, which is well retained in the Al matrix of the 8 wt.% HEA/AA composite. Moreover, the interfacial layer of length 2 – 3 µm

can be seen at the interface of the Al matrix and HEA particles in Figure 5.7 (b). Whereas, Figure 5.7 (d) shows the XRD pattern of HEA/AA composites for different reinforcement percentages. The primary phases of composites can be seen to be Al, HEA, and Mg_2Si. At 43.37°, the peak of the strengthening HEA phase is observed, which is comparable to that of 42 h milled HEA powder, indicating that no phase transition happened in HEA throughout the processing stage [71].

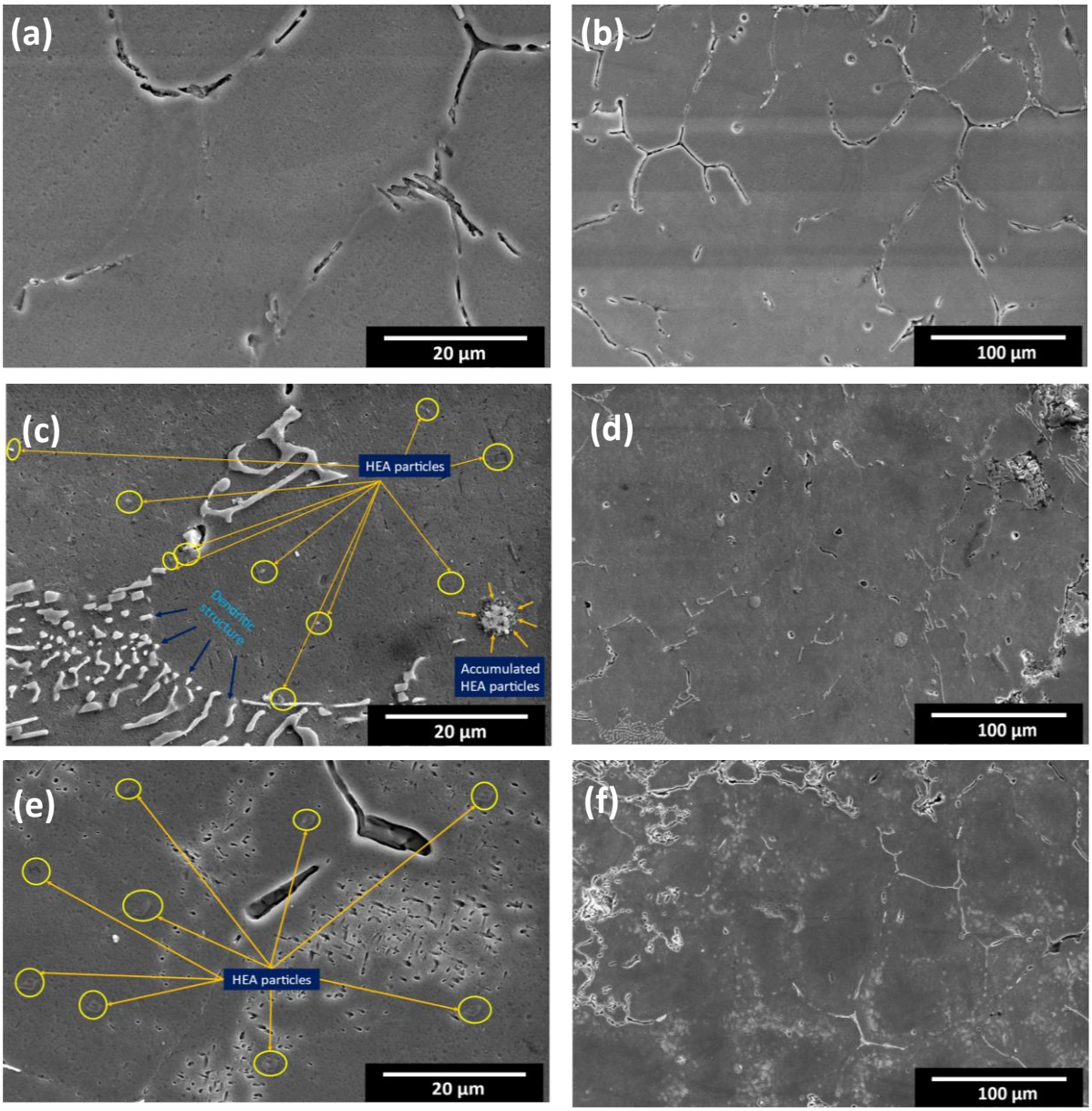

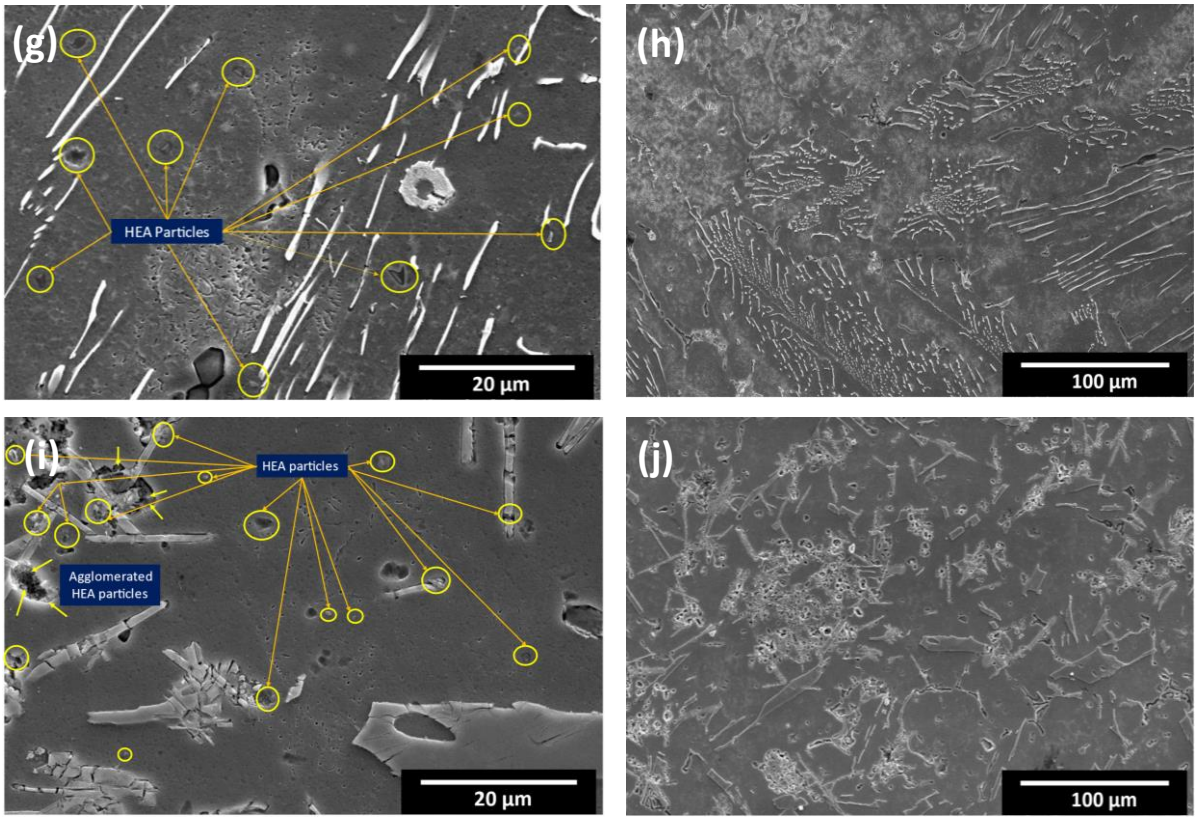

Figure 5.6 FESEM images: (a)-(b) AA 6082 Alloy; (c)-(d) 2 wt.% HEA/AA; (e)-(f) 4 wt.% HEA/AA; (g)-(h) 6 wt.% HEA/AA; (i)-(j) 8 wt.% HEA/AA.

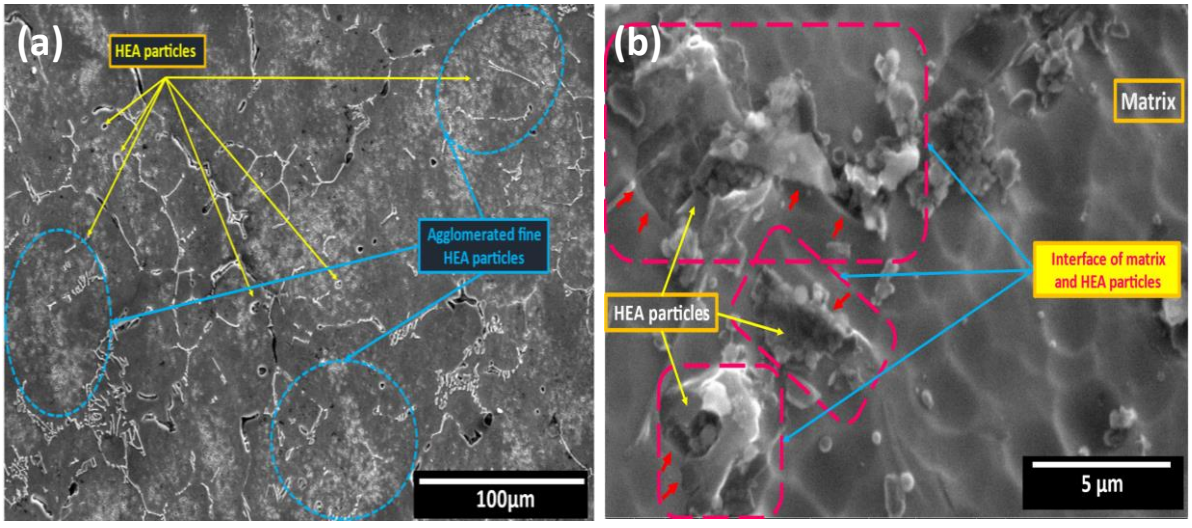

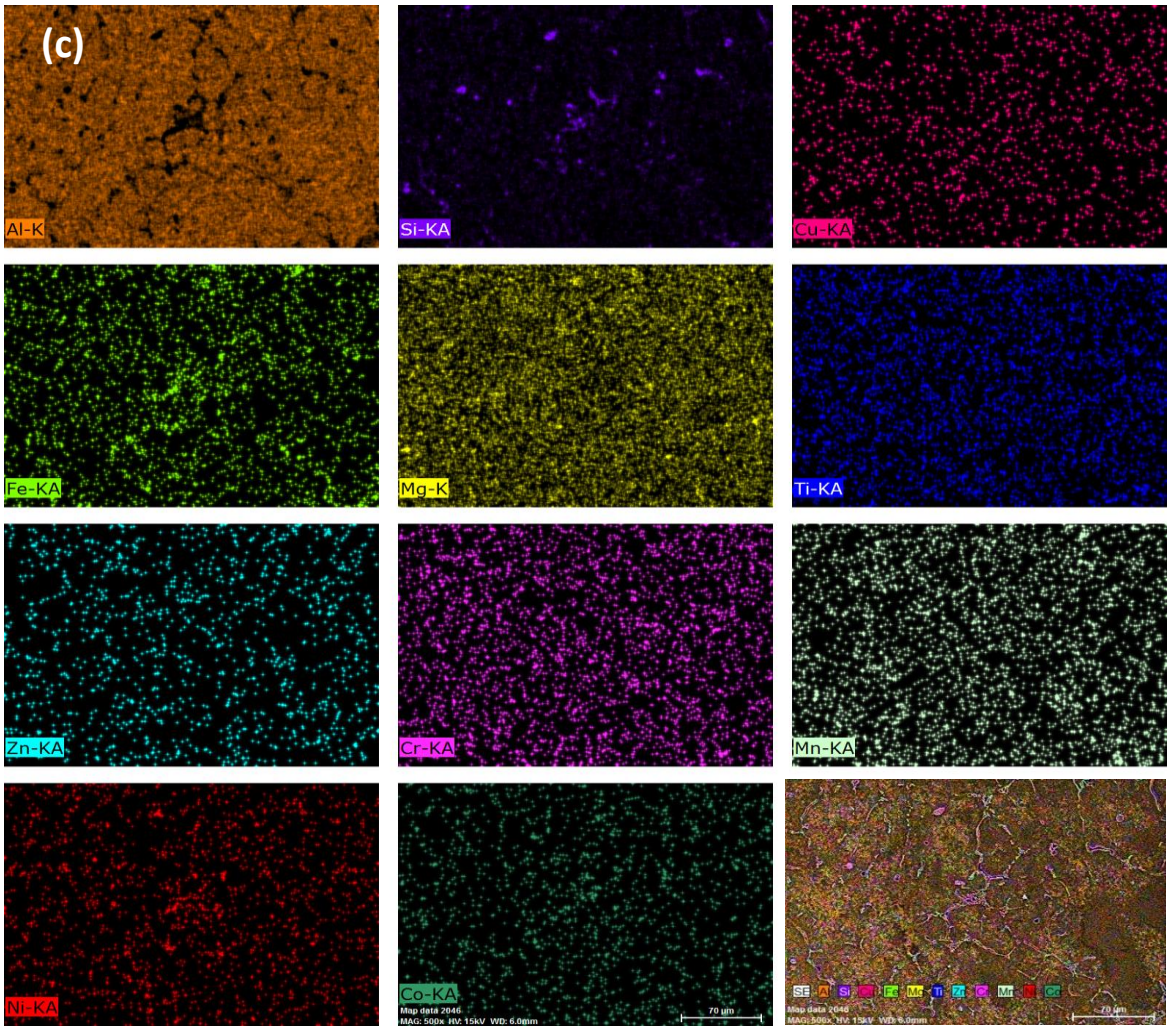
(c)
Al-K
Si-KA
Cu-KA
Fe-KA
Mg-K
Ti-KA
Zn-KA
Cr-KA
Mn-KA
Ni-KA
Co-KA
Map data 2046
MAG: 500x HV: 15kV WD: 6.0mm
70 µm
SE Al Si Cu Fe Mg Ti Zr Cr Mn Ni Cd
Map data 2046
MAG: 500x HV: 15kV WD: 6.0mm
70 µm

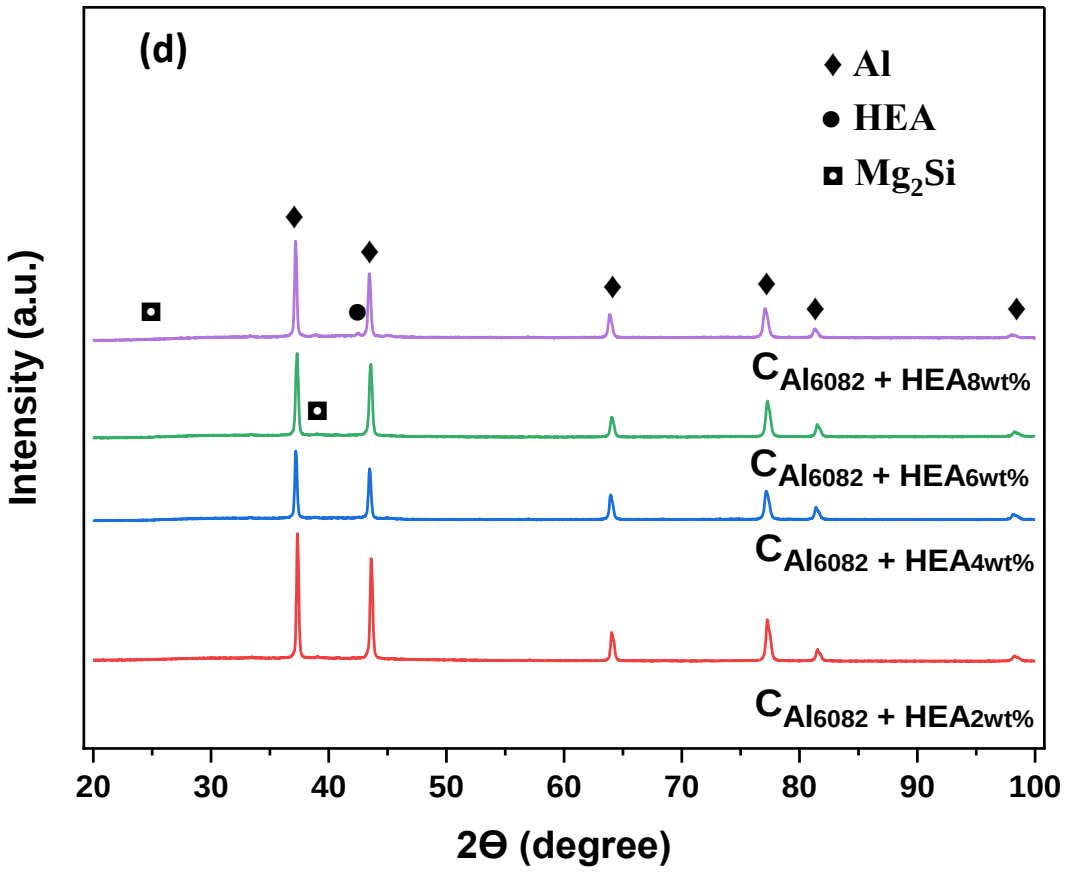

Figure 5.7: FESEM images (a)-(b) 8 wt.% HEA/AA composite; (c) EDS mapping analysis of 8wt.% HEA/AA composite; (d) XRD plots of HEA/AA Composites.

The EDS mapping analysis of 8 wt.% HEA/AA samples is shown in Figure 5.7 (c). EDS mapping images reveal the element distribution of the composite. As demonstrated in Figure 5.7 (a), the grains noticed in composites are equiaxed ultrafine grains or fine elongated grains. These materials are obtained through the stir squeeze casting route, which accounts for controlled grain [316]. The average grain size of the 8 wt.% HEA/AA composites is 12.897 µm which is significantly smaller than AA 6082, which demonstrates that due to the inclusion of HEA particles grain refinement occurred. It is concluded that the inclusion of HEA particles inhibited grain boundary motion and reduced grain expansion during thermomechanical processes. It is noteworthy that the grain of the HEA/AA composite exhibits a heterogeneous grain structure that consists of ultrafine grains and a few large elongated grains [317].

Table 5.1. The elemental concentration (wt.%) is shown in Figure 5.6, and Fig. 5.7 (a) by EDS analysis.

Elements		Al	Mg	Si	Zn	Mn	Fe	Co	Cr	Ni	Cu	Ti
Figure 5.6(b)	AA 6082	96.06	1.46	0.97	0.44	0.55	0.29	-	0.06	-	0.06	0.04
Figure 5.6(d)	2 wt.% HEA/AA	95.43	1.52	1.64	0.41	0.35	0.06	0.15	0.06	0.13	0.19	0.04
Figure 5.6(f)	4 wt.% HEA/AA	94.81	1.49	1.22	0.53	0.61	0.41	0.10	0.08	0.58	0.14	0.03
Figure 5.6(h)	6 wt.% HEA/AA	94.56	1.58	1.16	0.45	0.73	0.64	0.06	0.09	0.51	0.19	0.04
Figure 5.6(j)	8 wt.% HEA/AA	91.46	1.31	0.90	0.79	0.75	1.21	1.26	0.46	1.15	0.63	0.07
Figure 5.7(a)	8 wt.% HEA/AA	90.70	2.87	0.56	0.49	0.84	1.09	1.30	0.79	0.91	0.41	0.05

5.2 T6 AGEING CYCLE

The ageing behavior of an Al-mg-Si matrix alloy was examined during heat treatment optimization for several ageing temperature ranges, notably 115, 130, 145, 160, 175, 190, 205, 220, and 235 ℃ at a constant ageing duration of 6 hr. Table 5.2 shows the reported hardness value during optimization. The hardness of the AA6082 matrix increased with the ageing temperature and reached a maximum of 190 ℃, although when the ageing temperature increased further, the hardness achieved reduced. As a result, the maximum ageing temperature (T6 peak) for monolithic alloy was specified as 190 ℃. Figure 5.8 (a) shows an Al-Mg-Si matrix alloy's hardening behavior at differing ageing temperatures, allowing a schematic interpretation of how precipitates change in microstructure as the ageing temperature rises.

The sequencing of precipitates produced by the supersaturated solid solution (SSSS) for medium-strength aluminium alloys could be written as SSSS → early precipitation region (GP region) → β phase → β’ phase → β” (Mg_2Si).

Table 5.2: Variation of hardness with varying artificial ageing (T6) temperature

Artificial Ageing Temperature (°C)	115	130	145	160	175	190	205	220	235
Hardness (HRB)	50.01	54.77	59.04	63.80	68.52	74.814	70.03	63.41	60.91

The microstructure of aged alloy and composite is well depicted in Figure 5.8 (b) and the elemental distribution of alloy and composites is listed in Table 5.2. FESEM images of matrix alloy under peak aged conditions showed very fine Guinier-Preston region (GP region) precipitates evenly distributed across the grains, as well as the coarser size and less spaced grain boundary precipitates. The existence of such a finer precipitates structure of the GP region and metastable phase is the primary reason for matrix alloy strengthening.

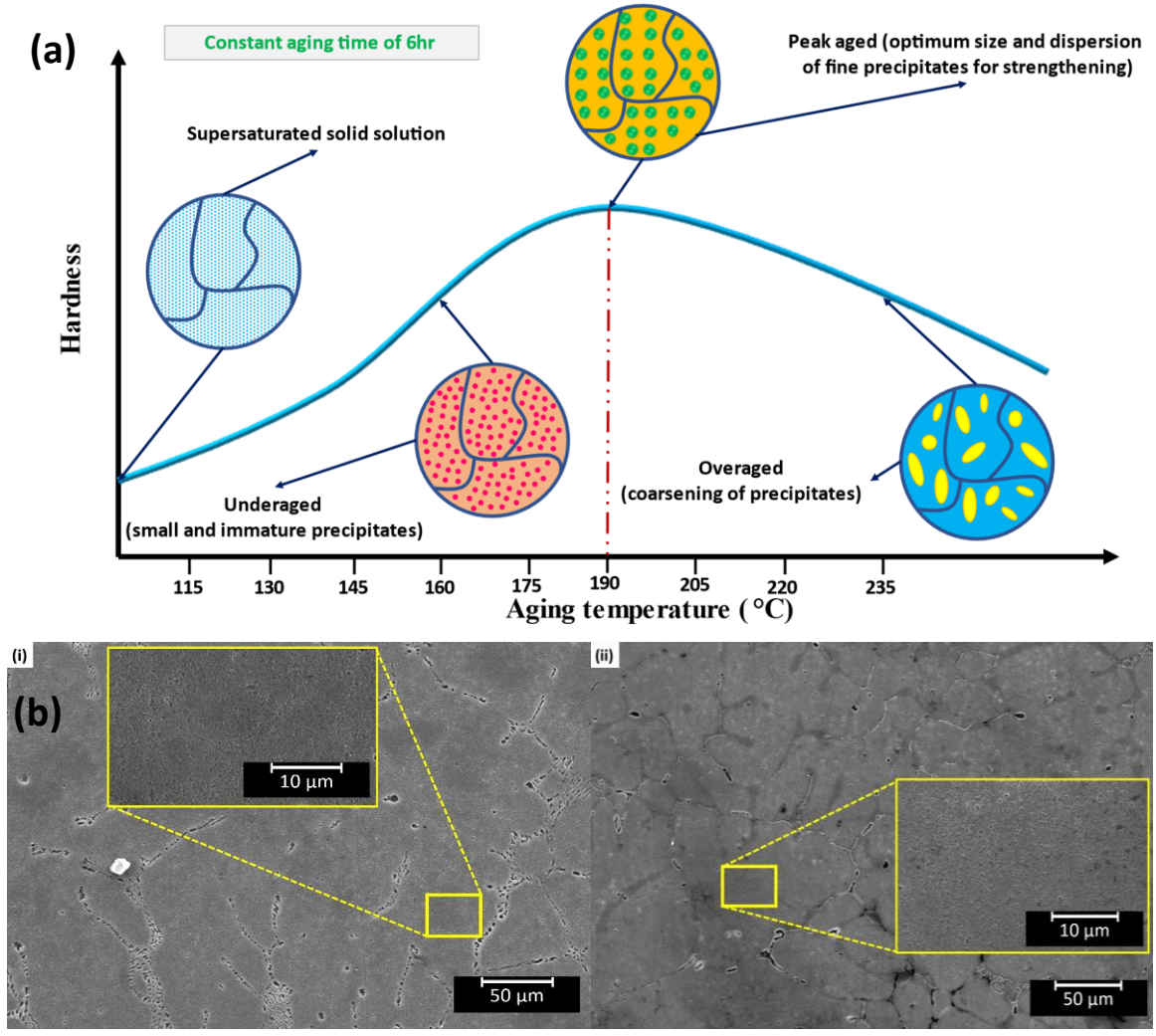

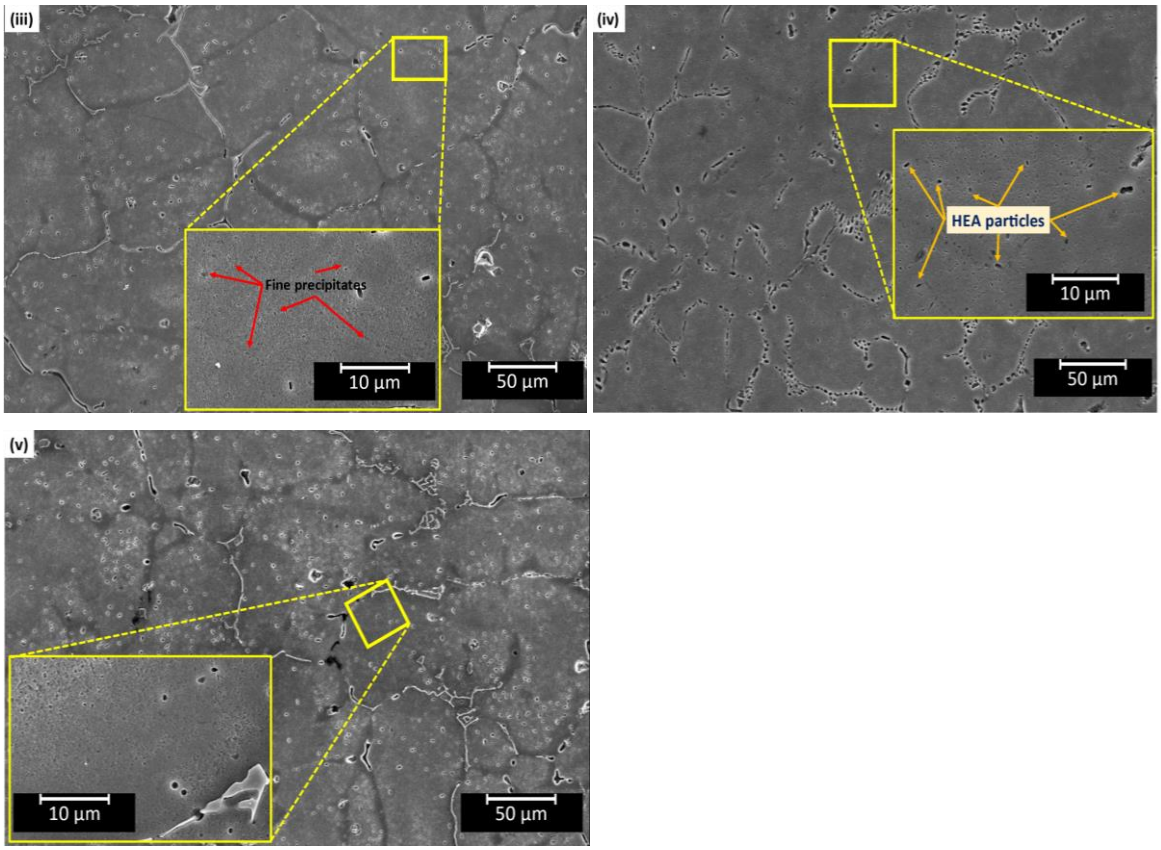

Figure 5.8: (a) Transformation of Microstructure during artificial ageing; (b) Metallographic microstructure for the artificial ageing condition: (i) AA 6082; (ii) 2 wt.% HEA/AA composite; (iii) 4 wt.% HEA/AA composite; (iv) 6 wt.% HEA/AA composite; (v) 8 wt.% HEA/AA composite.

Table 5.2: Elemental distribution in AA-6082 and HEA/AA composite for as-cast condition and artificial aged condition.

Elements / Figures	Al	Mg	Si	Mn	Zn	Fe	Cu	Cr	Ti	Co	Ni
Figure 5.8 (i)	96.06	1.46	0.97	0.55	0.44	0.29	0.15	0.06	0.04	-	-
Figure 5.8 (ii)	92.49	1.25	0.65	0.62	1.26	0.42	0.78	0.37	0.24	1.06	0.86

Figure 5.8 (iii)	91.86	2.48	1.18	0.26	1.60	0.36	0.67	0.30	0.18	0.45	0.65
Figure 5.8 (iv)	91.05	2.19	1.04	2.88	0.67	0.21	0.38	0.24	0.21	0.43	0.70
Figure 5.8 (v)	89.28	2.16	0.83	2.57	1.80	1.27	0.58	0.28	0.19	0.57	0.46

The analysis clearly shows that coherent precipitates have a very high probability of forming at peak ageing temperatures. Up to a specific temperature limit, the as-cast matrix phase and the precipitates have lattice coherency; however, once that temperature limit is exceeded, lattice vibration results in non-coherent precipitates inside the matrix. Additionally, it is well known that a moderate amount of fine precipitates that develop on the soft matrix phase of the alloy during artificial ageing after solution heat treatment (SHT) improve its mechanical properties [318]. Nevertheless, above-peak aged coarsen precipitates were seen, which led to mediocre alloy hardening.

It should be emphasized that the research (which includes measurements of hardness, impact behavior, and tensile strength of alloy and composite) uses the optimal peak ageing state or 190 ℃.

5.3 MECHANICAL PROPERTIES

The densities and porosities of the AA 6082 alloy and HEA/AA composites are illustrated in Figure 5.9 (a) It is clear that the actual densities, regardless of composition, are lower than the predicted densities, indicating the existence of pores. The actual densities increased as the HEA content increased, and the maximum density was obtained for 8wt.% HEA/AA composite. It is also unveiled that theoretical densities nearly matched actual density with a difference of 2-5 %. The porosity observed in 6 wt.% HEA/AA more than 4 wt.% HEA/AA, which may be attributed to factors such as (i) casting flaws, (ii) H_2 evolution, (iii) gas trapped during cooling, and (iv) HEA particle agglomeration.

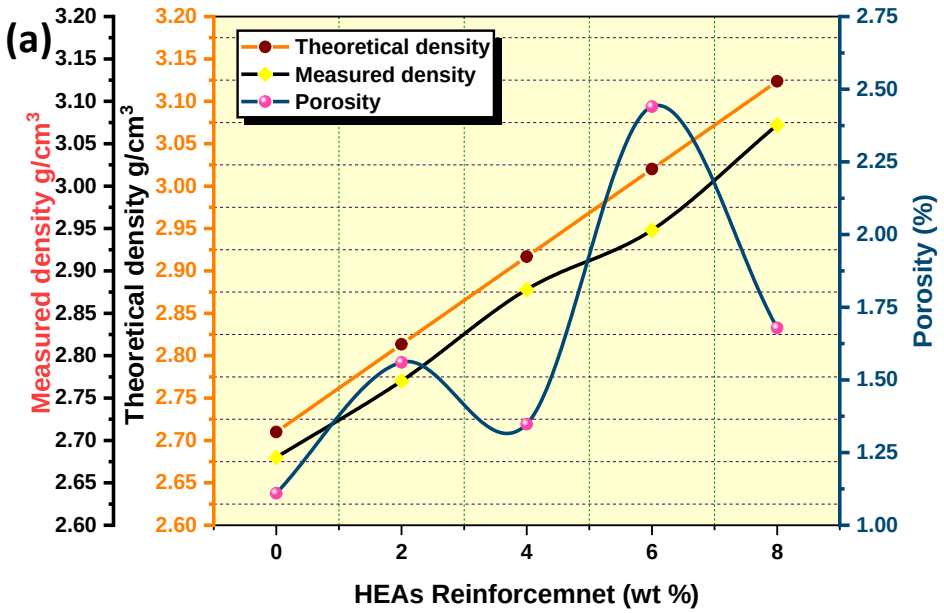
(a)
Theoretical density
Measured density
Porosity
Measured density g/cm³
Theoretical density g/cm³
Porosity (%)
HEAs Reinforcemnet (wt %)

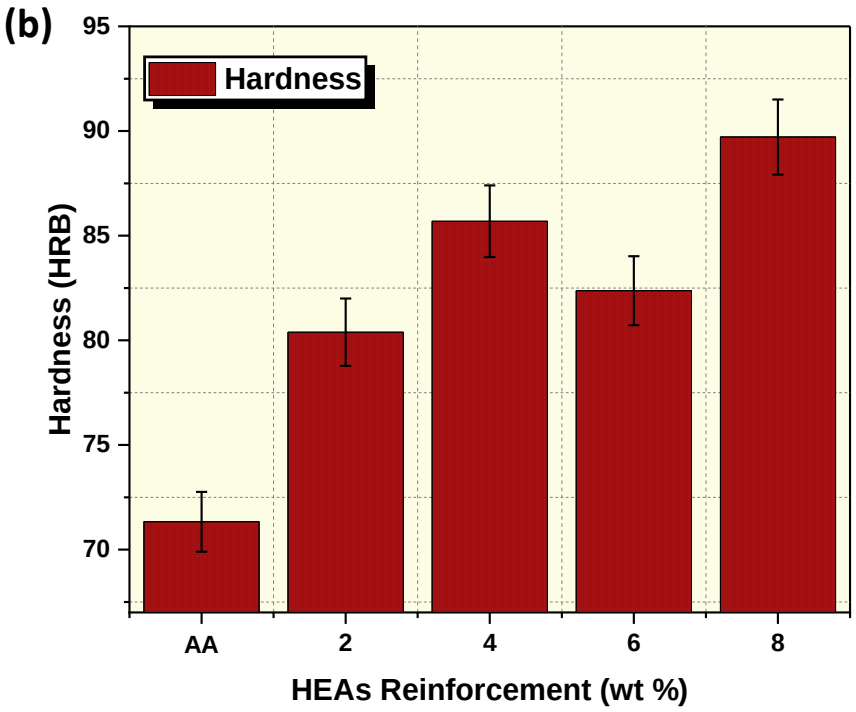
(b)
Hardness
Hardness (HRB)
AA
HEAs Reinforcement (wt %)

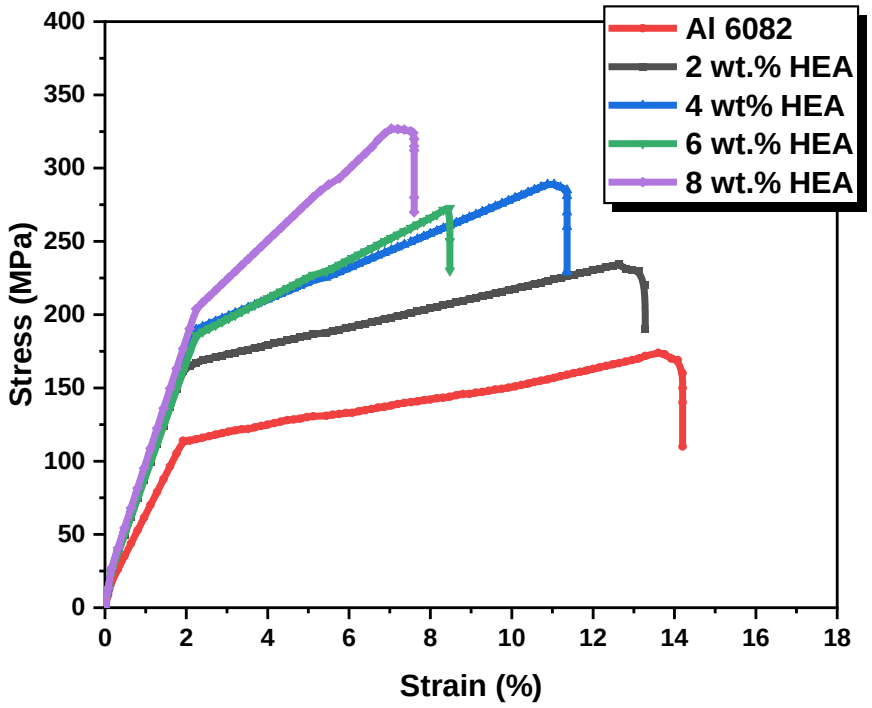

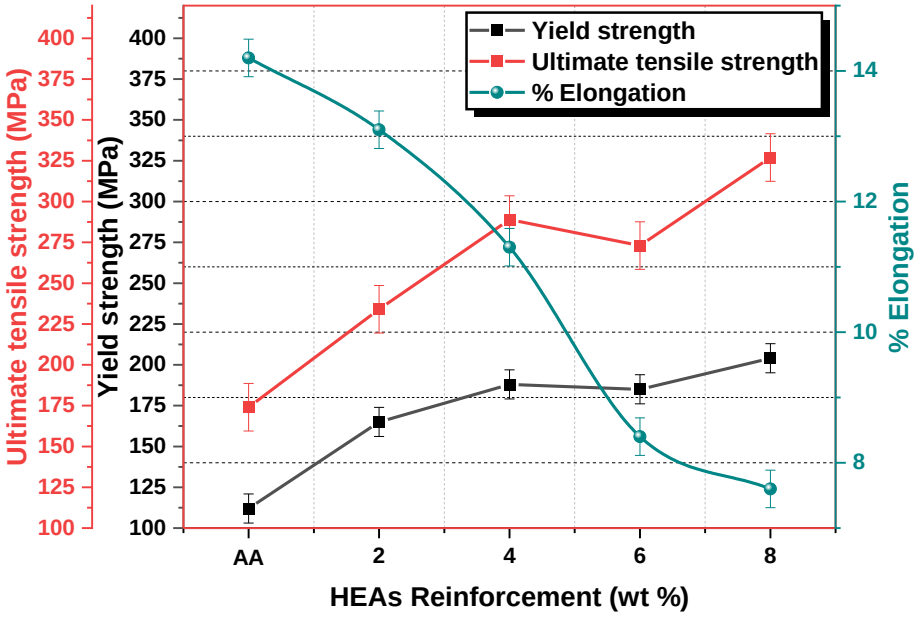

Figure 5.9: (a) Variation in density (measured and theoretical) and porosity; (b) Variation of hardness with varying HEA concentrations; (c) Engineering stress vs strain curve; (d) Tensile strength of HEA/AA composites

The average value of hardness for the AA 6082 alloy and composites is depicted in Figure 5.9 (b). It is confirmed that in composites irrespective of the content, the hardness obtained is

superior to the base alloy which indicates that the inclusion of HEA particles contributes significantly to the material's hardness. Whereas the 8wt.% HEA/AA shows the highest hardness and is more than 28.57 % from matrix alloy. The decrease in hardness value for 6 wt.% HEA is due to accumulation of HEA particles within the matrix phase which are responsible for voids. However, the increase in the hardness value for 8 wt.% HEA/AA is due to back stress hardening and dislocation hardening.

The specimens for tensile strength testing have been processed according to the ASTM E8M standard for the as-cast alloy and composites. The tensile strength was evaluated for each distinct reinforcement condition using computerized universal testing equipment ((FIE make, model: UNITEK 94100-100 kN). Figure 5.9 (c) illustrates the engineering stress-strain curve whereas, Figure 5.9 (d) depicts the alloy and composite characteristics, such as percentage elongation, yield strength, and ultimate tensile strength that are investigated for varying HEAs reinforcement content at room temperature.

With the inclusion of HEA particles mechanical properties of HEA/AA are highly improved irrespective of the reinforcement content when equated to base alloy, which has a yield strength of 112 MPa. The yield strength, ultimate tensile strength, and fracture strain of 2 wt.% HEA/AA composite is reported as 169 MPa, 234 MPa, and 13.1 % respectively. The HEA/AA composite obtained at 8 wt.% HEA reinforcement content exhibited optimal mechanical properties, and its yield strength, ultimate tensile strength, and fracture strain are reported as 201 MPa, 327 MPa, and 7.6 % respectively. The percentage elongation eventually decreases as the HEA reinforcement content increases which might also be ascribed to an increase in porosity. All the composites demonstrated a greater strain hardening rate in the initial stages of deformation than the as-cast AA 6082 alloy, indicating that the HEA particles are capable of successfully capturing sliding dislocations and aggregating dislocation in the aluminium matrix [319][320]. As a result, several dislocations occur and congregate nearby HEA particles in the composite samples in the initial phases of deformation, resulting in an improved rate of strain hardening and better yield strength of the composites than the as-cast AA 6082 alloy [321]. It is observed that 4wt.% HEA/AA composites with a uniform distribution of HEA particles are often more competent in accruing dislocations in the aluminium matrix and surrounding the HEA particles than 6 wt.% HEA/AA composites. As a

result, 4wt.% HEA/AA composites composite yield strength and ultimate tensile strength improved. Dislocation hardening and Back stress hardening are two key factors that 8 wt.% HEA/AA composites composite has superior mechanical characteristics than 6 wt.% HEA/AA composites composite, which is primarily due to the establishment of clearly heterogeneous grain structure. [31], [322], [323]. Also, the grains are refined by the inclusion of HEA particles, which affect grain growth and act as heterogeneous nucleation during the solidification process, potentially increasing the number of grains and refining the grains. The finer the metal matrix grains, the greater the measured strength.

The fractured surface morphology of AA 6082 alloy and HEA/AA composites with varied concentrations of HEA reinforcement are presented in Figure 5.10 The fracture surfaces have dimples and tear ridges, revealing that ductile fracture developed in the matrix alloy under tensile deformation. When the reinforcing weight percent exceeds 4%, the dimples get shallower and the tear ridges become blunted. The interfacial de-bonding between HEAs and Al matrix, as well as brittle fracture of HEA particles, are found to be the two most common failure mechanisms in the HEA/AA composite. Particle pull-out and particle fracture are two types of HEA particle failure. The findings confirmed that particle failure is a major key element in the failure of HEA/AA composites, indicating that the optimum load distribution occurred from the Al matrix to the HEA reinforcement particles. With a rise of HEA-reinforced particles, this tendency is accompanied by a substantial loss in ductility. As a result, deformation and fracture failure are predominantly caused by three fracture mechanisms in HEA/AA composites. i.) HEA particle fracture ii.) aluminium matrix ductile fracture, 3.) interface de-bonding between the Al matrix and HEA particles.

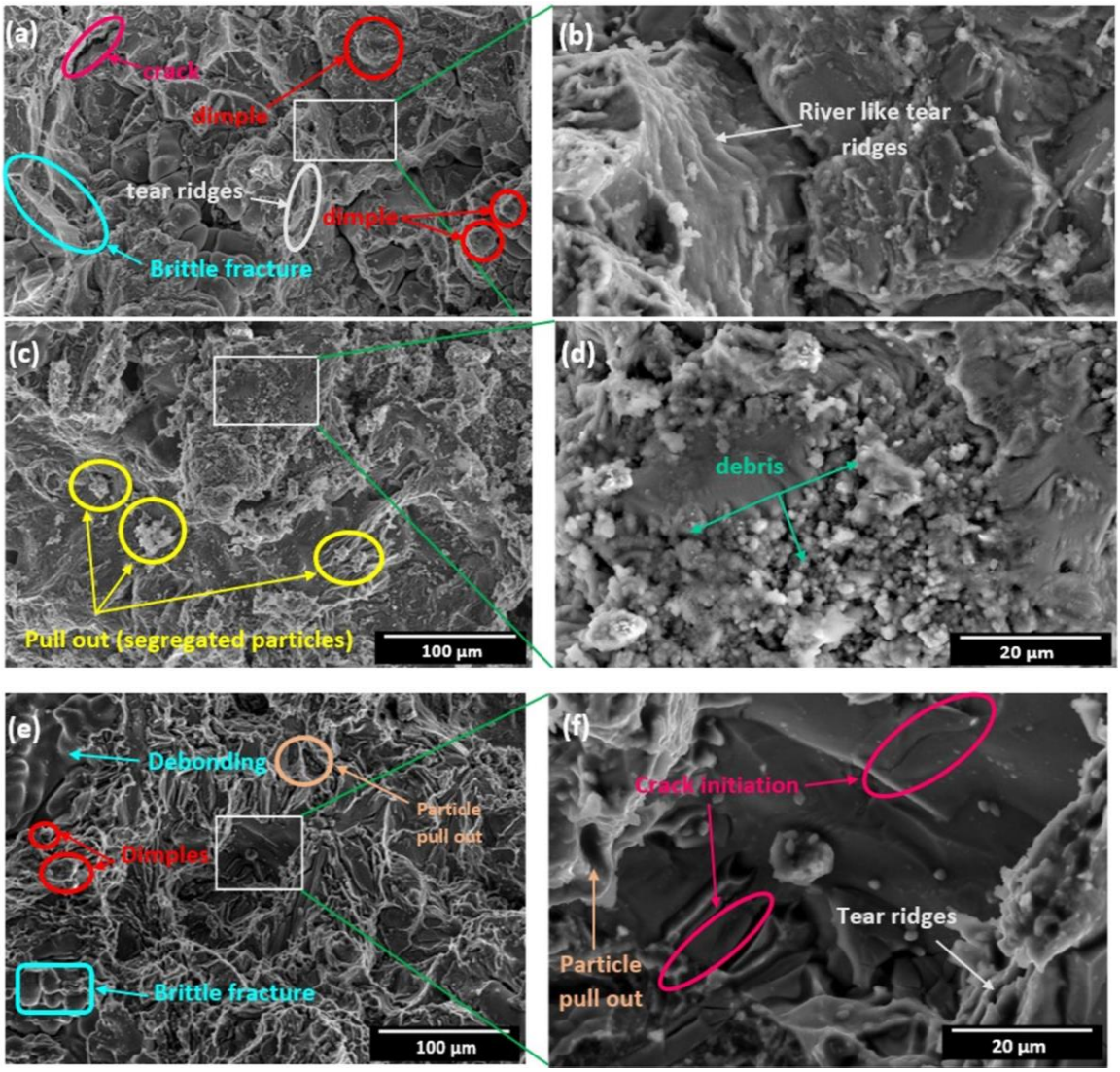
(a)
crack
dimple
tear ridges
dimple
Brittle fracture
(b)
River like tear ridges
(c)
Pull out (segregated particles)
100 µm
(d)
debris
20 µm
(e)
Debonding
Particle pull out
Dimples
Brittle fracture
100 µm
(f)
Crack initiation
Tear ridges
Particle pull out
20 µm

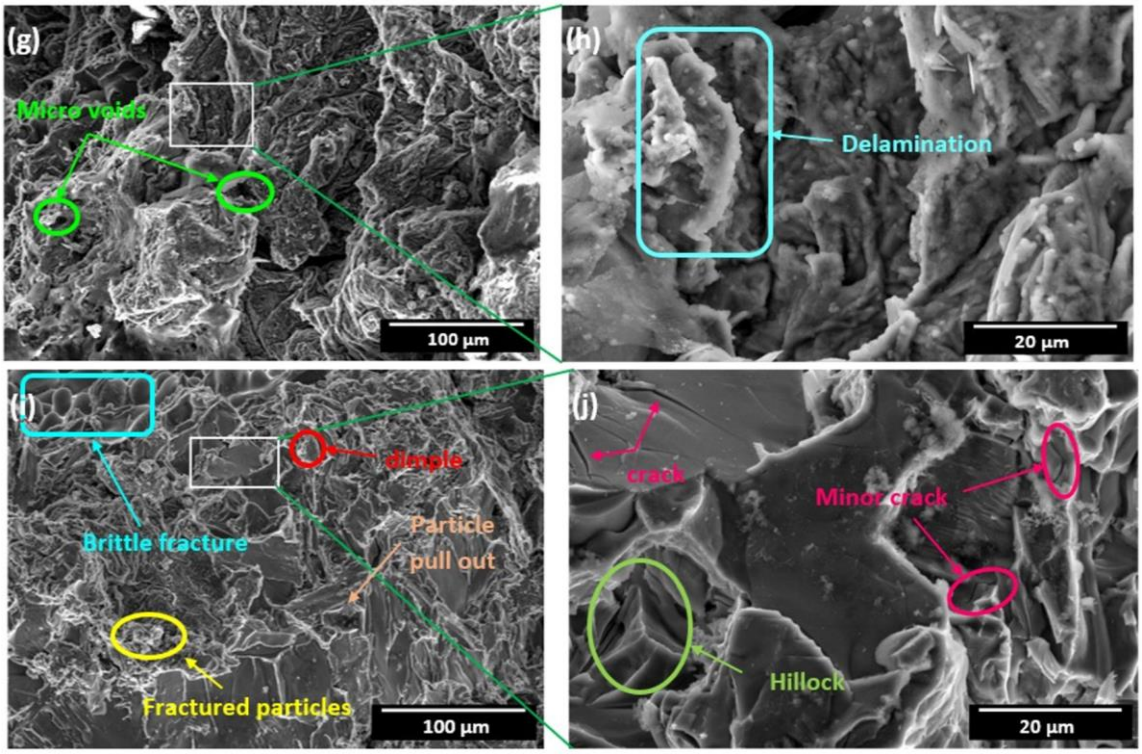

Figure 5.10: FESEM images of fractured surfaces of composites with varying concentrations of CoCrFeMnNi HEA reinforcement: (a)-(b) AA 6082 alloy; (c)-(d) 2wt.% HEA/AA composite; (e)-(f) 4 wt.% HEA/AA ; (g)-(h) 6 wt.% HEA/AA; (i)-(j) 8 wt.% HEA/AA.

From Figure 5.11 (c) it is evident that with the inclusion of HEA, particles resulted in improved mechanical properties significantly. The improved properties may be derived from the strengthening mechanism of nano and submicron HEA reinforcement particles in Al matrix composite. It is observed that the dislocation line when encountering the undeformed HEA particles passes nearby and forms dislocation rings around the particles can be seen in Figure 5.11 (c)(v). As the dislocation rings accumulated it causes obstacles that tend to enhance the strength of the composite [324]. In various studies, it is revealed that as the particles dispersed in the grains, orowan strengthening predominates, this is due to dislocation lines traveling grain to grain boundaries and as the HEA particles segregated near grain boundaries and owing to the effect hindrance of nano and sub-micron HEA particles get diminish, that is why yield

strength increase by orowan strengthening, which is consistent with one of the existing results [325].

Further, the microstructural investigation of as-cast aluminium and HEA-reinforced composite were carried out through TEM. Figure 5.11 (b) (i) and Figure 5.11 (b) (ii) represent the bright field image whereas Figure 5.11 (b) (iii) depicts the corresponding FFT, and Figure 5.11 (b) (iv) and 5.11 (b) (v) represent the composite. The dislocation density in the composite is inevitably more as compared to the as-cast alloy which is due to the presence of HEA particles. The interface between HEA particles and the aluminium matrix is smooth which proves the high wettability between the aluminium matrix and HEA particles.

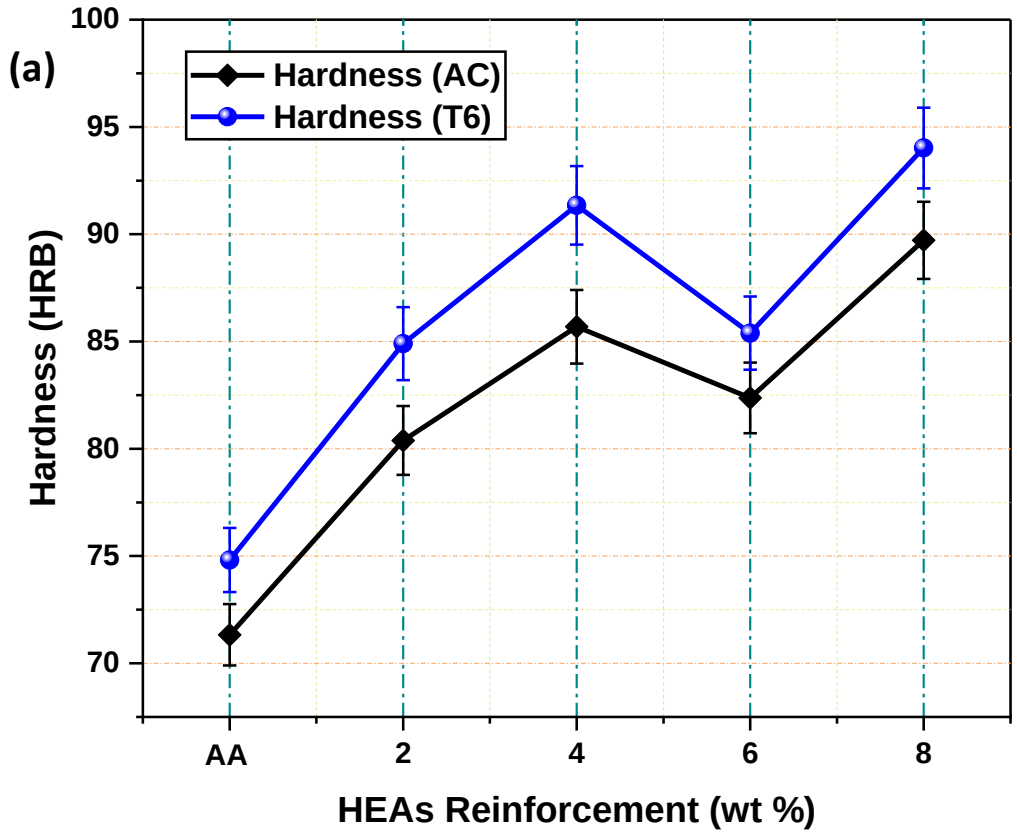

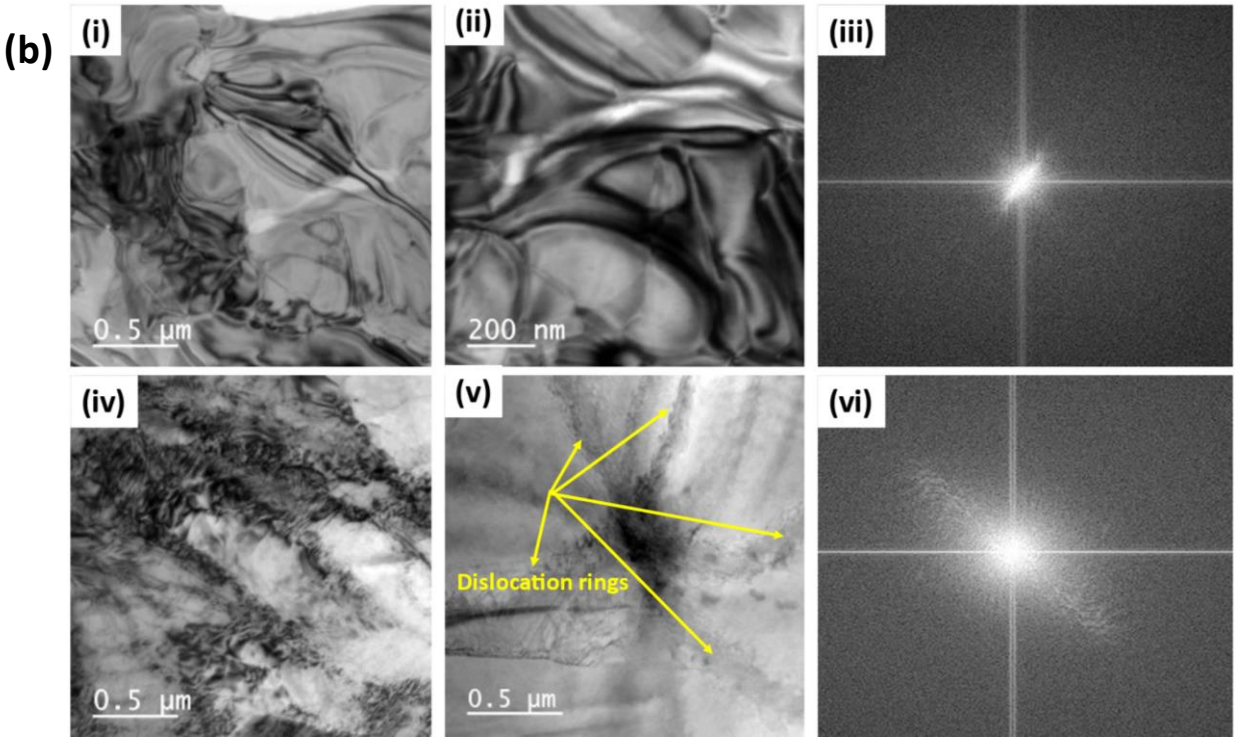

Figure 5.11: (a) Hardness value at different HEA reinforcement content corresponding to as-cast, and artificial Ageing conditions, (b) TEM images of dislocations evolved: (i) As-cast AA 6082, (ii) high magnification image of as-cast AA 6082, (iii) FFT of as-cast AA 6082, (iv) and (v) 8 wt.% HEA/AA composite, and (vi) FFT of 8 wt.% HEA/AA composite.

The inclusion of HEA particles in an Aluminium alloy matrix leads to grain refinement which is classified into two parts 1.) HEA particles distributed at grain boundaries and, 2.) HEA particles at the liquid-solid interface hinder grain growth with controlled solidification, act as heterogenous nucleation, refinement of grains, and increase the count of grains. As the grain was finer it resulted in enhanced strength, toughness, and plasticity of alloy [326]. The grain boundaries restrict the motion of dislocations and promote the accumulation of dislocation near grain boundaries which is the main reason to increase the strength of alloys or composites.

5.4 THERMAL AGEING'S EFFECTS ON TENSILE PROPERTIES

Figure 5.12 demonstrates the impact of thermal ageing on the tensile behavior of the Al-Mg-Si matrix alloy. When compared to as-cast conditions, thermally aged alloy and composite materials showed higher UTS and yield stress. The maximum yield stress and UTS of the aged hardened 8% composites are 303 MPa and 486 MPa, respectively. The material condition, on the other hand, demonstrated a hazy ductility trend. The ductility of all as-cast materials was greater than that of the T6 condition material. The reported value of artificial aged as-cast alloy was 13.34 % which decreases with reinforcement and reached the lowest of 6.1 % for artificial aged 8 wt.% HEA/AA.

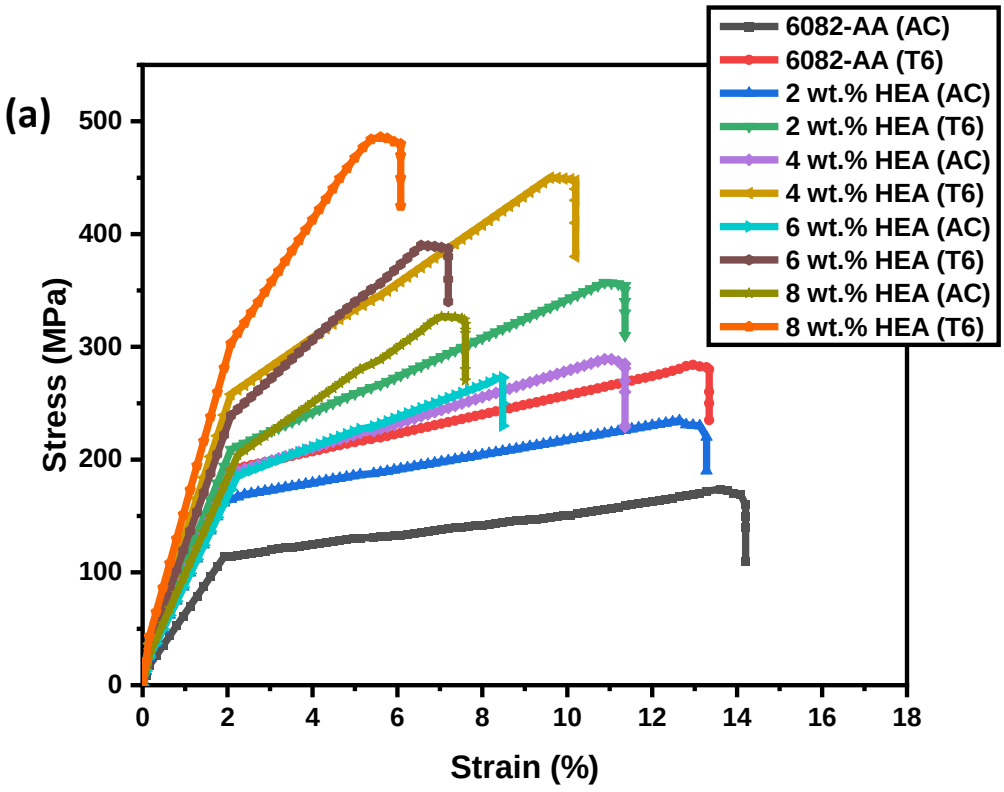

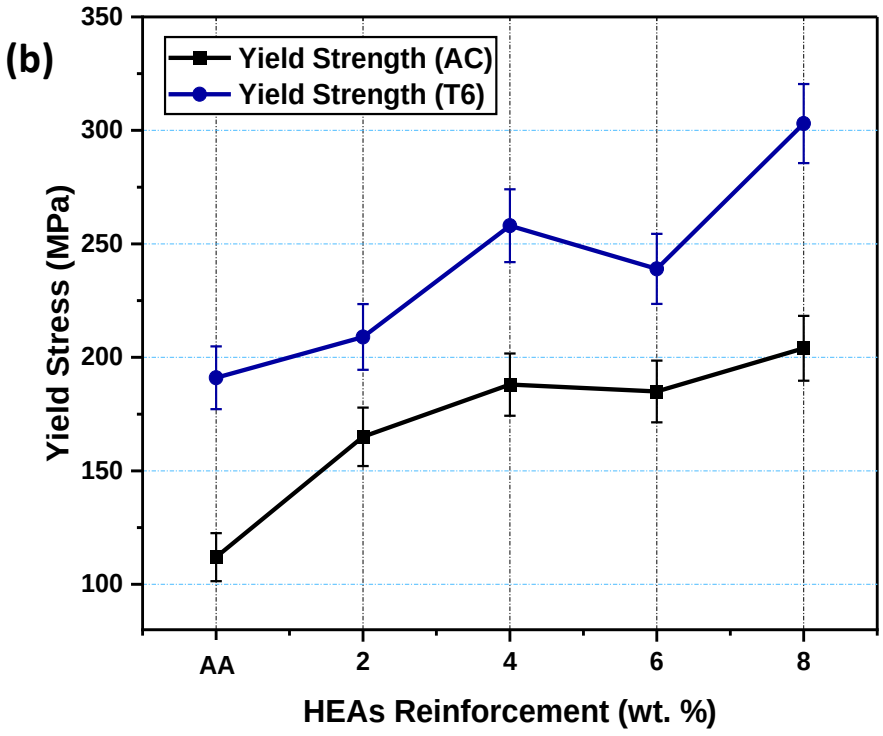
(b)
Yield Strength (AC)
Yield Strength (T6)
Yield Stress (MPa)
350
300
250
200
150
100
AA
2
4
6
8
HEAs Reinforcement (wt. %)

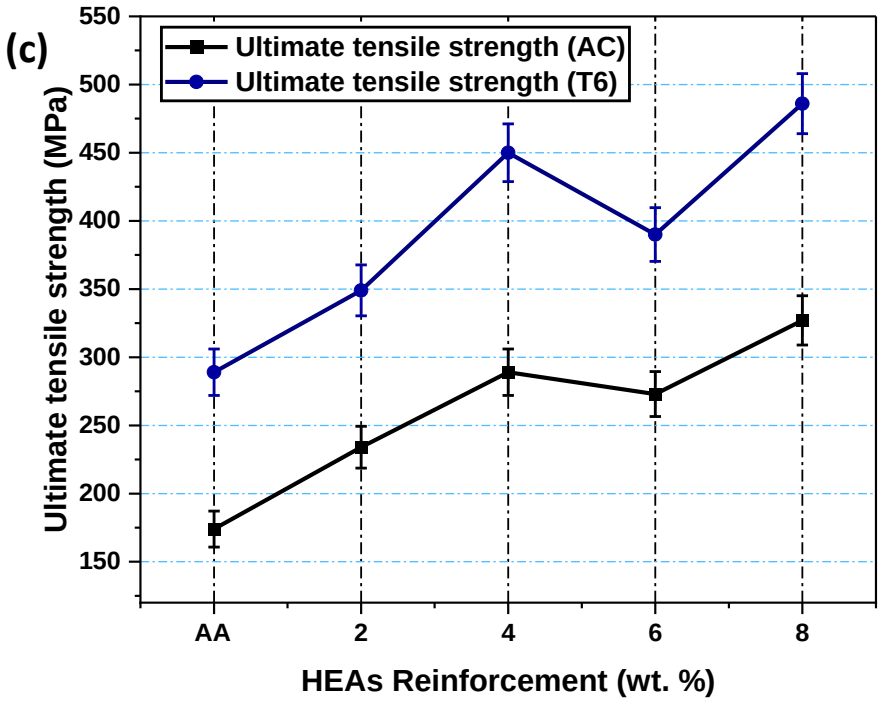
(c)
Ultimate tensile strength (AC)
Ultimate tensile strength (T6)
Ultimate tensile strength (MPa)
550
500
450
400
350
300
250
200
150
AA
2
4
6
8
HEAs Reinforcement (wt. %)

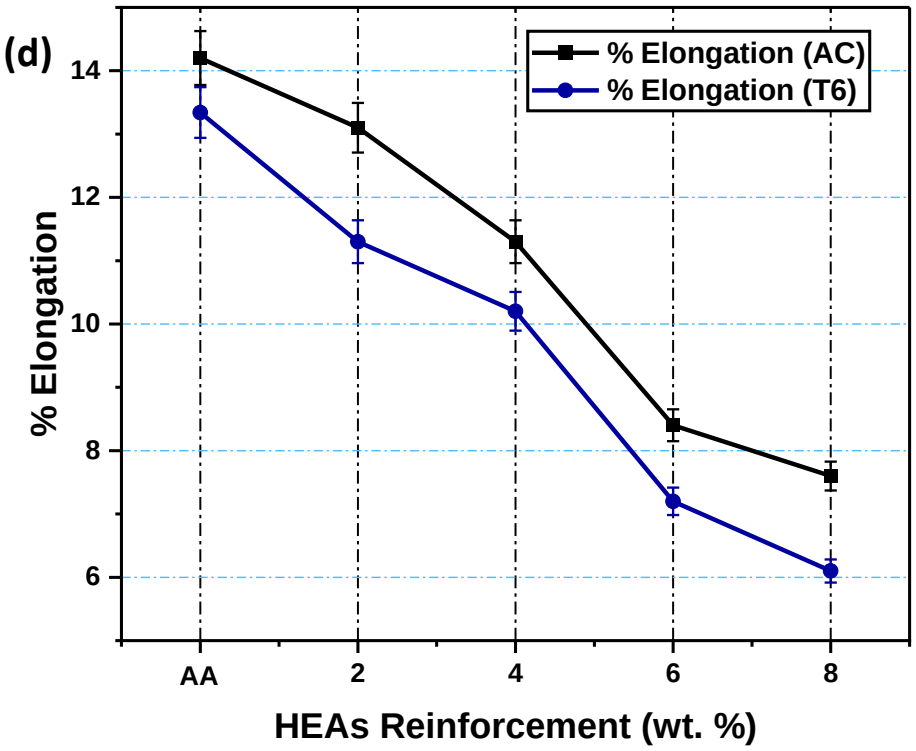

Figure 5.12: Mechanical properties of as-cast and artificial aged (T6): a) Stress vs strain Curve, b) yield strength variation with HEA content, (c) ultimate tensile strength variation with HEA content, (d) % elongation variation with HEA content.

From Figure 5.12 (iv) it is observed that with the heat treatment elongation of the composite decreased. The main cause of to decline in elongation is the formation of uniform and finer precipitates which are the main source of the strengthening phase after ageing [54]. The matrix alloy/composite distorts by the strengthening phase, when the alloy is deformed, this distortion will impede the dislocation movement and impair the plasticity of the metal elements.

The mobility of dislocations is restricted when the secondary phase precipitates grow to their ideal size, increasing the strength [327]. For the further movement of dislocations, it needs to slice through the precipitates or penetrates through them. In both cases, higher stress is vital in comparison to the matrix which doesn't comprehend precipitated particles. The TEM analysis was utilized to identify the secondary phase particles near and within the grain boundaries as shown in Figure 5.13. The bright field and dark field images of alloy and composites confirm the round shape of dispersoids (β), and needle shape fine precipitates (β'). The confirmation of the most likely precipitate i.e., Mg_2Si (β") contributes maximum in

improvising the hardness of the alloy/composites which are dot at one end and followed by needle arranged perpendicular in the Aluminium matrix with the 3 cube axes. It is important to notice that a tiny spherical solute cluster formed just after SHT by natural ageing in AA 6082.

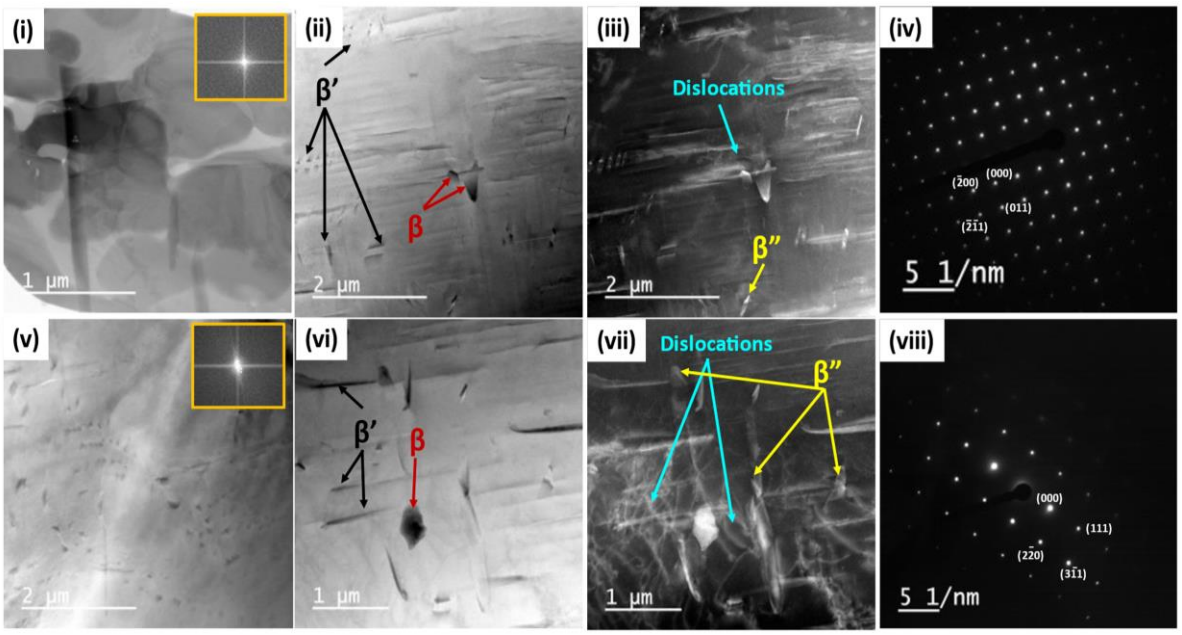

Figure 5.13: TEM Micrographs of As-cast and artificial aged AA6082 and HEA/AA composite: (i) Bright-field image of as-cast AA6082 embedded with FFT, (ii) bright field image of artificial aged AA6082, (iii) dark field image of artificial aged AA6082, (iv) SAED image of AA6082, (v) bright field image of 4 wt.% HEA/AA embedded with FFT, (vi) bright field image of artificial aged 4 wt.% HEA/AA, (vii) dark field image of artificial aged 4 wt.% HEA/AA, (viii) SAED image of 4 wt.% HEA/AA.

5.5 DRY SLIDING WEAR ATTRIBUTES

Figure 5.14 and Figure 5.15 depicts the rate of wear for the corresponding materials as the function of sliding distance (fixed 5000 meters) and normal applied pressure values of 0.25 MPa, 0.5 MPa, 0.75 MPa, 1.1 MPa, and 1.27 MPa, respectively for as-cast and heat treated (T6) conditions the selection of normal applied pressure and sliding distance selected on the basis of prior literature. The obtained results revealed that an increase in wear is noticed with the sliding distance for all normal applied pressures. The AA 6082 alloy had the highest rate

of wear among all compositions and normal applied pressures. On the other hand, the addition of HEA particles improved the wear resistance and reduced the wear rate. The 8 wt.% HEA/AA (HT) composite had the lowest wear rate among all compositions and normal applied pressures. It is noteworthy to mention that the wear rate was almost constant in the initial sliding distance, but increased sharply after reaching the critical value, leading to a phenomenon known as the seizure. During the seizure, the material not only experiences loss of material but also adheres to the counter surface material. Chattering noise and high vibrations were reported at the seizure point. The as-cast AA 6082 alloy gets seizure at a sliding distance of 4000 m and normal applied pressure of 0.75 MPa, with a corresponding wear rate of 6.788×10^{-3} mm^3/m whereas for heat-treated condition AA 6082 gets seizure at a sliding distance of 4000 m and normal applied pressure of MPa and wear rate reported as 5.20×10^{-3} mm^3/m. Meanwhile, the 2 wt.% HEA/AA composite seized at a sliding distance of 5000 m and normal applied pressure of 0.75 MPa, with a corresponding wear rate of 5.31×10^{-3} mm^3/m however the heat treated 2 wt.% HEA/AA composite get seizure at 4000 m and normal applied pressure of 1.018 MPa and the wear rate noticed was 5.5×10^{-3} mm^3/m. The 8 wt.% HEA/AA composite seized at a sliding distance of 5000 m and normal applied pressure of 1.27 MPa, with a corresponding wear rate of 7.09×10^{-3} mm^3/m and the heat treated 8 wt.% HEA/AA composite seized at a sliding distance of 5000 m and normal applied pressure 1.2732 MPa and the wear rate reported as 6.509×10^{-3} mm^3/m.

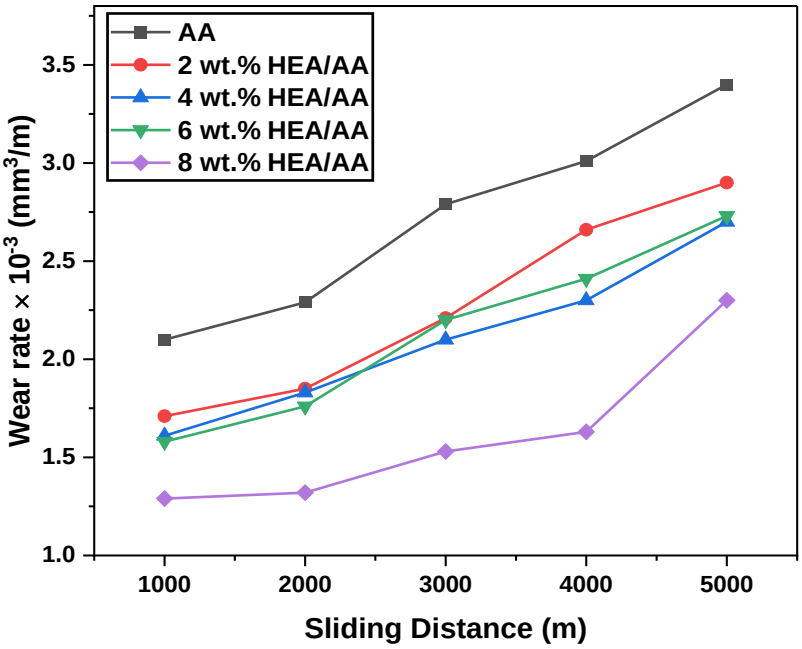

Figure 5.14: Wear rate corresponding to the sliding distance for different material compositions at a normal applied pressure of 0.254 MPa.

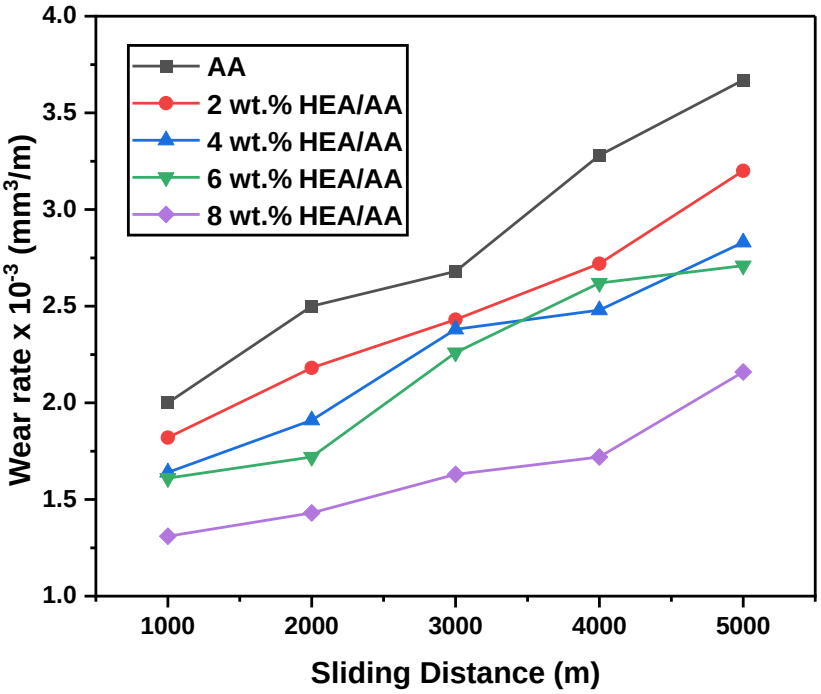

Figure 5.15: Wear rate corresponding to the sliding distance for different material compositions at a normal applied pressure of 0.509 MPa.

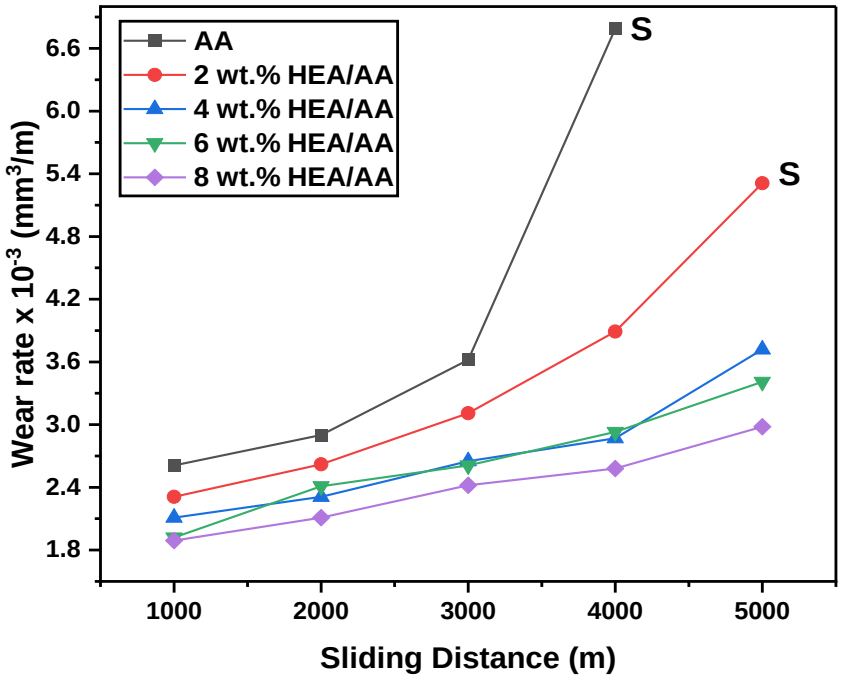

Figure 5.16: Wear rate corresponding to the sliding distance for different material compositions at a normal applied pressure of 0.763 MPa (**S**: Seizure).

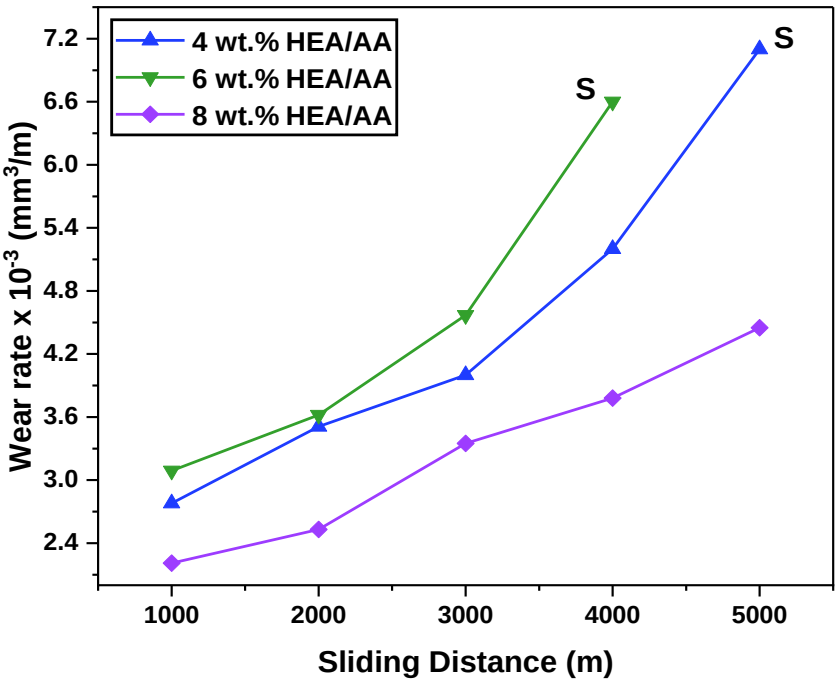

Figure 5.17: Wear rate corresponding to the sliding distance for different material compositions at a normal applied pressure of 1.018 MPa (**S**: Seizure).

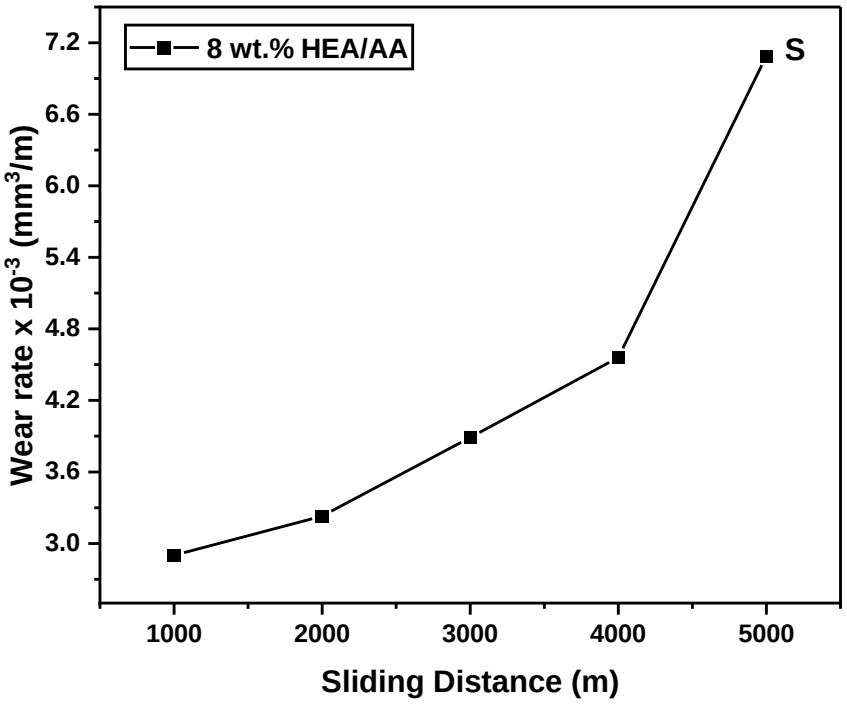

Figure 5.18: Wear rate corresponding to the sliding distance for 8 wt.% HEA/AA Composite at a normal applied pressure of 1.2732 MPa (**S**: Seizure).

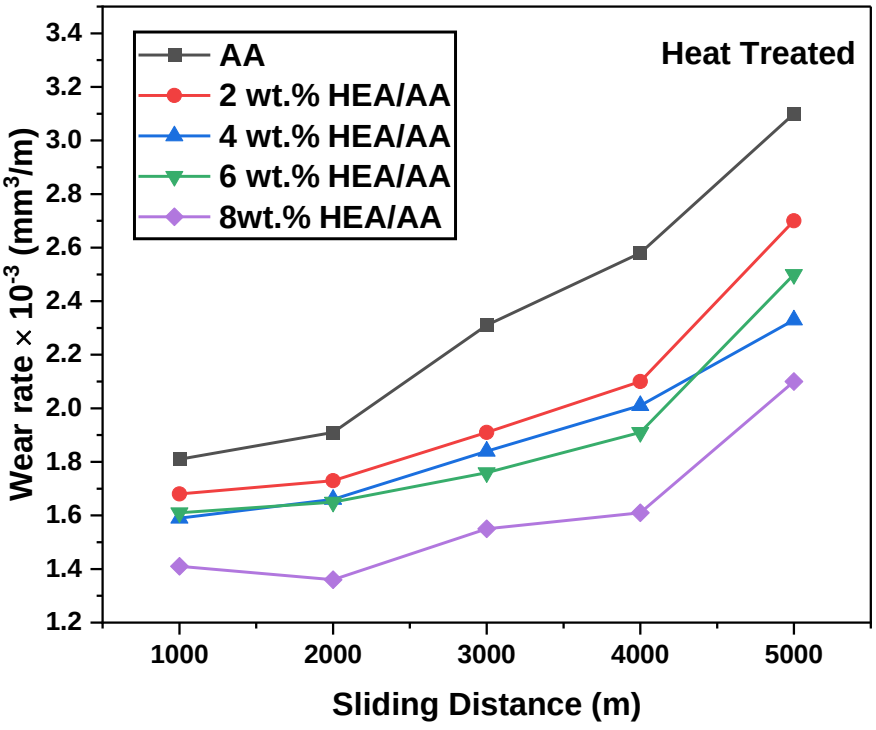

Figure 5.19: Wear rate corresponding to the sliding distance for different material compositions at a normal applied pressure of 0.254 MPa (HT).

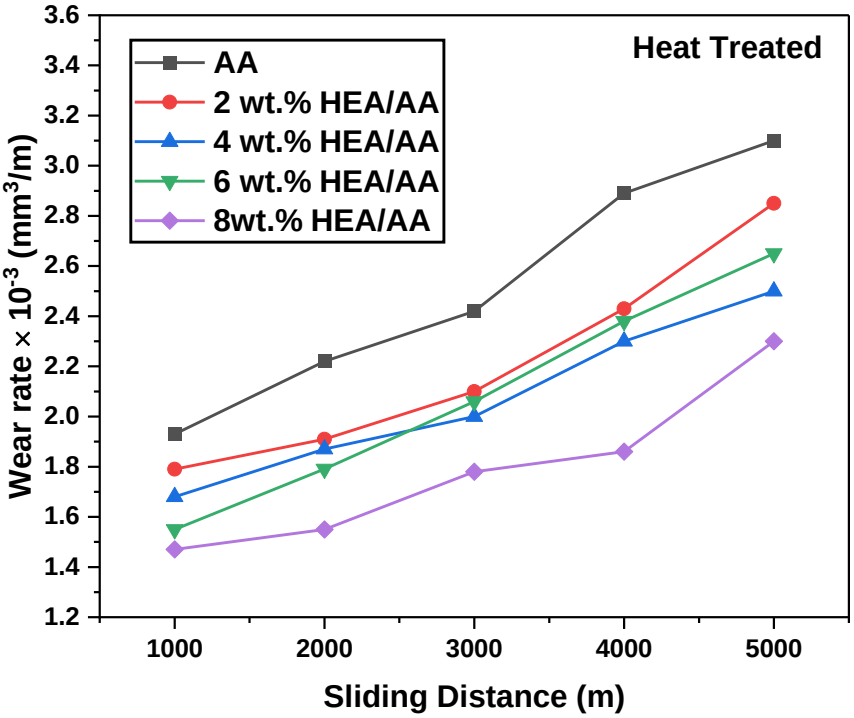

Figure 5.20: Wear rate corresponding to the sliding distance for different material compositions at a normal applied pressure of 0.509 MPa (HT).

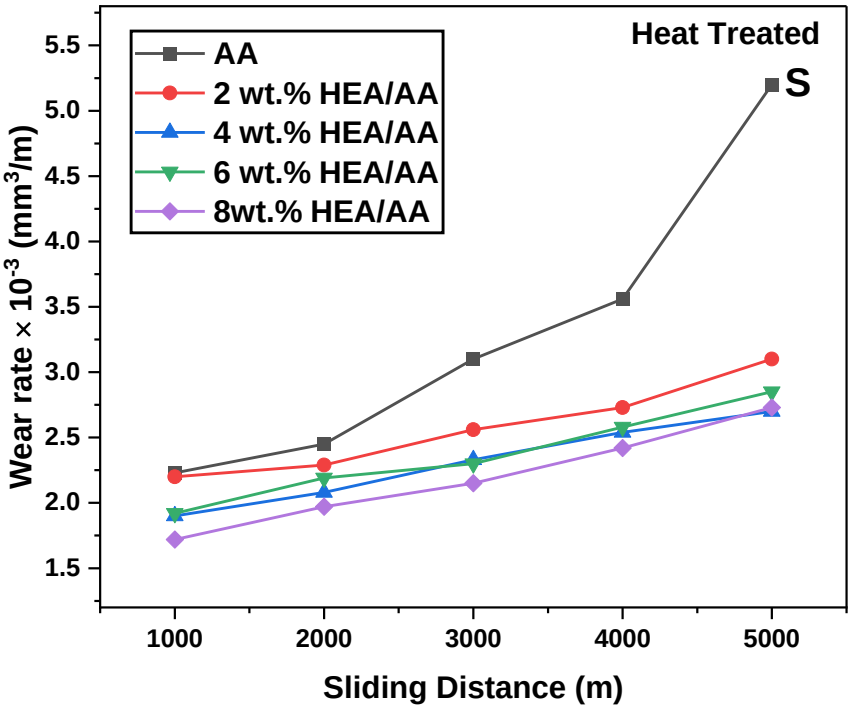

Figure 5.21: Wear rate corresponding to the sliding distance for different material compositions at a normal applied pressure of 0.763 MPa (**S**: Seizure) (HT).

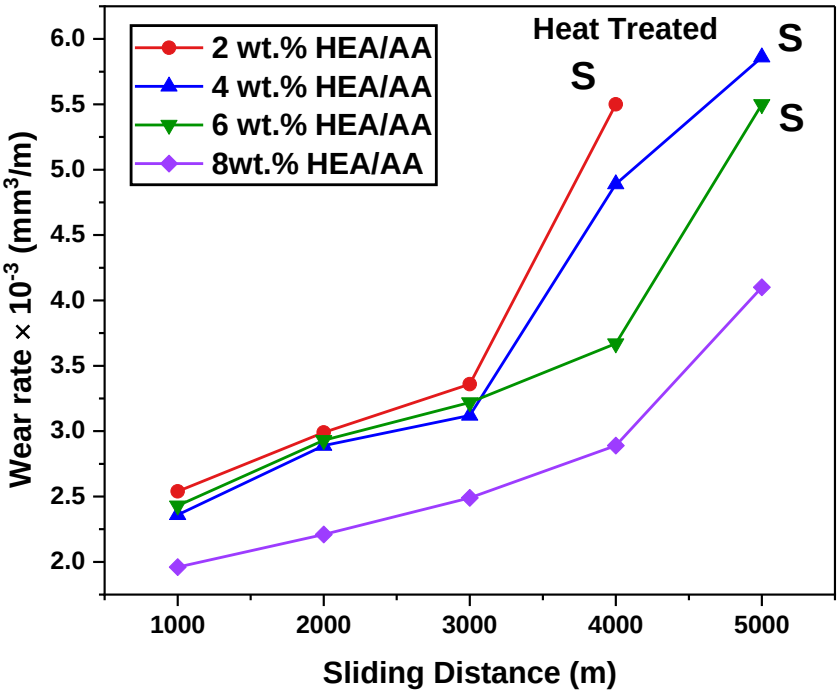

Figure 5.22: Wear rate corresponding to the sliding distance for different material compositions at a normal applied pressure of 1.018 MPa (**S**: Seizure) (HT).

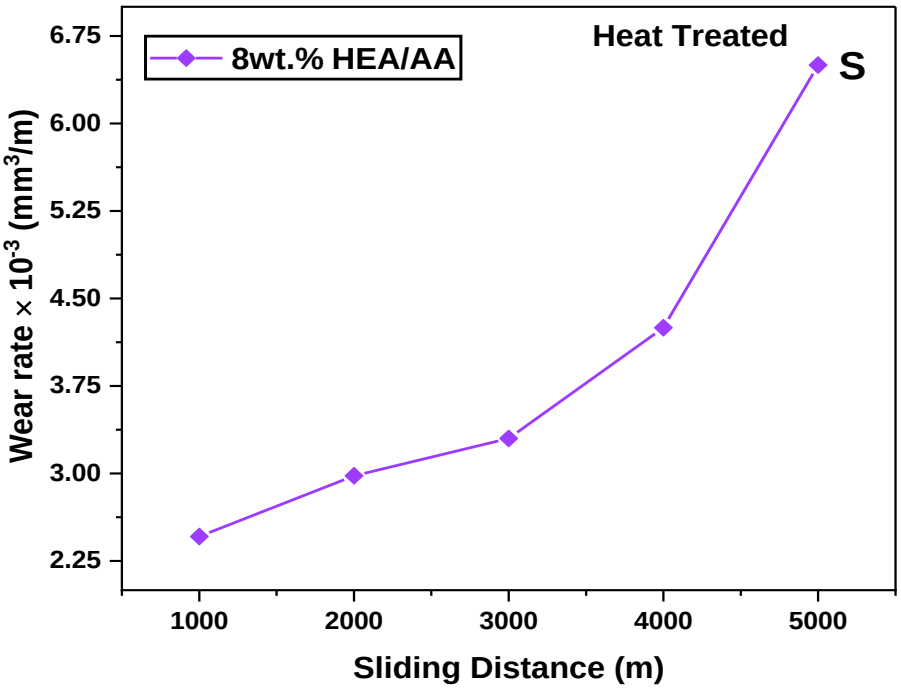

Figure 5.23: Wear rate corresponding to the sliding distance for 8 wt.% HEA/AA Composite at a normal applied pressure of 1.2732 MPa (**S**: Seizure) (HT).

5.6 COEFFICIENT OF FRICTION VISA-A-VIS SLIDING DISTANCE

Figure 5.16 and Figure 5.17 depicts the evolution of the coefficient of friction of as-cast and heat-treated condition alloy and composites as a function of sliding distance under various normal applied pressures of 0.25 MPa, 0.50 MPa, 0.76 MPa, 1.1 MPa, and 1.27 MPa, respectively. The trend of the coefficient of friction with sliding distance exhibits a zigzag pattern, making it challenging to deduce a clear conclusion from the observed trends. However, it can be observed that the as-cast AA6082 alloy exhibits the highest coefficient of friction, and the heat treated 8 wt.% HEA/AA composite exhibits the lowest coefficient of friction, regardless of the applied pressure. As the normal applied pressure increases, the values of the coefficient of friction converge. Beyond a critical sliding distance, the coefficient of friction suddenly increases, which marks the onset of the seizure. The as-cast AA6082 alloy experiences seizure at 0.75 MPa, where the coefficient of friction was reported as 0.53, and for the heat-treated AA 6082 alloy seizure get at 0.75 MPa and the coefficient of friction value reported was 0.51. Similarly, the 2 wt.% HEA/AA composite experiences seizure at 0.75 MPa with a corresponding coefficient of friction of 0.49 however the heat treated 2 wt.% HEA/AA gets seized at 1.018 MPa and the corresponding value of the coefficient of friction is reported as 0.56. The 4 wt.% HEA/AA and 6 wt.% HEA/AA composites experience a seizure at 1.01 MPa with corresponding coefficients of friction of 0.58 and 0.56, respectively, Likewise, the heat treated 4 wt.% HEA/AA and 6 wt.% HEA/AA composites experience a seizure at 1.01 MPa with corresponding coefficients of friction of 0.58 and 0.56, respectively. The 8 wt.% HEA/AA composite experiences seizure at 1.27 MPa with a corresponding coefficient of friction of 0.61 and the heat treated 8 wt.% HEA/AA composite experiences seizure at 1.27 MPa with a corresponding coefficient of friction of 0.61.

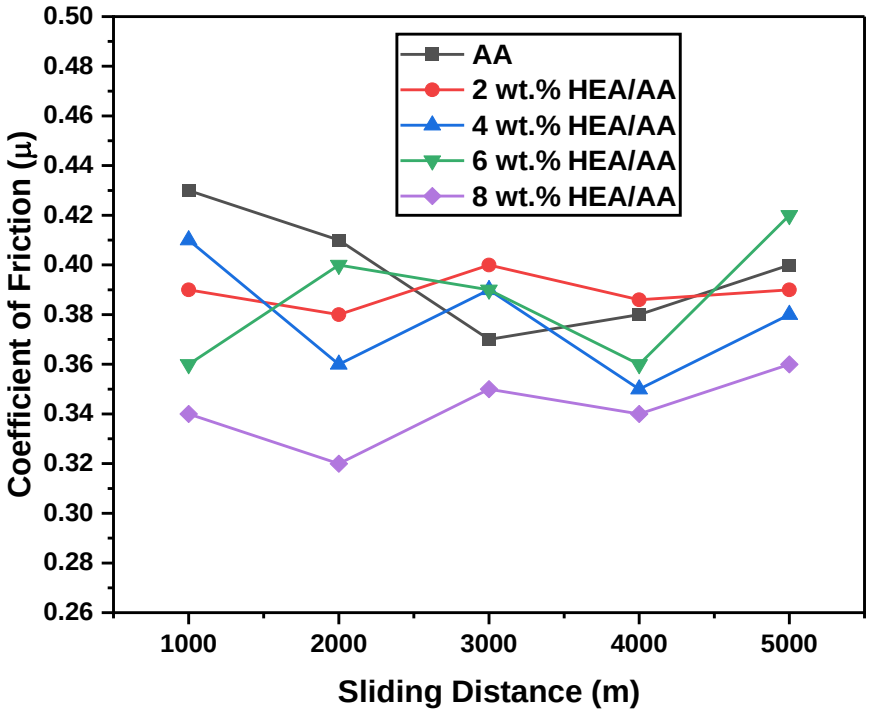

Figure 5.24: Variation of coefficient of friction with sliding distance for different material compositions at a normal applied pressure of 0.254 MPa.

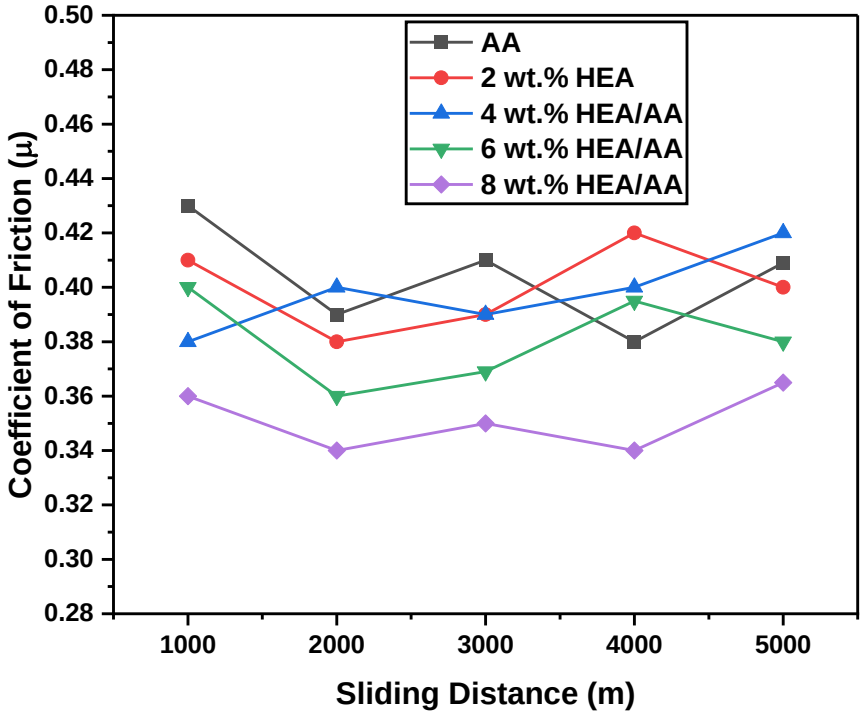

Figure 5.25: Variation of coefficient of friction with sliding distance for different material compositions at a normal applied pressure of 0.509 MPa.

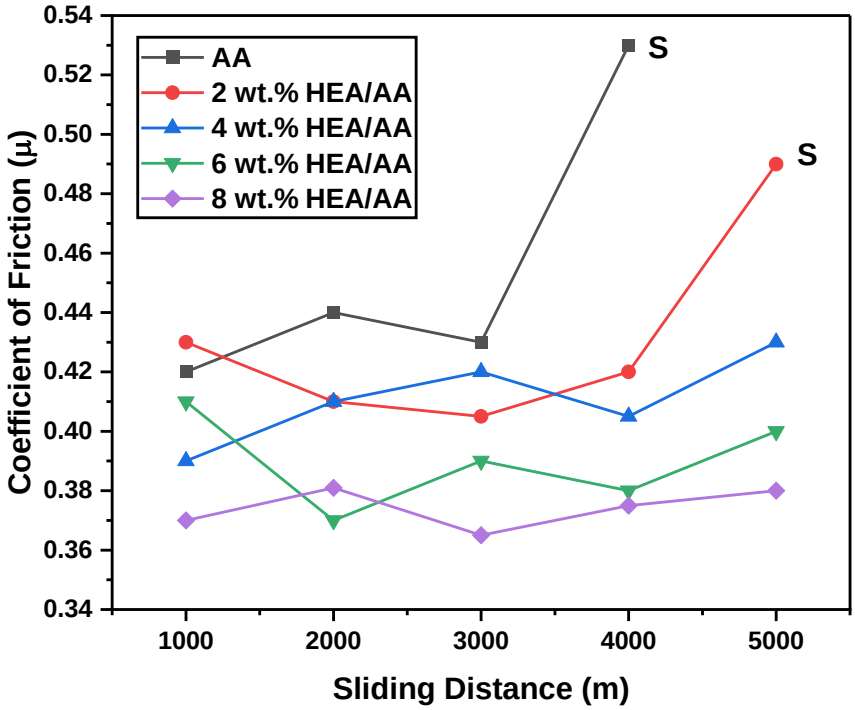

Figure 5.26: Variation of coefficient of friction with sliding distance for different material compositions at a normal applied pressure of 0.763 MPa (**S**: Seizure).

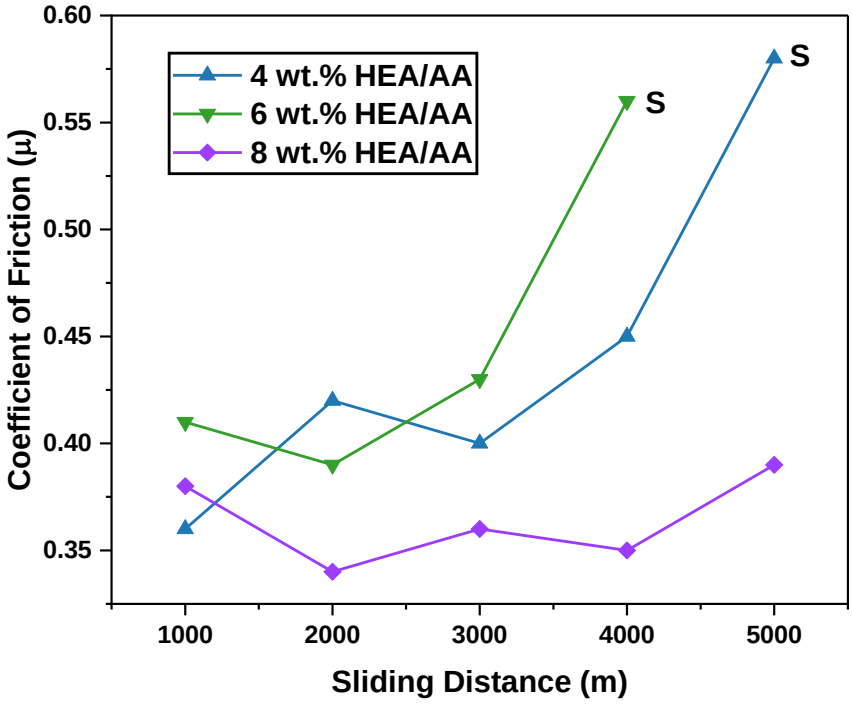

Figure 5.27: Variation of coefficient of friction with sliding distance for different material compositions at a normal applied pressure of 1.018 MPa (**S**: Seizure).

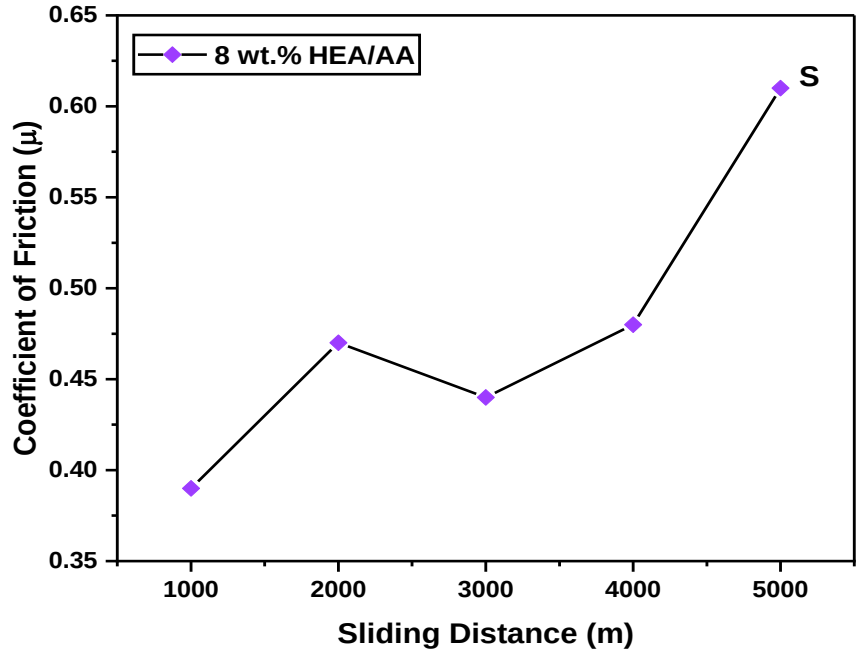

Figure 5.28: Variation of coefficient of friction with sliding distance for 8 wt.% HEA/AA Composite at a normal applied pressure of 1.2732 MPa (**S**: Seizure).

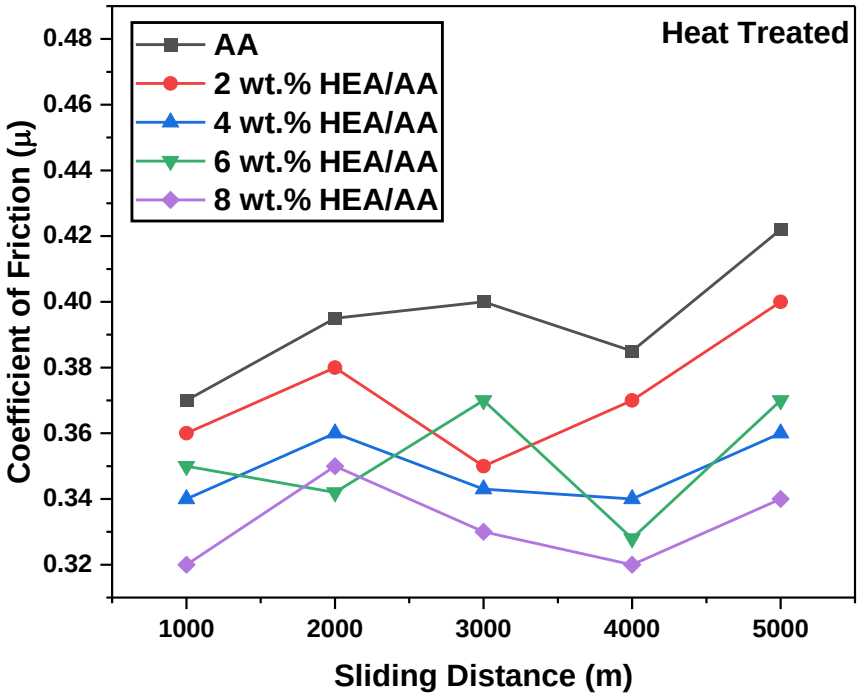

Figure 5.29: Variation of coefficient of friction with sliding distance for different material compositions at a normal applied pressure of 0.254 MPa (HT).

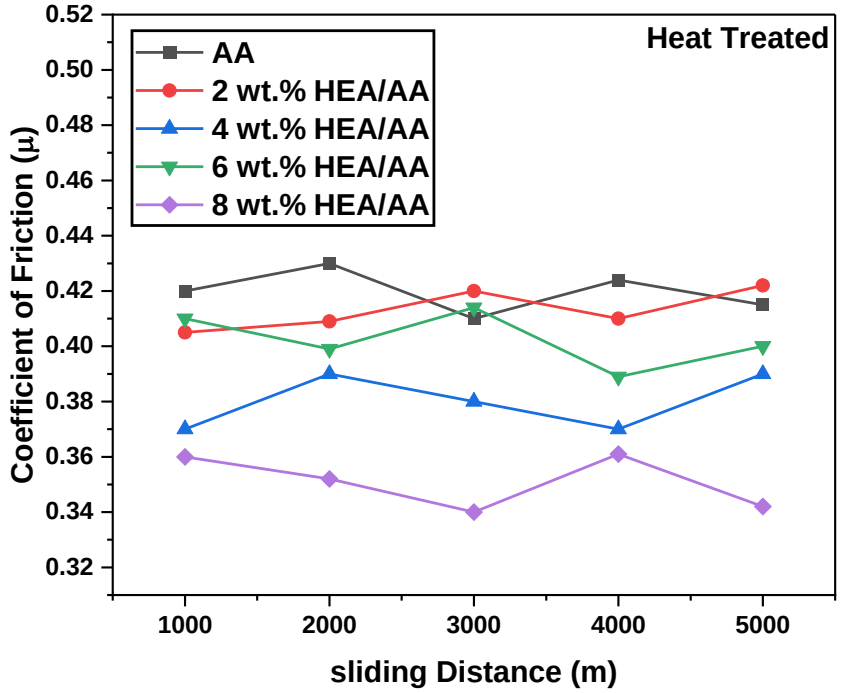

Figure 5.30: Variation of coefficient of friction with sliding distance for different material compositions at a normal applied pressure of 0.509 MPa (HT).

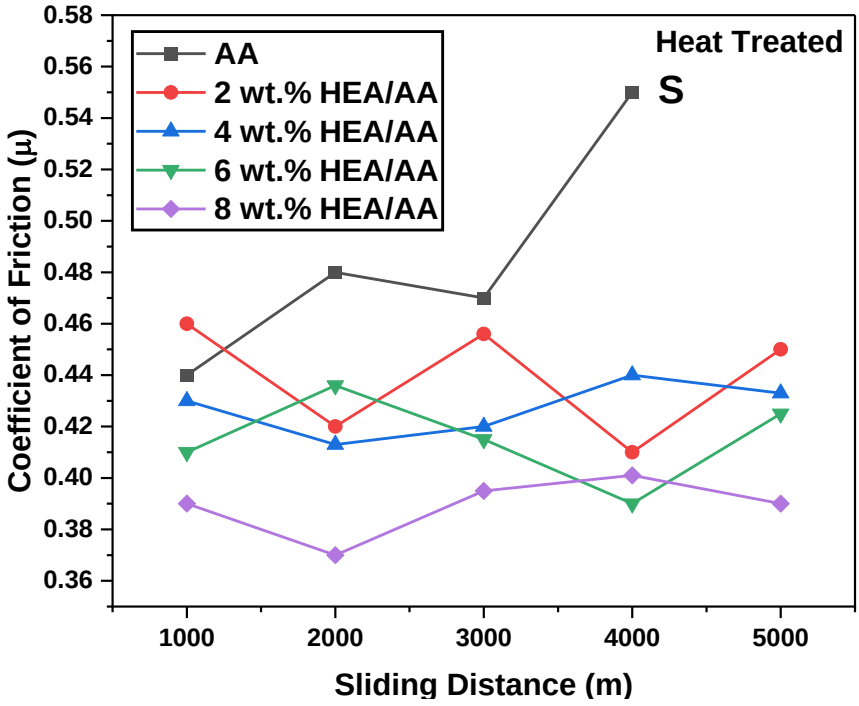

Figure 5.31: Variation of coefficient of friction with sliding distance for different material compositions at a normal applied pressure of 0.763 MPa (**S**: Seizure) (HT).

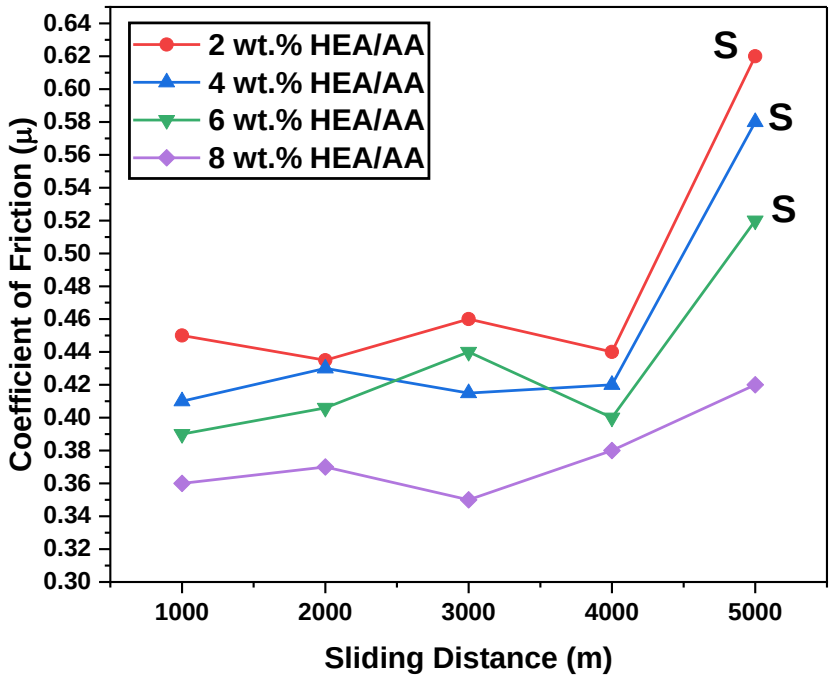

Figure 5.32: Variation of coefficient of friction with sliding distance for different material compositions at a normal applied pressure of 1.018 MPa (**S**: Seizure) (HT).

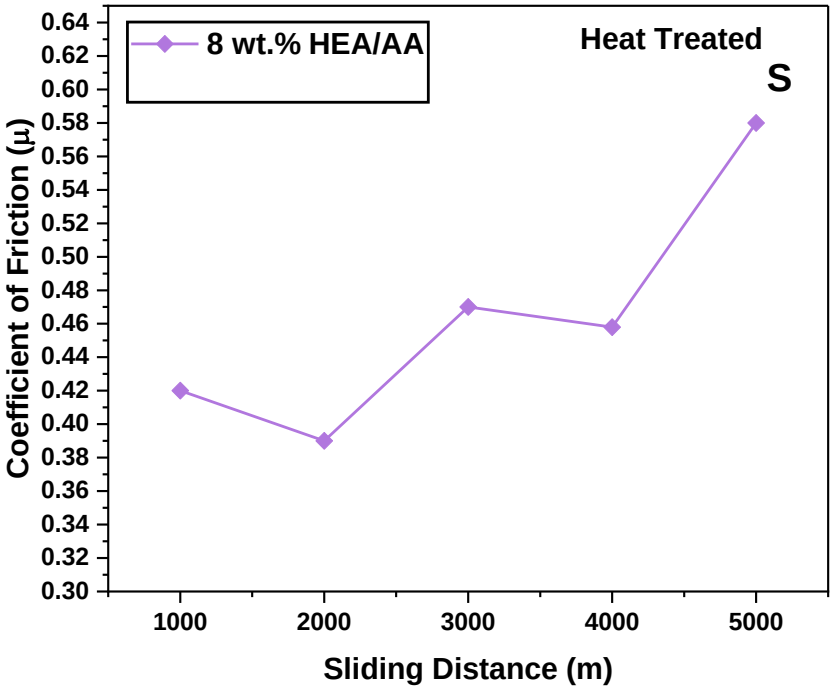

Figure 5.33: Variation of coefficient of friction with sliding distance for 8 wt.% HEA/AA Composite at a normal applied pressure of 1.2732 MPa (HT).

5.7 WEAR COEFFICIENT VIS-À-VIS APPLIED PRESSURE

Figure 5.18 and Figure 5.19 present the correlation between the normal applied pressure and the wear coefficient of alloy and composites at as-cast and heat-treated conditions. It was discovered that as the normal applied pressure increases, a decline in the wear coefficient is observed for all composites. The as-cast AA6082 alloy and the 2 wt.% HEA/AA composites were found to have seized at a normal applied pressure of 0.75 MPa, resulting in a marginal increase in the wear coefficient of the alloy from 4.13 to 5.09 while the wear coefficient of the 2 wt.% HEA/AA composite changed from 4.01 to 4.33.

For the 4 wt.% HEA/AA and 6 wt.% HEA/AA composites, a sharp decrease in the wear coefficient trend was noted, especially between the normal applied pressures of 0.25 MPa to 0.50 MPa. A further decrease was observed from 0.50 MPa to 0.75 MPa, although at a slower rate. An increase in the wear coefficient was recorded for both composites as the normal applied pressure was increased from 0.75 MPa to 1.00 MPa, with the corresponding wear coefficients at seizure being 4.88 and 4.33 respectively.

However, the wear coefficient for the 8 wt.% HEA/AA composite remained relatively constant between the normal applied pressures of 0.50 MPa to 1.1 MPa. The seizure for this composite was reported at 1.27 MPa, with the corresponding wear coefficient being 4.254.

For the heat-treated condition, the trend is almost similar to the as-cast condition in which the wear coefficient value of the respective alloy and composite decreased initially while increasing after certain normal applied pressure. As in AA 6082 alloy and 2 wt.% HEA/AA composite the sharp value of wear coefficient declined notice between 0.25 MPa to 0.50 MPa which changes from 6.95 to 3.609 and 6.75 to 3.5625 and then a slight increment is noticed between normal applied pressure 0.50 MPa to 0.75 MPa. For 4 wt.% HEA/AA composite and 6 wt.% HEA/AA a sharp decrease in the value of the wear coefficient is observed between 0.25 MPa to 0.50 MPa and a further decrease is observed between 0.50 MPa to 0.75 MPa. The wear coefficient then increases between 0.75 MPa to 1.018 MPa and attained seizure at 1.018 MPa and the respective wear coefficient value visualized at seizure was 4.028 and 3.3 respectively. Whereas as the wear coefficient value of 8 wt.% HEA is almost constant between

0.50 MPa and 1.018 MPa and an increase in value is noticed between 1.018 and 1.25 MPa the corresponding wear coefficient value is observed as 2.33 and 2.8. At 1.25 MPa which was also a seizure pressure for the composite, the coefficient of wear was noticed as 3.9.

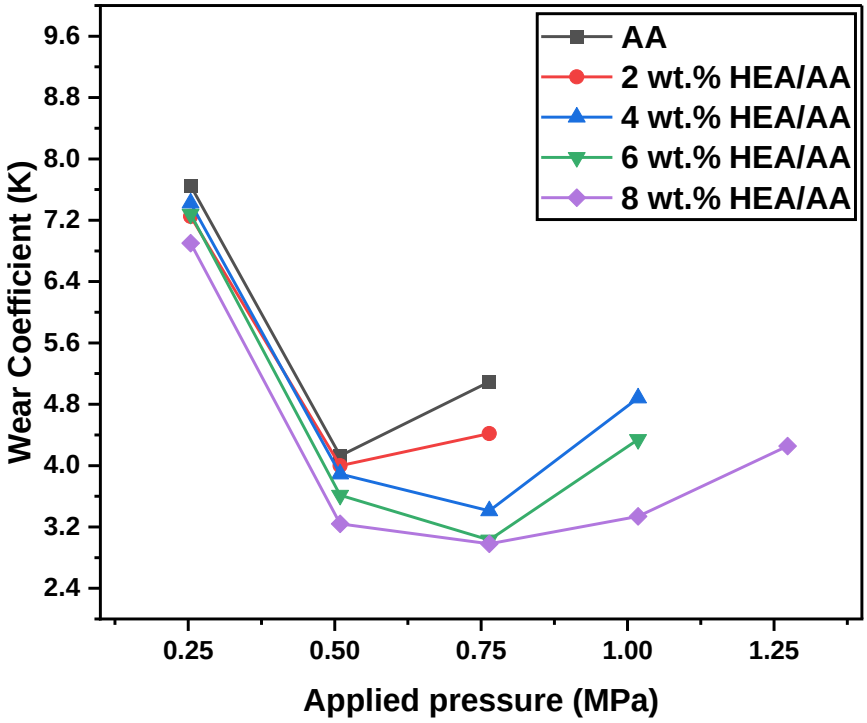

Figure 5.34: Variation of wear coefficient with Normal applied pressure for different material compositions

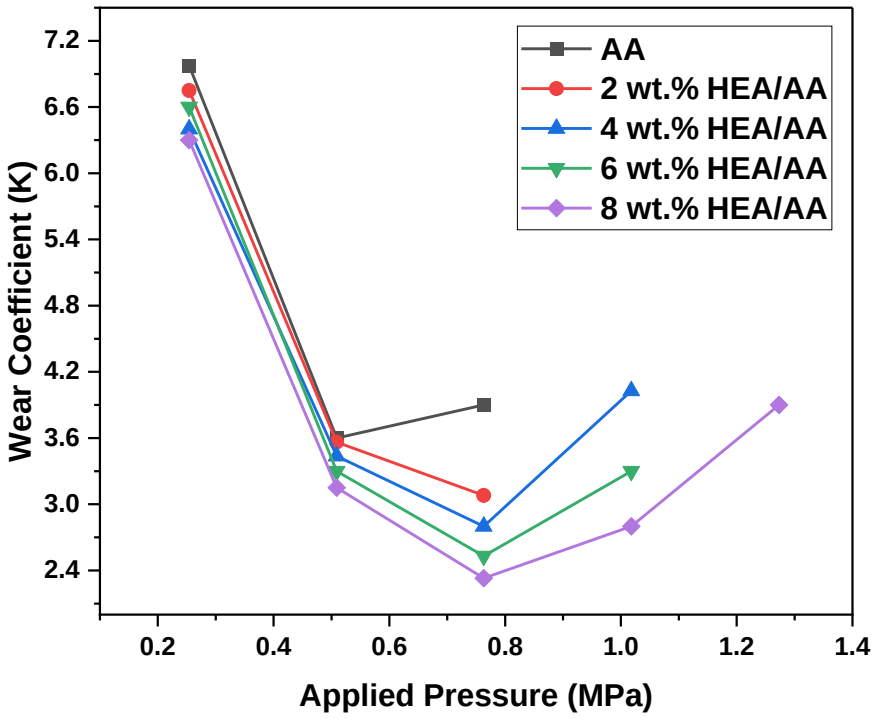

Figure 5.35: Variation of wear coefficient with Normal applied pressure for different material compositions (HT)

5.8 WEAR-OUT SURFACE ANALYSIS

In the wear sliding test, when surfaces come in contact, asperities to asperities contact occurred. In this work, softer aluminium asperities slide over harder steel asperities which grooves to form an aluminium surface. As the load increases which resulted in an increase of pressure at contact lead to deep grooves which can be visualized. At the intermediate pressure, grooves get deeper and more damage to the surface. It was evident that at high-pressure conditions initiation and propagation of cracks are more predominant. It is noteworthy to mention during sliding motion, with an increase in pressure cracks developed at the surface and propagate transversely and longitudinally. The transverse cracks meet the grooves and form small debris at the worn surface. The AA 6082 gets seizure at 0.75 MPa, as the alloy experience intense frictional heat that is realized at higher pressure, the material gets softened and the micro weld is visualized more often at seizure condition severe damage surface with surface tearing and wear patches illustrates in Figure 5.20 (b)-((i)-(ii)).

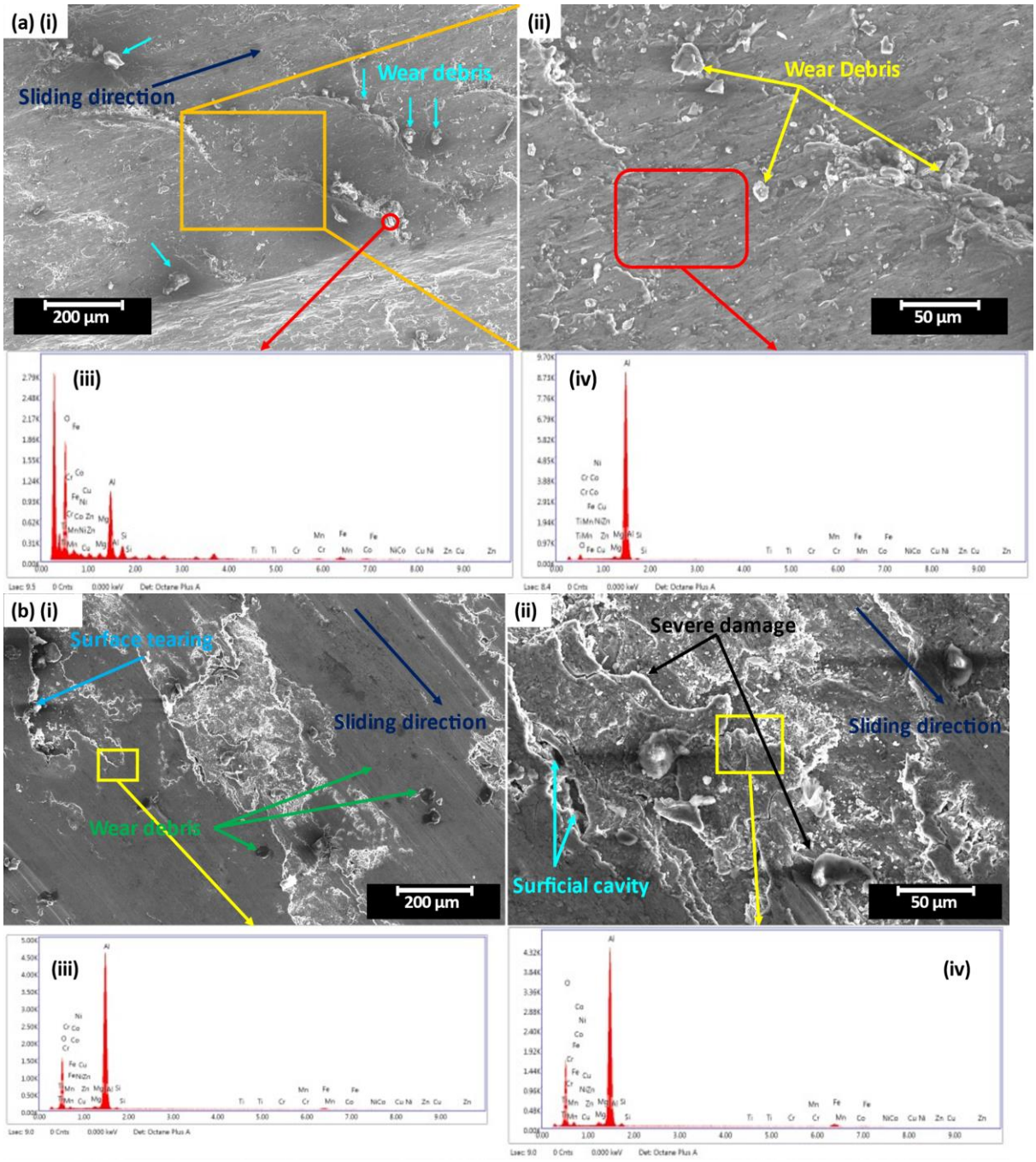
(a) (i)
Sliding direction
Wear debris
200 µm
(ii)
Wear Debris
50 µm
(iii)
(iv)
(b) (i)
Surface tearing
Sliding direction
Wear debris
200 µm
(ii)
Severe damage
Sliding direction
Surficial cavity
50 µm
(iii)
(iv)

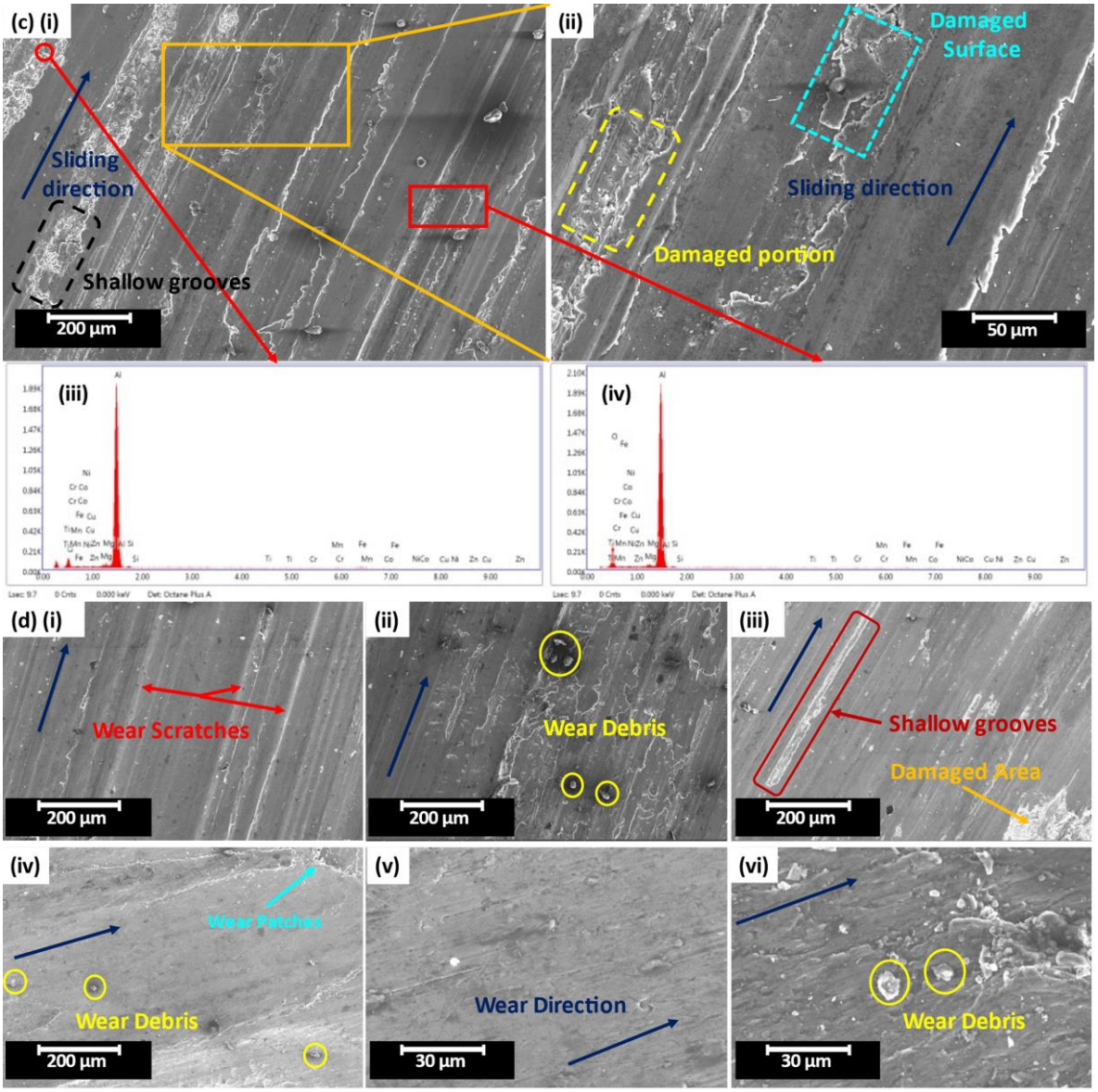

Figure 5.36: low and high magnification wear micrographs with EDS graph (a) AA6082; (b) 4wt.% HEA/AA; (c) and (d) 8wt.% HEA/AA.

For the 4 wt.% HEA/AA composition the seizure is observed at 1.01 MPa and is categorized by severe surface damage, surface tear, and development of parallel lips as shown in Figure 5.20 (b)-((i)-(ii)). for the 8wt.% composite at lower pressure of 0.25 MPa grooves formation is not observed, and the wear surface is almost smooth with minute scratches. when the pressure reaches 0.75 MPa shallow grooves are observed. At this juncture, small debris can be observed. When the pressure reaches 1.25 MPa, the material gets seizure and severe

damage, as well as the parallel lips can be seen in Figure 5.20 (c)-((i)-(ii)). Figure 5.20 (d) revealed the worn surfaces at seizure condition for 8 wt.% HEA/AA composite at the different parts of the wear surface.

Figure 5.21 portrays a typical wear surface of a HEA-reinforced composite in T6 HT condition at seizure, demonstrating crack propagation and wear debris on the surface. Notably, in this case, the wear surface damage is less prominent. The Figure shows a damaged region that clearly depicts HEA particles protruding from the wear surface, alongside surface cracks in both the longitudinal and transverse directions. The sample experiences severe damage and cracking, producing large flaky-shaped debris, as shown in Figure 5.21 (a) (ii) and b(ii). This pressure leads to the seizure of the composite sample, characterized by the emergence of wear patches and the formation of parallel lips. Figure 5.21 (c) (i) and (ii) depicts a prototypical wear surface of an as-cast 8 wt.% HEA/AA composite at an applied pressure of 1.21 MPa. Notably, it displays continuous pits and grooves, which may arise from the coexistence of a soft matrix interface with the hard particle phases. As the applied pressure is raised, the wear surface exhibits the formation of deep wear grooves and pitting, as well as a more noticeable initiation and spread of cracks. These cracks typically amalgamate to form flaky-shaped debris.

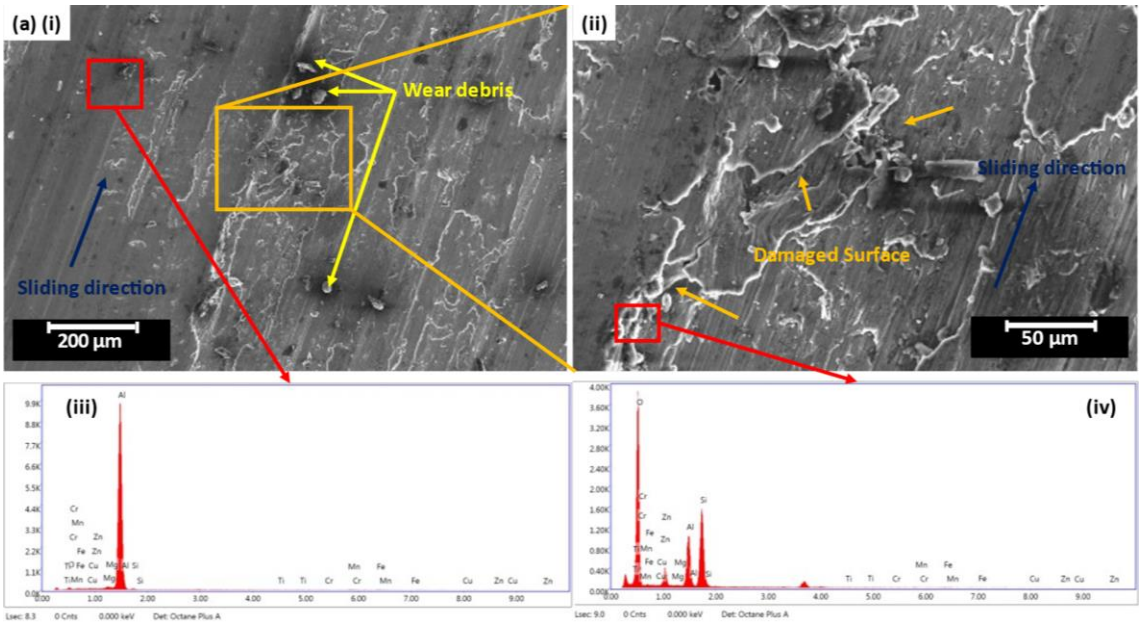

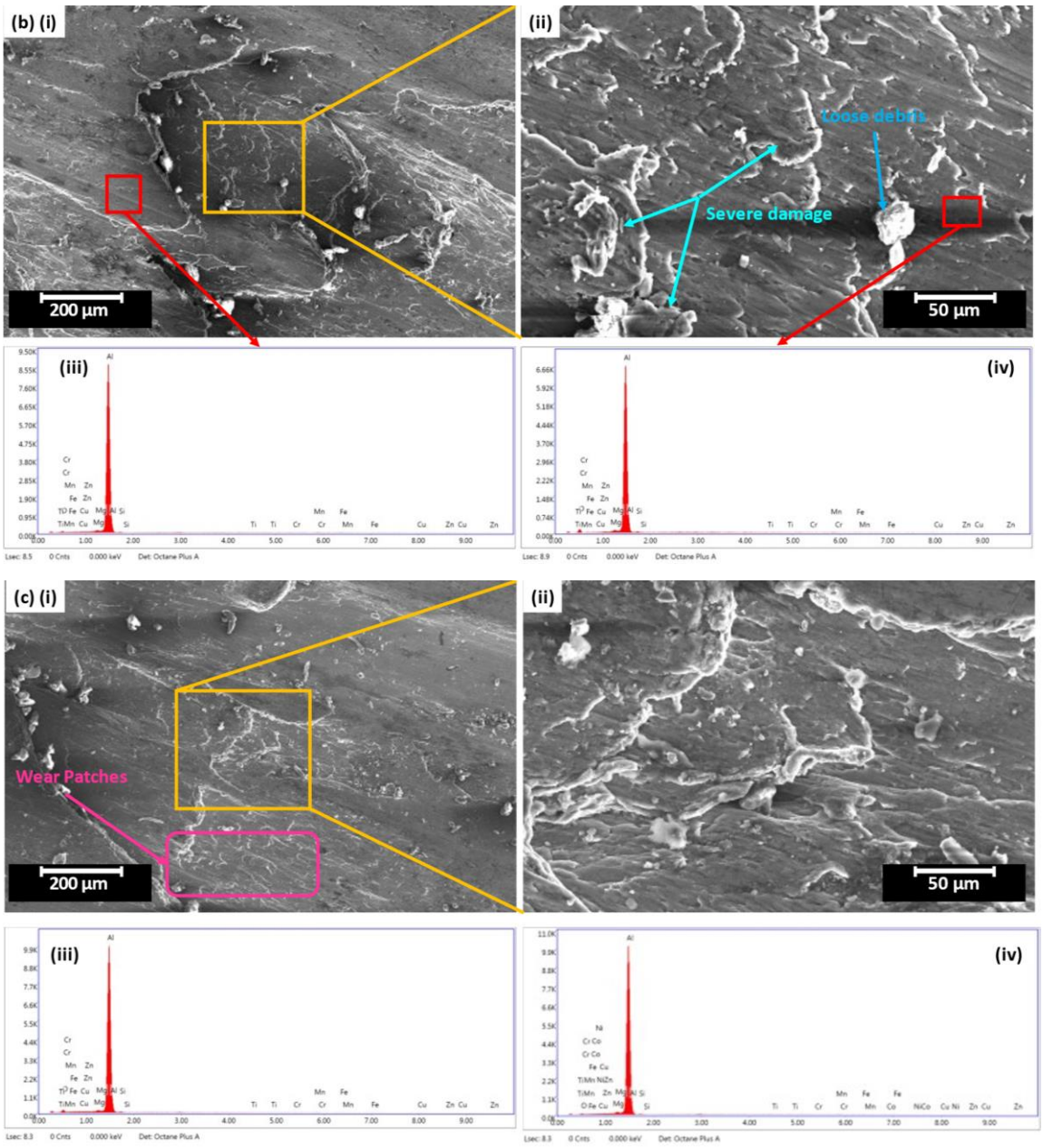

Figure 5.37: Low and high magnification wear micrographs with EDS graph at heat treated condition (a) AA6082; (b) 4wt.% HEA/AA; (c) and (d) 8wt.% HEA/AA.

The optical profilometer micrograph was utilized to analyze the worn surface of AA6082 alloy and HEA/AA composites at as-cast and heat-treated (T6) conditions which provide an overview of the wear behavior of alloy and composites illustrated in Figure 5.22 and Figure 5.23. The wear surfaces have peaks and valleys which were developed due to loss of material

during the sliding wear test and the intensity of wear was evaluated by average roughness which is obtained in XZ (X profile) and YZ (Y profile) form through optical profilometer. It is important to note as the HEA content increased wear resistant properties improved, as the specific wear rate decreased with HEA content, and also with the artificial ageing the wear-resistant properties improved.

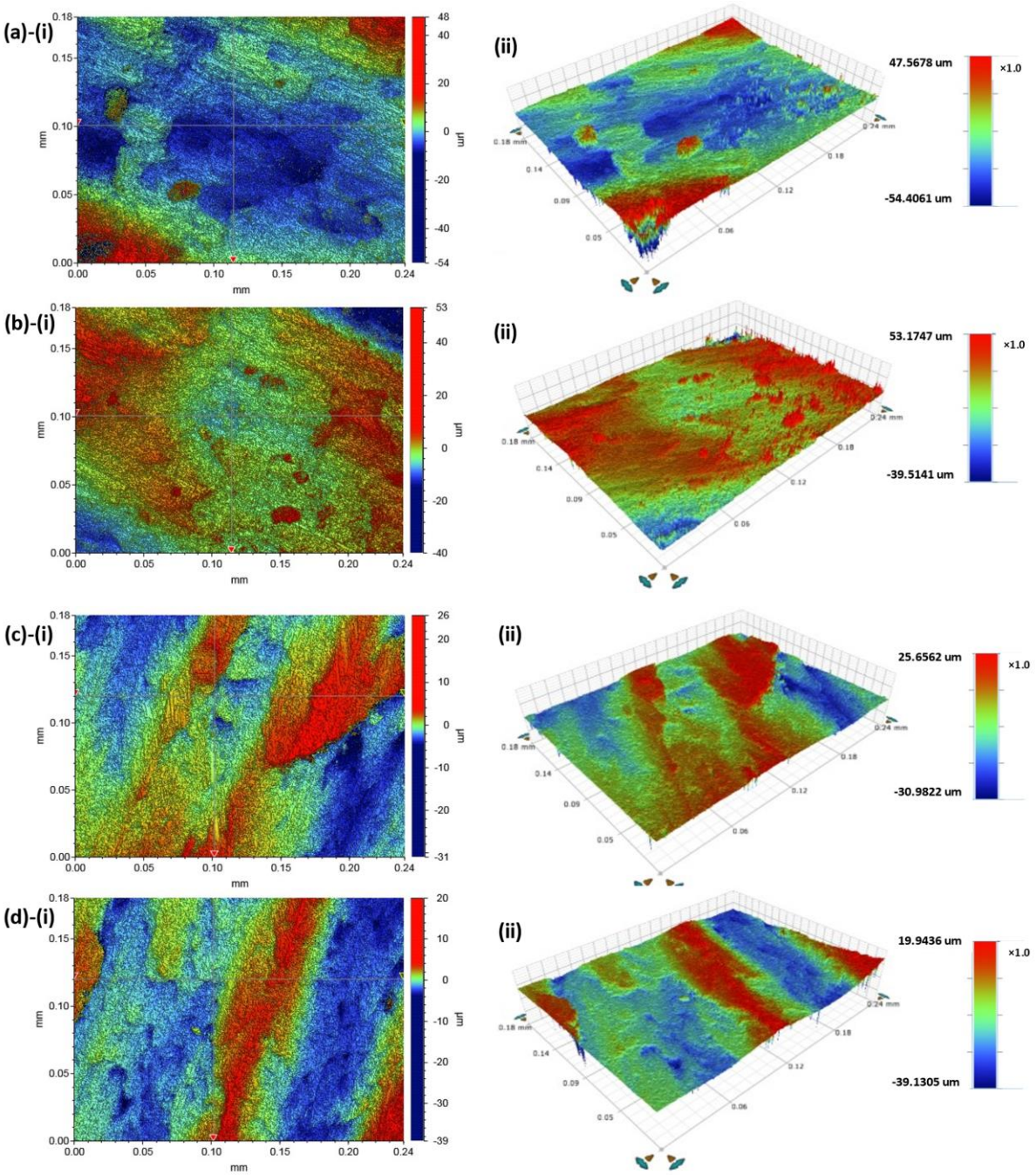

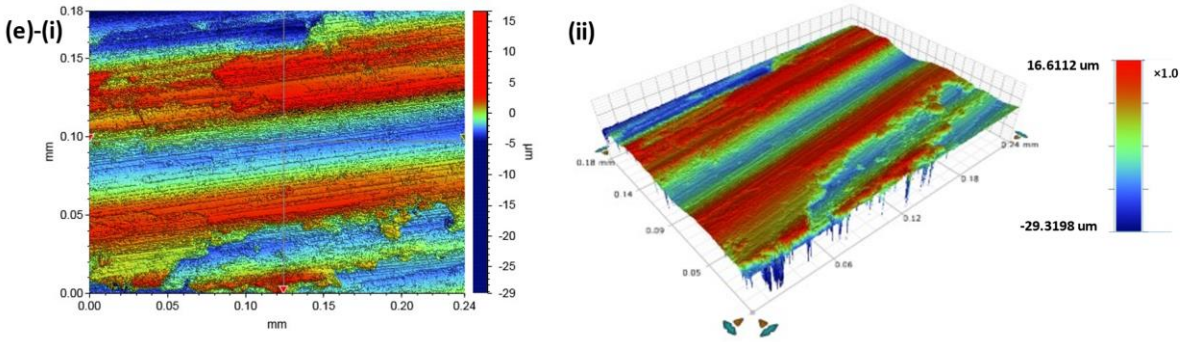

Figure 5.38: Optical profilometer micrographs for different material compositions at seizure: (a) AA 6082; (b) 2 wt.% HEA/AA composite; (c) 4 wt.% HEA/AA composite; (d) 6 wt.% HEA/AA composite; (e) 8 wt.% HEA/AA composite

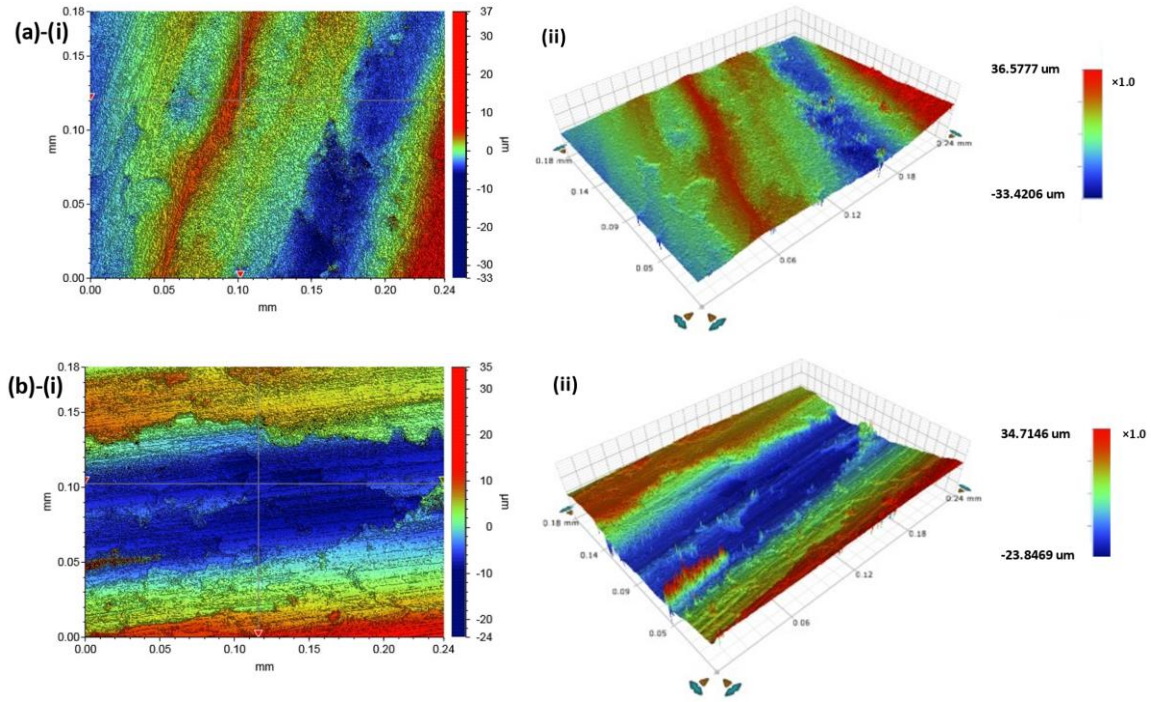

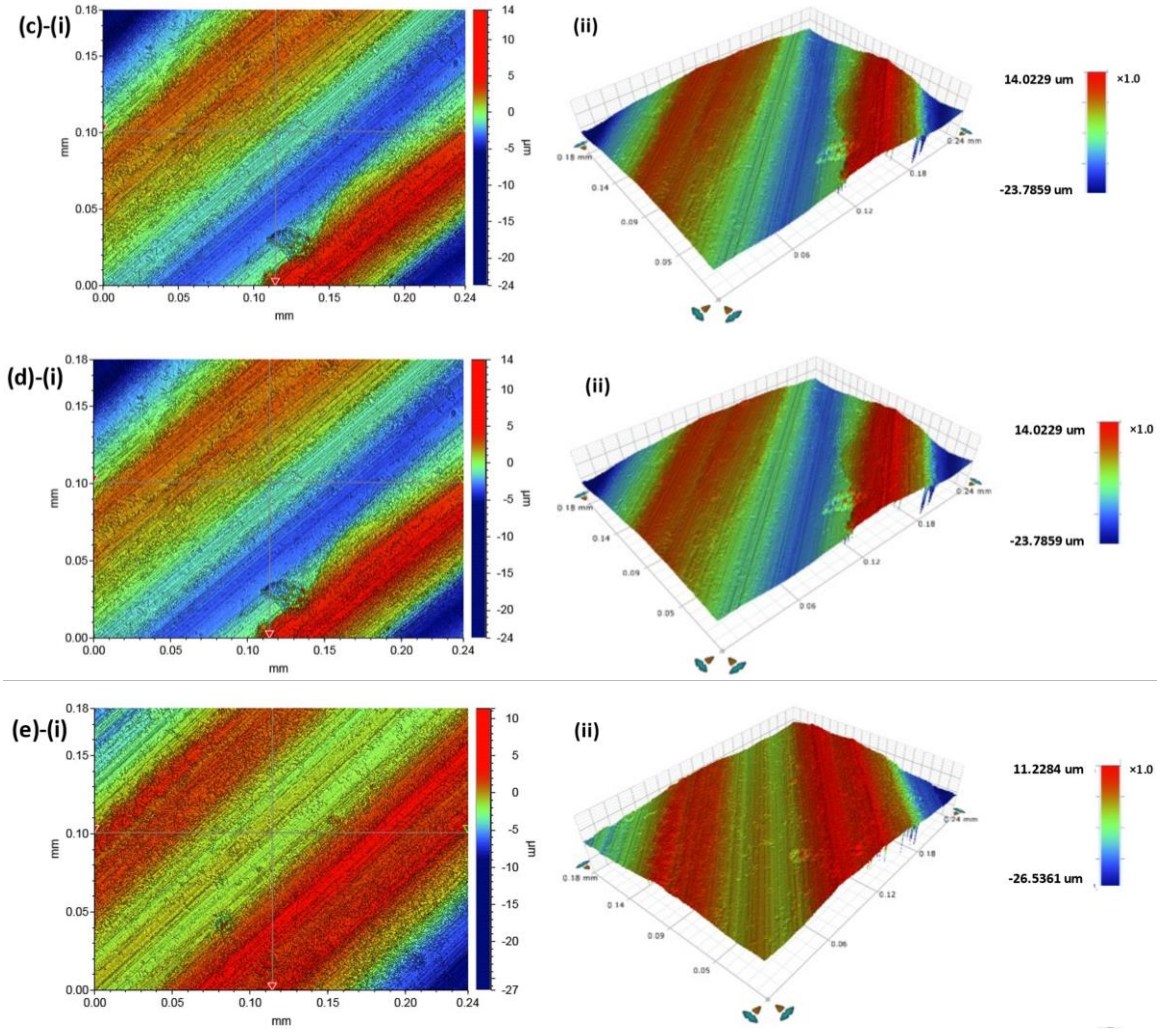

Figure 5.39: Optical profilometer micrographs for different material compositions at seizure for heat treated condition: (a) AA 6082; (b) 2 wt.% HEA/AA composite; (c) 4 wt.% HEA/AA composite; (d) 6 wt.% HEA/AA composite; (e) 8 wt.% HEA/AA composite

5.9 SUBSURFACE ANALYSIS

The microstructural analysis of the subsurface of AA6082 and HEA/AA composites at as-cast and heat-treated (T6) conditions revealed three distinct regions: 1) the Undeformed Region (UDR), 2) the Plastically Deformed Region (PDR), and 3) the Mechanically Mixed Layer (MML). Figure 5.24 (i)-(ii) and Figure 5.25 (i)-(ii) showed that at 0.763 MPa, the MML was observed to be approximately 132.17 µm and 91.32 µm respectively for as cast and heat-treated conditions in thickness, with the PDR measuring 72.215 µm and 69.983 µm. It was

noted that crack initiation occurred at the intersection of the bulk UDR and the severely deformed zone, which moved in the longitudinal direction and eventually transformed into MML over time. Further, sliding wear action caused the detachment of the MML and generated wear debris.

It was also noted that during the sliding motion, the grains of aluminium below the PDR flowed along the direction of sliding. The subsurface of as cast and heat treated 2 wt.% HEA/AA subjected to seizure under normal applied pressure (0.763 MPa and 1.018 MPa respectively) was depicted in the micrograph (Figure 5.24 (iii)-(iv) and Figure 5.25 (iii)-(iv)). Figure 5.24 (v)-(vi) and Figure 5.25 (v)-(vi) showed two different zones of as cast and heat treated 4 wt.% HEA/AA composite, the bulk deformed zone, and the highly deformed zone. During the seizure, the MML was detached from the subsurface, the thickness was reported as 61.3167 µm (as-cast) and 20.018 µm (T6), and the PDR was evaluated as 39.814 µm (as-cast) and 45.31 µm (T6).

The research emphasized the nucleation and propagation of cracks, microstructure, and phase morphology of the different zones. Figures 5.24 (vii)-(viii) and 5.25 (vii)-(viii) represented the subsurface formation of the as-cast and heat treated 6 wt.% HEA/AA composite at 1.018 MPa pressure, revealing an MML thickness of approximately 56.31 µm and 45.91 µm depth respectively. The PDR, measuring approximately 47.87 µm (as-cast) and 19.71 µm (T6), was found below the MML. It was noteworthy, at this stage, the HEA particles remained intact and no fragmentation of particles was observed in the MML. There was no observed particle pullout or debonding, which confirmed the good interfacial bonding between the HEA particles and the aluminium matrix. The 8wt.% HEA/AA get seizure at 1.273 MPa for as cast and heat-treated (T6) condition as well, the composite underwent seizure and the MML (30.416 µm (as-cast) and 12.31 µm (heat treated) transformed into the PDR, as shown in Figure 5.24 (ix)-(x) and Figure 5.25 (ix)-(x). The plastically deformed zone extended up to 34.681 µm (as cast) and 17 µm (T6) at 1.25 MPa

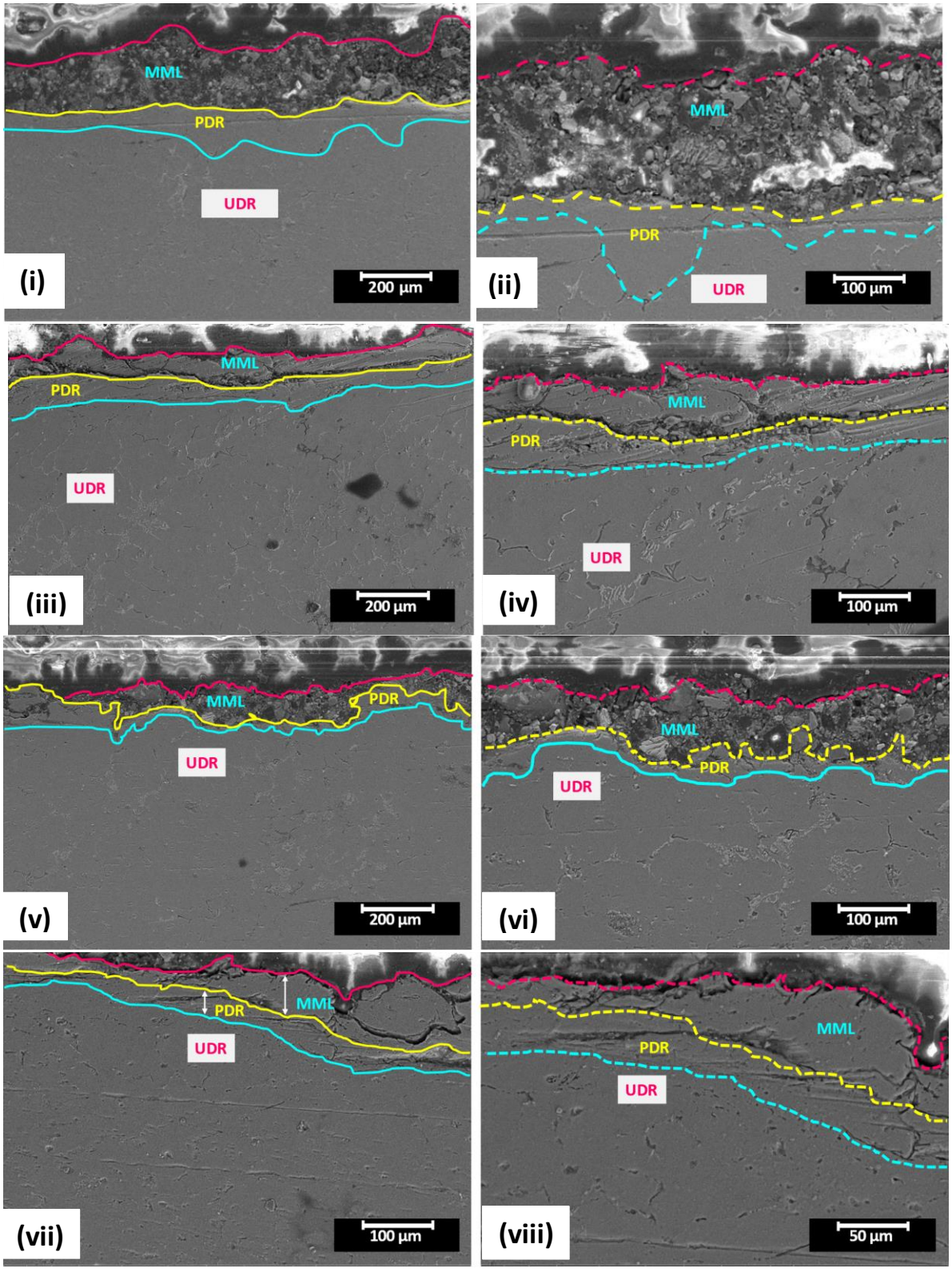
MML
PDR
UDR
(i)
200 µm
MML
PDR
UDR
(ii)
100 µm
MML
PDR
UDR
(iii)
200 µm
MML
PDR
UDR
(iv)
100 µm
MML
PDR
UDR
(v)
200 µm
MML
PDR
UDR
(vi)
100 µm
PDR
MML
UDR
(vii)
100 µm
MML
PDR
UDR
(viii)
50 µm

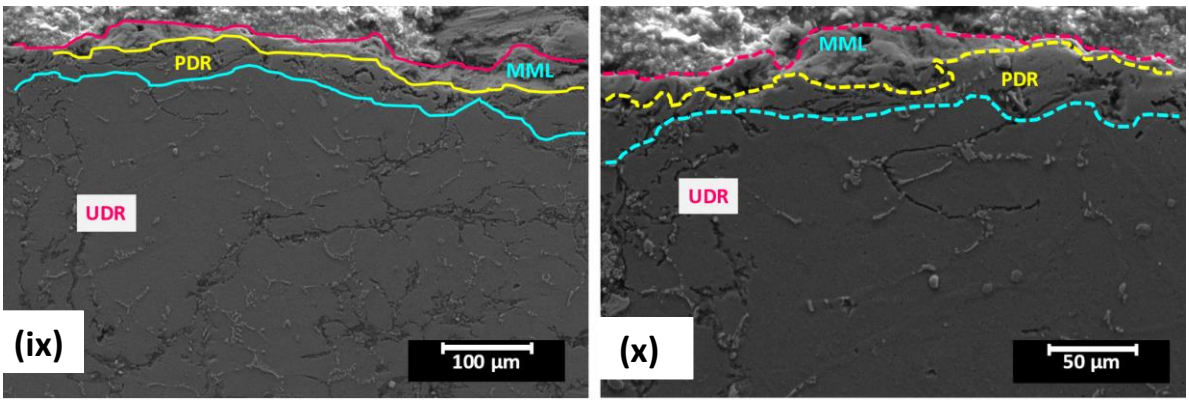

Figure 5.40: Lower and higher magnification micrograph images at seizure for the as-cast condition: (i) and (ii) AA 6082 (MPa); (iii) and (iv) 2 wt.% HEA/AA (MPa); (v) and (vi) 4 wt.% HEA/AA (MPa); (vii) and (viii) 6 wt.% HEA/AA (MPa); 8 wt.% HEA/AA (MPa).

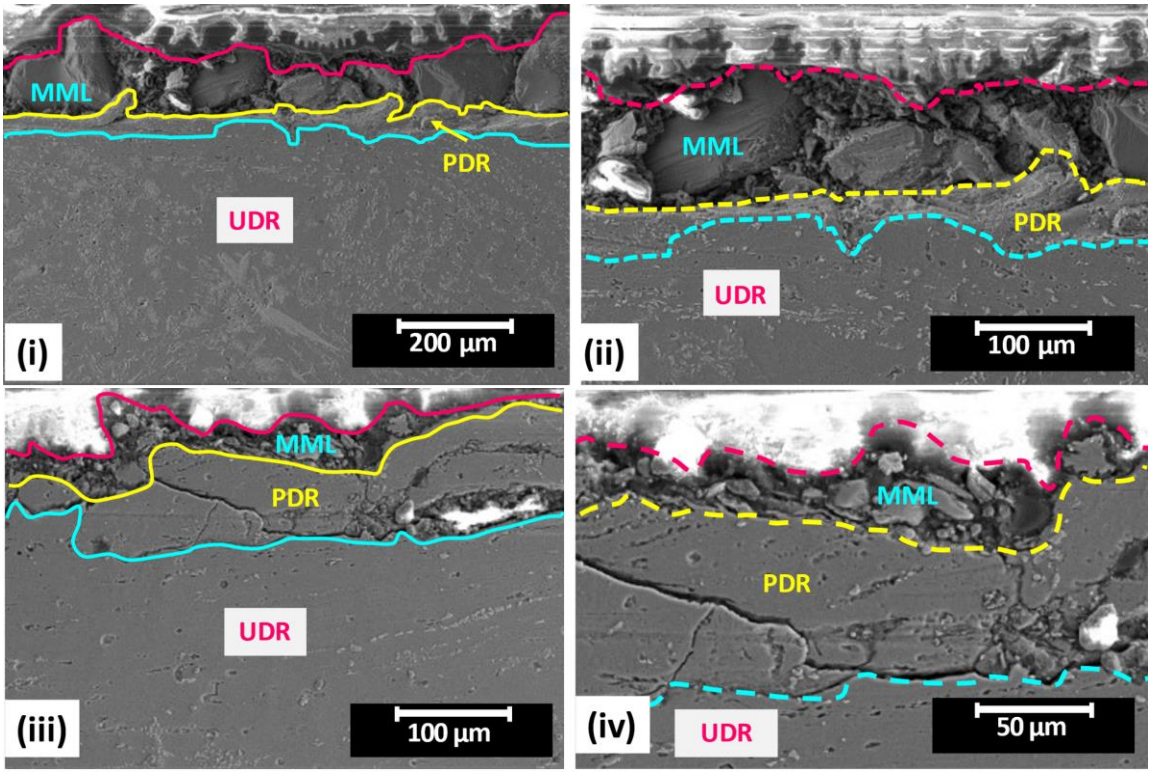

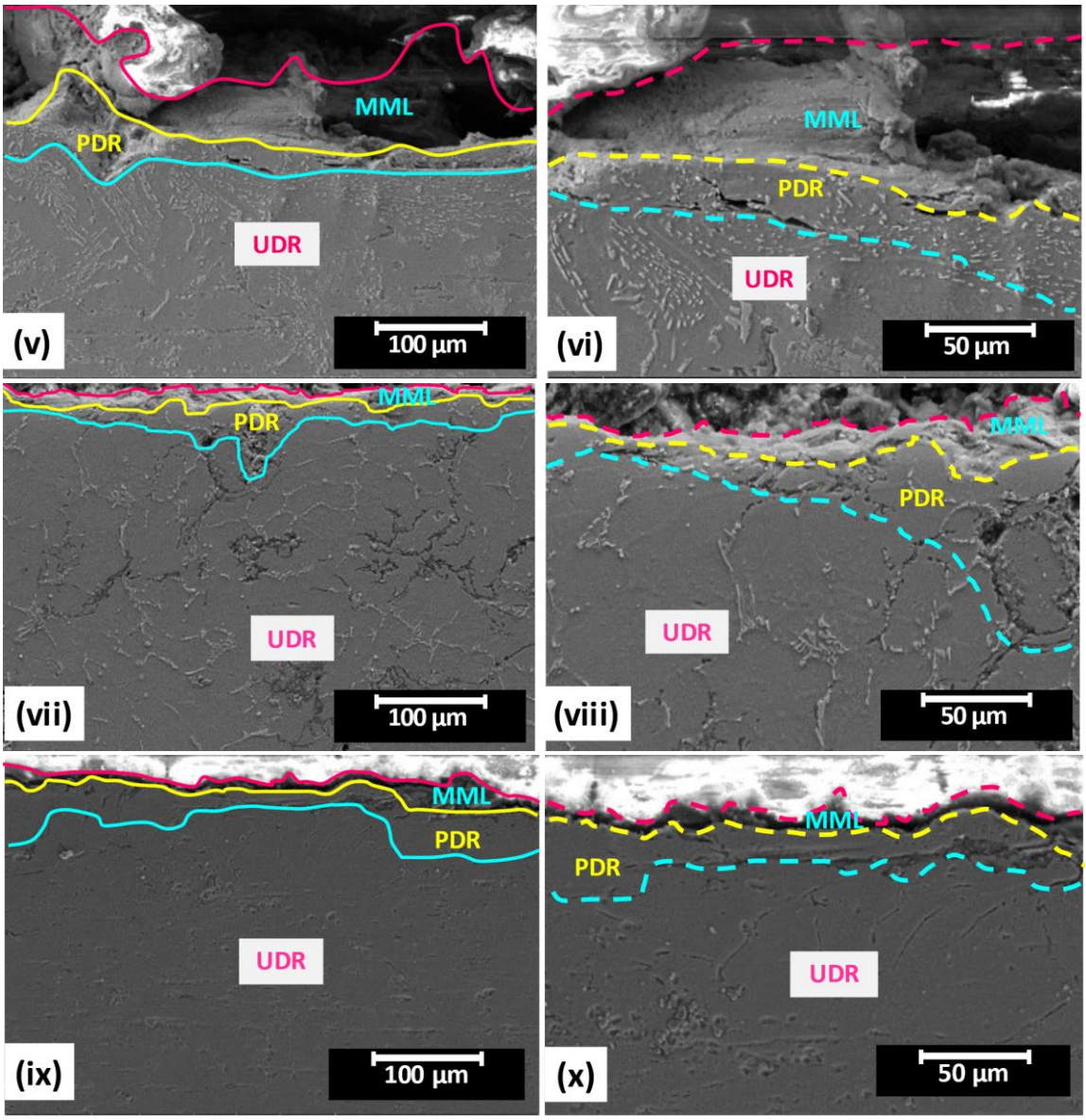

Figure 5.41: Lower and higher magnification micrograph images at seizure for heat treated condition: (i) and (ii) AA 6082 (MPa); (iii) and (iv) 2 wt.% HEA/AA (MPa); (v) and (vi) 4 wt.% HEA/AA (MPa); (vii) and (viii) 6 wt.% HEA/AA (MPa); 8 wt.% HEA/AA (MPa).

CHAPTER – 6

DISCUSSIONS

6.0 EVOLUTION OF PHASES IN CoCrFeMnNi HEA

Contrary to traditional alloys, the development of solid solution phases in HEAs is counterintuitive to the principles of physical metallurgy. Simple solid solutions form in HEAs due to the high entropy effect as it is evident that it enhances solid solution solubility limits. The evolution of phases of CoCrFeMnNi HEA can be estimated using different thermodynamic parameters as shown in Table 6.1 such as ΔH_{mix} (enthalpy of mixing), ΔS_{mix} (entropy of mixing), VEC (valence electron concentration), and δ (atomic size mismatch). The mixing enthalpy of CoCrFeMnNi HEA was evaluated using Miedema's approach [328] which utilizes binary mixing enthalpy as listed in Table 6.2 and ΔH_{mix} is reported as $-4.16\ KJ/mol$. Furthermore, the entropy of mixing is determined as per the Boltzmann hypothesis [329] to be $13.38\ J/mol.K$. Ω is also a crucial thermodynamic attribute which is defined as the ratio between the entropy of mixing and enthalpy of mixing. The development of stable solid solution $\Omega \geq 1$, whereas $\Omega < 1$, favors the emergence of intermetallic phases in HEAs. Ω for CoCrFeMnNi is reported as 5.77 which indicates the formation of stable solid solution phases in CoCrFeMnNi HEAs. As proposed by Zhang et al. [329] δ atomic size mismatch is around 0.98 % from the expression mentioned in Table 6.2 in which atomic radii of ith elements listed in Table 6.3, r_{avg} is the average atomic radii. The VEC > 8, encourages the formation of FCC phase, while VEC < 6.87 leads to emergence of BCC phase. In the current investigation of CoCrFeMnNi HEA, VEC = 8.3 and $\Omega = 5.77$, supporting the claim of forming FCC phase solid solution of CoCrFeMnNi HEA.

6.1 GOVERNING MECHANISM DURING MECHANICAL ALLOYING

It is widely recognized that the microstructure of mechanically alloyed HEA has a significant impact on its morphology. Figure 6.1 (a) illustrates the HEA particle behavior during mechanical alloying and based on the revelation milling is categorized into three different regions such as cold welding dominated region, fracture dominated region, and

dynamic equilibrium region. The morphology of HEA particles at different milling time illustrated the Figure 5.2 and Figure 5.3.

Table 6.1 Binary mixing enthalpy of diverse pairs of CoCrFeMnNi HEA

Elements	Co	Cr	Fe	Mn	Ni
Co	-	-4	-1	-5	0
Cr	-4	-	-1	2	-7
Fe	-1	-1	-	0	-2
Mn	-5	2	0	-	-8
Ni	0	-7	-2	-8	-

Table 6.2 Different important thermodynamic parameters and corresponding values of CoCrFeMnNi HEA.

Thermodynamic Parameters	Equation	CoCrFeMnNi HEA
Enthalpy of Mixing	$\Delta H_{mix} = 4 \sum_{i=1, i\neq j}^{n} x_i \, x_j \Delta H_{i-j}^{mix}$	$-4.16 \ \frac{KJ}{mol}$
Entropy of Mixing	$\Delta S_{mix} = -R \sum_{i=1}^{n} x_i \, ln x_i$	$13.38 \ \frac{J}{mol \, K}$
Ω	$\Omega = \frac{T_m \, \Delta S_{mix}}{\lvert \Delta H_{mix} \rvert}$	5.77
Atomic Size Mismatch	$\delta(\%) = 100 \sqrt{\sum_{i=1}^{n} x_i \left(1 - \frac{r_i}{r_{avg}}\right)^2}$	0.92
Valence electron concentration	$VEC = \sum_{i=1}^{n} x_i \, (VEC)_i$	8.33

Table 6.3 The atomic radius of different elements in CoCrFeMnNi HEA.

Elements	Co	Cr	Fe	Mn	Ni	Refer.

Radius (nm)	0.12510	0.12491	0.12412	0.13500	0.12459	[182]

In this study, HEA powder is relatively softer from 0 h to 6 h. Cold welding and plastic deformation are noticeable, culminating in a perceptible increase in particle size as well as irregular and angular morphology. From 6 h to 24 h milling time grain refinement took place whereas, lattice strain increased. Furthermore, persistent atom diffusion and dissolution led to severe lattice distortion [14]. These factors caused the milled powder to harden, in order to make it easier to fracture, and henceforth it can be concluded that during milling between 6 h and 24 h, fracturing dominated region form. The size of the milled powder progressively stabilized as the milling duration reached 42 h, as the cold welding and fracturing reached a dynamic equilibrium, and spherical morphology appeared. As the milling period exceeds 42 h, it becomes unfavorable, and continued milling has a negative influence on the phase identification of powder [103], undesired phases are noticed, and contamination issues are noticeable [221]. As a finding, the optimal milling time for CoCrFeMnNi HEA is 42 h.

6.2 STRENGTHENING MECHANISM FOR CoCrFeMnNi HEA

The mechanical properties of the composites predominately relied on the microstructure and distribution of HEA-reinforced particles. From the FESEM micrograph as shown in Figure 5.6 (j) and Figure 5.7 (a) it is evident that the HEA particles distribution in 8 wt.% HEA/AA has more uniform as compared with other composites, which leads to better plasticity and strength [330][331]. 8 wt.% HEA/AA composites have the highest strength and heterogeneous grain structure is the predominant cause for superior properties [332][333].

It is widely acknowledged that the strength of as-cast composites is highly influenced by particle size and concentration. Figure 6.1 (b) shows a schematic diagram of particle distribution and their effect on the Al matrix of AA 6082 alloy, and HEA/AA composite for the HEA particle distribution and their effect in the Al matrix of the composite.

According to the dispersion strengthening principle, larger particles develop voids around them, potentially causing mechanical properties to deteriorate [334]. It has been shown that lowering particle size minimizes particle-to-particle distances in composites, creating a barrier

for dislocation motion and compelling them to exhibit better strength [335]. Also, the small size particles are effectively responsible for hardening which contributes to the strength of the composites [325]. Reduced reinforced particle size decreases stress concentration at reinforced particle edges and increases dislocation-reinforced particle interaction, leading to increased strength [336]. The existence of small particles as reinforcement pins the matrix grain boundaries, causing the refined grain boundaries to appear [337] and restricting grain boundary movement [326]. A fine-grained grain structure and a great barrier to dislocation movement increase composite strength.

The formation of high-density dislocations is shown to be the principal strengthening method in Al composites. The high-density dislocation, on the other hand, could induce a stress concentration along with the interfaces of the HEA particles and the Al matrix, enabling the composites' fracture strength and plasticity to deteriorate. [42]. Figure 6.1 (c)- (i), (ii), and (iii) presents geometrically necessary dislocations through TEM images of the AA 6082 alloy, 2 wt.% HEA/AA and 8 wt.% HEA/AA respectively in which it is evident that more dislocation density was reported in 8 wt.% HEA/AA as compared to AA 6082 alloy and 2 wt.% HEA/AA.

The inclusion of HEA particles improves the yield strength of composites in this work. The following factors contribute to this: (i) Hall-Petch strengthening due to grain refinement; (ii) Load transfer effect induced by the proximity of HEAs particles; (iii) Geometrical necessary dislocation strengthening caused by elastic modulus difference and thermal expansion difference between the HEA particles and Al matrix; and (iv) orowan strengthening induced by the resistance of densely packed HEAs to the passing of dislocations [338]. The composite's estimated overall yield strength may be determined as follow:

$$\sigma_{CY} = \sigma_{A_mY} + \sigma_{LT} + \sigma_{HP} + \sqrt{\Delta\sigma_{OR}^2 + \Delta\sigma_{GND}^2}$$

The yield strength of the composite is σ_{CY}, while the yield strength of the 6082 Al matrix is σ_{A_mY}. The volume fraction of HEA reinforcements is denoted as f_v. The following expression can be used to compute the increase in the strength induced by orowan strengthening, geometrically required dislocations, load transfer effect, and grain boundary strengthening respectively [339]:

$$\sigma_{HP} = K_H[d_c^{-\frac{1}{2}} - d_{A_m}^{-\frac{1}{2}}]$$

$$\Delta\sigma_{LT} = {}^{1}/_{2}\,\sigma_{A_mY} f_v$$

$$\Delta\sigma_{OR} = \emptyset \frac{b_M G_M}{L}$$

For AA 6082, $K_H = 1.2\ MPa.mm^{1/2}$ where K_H stands for Hall-Petch constant, d_c and d_{A_m} are the average grain size of the composite and matrix of the base alloy. f_v expressed as the volume fraction of HEA reinforcement. $\emptyset$ is a constant (for AA 6082, $\emptyset = 2$). b_M and G_M are the burger vector and shear modulus ($b_M = 0.286\ nm$ and $G_M = 25.6\ GPa$) respectively. L is denoted for interparticle spacing of HEA reinforcements which is given by:

$$L = d\left(\frac{\pi}{6f_v}\right)^{1/3}$$

where d is the average diameter of reinforcements. The enhancement of strength owing to geometrically necessary dislocations (GNDs) is estimated by Refer. [45]:

$$\Delta\sigma_{GND} = \omega b_M G_M \sqrt{\rho_{GND}}$$

ω is the constant of 1.25, ρ_{GND} is the density of GNDs

$$\rho_{GND} = \rho_E + \rho_{CTE} = \frac{8f_v\varepsilon_y}{b_M d} + \frac{12\Delta\alpha.\Delta T.f_v}{b_M d(1-f_v)}$$

ρ_{GND} classified into two parts: ρ_E is the density of GNDs owing to elastic modulus difference and ρ_{CTE} is the density of GNDs owing to the CTE difference between HEA reinforcement and the Al matrix [45]. ε_y is the yield strain associated with Al matrix, $\Delta\alpha$ is the difference between the thermal expansion coefficient of the Al matrix and HEA reinforcement ($CTE_{6082\,AA} = 22.8 \times 10^{-6}/\,°K$ and $CTE_{HEA} = 15 \times 10^{-6}/\,°K$) and ΔT is the difference in temperature between synthesis temperature (550 ℃) and ambient temperature (25 ℃).

Table 6.4 The augmented yield strength is evaluated through different strengthening mechanisms.

HEA reinforcement (wt.%)	Enhancive yield strength (MPa)			
	$\Delta\sigma_{Orowan}$	$\Delta\sigma_{GND}$	$\Delta\sigma_{Hall-Petch}$	$\Delta\sigma_{Load}$
2	4.1319	52.1384	3.8335	0.3860
4	5.2291	69.3456	8.5843	0.7824
6	6.0133	74.7792	7.2616	1.1898
8	6.6490	83.2007	14.1424	2.0393

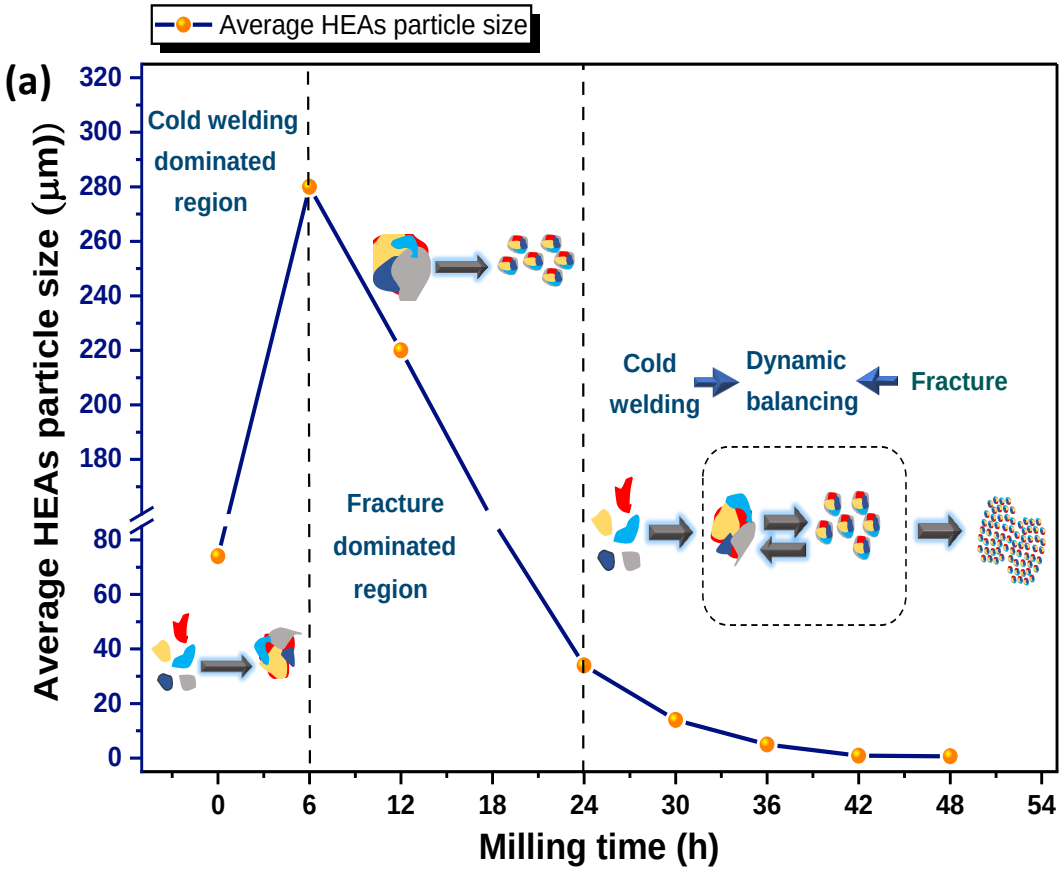

(b)

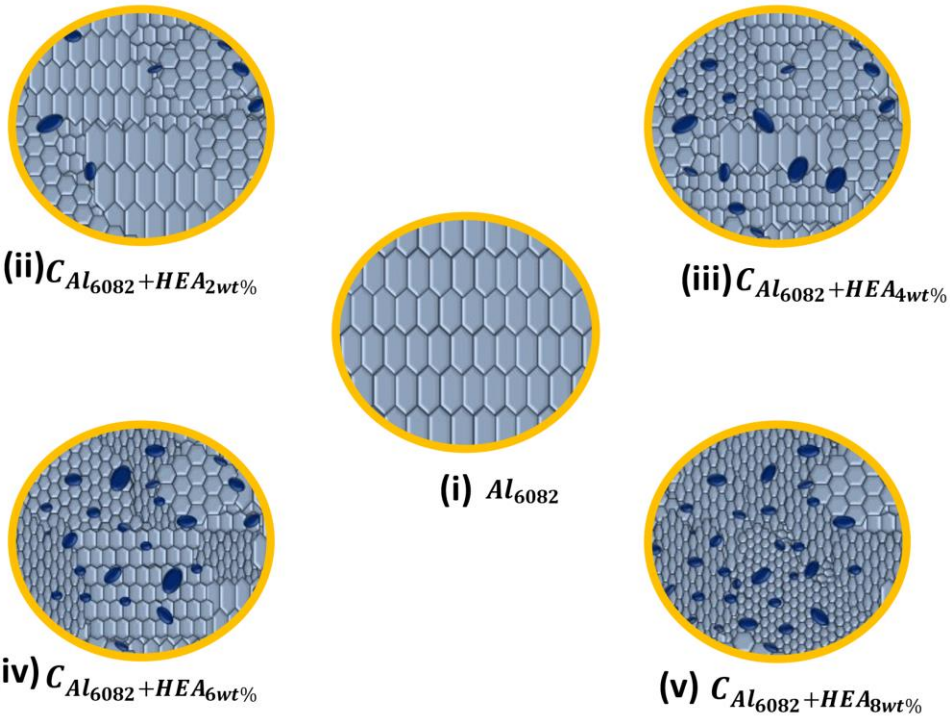
(ii) $C_{Al_{6082}+HEA_{2wt\%}}$
(iii) $C_{Al_{6082}+HEA_{4wt\%}}$
(i) Al_{6082}
(iv) $C_{Al_{6082}+HEA_{6wt\%}}$
(v) $C_{Al_{6082}+HEA_{8wt\%}}$

(c) (i)

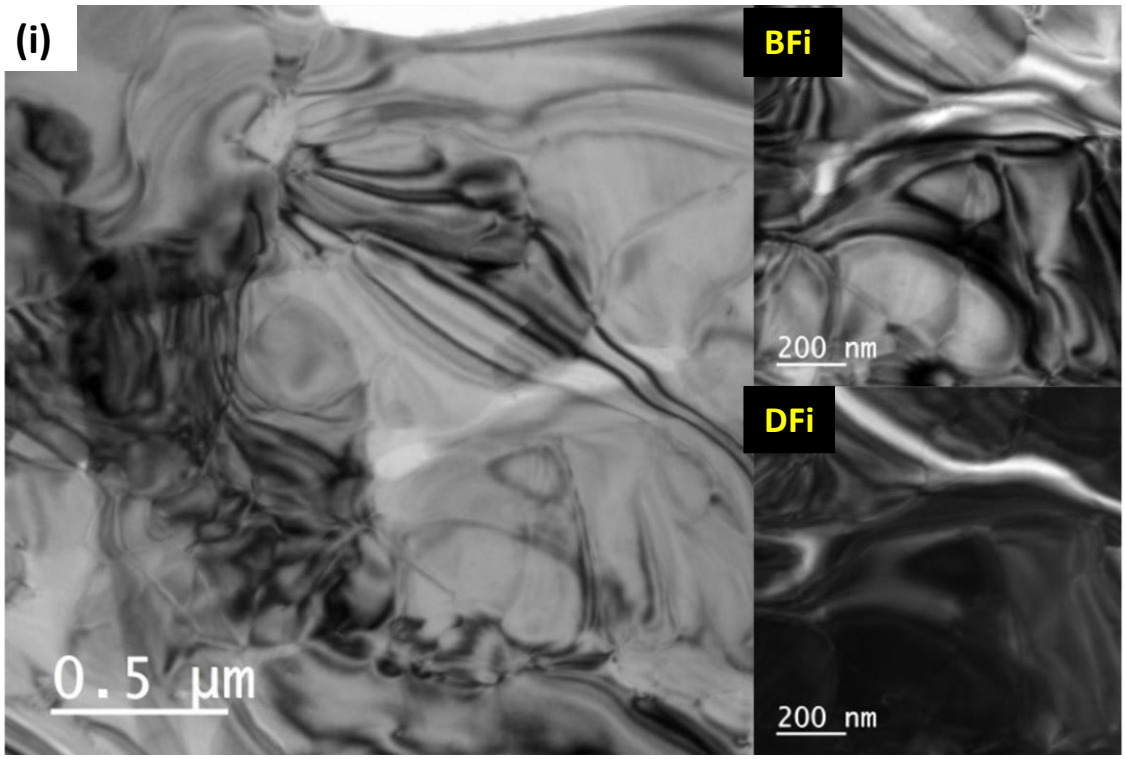
BFi
200 nm
DFi
200 nm
0.5 µm

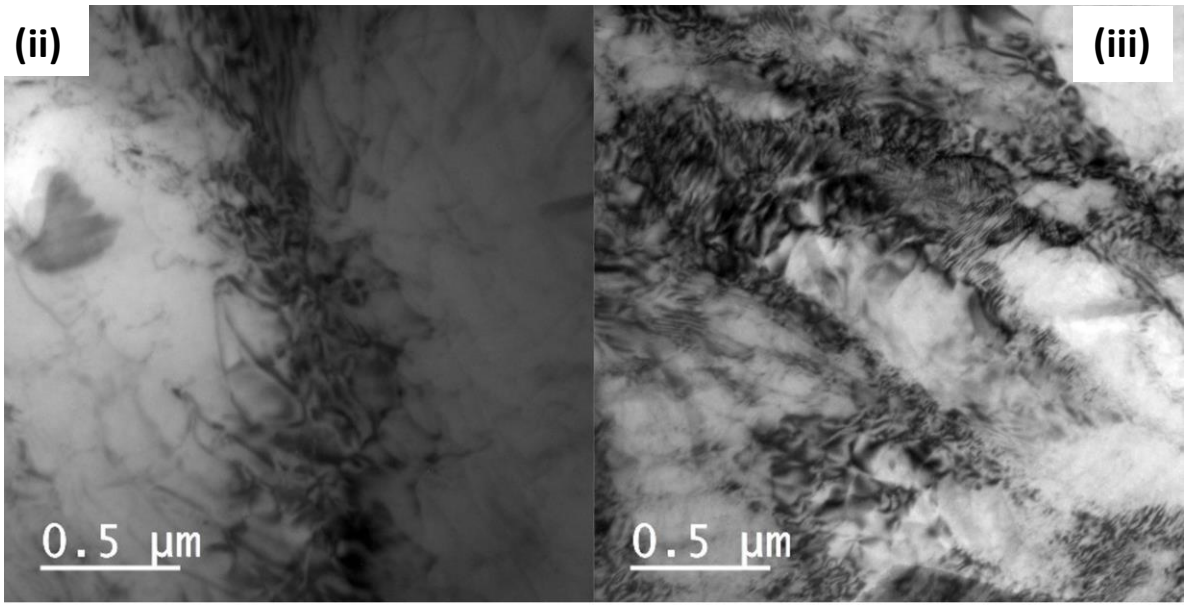
(ii)
(iii)
0.5 µm
0.5 µm

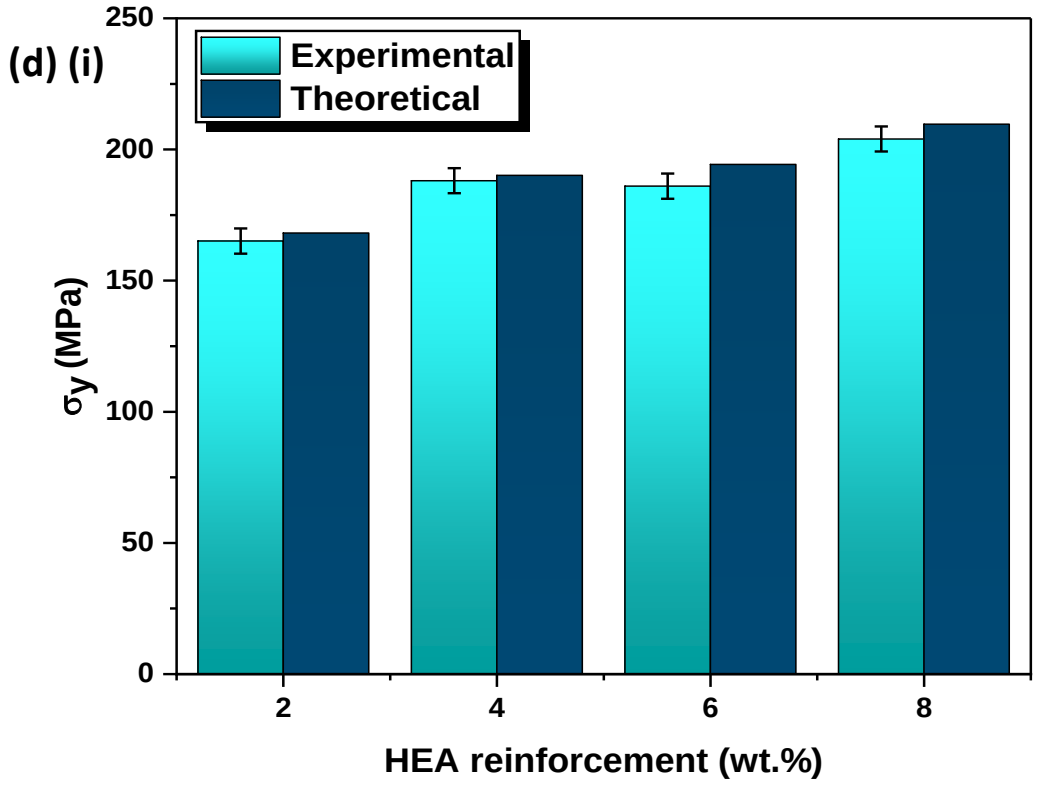
(d) (i)
Experimental
Theoretical
σy (MPa)
250
200
150
100
50
0
2
4
6
8
HEA reinforcement (wt.%)

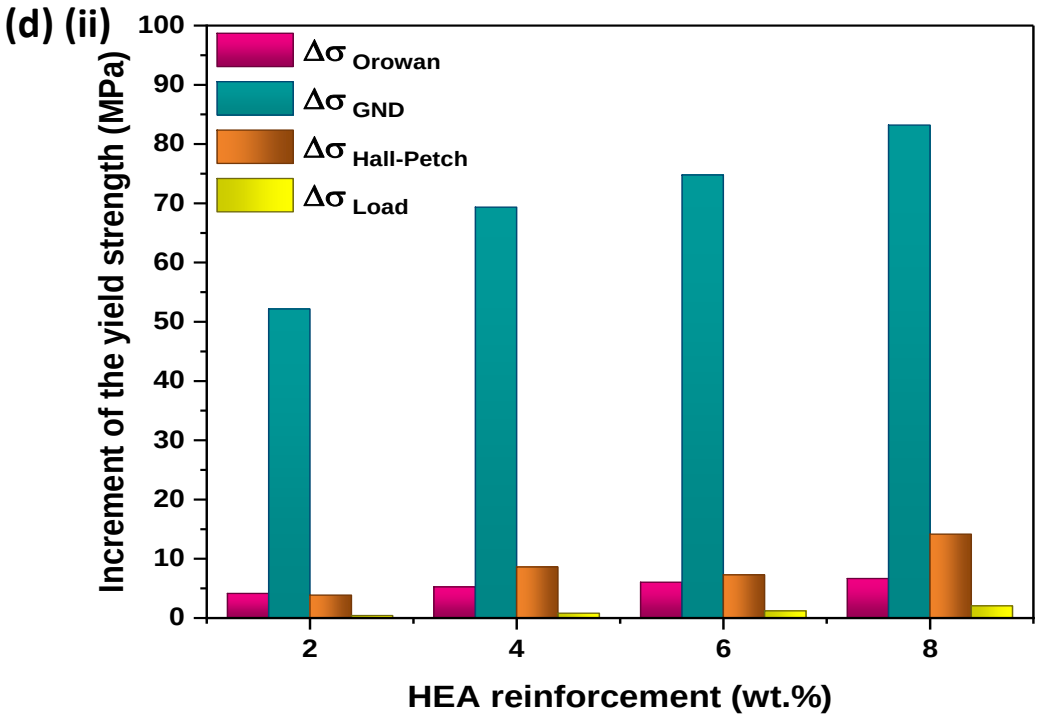

Figure 6.1: (a) variation of average particle size of CoCrFeMnNi HEA with milling time; (b) Schematic diagram of AA 6082 alloy and HEA/AA composites; (c) Geometrically necessary dislocation (GND) observed through TEM images of the as-cast alloy and composites: (i) dislocation present in AA 6082 alloy also a bright field image and a dark field image, (ii) dislocations present in 2 wt.% HEA/AA composite, and (iii) dislocations present in 8 wt.% HEA/AA composite; (d) (i) The comparison of theoretical and experimental values using σ_y. The standard deviation of data samples is indicated by the error bars, and (ii) Different strengthening is used to estimate the increase in yield strength.

The contribution of different strengthening effects in the increment of yield strength is listed in Table 6.4 and Figure 6.1 (d)-(ii). Grain boundary strengthening contributes the utmost to the composite yield strength, and the theoretical values for varying compositions were found to be consistent with the actual values as shown in Figure 6.1 (d)-(i).

The mechanical properties of the HEA/AA composite are thought to be enhanced further by optimizing several aspects of mechanical alloying, manufacturing processes, and heat treatment, which are the most significant influences on grain structure.

6.3 WEAR RATE

The 8 wt.% HEA/AA high entropy alloy composite exhibits superior resistance to wear and seizure compared to the base alloy. The improved wear resistance is attributed to the presence of hard particles that contribute to increased strength at elevated temperatures and provide plastic constraints. Furthermore, these hard particles act as projections that facilitate adhesion between the material and the counter surface of the hardened steel disk. It has been demonstrated that intermediate pressure during sliding results in the formation of an oxide layer that causes oxidational wear. As pressure increases, a mechanically mixed layer is formed that eventually disintegrates, resulting in delaminating wear. Additionally, the presence of soft dispersoids acts as a lubricating agent, promoting the development of a lubricating film at the interface of the interacting regions, thus reducing friction and overall material loss.

6.4 GOVERNING WEAR MECHANISM

During the sliding motion, the two interacting surfaces are exposed to both normal and shear loading. The contact between these surfaces, which are characterized by irregular asperities of varying shapes and sizes, leads to the piercing of the softer material's asperities by the harder ones, resulting in material loss. As the normal applied pressure increases, the harder asperities of the steel disk penetrate deeper into the asperities of the as-cast alloy and composites, causing deformation and fracture of the softer surface asperities. It has been observed that up to a certain pressure, which varies depending on the composition, the wear rate follows a linear path. However, when the pressure exceeds this limit, excessive heat is generated, which increases the local adhesion between the mating surfaces. The heat-softened material experiences increased penetration of asperities, leading to significant wear. At this stage, weight loss due to delamination at the micro-cutting, fracture, and adhesion regions are prevalent. This results in the destruction of the mechanically mixed layer (MML) that forms at lower pressures. Beyond the critical pressure, the wear rate abruptly increases, changing from linear to a sharp increase. At low pressures, the pin surface asperities are sharper and stronger compared to those at high pressures, leading to deformation and fracture. In these low-pressure conditions, the healthy engagement between the asperities of the contacting surfaces is

governed by the MML. It has been observed that the thickness of the MML in the unreinforced phase is thinner than in the reinforced phase.

6.5 WEAR MAP

The wear map depicted in Figure 6.2 provides a comprehensive representation of the synergistic influence of sliding distance and normal applied pressure on the wear rate of AA 6082 alloy and composites for as-cast and heat-treated conditions. The significance of the wear rate in relation to applied pressure and sliding distance is depicted via a color-coded scheme.

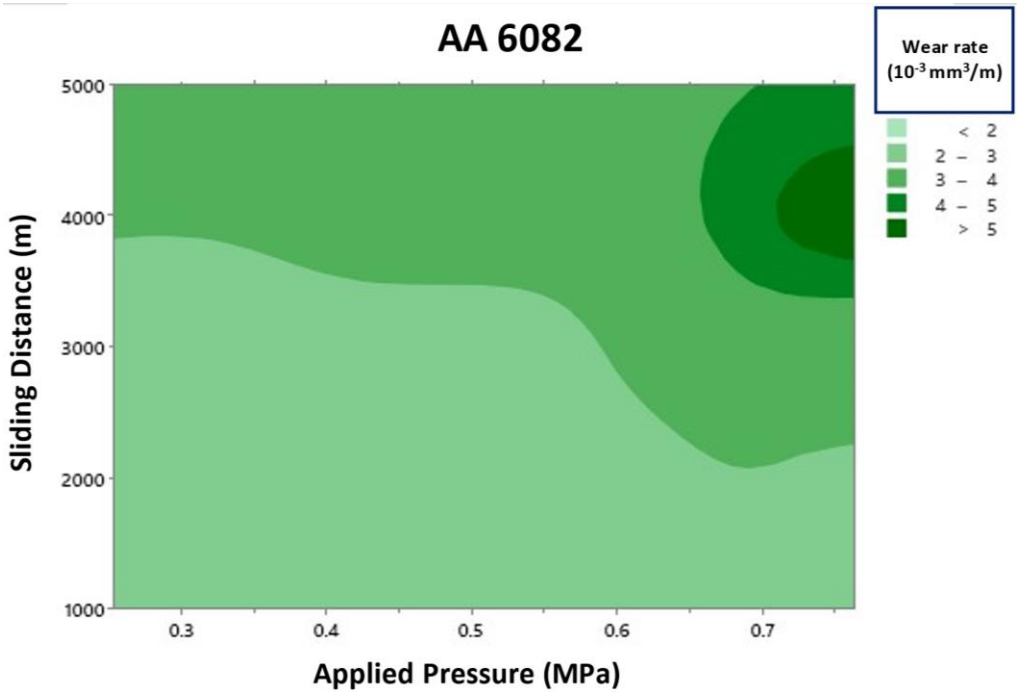

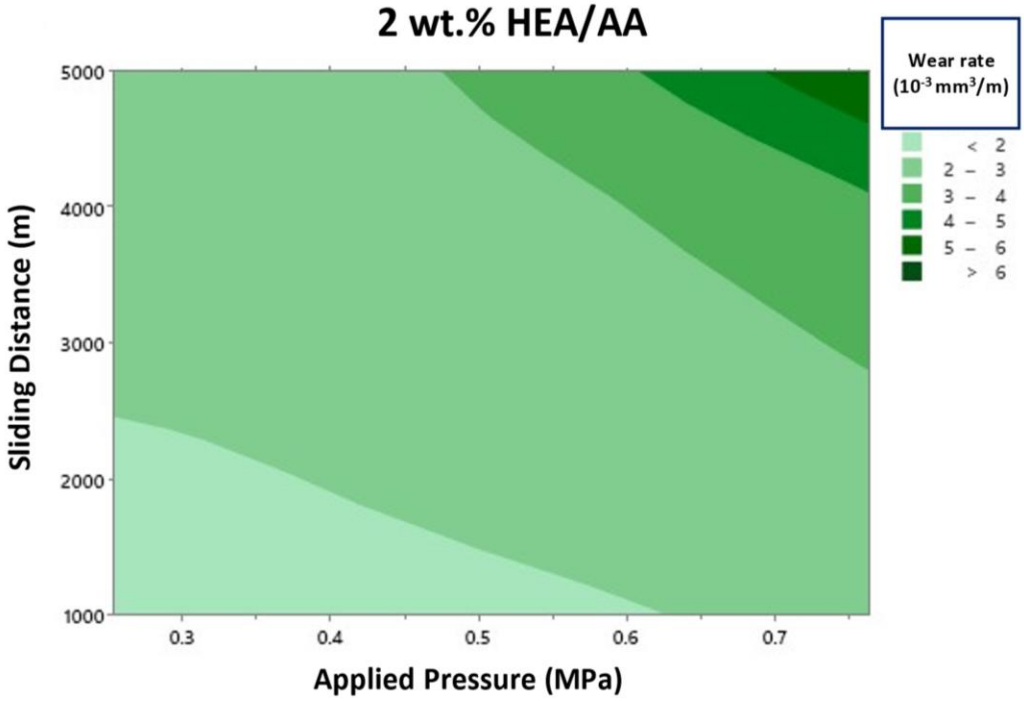
2 wt.% HEA/AA
Wear rate
(10^{-3} mm^3/m)
< 2
2 – 3
3 – 4
4 – 5
5 – 6
> 6
Sliding Distance (m)
5000
4000
3000
2000
1000
0.3
0.4
0.5
0.6
0.7
Applied Pressure (MPa)

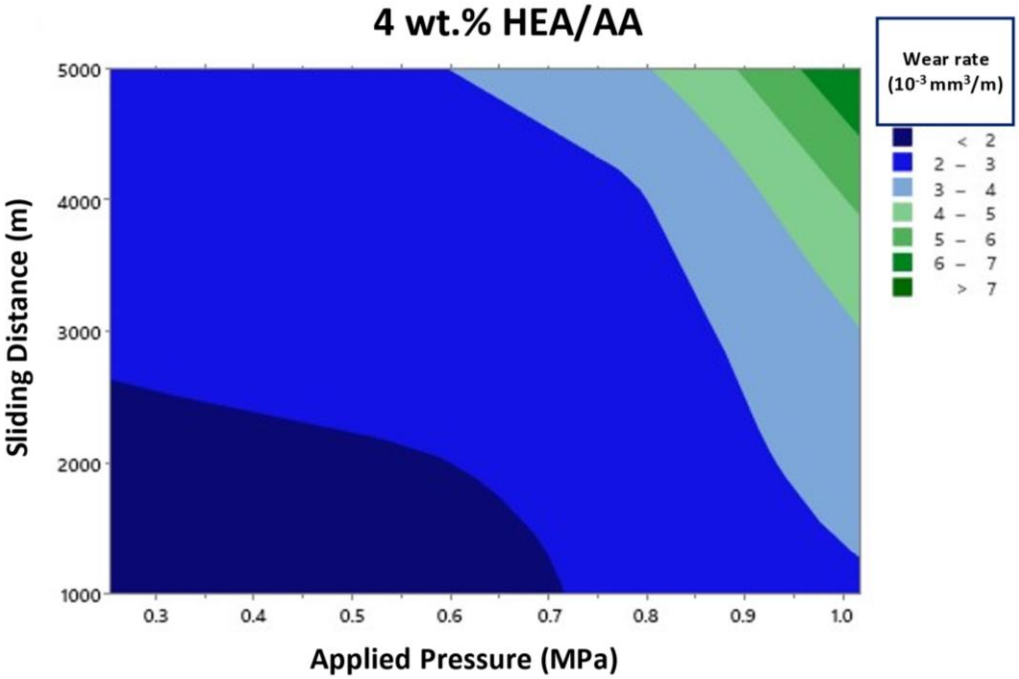
4 wt.% HEA/AA
Wear rate
(10^{-3} mm^3/m)
< 2
2 – 3
3 – 4
4 – 5
5 – 6
6 – 7
> 7
Sliding Distance (m)
5000
4000
3000
2000
1000
0.3
0.4
0.5
0.6
0.7
0.8
0.9
1.0
Applied Pressure (MPa)

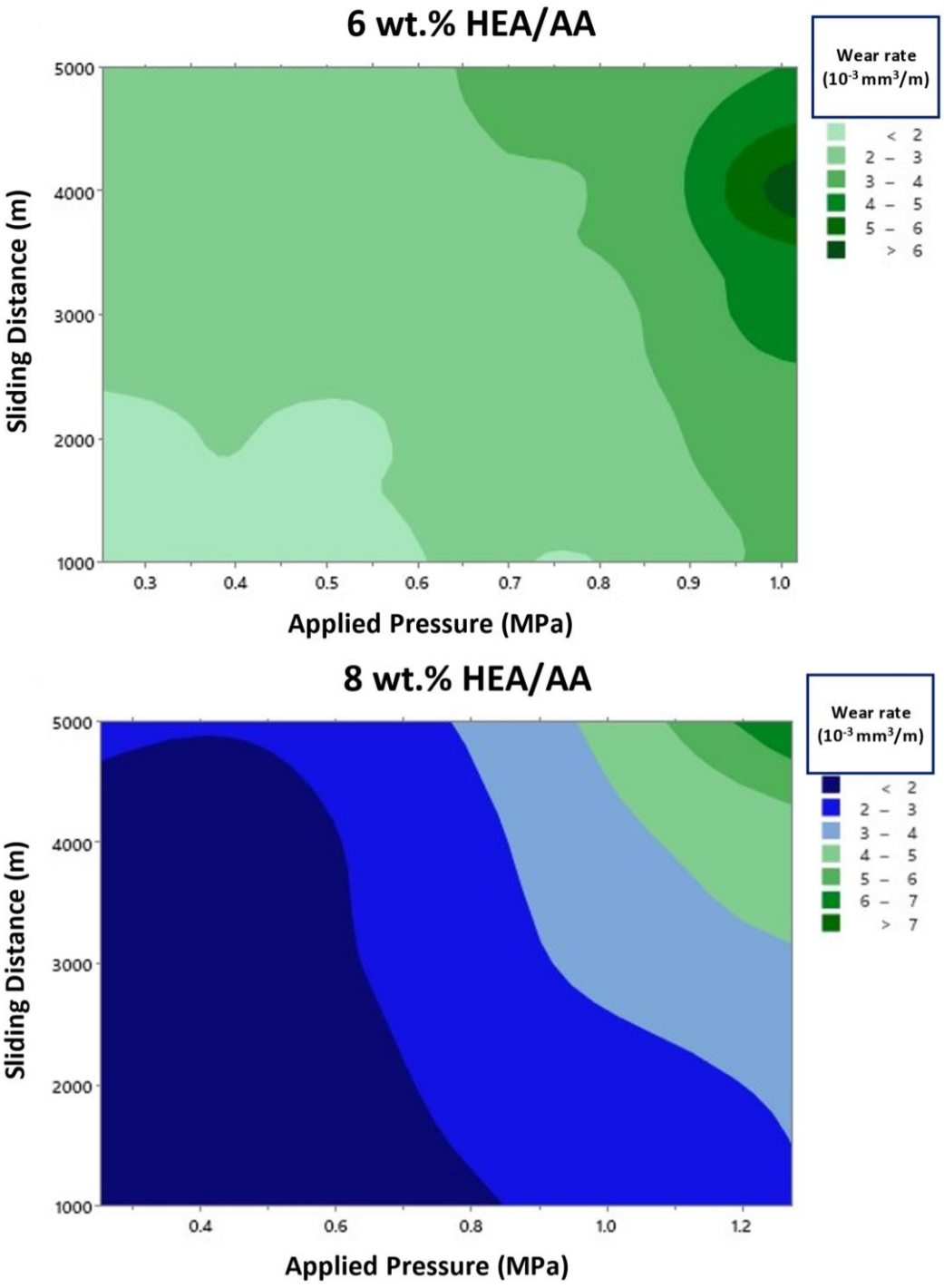

Figure 6.2: wear map for normal applied pressure and sliding distance for AA 6082 and HEA/AA composites (As-cast condition).

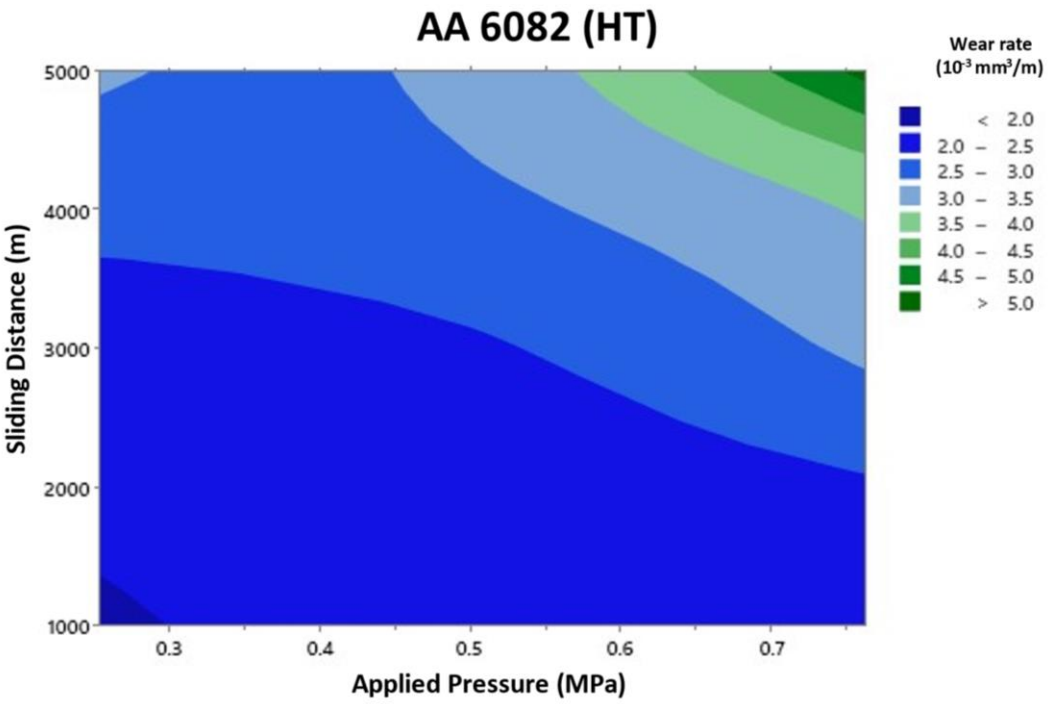
AA 6082 (HT)
Wear rate
(10^{-3} mm^3/m)
< 2.0
2.0 – 2.5
2.5 – 3.0
3.0 – 3.5
3.5 – 4.0
4.0 – 4.5
4.5 – 5.0
> 5.0
Sliding Distance (m)
5000
4000
3000
2000
1000
0.3
0.4
0.5
0.6
0.7
Applied Pressure (MPa)

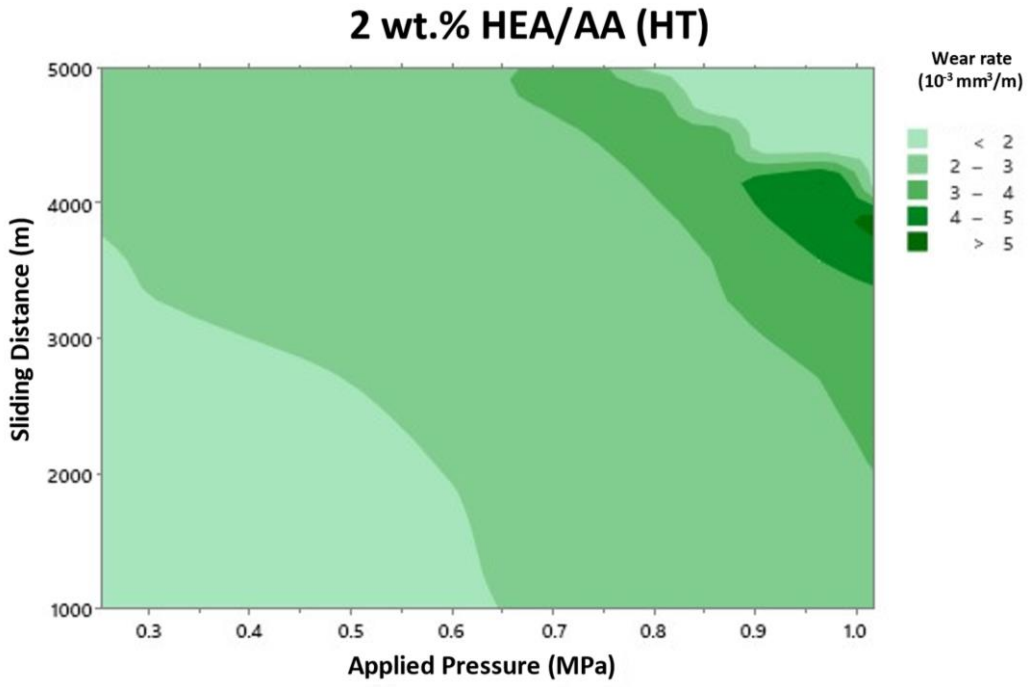
2 wt.% HEA/AA (HT)
Wear rate
(10^{-3} mm^3/m)
< 2
2 – 3
3 – 4
4 – 5
> 5
Sliding Distance (m)
5000
4000
3000
2000
1000
0.3
0.4
0.5
0.6
0.7
0.8
0.9
1.0
Applied Pressure (MPa)

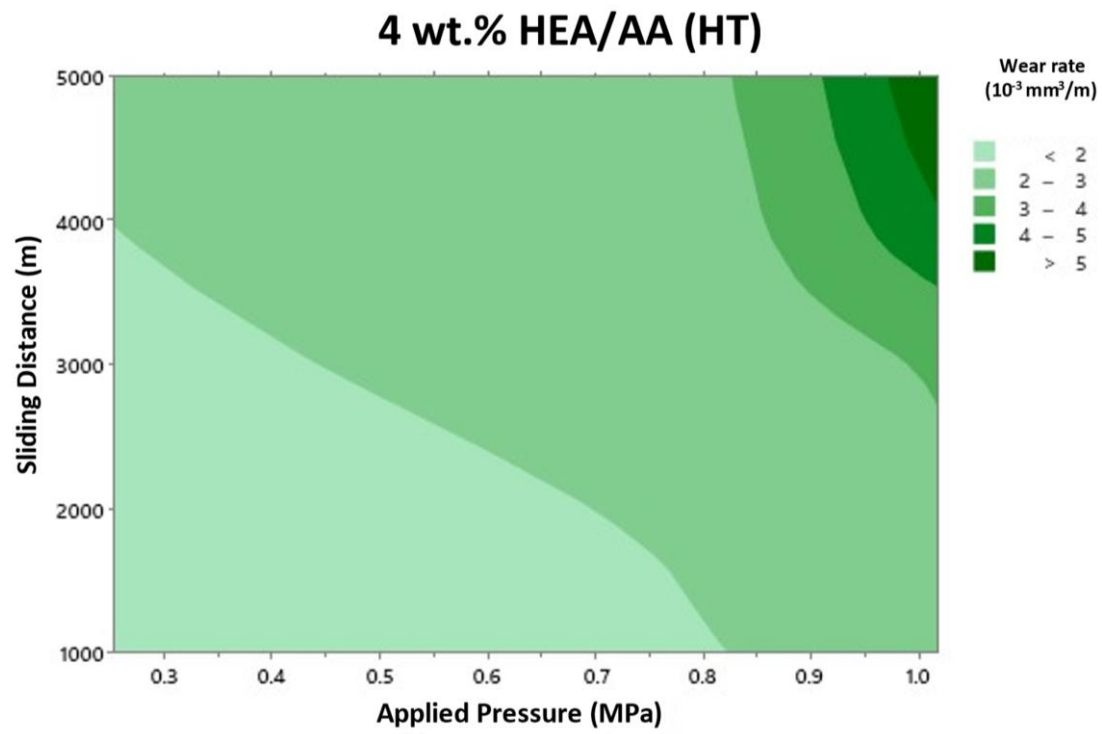
4 wt.% HEA/AA (HT)
Wear rate
(10^{-3} mm³/m)
< 2
2 – 3
3 – 4
4 – 5
> 5
Sliding Distance (m)
5000
4000
3000
2000
1000
0.3
0.4
0.5
0.6
0.7
0.8
0.9
1.0
Applied Pressure (MPa)

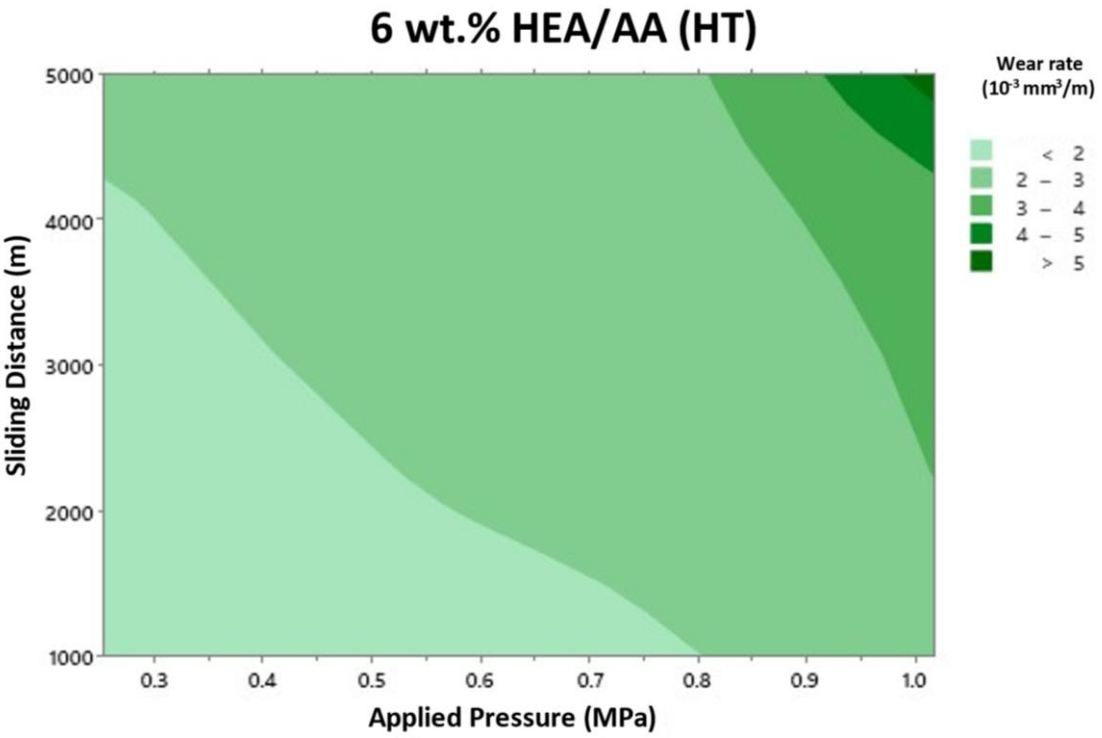
6 wt.% HEA/AA (HT)
Wear rate
(10^{-3} mm³/m)
< 2
2 – 3
3 – 4
4 – 5
> 5
Sliding Distance (m)
5000
4000
3000
2000
1000
0.3
0.4
0.5
0.6
0.7
0.8
0.9
1.0
Applied Pressure (MPa)

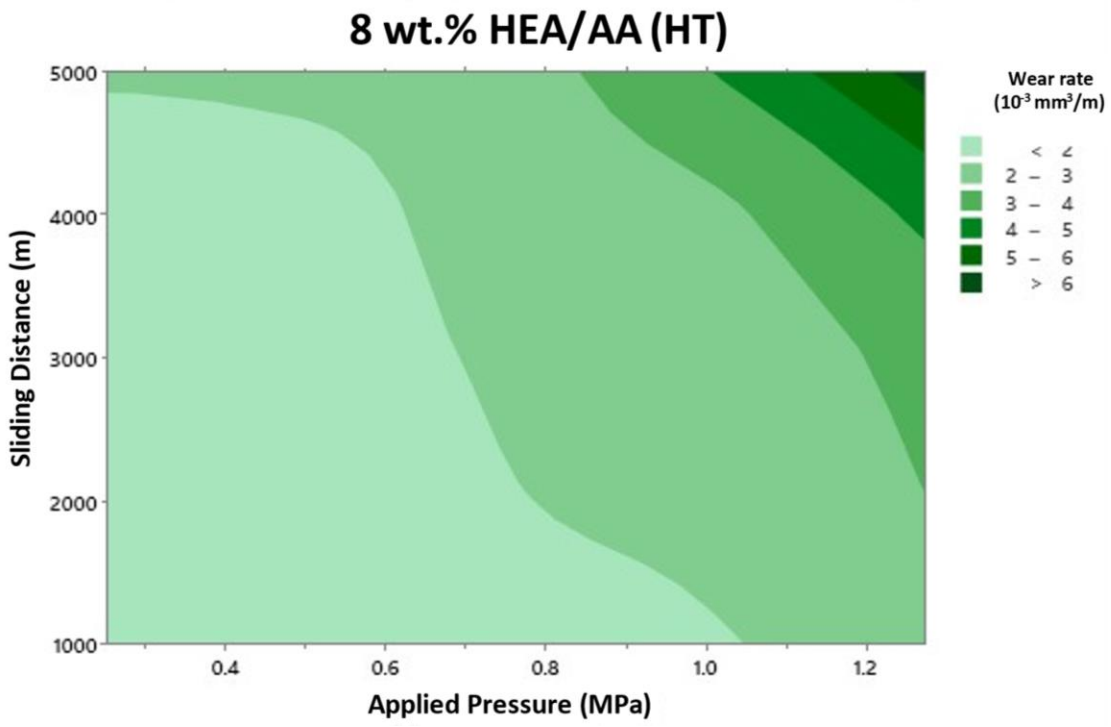

Figure 6.3: wear map for normal applied pressure and sliding distance for AA 6082 and HEA/AA composites (Heat treated condition).

6.6 COEFFICIENT OF FRICTION

The initiation of metal-to-metal contact triggers abrasive wear and material loss regulation. The application of pressure may lead to the growth of an oxide layer due to frictional heating, elevating the temperature. This oxide layer functions as a lubricant film, inhibiting effective contact between the sliding surfaces, thereby accounting for the absence of a discernible rise in the coefficient of friction during the initial sliding runs. In the context of dry sliding wear scenarios, two mechanisms often occur simultaneously, namely surface work hardening and fracture tendency. During the early stages of sliding, the soft Al surface undergoes work hardening, leading to increased efficiency over extended sliding distances [49]. Subsequent sliding will cause cracks to form and result in surface fracturing once the surface has been work-hardened. This causes fluctuations in the coefficient of friction (COF), which will be lower in cases of work hardening and greater in cases of fracturing. Both the AA 6082 alloy and composites exhibit this characteristic. In some instances, the COF is reported to remain essentially unchanged in relation to the sliding distance, potentially due to the balancing of the

rates of hardening and fracturing. However, significant adhesion between opposing surfaces during seizure requires a greater amount of frictional energy to overcome the bonding, resulting in a dramatic increase in the COF during the seizure.

6.7 SEIZURE PRESSURE

The correlation between the seizure pressure and the corresponding maximum pressure for various composites at as-cast and heat-treated conditions is depicted in the accompanying Figure 6.4 and Figure 6.5 respectively. It is evident that the addition of HEA particles results in a noticeable increase in seizure pressure. The reinforcement content was observed to improve seizure resistance, with 2 wt.% HEA/AA exhibiting a seizure pressure of 0.763 MPa. Further increments in the reinforcement content to 4 wt.% HEA/AA and 6 wt.% HEA/AA led to observed seizure pressures of 1.018 MPa, demonstrating the positive effect of higher thermal stability on the composite. A substantial improvement in seizure resistance was observed for 8 wt.% HEA/AA.

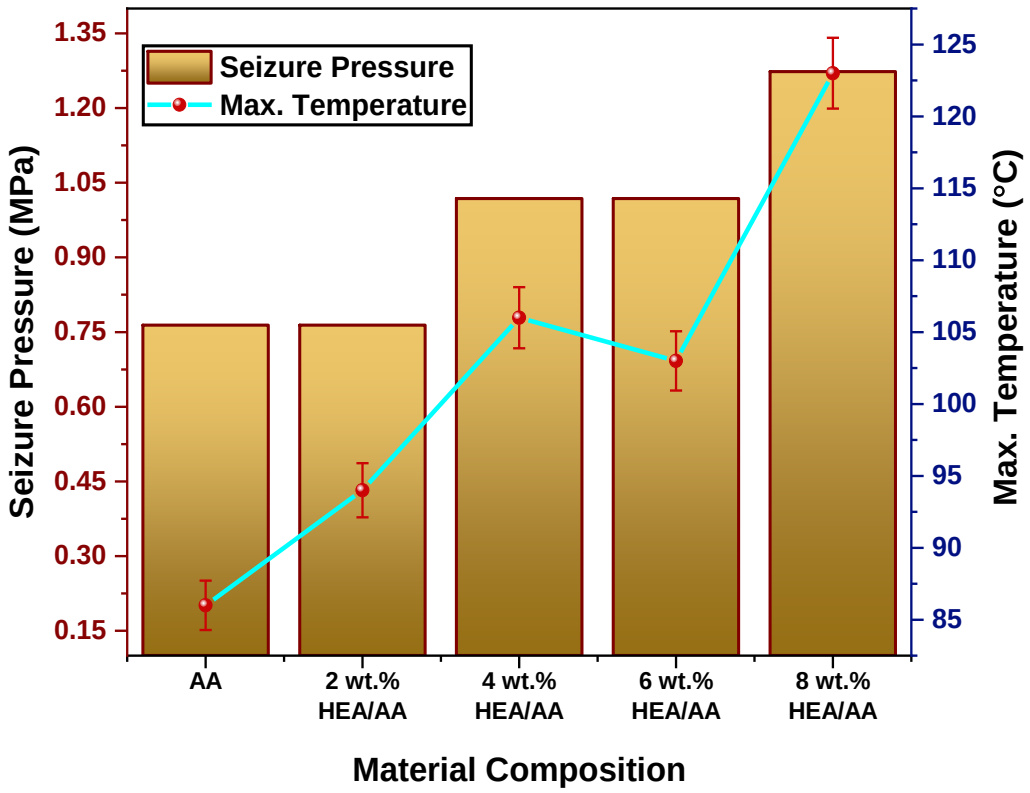

Figure 6.4: variation of seizure pressure and maximum temperature corresponding to different materials (As-cast condition).

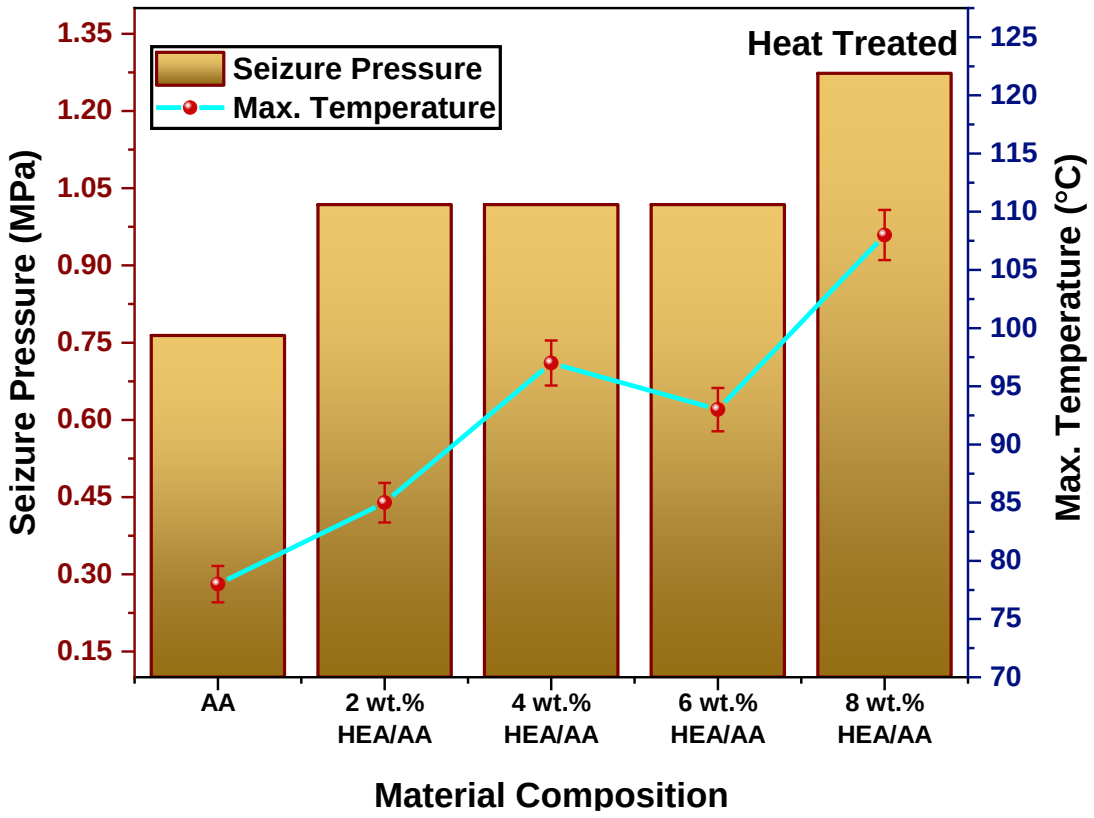

Figure 6.5: variation of seizure pressure and maximum temperature corresponding to different materials at heat-treated conditions.

6.8 WEAR COEFFICIENT

The prediction of the formation of wear debris, which is determined by the wear coefficient, can be quantified utilizing the equation Q = KW/H where Q is wear rate, K is wear coefficient, W is Load (N), and H is hardness. From this equation, the wear coefficient can be determined and plotted against the applied pressure. It is observed that the wear coefficient remains relatively constant and fluctuates within a narrow range at intermediate applied pressure values. This constant value of the wear coefficient indicates that the likelihood of the formation of wear debris remains consistent. It has been established that the wear coefficient (i.e., the probability of wear debris formation) is proportional to the hardness of the materials and

inversely proportional to the applied pressure. When the pressure is elevated, the material becomes more susceptible to deformation, leading to strain hardening of the surface and reducing the possibility of debris formation. Conversely, for harder materials, the tendency towards fracture increases, thus resulting in greater wear debris formation.

CHAPTER – 7

CONCLUSIONS

7.0 SUMMARY AND CONCLUSIONS

In summary, we systematically discussed the successful development of CoCrFeMnNi HEA powder by mechanical alloying and composites subsequently processed through stir squeeze casting. The effect of varying concentrations of HEA addition on microstructure evolution and the mechanical properties of the composites is observed. Some conclusions derived from the investigation are stated below:

1. The OM and FESEM micrograph revealed that fairly enough even dispersion of HEA particles was observed in AMCs. The elemental concentration was confirmed by EDX analysis, whereas the presence of different elements and phases was confirmed by XRD analysis. TEM was used to study the dislocations lattice structure of AMCs along with the morphology of HEA particles.
2. The microstructural characterization confirms that HEA particles are uniformly distributed throughout the Aluminium matrix with no trace of impurity and oxides formation.
3. FESEM micrograph analysis indicated that coarser HEA particles are evenly disseminated in the Al matrix, whereas smaller particles agglomerate and segregate.
4. The wettability of the HEAs particles and the Al matrix is enhanced by the squeezed pressure. In addition, when HEA particles are added to the composites, the density rose to 14.62 % to the AA 6082 base alloy.
5. The addition of HEA particles in the composite showed improved hardness, enhanced ultimate tensile strength, and, better yield strength for 8wt. % HEA/AA composite which is 28.57 %, 79.46 %, and 87.931 % than the AA6082 alloy.
6. The milling duration has a substantial impact on the uniform distribution of HEA particles in the composites, particle size and shape, and composite mechanical behavior. Dynamic equilibrium between fracturing and severe cold welding among the HEA particles is achieved after 42 h of milling time.

7. As per the theoretical prediction, geometrically necessary dislocation strengthening is more dominating followed by the hall petch mechanism, orowan strengthening, and load transfer effect. It is established that when reinforcement concentration increased, the dislocation interaction between the matrix and particles increased monotonically.
8. It should be noted that the HEA particles and improved interface between the HEA particles and Al matrix enable appropriate ductility and strength of the $C_{Al_{6082}+HEA}$ composite. As a result, HEA has been demonstrated to be the best HEA alternative for reinforcement in Al matrix composites.
9. The microstructure of alloy and composites revealed along with α-matrix, intermetallic (α-Al(FeMn)Si, β-Al_5FeSi, and Mg_2Si) also formed which was confirmed by optical microscope images and XRD pattern.
10. Artificial Ageing significantly improved the mechanical properties of alloy and composites and accomplish the best properties for 8 wt.% HEA/AA composite. However, the ductility was impacted negatively.
11. The worn surface morphology and specific wear rate indicate that irrespective of HEA content composite exhibits superior wear resistance properties than the monolithic alloy.
12. The variation of temperature with sliding distance eventually in the same manner as the wear rate for all normal applied pressure.
13. The seizure resistance of 8 wt.% HEA/AA was significantly enhanced over monolithic AA 6082 by 66.86 %. Whereas 8 wt.% HEA exhibit better wear resistance property over as-cast condition and heat-treated condition.
14. The worn surface includes damaged patches, wear debris, and tiny grooves under low normal applied pressure, whereas parallel ridges, surface tearing, and heavily damaged surfaces were observed during the seizure conditions.
15. The composite exhibits a lower wear rate with the inclusion of HEA particles. It was observed that as the normal applied pressure increased up to a certain limit, material loss abruptly increased during the seizure condition.

CHAPTER – 8

FUTURE SCOPE

Based on conclusions drawn from the study following work on CoCrFeMnNi HEA reinforced aluminium metal matrix composite may be performed in the future.

1. More studies on the non-equiatomic CoCrFeMnNi and other elemental compositions can be carried out and derived the result used as the reinforcement in AMCs.
2. A computation study can be carried out to investigate different attributes of HEAs as reinforcement of different characteristics of AMCs.
3. There is more need to study different processing parameters of milling on HEA particle's microstructure and phase evolution and their effect on AMCs.
4. A comparative study can be done on different processing routes and their effect on microstructure, mechanical properties, and tribological behavior.
5. Compression and fatigue behavior can be examined and their mode of failure can be studied in more detail.
6. To investigate high-temperature suitability, an oxidation study can be performed.
7. The corrosion behavior of AMCs can be examined for suitability in environmental conditions.
8. A detailed microstructure study through TEM can be performed for the cause of particle segregation and investigate different diffusion kinetics involved in HEAs.

CHAPTER – 9

PUBLICATIONS

SCI/SCIE PUBLICATIONS

1) Akshay Kumar, Alok Singh, Amit Suhane, mechanically alloyed high entropy alloys: existing challenges and opportunities, **Journal of Materials Research & Technology (JMRT)**, Elsevier, 2022, **(SCIE Q1 IF 6.4, Published)**.
2) Akshay Kumar, Alok Singh, Amit Suhane, Synthesis and characterization of a novel CoCrFeMnNi high-entropy alloy reinforced AA6082 composite, **Journal of Materials Research (JMR)**, Springer, 2022, **(SCIE Q1 IF 3.021, Published)**.
3) Akshay Kumar, Alok Singh, Amit Suhane, A critical review on mechanically alloyed high entropy alloys: processing challenges and properties, Materials Research Express (MRX), IOP, 2022, **(SCIE Q2 IF 2.3, Published)**.
4) Akshay Kumar, Alok Singh, Amit Suhane, Influence of cantor alloy particles on microstructure and wear behavior of Aluminium metal matrix composite, International Journal of MetalCasting, Elsevier, 2023, **(SCIE Q2 IF 2.6, Accepted).**
5) Akshay Kumar, Alok Singh, Amit Suhane, Artificial Age hardening behavior of a squeeze cast CoCrFeMnNi high entropy alloy reinforced 6082-Aluminium metal matrix composite, **Material Characterization**, Elsevier, 2023, **(SCIE Q1 IF 4.7, under review).**

OTHER PUBLICATIONS

6) Akshay Kumar, Alok Singh, Amit Suhane, Effect of Mechanical alloying on High entropy alloys, MMPM Conference, MANIT Bhopal, 2021 **(Published).**
7) Akshay Kumar, Alok Singh, Amit Suhane, Ashish Kumar Singh, Pradip Kumar Verma, Impact Strength of 6082- Aluminium composite reinforced with CoCrFeMnNi HEA particles ICRAM-IIT Jodhpur, Scopus Proceedings, 2022 **(Accepted).**
8) Akshay Kumar, Alok Singh, Amit Suhane, Ashish Kumar Singh, Pradip Kumar Verma, Effect of Process controlling agent on the microstructural evolution of CoCrFeMnNi

High entropy alloy processed through mechanical alloying, IMME 2022, MNNIT Allahabad, Scopus **(Published).**

9) Akshay Kumar, Alok Singh, Amit Suhane, Ashish Kumar Singh, Pradip Kumar Verma, Wear and Corrosion Behavior of High Entropy Alloys, CHEMSMART-22, Materials today proceedings, Elsevier, NIT Rourkela, 2022 **(Published).**

BIBLIOGRAPHY

[1] A. Ramanathan, P. K. Krishnan, and R. Muraliraja, "A review on the production of metal matrix composites through stir casting – Furnace design, properties, challenges, and research opportunities," *J. Manuf. Process.*, vol. 42, no. April, pp. 213–245, 2019, doi: 10.1016/j.jmapro.2019.04.017.

[2] A. Macke, B. F. Schultz, and P. Rohatgi, "Metal matrix: Composites offer the automotive industry an opportunity to reduce vehicle weight, improve performance," *Adv. Mater. Process.*, vol. 170, no. 3, pp. 19–23, 2012.

[3] Y. Liu, R. Asthana, and P. Rohatgi, "A map for wear mechanisms in aluminium alloys," *J. Mater. Sci.*, vol. 26, no. 1, pp. 99–102, 1991, doi: 10.1007/BF00576038.

[4] O. B. Bembalge and S. K. Panigrahi, "Influence of SiC ceramic reinforcement size in establishing wear mechanisms and wear maps of ultrafine grained AA6063 composites," *Ceram. Int.*, vol. 45, no. 16, pp. 20091–20104, 2019, doi: 10.1016/j.ceramint.2019.06.274.

[5] S. Wilson and A. T. Alpas, "Wear mechanism maps for metal matrix composites," *Wear*, vol. 212, no. 1, pp. 41–49, 1997, doi: 10.1016/S0043-1648(97)00142-7.

[6] J. Zhang and A. T. Alpas, "Wear regimes and transitions in Al2O3 particulate-reinforced aluminum alloys," *Mater. Sci. Eng. A*, vol. 161, no. 2, pp. 273–284, 1993, doi: 10.1016/0921-5093(93)90522-G.

[7] J. James and A. Raja Annamalai, "Tribological behaviour and wear fashion of processed AA6061/ZrO2 composite," *Ind. Lubr. Tribol.*, vol. 70, no. 9, pp. 1815–1824, 2018, doi: 10.1108/ILT-12-2017-0382.

[8] M. Ramachandra, A. Abhishek, P. Siddeshwar, and V. Bharathi, "Hardness and Wear Resistance of ZrO2 Nano Particle Reinforced Al Nanocomposites Produced by Powder Metallurgy," *Procedia Mater. Sci.*, vol. 10, no. Cnt 2014, pp. 212–219, 2015,

doi: 10.1016/j.mspro.2015.06.043.

[9] X. Y. Li and K. N. Tandon, “Microstructural characterization of mechanically mixed layer and wear debris in sliding wear of an Al alloy and an Al based composite,” *Wear*, vol. 245, no. 1–2, pp. 148–161, 2000, doi: 10.1016/S0043-1648(00)00475-0.

[10] M. R. Rosenberger, C. E. Schvezov, and E. Forlerer, “Wear of different aluminum matrix composites under conditions that generate a mechanically mixed layer,” *Wear*, vol. 259, no. 1–6, pp. 590–601, 2005, doi: 10.1016/j.wear.2005.02.003.

[11] S. Basavarajappa, G. Chandramohan, A. Mahadevan, M. Thangavelu, R. Subramanian, and P. Gopalakrishnan, “Influence of sliding speed on the dry sliding wear behaviour and the subsurface deformation on hybrid metal matrix composite,” *Wear*, vol. 262, no. 7–8, pp. 1007–1012, 2007, doi: 10.1016/j.wear.2006.10.016.

[12] I. Ganesh and I. Advanced, “Correlation between the characteristics of the mechanically mixed layer and wear behaviour of aluminium , Al-7075 alloy and Al-MMCs and wear behaviour of aluminium , Al-7075 alloy and Al-MMCs,” *Wear*, vol. 245, no. July, pp. 22–38, 2016.

[13] M. Uthayakumar, S. Aravindan, and K. Rajkumar, “Wear performance of Al-SiC-B4C hybrid composites under dry sliding conditions,” *Mater. Des.*, vol. 47, pp. 456–464, 2013, doi: 10.1016/j.matdes.2012.11.059.

[14] Surappa M.K., “Aluminium Matrix Composites: Challenges and Opportunities // Sadhana. Department of Metallurgy, Indian Institute of Science, Bangalore 560 012, India,” *S¯adhan¯a*, vol. 28, no. 1–2, pp. 319–334, 2003.

[15] R. Dasgupta, “Aluminium Alloy-Based Metal Matrix Composites: A Potential Material for Wear Resistant Applications,” *ISRN Metall.*, vol. 2012, pp. 1–14, 2012, doi: 10.5402/2012/594573.

[16] Z. Wen, T. Itoh, T. Uno, M. Kubo, and O. Yamamoto, “Thermal, electrical, and mechanical properties of composite polymer electrolytes based on cross-linked poly(ethylene oxide-co-propylene oxide) and ceramic filler,” *Solid State Ionics*, vol.

160, no. 1–2, pp. 141–148, 2003, doi: 10.1016/S0167-2738(03)00129-2.

[17] J. Zhu *et al.*, “Reinforcing epoxy polymer composites through covalent integration of functionalized nanotubes,” *Adv. Funct. Mater.*, vol. 14, no. 7, pp. 643–648, 2004, doi: 10.1002/adfm.200305162.

[18] A. A. Azeez, K. Y. Rhee, S. J. Park, and D. Hui, “Epoxy clay nanocomposites - Processing, properties and applications: A review,” *Compos. Part B Eng.*, vol. 45, no. 1, pp. 308–320, 2013, doi: 10.1016/j.compositesb.2012.04.012.

[19] H. Ohnabe, S. Masaki, M. Onozuka, K. Miyahara, and T. Sasa, “Potential application of ceramic matrix composites to aero-engine components,” *Compos. Part A Appl. Sci. Manuf.*, vol. 30, no. 4, pp. 489–496, 1999, doi: 10.1016/S1359-835X(98)00139-0.

[20] A. Baradeswaran and A. Elaya Perumal, “Influence of B4C on the tribological and mechanical properties of Al 7075-B4C composites,” *Compos. Part B Eng.*, vol. 54, no. 1, pp. 146–152, 2013, doi: 10.1016/j.compositesb.2013.05.012.

[21] K. Shirvanimoghaddam *et al.*, “Carbon fiber reinforced metal matrix composites: Fabrication processes and properties,” *Compos. Part A Appl. Sci. Manuf.*, vol. 92, pp. 70–96, 2017, doi: 10.1016/j.compositesa.2016.10.032.

[22] A. Mazahery and M. O. Shabani, “Existence of good bonding between coated B4C reinforcement and al matrix via semisolid techniques: Enhancement of wear resistance and mechanical properties,” *Tribol. Trans.*, vol. 56, no. 3, pp. 342–348, 2013, doi: 10.1080/10402004.2012.752552.

[23] T. P. D. Rajan, R. M. Pillai, and B. C. Pai, “Reinforcement coatings and interfaces in aluminium metal matrix composites,” *J. Mater. Sci.*, vol. 33, no. 14, pp. 3491–3503, 1998, doi: 10.1023/A:1004674822751.

[24] M. A. Kashfipour, N. Mehra, and J. Zhu, “A review on the role of interface in mechanical, thermal, and electrical properties of polymer composites,” *Adv. Compos. Hybrid Mater.*, vol. 1, no. 3, pp. 415–439, 2018, doi: 10.1007/s42114-018-0022-9.

[25] J. Zhu, W. Jiang, G. Li, F. Guan, Y. Yu, and Z. Fan, "Microstructure and mechanical properties of SiCnp/Al6082 aluminum matrix composites prepared by squeeze casting combined with stir casting," *J. Mater. Process. Technol.*, vol. 283, no. March, p. 116699, 2020, doi: 10.1016/j.jmatprotec.2020.116699.

[26] R. L. Deuis, C. Subramanian, and J. M. Yellup, "Dry sliding wear of aluminium composites - A review," *Compos. Sci. Technol.*, vol. 57, no. 4, pp. 415–435, 1997, doi: 10.1016/S0266-3538(96)00167-4.

[27] K. Ravikumar, K. Kiran, and V. S. Sreebalaji, "Characterization of mechanical properties of aluminium/tungsten carbide composites," *Meas. J. Int. Meas. Confed.*, vol. 102, pp. 142–149, 2017, doi: 10.1016/j.measurement.2017.01.045.

[28] H. Wan *et al.*, "Fabrication and characterisation of alumina/aluminium composite materials with a nacre-like micro-layered architecture," *Mater. Des.*, vol. 223, 2022, doi: 10.1016/j.matdes.2022.111190.

[29] P. Roy, S. Singh, and K. Pal, "Enhancement of mechanical and tribological properties of SiC- and CB-reinforced aluminium 7075 hybrid composites through friction stir processing," *Adv. Compos. Mater.*, vol. 28, no. sup1, pp. 1–18, 2019, doi: 10.1080/09243046.2017.1405596.

[30] S. Scudino, G. Liu, M. Sakaliyska, K. B. Surreddi, and J. Eckert, "Powder metallurgy of Al-based metal matrix composites reinforced with β-Al3Mg2 intermetallic particles: Analysis and modeling of mechanical properties," *Acta Mater.*, vol. 57, no. 15, pp. 4529–4538, 2009, doi: 10.1016/j.actamat.2009.06.017.

[31] Z. Wang *et al.*, "Tensile properties of Al – 12Si matrix composites reinforced with Ti – Al-based particles," *J. Alloys Compd.*, vol. 630, pp. 256–259, 2015, doi: 10.1016/j.jallcom.2014.12.254.

[32] J. W. Yeh *et al.*, "Nanostructured high-entropy alloys with multiple principal elements: Novel alloy design concepts and outcomes," *Adv. Eng. Mater.*, vol. 6, no. 5, pp. 299–303, 2004, doi: 10.1002/adem.200300567.

[33] B. Cantor, I. T. H. Chang, P. Knight, and A. J. B. Vincent, “Microstructural development in equiatomic multicomponent alloys,” *Mater. Sci. Eng. A*, vol. 375–377, no. 1-2 SPEC. ISS., pp. 213–218, 2004, doi: 10.1016/j.msea.2003.10.257.

[34] J. W. Yeh, “Alloy design strategies and future trends in high-entropy alloys,” *Jom*, vol. 65, no. 12, pp. 1759–1771, 2013, doi: 10.1007/s11837-013-0761-6.

[35] S. Varalakshmi, G. Appa Rao, M. Kamaraj, and B. S. Murty, “Hot consolidation and mechanical properties of nanocrystalline equiatomic AlFeTiCrZnCu high entropy alloy after mechanical alloying,” *J. Mater. Sci.*, vol. 45, no. 19, pp. 5158–5163, 2010, doi: 10.1007/s10853-010-4246-5.

[36] Y. Wu, P. K. Liaw, and Y. Zhang, “Preparation of bulk tizrnbmov and nbtialtav high-entropy alloys by powder sintering,” *Metals (Basel).*, vol. 11, no. 11, pp. 1–12, 2021, doi: 10.3390/met11111748.

[37] S. Varalakshmi, M. Kamaraj, and B. S. Murty, “Synthesis and characterization of nanocrystalline AlFeTiCrZnCu high entropy solid solution by mechanical alloying,” *J. Alloys Compd.*, vol. 460, no. 1–2, pp. 253–257, 2008, doi: 10.1016/j.jallcom.2007.05.104.

[38] G. S. Firstov, T. A. Kosorukova, Y. N. Koval, and V. V Odnosum, “High entropy shape memory alloys,” *Mater. Today Proc.*, vol. 2, pp. S499–S503, 2015, doi: 10.1016/j.matpr.2015.07.335.

[39] H. Cheng, X. Liu, Q. Tang, W. Wang, X. Yan, and P. Dai, “Microstructure and mechanical properties of FeCoCrNiMnAlx high-entropy alloys prepared by mechanical alloying and hot-pressed sintering,” *J. Alloys Compd.*, vol. 775, pp. 742–751, 2019, doi: 10.1016/j.jallcom.2018.10.168.

[40] J. T. Liang, K. C. Cheng, and S. H. Chen, “Effect of heat treatment on the phase evolution and mechanical properties of atomized AlCoCrFeNi high-entropy alloy powders,” *J. Alloys Compd.*, vol. 803, pp. 484–490, 2019, doi: 10.1016/j.jallcom.2019.06.301.

[41] S. Praveen, B. S. Murty, and R. S. Kottada, “Effect of molybdenum and niobium on the phase formation and hardness of nanocrystalline CoCrFeNi high entropy alloys,” *J. Nanosci. Nanotechnol.*, vol. 14, no. 10, pp. 8106–8109, 2014, doi: 10.1166/jnn.2014.9441.

[42] L. Shaw, M. Zawrah, J. Villegas, H. Luo, and D. Miracle, “Effects of process-control agents on mechanical alloying of nanostructured aluminum alloys,” *Metall. Mater. Trans. A Phys. Metall. Mater. Sci.*, vol. 34, no. 1, pp. 159–170, 2003, doi: 10.1007/s11661-003-0217-7.

[43] A. Kumar, A. Singh, and A. Suhane, “Mechanically alloyed high entropy alloys: existing challenges and opportunities,” *J. Mater. Res. Technol.*, vol. 17, pp. 2431–2456, 2022, doi: 10.1016/j.jmrt.2022.01.141.

[44] L. Tian, M. Fu, and W. Xiong, “materials Microstructural Evolution of AlCoCrFeNiSi High-Entropy Alloy Powder during Mechanical Alloying and Its Coating Performance,” 2018, doi: 10.3390/ma11020320.

[45] X. Du, T. Gao, Z. Qian, Y. Wu, and X. Liu, “The in-situ synthesis and strengthening mechanism of the multi-scale SiC particles in Al-Si-C alloys,” *J. Alloys Compd.*, vol. 750, pp. 935–944, 2018, doi: 10.1016/j.jallcom.2018.04.006.

[46] X. Xie *et al.*, “Synthesis of carbon nanotube reinforced Al matrix composite coatings via cold spray deposition,” *Surf. Coatings Technol.*, vol. 405, no. October 2020, p. 126676, 2021, doi: 10.1016/j.surfcoat.2020.126676.

[47] P. Garg, A. Jamwal, D. Kumar, K. K. Sadasivuni, C. M. Hussain, and P. Gupta, “Advance research progresses in aluminium matrix composites: manufacturing & applications,” *J. Mater. Res. Technol.*, vol. 8, no. 5, pp. 4924–4939, 2019, doi: 10.1016/j.jmrt.2019.06.028.

[48] M. B. N. Shaikh, S. Arif, T. Aziz, A. Waseem, M. A. N. Shaikh, and M. Ali, “Microstructural, mechanical and tribological behaviour of powder metallurgy processed SiC and RHA reinforced Al-based composites,” *Surfaces and Interfaces*,

vol. 15, no. March, pp. 166–179, 2019, doi: 10.1016/j.surfin.2019.03.002.

[49] A. K. Singh, S. Soni, and R. S. Rana, “Mechanical and sliding wear behavior of stir-squeeze cast and T6 heat-treated AA7068-ZrO2p composite,” *Compos. Interfaces*, vol. 00, no. 00, pp. 1–27, 2022, doi: 10.1080/09276440.2022.2120736.

[50] K. Sekar, K. Allesu, and M. A. Joseph, “Mechanical and Wear Properties of Al–Al2O3 Metal Matrix Composites Fabricated by the Combined Effect of Stir and Squeeze Casting Method,” *Trans. Indian Inst. Met.*, vol. 68, no. 2, pp. 115–121, 2015, doi: 10.1007/s12666-015-0520-1.

[51] E. Ananiadis, K. T. Argyris, T. E. Matikas, A. K. Sfikas, and A. E. Karantzalis, “Microstructure and corrosion performance of aluminium matrix composites reinforced with refractory high-entropy alloy particulates,” *Appl. Sci.*, vol. 11, no. 3, pp. 1–12, 2021, doi: 10.3390/app11031300.

[52] H. Yu *et al.*, “Microstructural evolution, mechanical and physical properties of graphene reinforced aluminum composites fabricated via powder metallurgy,” *Mater. Sci. Eng. A*, vol. 802, no. September 2020, 2021, doi: 10.1016/j.msea.2020.140669.

[53] K. Nithesh, M. C. Gowrishankar, R. Nayak, and S. Sharma, “Effect of light weight reinforcement and heat treatment process parameters on morphological and wear aspects of hypoeutectic Al-Si based composites - a critical review,” *J. Mater. Res. Technol.*, vol. 15, pp. 4272–4292, 2021, doi: 10.1016/j.jmrt.2021.10.019.

[54] B. Dutta and M. K. Surappa, “Age - hardening behaviour of Al-Cu-SiCp composites synthesized by casting route,” *Scr. Metall. Mater.*, vol. 32, no. 5, pp. 731–736, 1995, doi: 10.1016/0956-716X(95)91594-F.

[55] H. Kurita, T. Miyazaki, A. Kawasaki, Y. Lu, and J. F. Silvain, “Interfacial microstructure of graphite flake reinforced aluminum matrix composites fabricated via hot pressing,” *Compos. Part A Appl. Sci. Manuf.*, vol. 73, pp. 125–131, 2015, doi: 10.1016/j.compositesa.2015.03.013.

[56] S. Z. Zhu, D. Wang, B. L. Xiao, and Z. Y. Ma, “Effects of natural aging on

precipitation behavior and hardening ability of peak artificially aged SiCp/Al-Mg-Si composites," *Compos. Part B Eng.*, vol. 236, no. October 2021, 2022, doi: 10.1016/j.compositesb.2022.109851.

[57] R. P.-B. Et.al., "The effect of heat treatment on microstructure evolution in artificially aged carbon nanotube/Al2024 composite synthesized by mechanical alloying." Elsevier, pp. 28–34, 2017.

[58] A. R. Prabhukhot, "Effect of Heat Treatment on Hardness and Corrosion Behavior of 6082-T6 Aluminium Alloy in Artificial Sea Water," *Rev. Matéria*, vol. 3, no. 4, pp. 544–549, 2015, doi: 10.17706/ijmse.2015.3.4.287-294.

[59] H. Z. Ye and X. Y. Liu, "Review of recent studies in magnesium matrix composites," *J. Mater. Sci.*, vol. 39, no. 20, pp. 6153–6171, 2004, doi: 10.1023/b:jmsc.0000043583.47148.31.

[60] S. N. Alam and H. Singh, "Development of copper-based metal matrix composites : An analysis by SEM , EDS and XRD," *Microsc. Anal.*, vol. 28, no. 4, pp. S8–S13, 2014, [Online]. Available: https://www.researchgate.net/publication/271707140_metal_matrix_COMPOSITES_S8_Development_of_copper-based_metal_matrix_composites_An_analysis_by_SEM_EDS_and_XRD.

[61] B. Vijaya Ramnath, C. Elanchezhian, M. Jaivignesh, S. Rajesh, C. Parswajinan, and A. Siddique Ahmed Ghias, "Evaluation of mechanical properties of aluminium alloy-alumina-boron carbide metal matrix composites," *Mater. Des.*, vol. 58, pp. 332–338, 2014, doi: 10.1016/j.matdes.2014.01.068.

[62] K. Kondoh, H. Oginuma, J. Umeda, and T. Umeda, "Innovative reuse of agricultural wastes as industrial raw materials to form magnesium composites," *Mater. Trans.*, vol. 46, no. 12, pp. 2586–2591, 2005, doi: 10.2320/matertrans.46.2586.

[63] V. S. Aigbodion and S. B. Hassan, "Experimental correlations between wear rate and wear parameter of Al-Cu-Mg/bagasse ash particulate composite," *Mater. Des.*, vol. 31,

no. 4, pp. 2177–2180, 2010, doi: 10.1016/j.matdes.2009.10.055.

[64] M. K. Akbari, H. R. Baharvandi, and O. Mirzaee, “Nano-sized aluminum oxide reinforced commercial casting A356 alloy matrix: Evaluation of hardness, wear resistance and compressive strength focusing on particle distribution in aluminum matrix,” *Compos. Part B Eng.*, vol. 52, pp. 262–268, 2013, doi: 10.1016/j.compositesb.2013.04.038.

[65] N. Srivastava and G. P. Chaudhari, “Strengthening in Al alloy nano composites fabricated by ultrasound assisted solidification technique,” *Mater. Sci. Eng. A*, vol. 651, pp. 241–247, 2016, doi: 10.1016/j.msea.2015.10.118.

[66] W. Zhang, Y. Hu, G. Zhang, and Z. Wang, “Formation of nanoscale metallic glassy particle reinforced al-based composite powders by high-energy milling,” *Metals (Basel).*, vol. 7, no. 10, pp. 21–23, 2017, doi: 10.3390/met7100425.

[67] Z. Wang, S. Scudino, M. Stoica, W. Zhang, and J. Eckert, “Al-based matrix composites reinforced with short Fe-based metallic glassy fiber,” *J. Alloys Compd.*, vol. 651, pp. 170–175, 2015, doi: 10.1016/j.jallcom.2015.08.098.

[68] M. S. Xie *et al.*, “Abnormal hot deformation behavior in a metallic-glass-reinforced Al-7075 composite,” *Mater. Sci. Eng. A*, vol. 785, no. February, pp. 4–9, 2020, doi: 10.1016/j.msea.2020.139212.

[69] S. Scudino *et al.*, “Mechanical properties of Al-based metal matrix composites reinforced with Zr-based glassy particles produced by powder metallurgy,” *Acta Mater.*, vol. 57, no. 6, pp. 2029–2039, 2009, doi: 10.1016/j.actamat.2009.01.010.

[70] Z. Wang *et al.*, “Mechanical behavior of Al-based matrix composites reinforced with Mg 58Cu28.5Gd11Ag2.5 metallic glasses,” *Adv. Powder Technol.*, vol. 25, no. 2, pp. 635–639, 2014, doi: 10.1016/j.apt.2013.10.005.

[71] T. Lu *et al.*, “The influence of nanocrystalline CoNiFeAl0.4Ti0.6Cr0.5 high-entropy alloy particles addition on microstructure and mechanical properties of SiCp/7075Al composites,” *Mater. Sci. Eng. A*, vol. 726, no. December 2017, pp. 126–136, 2018,

doi: 10.1016/j.msea.2018.04.080.

[72] Z. Wang *et al.*, "Tensile properties of Al-12Si matrix composites reinforced with Ti-Al-based particles," *J. Alloys Compd.*, vol. 630, pp. 256–259, 2015, doi: 10.1016/j.jallcom.2014.12.254.

[73] R. Zheng, H. Yang, T. Liu, K. Ameyama, and C. Ma, "Microstructure and mechanical properties of aluminum alloy matrix composites reinforced with Fe-based metallic glass particles," *Mater. Des.*, vol. 53, no. 2014, pp. 512–518, 2014, doi: 10.1016/j.matdes.2013.07.048.

[74] M. S. Xie, Z. Wang, G. Q. Zhang, C. Yang, W. W. Zhang, and K. G. Prashanth, "Microstructure and mechanical property of bimodal-size metallic glass particle-reinforced Al alloy matrix composites," *J. Alloys Compd.*, vol. 814, p. 152317, 2020, doi: 10.1016/j.jallcom.2019.152317.

[75] M. Yuan, D. C. Zhang, C. G. Tan, Z. C. Luo, Y. F. Mao, and J. G. Lin, "Microstructure and properties of Al-based metal matrix composites reinforced by Al60Cu20Ti15Zr5 glassy particles by high pressure hot pressing consolidation," *Mater. Sci. Eng. A*, vol. 590, pp. 301–306, 2014, doi: 10.1016/j.msea.2013.10.049.

[76] A. S. Edelstein, J. S. Murday, and B. B. Rath, "Challenges in nanomaterials design," *Prog. Mater. Sci.*, vol. 42, no. 1–4, pp. 5–21, 1997, doi: 10.1016/s0079-6425(97)00005-4.

[77] J. Ding, H. Xu, X. Li, M. Liu, and T. Zhang, "The similarity of elements in multi-principle element alloys based on a new criterion for phase constitution," *Mater. Des.*, vol. 207, p. 109849, 2021, doi: 10.1016/j.matdes.2021.109849.

[78] J. Joseph *et al.*, "Computational design of thermally stable and precipitation-hardened Al-Co-Cr-Fe-Ni-Ti high entropy alloys," *J. Alloys Compd.*, p. 161496, 2021, doi: 10.1016/j.jallcom.2021.161496.

[79] X. Wang, Y. Ma, B. Meng, and M. Wan, "Effect of equal-channel angular pressing on microstructural evolution, mechanical property and biodegradability of an ultrafine-

grained zinc alloy," *Mater. Sci. Eng. A*, vol. 824, no. August, p. 141857, 2021, doi: 10.1016/j.msea.2021.141857.

[80] A. Kumar and V. Parashar, "Investigation of Reinforcement Content, Load and Sliding Speed on the Tribological behaviour of Copper based Silicon Carbide Composite using Design of Experiments," *Indian J. Sci. Technol.*, vol. 9, no. 45, 2016, doi: 10.17485/ijst/2016/v9i45/94574.

[81] A. K. Singh, S. Soni, and R. S. Rana, " Microstructure evolution, mechanical behavior, and fracture analysis of ultrasonic-assisted stir-squeeze cast high strength AA7068/ZrO 2p /Gr p composite under thermal aging ," *Part. Sci. Technol.*, vol. 0, no. 0, pp. 1–20, 2021, doi: 10.1080/02726351.2021.1958398.

[82] C. N. C. Hitam, M. A. A. Aziz, A. H. Ruhaimi, and M. R. Taib, "Magnesium-based alloys for solid-state hydrogen storage applications: A review," *Int. J. Hydrogen Energy*, no. xxxx, 2021, doi: 10.1016/j.ijhydene.2021.03.153.

[83] H. Bai *et al.*, "A review on wear-resistant coating with high hardness and high toughness on the surface of titanium alloy," *J. Alloys Compd.*, vol. 882, p. 160645, 2021, doi: 10.1016/j.jallcom.2021.160645.

[84] A. D. Contla-Pacheco, M. Keddam, L. Lartundo-Rojas, M. Ortega-Avilés, I. Mejía-Caballero, and I. Campos-Silva, "Application of the Heat Balance Integral Method to the growth kinetics of nickel boride layers on an Inconel 718 superalloy," *Surf. Coatings Technol.*, vol. 420, no. May, 2021, doi: 10.1016/j.surfcoat.2021.127355.

[85] D. B. Miracle and O. N. Senkov, "A critical review of high entropy alloys and related concepts," *Acta Mater.*, vol. 122, pp. 448–511, 2017, doi: 10.1016/j.actamat.2016.08.081.

[86] L. S. Zhang, G. L. Ma, L. C. Fu, and J. Y. Tian, "Recent progress in high-entropy alloys," *Adv. Mater. Res.*, vol. 631–632, pp. 227–232, 2013, doi: 10.4028/www.scientific.net/AMR.631-632.227.

[87] Q. Tian, G. Zhang, K. Yin, W. Wang, W. Cheng, and Y. Wang, "The strengthening

effects of relatively lightweight AlCoCrFeNi high entropy alloy," *Mater. Charact.*, vol. 151, no. December 2018, pp. 302–309, 2019, doi: 10.1016/j.matchar.2019.03.006.

[88] M.A. Hemphill, T. Yuan, G.Y. Wang, J.W. Yeh, C.W. Tsai, A. Chuang, P.K. Liaw, "Fatigue behavior of Al 0.5CoCrCuFeNi high entropy alloys," *Acta Mater.*, vol. 60, no. 16, pp. 5723–5734, 2012, doi: 10.1016/j.actamat.2012.06.046.

[89] Bharat Gwalani, Sindhura Gangireddy, Shivakant Shukla, Christopher J. Yannetta, Sheena Grace Valentin, Rajiv S. Mishra, Rajarshi Banerjee, "Compositionally graded high entropy alloy with a strong front and ductile back," *Mater. Today Commun.*, vol. 20, no. March, p. 100602, 2019, doi: 10.1016/j.mtcomm.2019.100602.

[90] A. Ferrari and F. Körmann, "Surface segregation in Cr-Mn-Fe-Co-Ni high entropy alloys," *Appl. Surf. Sci.*, vol. 533, no. June, p. 147471, 2020, doi: 10.1016/j.apsusc.2020.147471.

[91] Y. Wang, Y. Yang, H. Yang, M. Zhang, and J. Qiao, "Effect of nitriding on the tribological properties of Al1.3CoCuFeNi2 high-entropy alloy," *J. Alloys Compd.*, vol. 725, pp. 365–372, 2017, doi: 10.1016/j.jallcom.2017.07.132.

[92] G. B. V. Kumar, C. S. P. Rao, N. Selvaraj, and M. S. Bhagyashekar, "Studies on Al6061-SiC and Al7075-Al₂O₃ Metal Matrix Composites," *J. Miner. Mater. Charact. Eng.*, vol. 09, no. 01, pp. 43–55, 2010, doi: 10.4236/jmmce.2010.91004.

[93] K. Li and W. Chen, "Recent progress in high-entropy alloys for catalysts: synthesis, applications, and prospects," *Mater. Today Energy*, vol. 20, 2021, doi: 10.1016/j.mtener.2021.100638.

[94] Q. F. He, Z. Y. Ding, Y. F. Ye, and Y. Yang, "Design of High-Entropy Alloy: A Perspective from Nonideal Mixing," *Jom*, vol. 69, no. 11, pp. 2092–2098, 2017, doi: 10.1007/s11837-017-2452-1.

[95] B. Cantor, I. T. H. Chang, P. Knight, and A. J. B. Vincent, "Microstructural development in equiatomic multicomponent alloys," *Mater. Sci. Eng. A*, vol. 375–377,

no. 1-2 SPEC. ISS., pp. 213–218, 2004, doi: 10.1016/j.msea.2003.10.257.

[96] A. L. Greer, J. H. Perepezko, F. Franks, B. Cantor, and R. W. Cahn, "Grain refinement of alloys by inoculation of melts," *Philos. Trans. R. Soc. A Math. Phys. Eng. Sci.*, vol. 361, no. 1804, pp. 479–495, 2003, doi: 10.1098/rsta.2002.1147.

[97] N. J. Peter *et al.*, "Early stage phase separation of AlCoCr0.75Cu0.5FeNi high-entropy powder at the nanoscale," *J. Alloys Compd.*, vol. 820, 2020, doi: 10.1016/j.jallcom.2019.153149.

[98] B. Gludovatz, E. P. George, and R. O. Ritchie, "Processing, Microstructure and Mechanical Properties of the CrMnFeCoNi High-Entropy Alloy," *Jom*, vol. 67, no. 10, pp. 2262–2270, 2015, doi: 10.1007/s11837-015-1589-z.

[99] M. Vaidya, A. Prasad, A. Parakh, and B. S. Murty, "Influence of sequence of elemental addition on phase evolution in nanocrystalline AlCoCrFeNi: Novel approach to alloy synthesis using mechanical alloying," *Mater. Des.*, vol. 126, no. January, pp. 37–46, 2017, doi: 10.1016/j.matdes.2017.04.027.

[100] D. B. Miracle, J. D. Miller, O. N. Senkov, C. Woodward, M. D. Uchic, and J. Tiley, "Exploration and development of high entropy alloys for structural applications," *Entropy*, vol. 16, no. 1, pp. 494–525, 2014, doi: 10.3390/e16010494.

[101] B. L. Musicó *et al.*, "The emergent field of high entropy oxides: Design, prospects, challenges, and opportunities for tailoring material properties," *APL Mater.*, vol. 8, no. 4, pp. 1–16, 2020, doi: 10.1063/5.0003149.

[102] M. H. Tsai and J. W. Yeh, "High-entropy alloys: A critical review," *Mater. Res. Lett.*, vol. 2, no. 3, pp. 107–123, 2014, doi: 10.1080/21663831.2014.912690.

[103] Y. Song, D. Kim, S. Nam, K. A. Lee, and H. Choi, "Effect of milling duration on oxide-formation behavior of oxide-dispersion-strengthened high-entropy alloys," *Arch. Metall. Mater.*, vol. 66, no. 3, pp. 735–740, 2021, doi: 10.24425/amm.2021.136371.

[104] M. Eisenforschung, A. Ludwig, and A. Savan, “Combinatorial metallurgical synthesis and processing of high-entropy alloys,” pp. 1–14, 2018, doi: 10.1557/jmr.2018.214.

[105] E. P. George, W. A. Curtin, and C. C. Tasan, “High entropy alloys: A focused review of mechanical properties and deformation mechanisms,” *Acta Mater.*, vol. 188, pp. 435–474, 2020, doi: 10.1016/j.actamat.2019.12.015.

[106] E. J. Pickering and N. G. Jones, “High-entropy alloys: a critical assessment of their founding principles and future prospects,” *Int. Mater. Rev.*, vol. 61, no. 3, pp. 183–202, 2016, doi: 10.1080/09506608.2016.1180020.

[107] M. C. Gao, P. K. Liaw, J. W. Yeh, and Y. Zhang, *High-entropy alloys: Fundamentals and applications*. 2016.

[108] S. Praveen and H. S. Kim, “High-Entropy Alloys: Potential Candidates for High-Temperature Applications – An Overview,” *Adv. Eng. Mater.*, vol. 20, no. 1, pp. 1–22, 2018, doi: 10.1002/adem.201700645.

[109] Q. L. Xu, Y. Zhang, S. H. Liu, C. J. Li, and C. X. Li, “High-temperature oxidation behavior of CuAlNiCrFe high-entropy alloy bond coats deposited using high-speed laser cladding process,” *Surf. Coatings Technol.*, vol. 398, p. 126093, 2020, doi: 10.1016/j.surfcoat.2020.126093.

[110] Hyun Seok Oh, Duancheng Ma, Gerard Paul Leyson, Blazej Grabowski, Eun Soo Park 1, Fritz Körmann, and Dierk Raabe, “Lattice distortions in the FeCoNiCrMn high entropy alloy studied by theory and experiment,” *Entropy*, vol. 18, no. 9, pp. 1–9, 2016, doi: 10.3390/e18090321.

[111] Z. Wang, J. Li, Q. H. Fang, B. Liu, and L. Zhang, “Investigation into nanoscratching mechanical response of AlCrCuFeNi high-entropy alloys using atomic simulations,” *Appl. Surf. Sci.*, vol. 416, pp. 470–481, 2017, doi: 10.1016/j.apsusc.2017.04.009.

[112] S. Ranganathan, “Alloyed pleasures: Multimetallic cocktails,” *Curr. Sci.*, vol. 85, no. 10, pp. 1404–1406, 2003.

[113] B. S. Murty, S. Ranganathan, J. W. Yeh, and P. P. Bhattacharjee, *High-entropy alloys*. 2019.

[114] B. E. MacDonald, Z. Fu, B. Zheng, W. Chen, Y. Lin, F. Chen, L. Zhang, J. Ivanisenko, Y. Zhou, H. Hahn & E. J. Lavernia., "Recent Progress in High Entropy Alloy Research," *Jom*, vol. 69, no. 10, pp. 2024–2031, 2017, doi: 10.1007/s11837-017-2484-6.

[115] Q. Wei, Q. Shen, J. Zhang, B. Chen, G. Luo, and L. Zhang, "Microstructure and mechanical property of a novel ReMoTaW high-entropy alloy with high density," *Int. J. Refract. Met. Hard Mater.*, vol. 77, no. May, pp. 8–11, 2018, doi: 10.1016/j.ijrmhm.2018.05.006.

[116] Y. Fan, Y. Zhang, H. Guan, H. Suo, and L. He, "AlNiCrFexMo0.2CoCu high entropy alloys prepared by powder metallurgy," *Xiyou Jinshu Cailiao Yu Gongcheng/Rare Met. Mater. Eng.*, vol. 42, no. 6, pp. 1127–1129, 2013, doi: 10.1016/s1875-5372(13)60074-0.

[117] P. Veronesi, R. Rosa, E. Colombini, and C. Leonelli, "Microwave-Assisted Preparation of High Entropy Alloys," *Technologies*, vol. 3, no. 4, pp. 182–197, 2015, doi: 10.3390/technologies3040182.

[118] X. W. Qiu, C. X. Huang, M. J. Wu, C. G. Liu, and Y. P. Zhang, "Structure and properties of AlCrFeNiCuTi six principal elements equimolar alloy," *J. Alloys Compd.*, vol. 658, pp. 1–5, 2016, doi: 10.1016/j.jallcom.2015.10.224.

[119] E. Colombini, R. Rosa, L. Trombi, M. Zadra, A. Casagrande, and P. Veronesi, "High entropy alloys obtained by field assisted powder metallurgy route: SPS and microwave heating," *Mater. Chem. Phys.*, vol. 210, pp. 78–86, 2018, doi: 10.1016/j.matchemphys.2017.06.065.

[120] A. Zhang, J. Han, J. Meng, B. Su, and P. Li, "Rapid preparation of AlCoCrFeNi high entropy alloy by spark plasma sintering from elemental powder mixture," *Mater. Lett.*, vol. 181, pp. 82–85, 2016, doi: 10.1016/j.matlet.2016.06.014.

[121] P. Veronesi, E. Colombini, R. Rosa, C. Leonelli, and M. Garuti, "Microwave

processing of high entropy alloys: A powder metallurgy approach," *Chem. Eng. Process. Process Intensif.*, vol. 122, no. 2016, pp. 397–403, 2017, doi: 10.1016/j.cep.2017.02.016.

[122] E. Holmström *et al.*, "High entropy alloys: Substituting for cobalt in cutting edge technology," *Appl. Mater. Today*, vol. 12, pp. 322–329, 2018, doi: 10.1016/j.apmt.2018.07.001.

[123] O. A. Waseem, J. Lee, H. M. Lee, and H. J. Ryu, "The effect of Ti on the sintering and mechanical properties of refractory high-entropy alloy TixWTaVCr fabricated via spark plasma sintering for fusion plasma-facing materials," *Mater. Chem. Phys.*, vol. 210, pp. 87–94, 2018, doi: 10.1016/j.matchemphys.2017.06.054.

[124] K. V Yusenko *et al.*, "High-pressure high-temperature tailoring of High Entropy Alloys for extreme environments," *J. Alloys Compd.*, vol. 738, pp. 491–500, 2018, doi: 10.1016/j.jallcom.2017.12.216.

[125] S. Zhou *et al.*, "High entropy alloy: A promising matrix for high-performance tungsten heavy alloys," *J. Alloys Compd.*, vol. 777, pp. 1184–1190, 2019, doi: 10.1016/j.jallcom.2018.11.089.

[126] U. Anselmi-tamburini, "The effect of electric field and pressure on the synthesis and consolidation of materials : A review of the spark plasma sintering method," no. May, 2014, doi: 10.1007/s10853-006-6555-2.

[127] G. Zhu, Y. Liu, and J. Ye, "Early high-temperature oxidation behavior of Ti(C,N)-based cermets with multi-component AlCoCrFeNi high-entropy alloy binder Gang," *Int. J. ofRefractory Met. Hard Mater.*, 2014, doi: 10.1016/j.ijrmhm.2014.01.005.

[128] C. Real and J. M. C, "Fabrication and characterization of WC-HEA cemented carbide based on the CoCrFeNiMn high entropy alloy," vol. 746, pp. 1–8, 2018, doi: 10.1016/j.jallcom.2018.02.292.

[129] Y. Liu, J. Chen, Z. Li, X. Wang, X. Fan, and J. Liu, "Formation of transition layer and its effect on mechanical properties of AlCoCrFeNi high-entropy alloy/Al composites,"

J. Alloys Compd., vol. 780, pp. 558–564, 2019, doi: 10.1016/j.jallcom.2018.11.364.

[130] C. C. Koch, "Nanocrystalline high-entropy alloys," *J. Mater. Res.*, vol. 32, no. 18, pp. 3435–3444, 2017, doi: 10.1557/jmr.2017.341.

[131] A. S. Sharma, S. Yadav, K. Biswas, and B. Basu, "High-entropy alloys and metallic nanocomposites: Processing challenges, microstructure development and property enhancement," *Mater. Sci. Eng. R Reports*, vol. 131, no. June, pp. 1–42, 2018, doi: 10.1016/j.mser.2018.04.003.

[132] M. Vaidya, G. M. Muralikrishna, and B. S. Murty, "High-entropy alloys by mechanical alloying: A review," *J. Mater. Res.*, vol. 34, no. 5, pp. 664–686, 2019, doi: 10.1557/jmr.2019.37.

[133] C. Suryanarayana and E. Ivanov, "Mechanical alloying for advanced materials," *Mater. Sci. Technol. 2003 Meet.*, pp. 169–178, 2003, doi: 10.1002/9781118984239.ch17.

[134] J. J. Suñol, "Mechanical alloying: Processing and materials," *Metals (Basel).*, vol. 11, no. 5, pp. 10–12, 2021, doi: 10.3390/met11050798.

[135] P. S. Gilman and J. S. Benjamin, "Mechanical alloying," *J. Japan Inst. Light Met.*, vol. 40, no. 11, pp. 850–855, 1990, doi: 10.2464/jilm.40.850.

[136] C. Suryanarayana, "Mechanical Alloying: A Novel Technique to Synthesize Advanced Materials," *Research*, vol. 2019, pp. 1–17, 2019, doi: 10.34133/2019/4219812.

[137] C. Suryanarayana and N. Al-aqeeli, "Progress in Materials Science Mechanically alloyed nanocomposites," *Prog. Mater. Sci.*, vol. 58, no. 4, pp. 383–502, 2013, doi: 10.1016/j.pmatsci.2012.10.001.

[138] B. S. Murty, S. Ranganathan, B. S. Murty, and S. Ranganathan, "Novel materials synthesis by mechanical alloying / milling Novel materials synthesis by mechanical alloying / milling," vol. 6608, 2013, doi: 10.1179/imr.1998.43.3.101.

[139] B. Zhang, Y. Duan, Y. Cui, G. Ma, T. Wang, and X. Dong, "A new mechanism for improving electromagnetic properties based on tunable crystallographic structures of FeCoNiSi x Al 0.4 high entropy alloy powders †," 2018, doi: 10.1039/c8ra01762j.

[140] Y. Tong, P. Qi, X. Liang, Y. Chen, Y. Hu, and Z. Hu, "Different-shaped ultrafine MoNbTaW HEA powders prepared via mechanical alloying," *Materials (Basel).*, vol. 10, no. 7, pp. 1–8, 2018, doi: 10.3390/ma11071250.

[141] V. Shivam, J. Basu, Y. Shadangi, M. K. Singh, and N. K. Mukhopadhyay, "Mechano-chemical synthesis , thermal stability and phase evolution in AlCoCrFeNiMn high entropy alloy," *J. Alloys Compd.*, vol. 757, pp. 87–97, 2018, doi: 10.1016/j.jallcom.2018.05.057.

[142] S. Lesz and and K. G. , Bartłomiej Hrapkowicz, Małgorzata Karolus, "Characteristics of the Mg-Zn-Ca-Gd Alloy after Mechanical Alloying," pp. 1–14, 2021.

[143] M. Amini *et al.*, "First-time synthesis of an unparalleled Al72Cr15Ni13 decagonal quasicrystalline phase with the help of mechanical alloying and annealing procedures: A comparative study," *Powder Technol.*, vol. 389, pp. 243–258, 2021, doi: 10.1016/j.powtec.2021.05.026.

[144] W. He *et al.*, "Bimodal-grained high-strength nickel-base ODS alloy fabricated by mechanical alloying and hot extrusion," *Mater. Today Commun.*, vol. 26, no. December 2020, p. 101921, 2021, doi: 10.1016/j.mtcomm.2020.101921.

[145] M. Prashanth, R. Karunanithi, S. RasoolMohideen, and S. Sivasankaran, "A comprehensive exploration on the development of nano Y2O3 dispersed in AA 7017 by mechanical alloying and hot-pressing technique," *Ceram. Int.*, vol. 47, no. 16, pp. 22924–22938, 2021, doi: 10.1016/j.ceramint.2021.05.006.

[146] B. Hrapkowicz, S. Lesz, M. Kremzer, M. Karolus, and W. Pakieła, "Mechanical alloying of Mg-Zn-Ca-Er alloy," vol. XX, pp. 1–7, 2021, doi: 10.24425/bpasts.2021.DOI.

[147] H. R. Ammar, S. Sivasankaran, and A. S. Alaboodi, "Investigation of the

microstructure and compressibility of biodegradable fe-mn-cu/w/co nanostructured alloy powders synthesized by mechanical alloying," *Materials (Basel).*, vol. 14, no. 11, 2021, doi: 10.3390/ma14113088.

[148] V. Shivam, Y. Shadangi, J. Basu, and N. K. Mukhopadhyay, "Evolution of phases, hardness and magnetic properties of AlCoCrFeNi high entropy alloy processed by mechanical alloying," *J. Alloys Compd.*, vol. 832, p. 154826, 2020, doi: 10.1016/j.jallcom.2020.154826.

[149] S. Praveen, B. S. Murty, and R. S. Kottada, "Phase Evolution and Densification Behavior of Nanocrystalline Multicomponent High Entropy Alloys During Spark Plasma Sintering," vol. 65, no. 12, pp. 1797–1804, 2013, doi: 10.1007/s11837-013-0759-0.

[150] M. D. Alcalá, C. Real, I. Fombella, I. Trigo, and J. M. Córdoba, "Effects of milling time, sintering temperature, Al content on the chemical nature, microhardness and microstructure of mechanochemically synthesized FeCoNiCrMn high entropy alloy," *J. Alloys Compd.*, 2018, doi: 10.1016/j.jallcom.2018.03.358.

[151] R. Zhao, B. Ren, G. Zhang, Z. Liu, and J. Zhang, "Effect of Co content on the phase transition and magnetic properties of Co x CrCuFeMnNi high-entropy alloy powders," *J. Magn. Magn. Mater.*, 2018, doi: 10.1016/j.jmmm.2018.07.072.

[152] P. Wang, X. Cheng, H. Cai, Y. Xue, and Y. Zhang, "Author ' s Accepted Manuscript," *Mater. Sci. Eng. A*, pp. 0–55, 2017, doi: 10.1016/j.msea.2017.09.119.

[153] A. Raza, B. Kang, J. Lee, H. J. Ryu, and S. H. Hong, "PT CR," *Mater. Des.*, p. #pagerange#, 2018, doi: 10.1016/j.matdes.2018.02.036.

[154] S. Yadav, A. Kumar, and K. Biswas, "Wear behaviour of high entropy alloys containing soft dispersoids (Pb, Bi)," *Mater. Chem. Phys.*, vol. 822, p. 153642, 2017, doi: 10.1016/j.matchemphys.2017.06.020.

[155] L. Tian, M. Fu, and W. Xiong, "Microstructural evolution of AlCoCrFeNiSi high-entropy alloy powder during mechanical alloying and its coating performance,"

Materials (Basel)., vol. 11, no. 2, 2018, doi: 10.3390/ma11020320.

[156] W. Wang *et al.*, "Alloying Behavior and Properties of - FeSiBAlNiCo x High Entropy Alloys Fabricated by Mechanical Alloying and Spark Plasma Sintering," *Met. Mater. Int.*, vol. 24, no. 5, pp. 1099–1106, 2018, doi: 10.1007/s12540-018-0047-1.

[157] S. Praveen, B. S. Murty, and R. S. Kottada, "Alloying behavior in multi-component AlCoCrCuFe and NiCoCrCuFe high entropy alloys," *Mater. Sci. Eng. A*, vol. 534, pp. 83–89, 2012, doi: 10.1016/j.msea.2011.11.044.

[158] B. Zhang, Y. Duan, Y. Cui, G. Ma, T. Wang, and X. Dong, "A new mechanism for improving electromagnetic properties based on tunable crystallographic powders †," *RSC Adv.*, vol. 8, pp. 14936–14946, 2018, doi: 10.1039/C8RA01762J.

[159] M. Murali *et al.*, "Processing and characterisation of nano crystalline AlCoCrCuFeTi x high-entropy alloy," *Powder Metall.*, vol. 0, no. 0, pp. 1–10, 2018, doi: 10.1080/00325899.2018.1438230.

[160] T. Lu *et al.*, "Materials Science & Engineering A particles addition on microstructure and mechanical properties of SiC p / 7075Al composites," vol. 726, no. April, pp. 126–136, 2018, doi: 10.1016/j.msea.2018.04.080.

[161] I. Moravcik *et al.*, "Microstructure and mechanical properties of Ni1,5Co1,5CrFeTi0,5 high entropy alloy fabricated by mechanical alloying and spark plasma sintering," *Mater. Des.*, vol. 119, pp. 141–150, 2017, doi: 10.1016/j.matdes.2017.01.036.

[162] H. Cheng, W. Chen, X. Liu, Q. Tang, Y. Xie, and P. Dai, "Effect of Ti and C additions on the microstructure and mechanical properties of the FeCoCrNiMn high-entropy alloy," *Mater. Sci. Eng. A*, vol. 719, no. January, pp. 192–198, 2018, doi: 10.1016/j.msea.2018.02.040.

[163] R. K. Mishra and R. R. Shahi, "Phase evolution and magnetic characteristics of TiFeNiCr and TiFeNiCrM (M = Mn, Co) high entropy alloys," *J. Magn. Magn. Mater.*, vol. 442, pp. 218–223, 2017, doi: 10.1016/j.jmmm.2017.06.124.

[164] C. D. Gómez-Esparza, F. Baldenebro-López, L. González-Rodelas, J. Baldenebro-López, and R. Martínez-Sánchez, "Series of nanocrystalline NiCoAlFe(Cr, Cu, Mo, Ti) high-entropy alloys produced by mechanical alloying," *Mater. Res.*, vol. 19, pp. 39–46, 2016, doi: 10.1590/1980-5373-MR-2015-0668.

[165] W. Ge *et al.*, "Characterization and properties of CuZrAlTiNi high entropy alloy coating obtained by mechanical alloying and vacuum hot pressing sintering," *Adv. Powder Technol.*, vol. 28, no. 10, pp. 2556–2563, 2017, doi: 10.1016/j.apt.2017.07.006.

[166] D. Oleszak, A. Antolak-Dudka, and T. Kulik, "High entropy multicomponent WMoNbZrV alloy processed by mechanical alloying," *Mater. Lett.*, vol. 232, pp. 160–162, 2018, doi: 10.1016/j.matlet.2018.08.060.

[167] G. M. Karthik, S. Panikar, G. D. J. Ram, and R. S. Kottada, "Additive manufacturing of an aluminum matrix composite reinforced with nanocrystalline high-entropy alloy particles," *Mater. Sci. Eng. A*, vol. 679, pp. 193–203, 2017, doi: 10.1016/j.msea.2016.10.038.

[168] S. Nam, M. J. Kim, J. Y. Hwang, and H. Choi, "Strengthening of Al0.15CoCrCuFeNiTix–C (x = 0, 1, 2) high-entropy alloys by grain refinement and using nanoscale carbides via powder metallurgical route," *J. Alloys Compd.*, vol. 762, pp. 29–37, 2018, doi: 10.1016/j.jallcom.2018.05.180.

[169] B. Kang, J. Lee, H. J. Ryu, and S. H. Hong, "Microstructure, mechanical property and Hall-Petch relationship of a light-weight refractory Al0.1CrNbVMo high entropy alloy fabricated by powder metallurgical process," *J. Alloys Compd.*, vol. 767, pp. 1012–1021, 2018, doi: 10.1016/j.jallcom.2018.07.145.

[170] C. Sun, P. Li, S. Xi, Y. Zhou, S. Li, and X. Yang, "A new type of high entropy alloy composite Fe18Ni23Co25Cr21Mo8WNb3C2 prepared by mechanical alloying and hot pressing sintering," *Mater. Sci. Eng. A*, vol. 728, no. May, pp. 144–150, 2018, doi: 10.1016/j.msea.2018.05.022.

[171] Y. Long, K. Su, J. Zhang, X. Liang, H. Peng, and X. Li, "Enhanced strength of a mechanical alloyed NbMoTaWVTi refractory high entropy alloy," *Materials (Basel).*, vol. 11, no. 5, pp. 1–8, 2018, doi: 10.3390/ma11050669.

[172] S. H. Joo *et al.*, "Structure and properties of ultrafine-grained CoCrFeMnNi high-entropy alloys produced by mechanical alloying and spark plasma sintering," *J. Alloys Compd.*, vol. 698, pp. 591–604, 2017, doi: 10.1016/j.jallcom.2016.12.010.

[173] F. Alijani, M. Reihanian, and K. Gheisari, "Study on phase formation in magnetic FeCoNiMnV high entropy alloy produced by mechanical alloying," *J. Alloys Compd.*, vol. 773, pp. 623–630, 2019, doi: 10.1016/j.jallcom.2018.09.204.

[174] A. I. Yurkova, V. V. Cherniavsky, V. Bolbut, M. Krüger, and I. Bogomol, "Structure formation and mechanical properties of the high-entropy AlCuNiFeCr alloy prepared by mechanical alloying and spark plasma sintering," *J. Alloys Compd.*, vol. 786, pp. 139–148, 2019, doi: 10.1016/j.jallcom.2019.01.341.

[175] H. CHENG, Y. chong XIE, Q. hua TANG, C. RAO, and P. qiang DAI, "Microstructure and mechanical properties of FeCoCrNiMn high-entropy alloy produced by mechanical alloying and vacuum hot pressing sintering," *Trans. Nonferrous Met. Soc. China (English Ed.*, vol. 28, no. 7, pp. 1360–1367, 2018, doi: 10.1016/S1003-6326(18)64774-0.

[176] P. Ajay Kumar and C. S. Perugu, "Synthesis of fecrvnbmn high entropy alloy by mechanical alloying and study of their microstructure and mechanical properties," *Miner. Met. Mater. Ser.*, vol. Part F12, pp. 669–675, 2018, doi: 10.1007/978-3-319-72526-0_63.

[177] G. Wang *et al.*, "Synthesis and thermal stability of a nanocrystalline MoNbTaTiV refractory high-entropy alloy via mechanical alloying," *Int. J. Refract. Met. Hard Mater.*, vol. 84, no. June, 2019, doi: 10.1016/j.ijrmhm.2019.104988.

[178] S. Das and P. S. Robi, "Mechanical Alloying of W-Mo-V-Cr-Ta High Entropy Alloys," *IOP Conf. Ser. Mater. Sci. Eng.*, vol. 346, no. 1, 2018, doi: 10.1088/1757-

899X/346/1/012047.

[179] Y. Sun *et al.*, "Phases, microstructures and mechanical properties of CoCrNiCuZn high-entropy alloy prepared by mechanical alloying and spark plasma sintering," *Entropy*, vol. 21, no. 2, 2019, doi: 10.3390/e21020122.

[180] A. Kumar, A. K. Swarnakar, and M. Chopkar, "Phase Evolution and Mechanical Properties of AlCoCrFeNiSix High-Entropy Alloys Synthesized by Mechanical Alloying and Spark Plasma Sintering," *J. Mater. Eng. Perform.*, vol. 27, no. 7, pp. 3304–3314, 2018, doi: 10.1007/s11665-018-3409-4.

[181] E. Abbasi and K. Dehghani, "Phase prediction and microstructure of centrifugally cast non-equiatomic Co-Cr-Fe-Mn-Ni(Nb,C) high entropy alloys," *J. Alloys Compd.*, vol. 783, pp. 292–299, 2019, doi: 10.1016/j.jallcom.2018.12.329.

[182] Y. Zhang *et al.*, "Microstructures and properties of high-entropy alloys," *Prog. Mater. Sci.*, vol. 61, no. October 2013, pp. 1–93, 2014, doi: 10.1016/j.pmatsci.2013.10.001.

[183] A. Takeuchi, K. Amiya, T. Wada, K. Yubuta, and W. Zhang, "High-Entropy Alloys with a Hexagonal Close-Packed Structure Designed by Equi-Atomic Alloy Strategy and Binary Phase Diagrams," *Jom*, vol. 66, no. 10, pp. 1984–1992, 2014, doi: 10.1007/s11837-014-1085-x.

[184] Y. Zhang *et al.*, "Guidelines in predicting phase formation of high-entropy alloys," *MRS Commun.*, vol. 4, no. 2, pp. 57–62, 2014, doi: 10.1557/mrc.2014.11.

[185] B. Chanda and J. Das, " Composition Dependence on the Evolution of Nanoeutectic in CoCrFeNiNb x ($0.45 \leq x \leq 0.65$) High Entropy Alloys ," *Adv. Eng. Mater.*, vol. 20, no. 4, p. 1700908, 2018, doi: 10.1002/adem.201700908.

[186] X. Yang, S. Y. Chen, J. D. Cotton, and Y. Zhang, "Phase Stability of Low-Density, Multiprincipal Component Alloys Containing Aluminum, Magnesium, and Lithium," *Jom*, vol. 66, no. 10, pp. 2009–2020, 2014, doi: 10.1007/s11837-014-1059-z.

[187] A. C. H. Y. Chen, C. W. Tsai, C. C. Tung, J. W. Yeh, T. T. Shun, C. C. Yang, and S.

K. Chen, “No Title,” *Sci. Mater.*, vol. 31, p. 360, 2006.

[188] C. Li, J. C. Li, M. Zhao, and Q. Jiang, “Effect of alloying elements on microstructure and properties of multiprincipal elements high-entropy alloys,” *J. Alloys Compd.*, vol. 475, no. 1–2, pp. 752–757, 2009, doi: 10.1016/j.jallcom.2008.07.124.

[189] Y. J. Zhou, Y. Zhang, Y. L. Wang, and G. L. Chen, “Solid solution alloys of AlCoCrFeNi Tix with excellent room-temperature mechanical properties,” *Appl. Phys. Lett.*, vol. 90, no. 18, 2007, doi: 10.1063/1.2734517.

[190] P. Li, A. Wang, and C. T. Liu, “Composition dependence of structure, physical and mechanical properties of FeCoNi(MnAl)x high entropy alloys,” *Intermetallics*, vol. 87, no. April, pp. 21–26, 2017, doi: 10.1016/j.intermet.2017.04.007.

[191] P. C. Chen *et al.*, “Interface and heterostructure design in polyelemental nanoparticles,” *Science (80-.).*, vol. 363, no. 6430, pp. 959–964, 2019, doi: 10.1126/science.aav4302.

[192] P.-C. Chen *et al.*, “Polyelemental nanoparticle libraries,” *Nanoscale*, vol. 352, no. 6293, pp. 0–5, 2015.

[193] Y. Yao *et al.*, “Carbothermal shock synthesis of high-entropy-alloy nanoparticles,” *Science (80-.).*, vol. 359, no. 6383, pp. 1489–1494, 2018, doi: 10.1126/science.aan5412.

[194] L. J. Santodonato *et al.*, “Deviation from high-entropy configurations in the atomic distributions of a multi-principal-element alloy,” *Nat. Commun.*, vol. 6, 2015, doi: 10.1038/ncomms6964.

[195] M. W. Glasscott, S. Voci, P. J. Kauffmann, A. I. Chapoval, and J. E. Dick, “Mapping Solvent Entrapment in Multiphase Systems by Electrogenerated Chemiluminescence,” *Langmuir*, vol. 37, no. 9, pp. 2907–2912, 2021, doi: 10.1021/acs.langmuir.0c03445.

[196] Y. Shi, B. Yang, X. Xie, J. Brechtl, K. A. Dahmen, and P. K. Liaw, “Corrosion of Al xCoCrFeNi high-entropy alloys: Al-content and potential scan-rate dependent pitting

behavior," *Corros. Sci.*, vol. 119, pp. 33–45, 2017, doi: 10.1016/j.corsci.2017.02.019.

[197] X. Huang, J. Miao, and A. A. Luo, "Lightweight AlCrTiV high-entropy alloys with dual-phase microstructure via microalloying," *J. Mater. Sci.*, vol. 54, no. 3, pp. 2271–2277, 2019, doi: 10.1007/s10853-018-2970-4.

[198] F. G. Coury, M. Kaufman, and A. J. Clarke, "Solid-solution strengthening in refractory high entropy alloys," *Acta Mater.*, vol. 175, pp. 66–81, 2019, doi: 10.1016/j.actamat.2019.06.006.

[199] H. Wu, S. Huang, C. Zhu, H. Zhu, and Z. Xie, "Influence of Cr content on the microstructure and mechanical properties of CrxFeNiCu high entropy alloys," *Prog. Nat. Sci. Mater. Int.*, vol. 30, no. 2, pp. 239–245, 2020, doi: 10.1016/j.pnsc.2020.01.012.

[200] K. M. Youssef, A. J. Zaddach, C. Niu, D. L. Irving, and C. C. Koch, "A novel low-density, high-hardness, high-entropy alloy with close-packed single-phase nanocrystalline structures," *Mater. Res. Lett.*, vol. 3, no. 2, pp. 95–99, 2014, doi: 10.1080/21663831.2014.985855.

[201] M. Feuerbacher, T. Lienig, and C. Thomas, "A single-phase bcc high-entropy alloy in the refractory Zr-Nb-Ti-V-Hf system," *Scr. Mater.*, vol. 152, pp. 40–43, 2018, doi: 10.1016/j.scriptamat.2018.04.009.

[202] W. Lu, C. H. Liebscher, G. Dehm, D. Raabe, and Z. Li, "Bidirectional Transformation Enables Hierarchical Nanolaminate Dual-Phase High-Entropy Alloys," *Adv. Mater.*, vol. 30, no. 44, pp. 1–10, 2018, doi: 10.1002/adma.201804727.

[203] M. J. Yao, K. G. Pradeep, C. C. Tasan, and D. Raabe, "A novel, single phase, non-equiatomic FeMnNiCoCr high-entropy alloy with exceptional phase stability and tensile ductility," *Scr. Mater.*, vol. 72–73, pp. 5–8, 2014, doi: 10.1016/j.scriptamat.2013.09.030.

[204] S. Huang *et al.*, "Mechanism of magnetic transition in FeCrCoNi-based high entropy alloys," *Mater. Des.*, vol. 103, pp. 71–74, 2016, doi: 10.1016/j.matdes.2016.04.053.

[205] N. Nayan *et al.*, "Hot deformation behaviour and microstructure control in AlCrCuNiFeCo high entropy alloy," *Intermetallics*, vol. 55, pp. 145–153, 2014, doi: 10.1016/j.intermet.2014.07.019.

[206] W. R. Wang, W. L. Wang, S. C. Wang, Y. C. Tsai, C. H. Lai, and J. W. Yeh, "Effects of Al addition on the microstructure and mechanical property of Al xCoCrFeNi high-entropy alloys," *Intermetallics*, vol. 26, no. December 2017, pp. 44–51, 2012, doi: 10.1016/j.intermet.2012.03.005.

[207] C. J. Tong *et al.*, "Mechanical performance of the AlxCoCrCuFeNi high-entropy alloy system with multiprincipal elements," *Metall. Mater. Trans. A Phys. Metall. Mater. Sci.*, vol. 36, no. 5, pp. 1263–1271, 2005, doi: 10.1007/s11661-005-0218-9.

[208] M. Zakeri, M. Ramezani, A. Nazari, Y. R. Club, S. Branch, and S. Branch, "Effect of Ball to Powder Weight Ratio on the Mechanochemical Synthesis of MoSi 2 -TiC Nanocomposite Powder," vol. 15, no. 6, pp. 891–897, 2012, doi: 10.1590/S1516-14392012005000111.

[209] M. Polanski, J. Bystrzycki, P. Kuziora, and M. Wyszy, "Why the ball to powder ratio (BPR) is insufficient for describing the mechanical ball milling process," vol. 9, pp. 1–5, 2014, doi: 10.1016/j.ijhydene.2014.03.009.

[210] C. Real and F. J. Gotor, "Effects of the speed ratio on the e fficiency of planetary mills," no. October 2018, pp. 1–14, 2019, doi: 10.1016/j.heliyon.2019.e01227.

[211] C. A. Manea *et al.*, "Hfnbtatizr high entropy alloy processed by mechanical alloying," *UPB Sci. Bull. Ser. B Chem. Mater. Sci.*, vol. 81, no. 3, pp. 201–208, 2019.

[212] M. Semen'Ko, R. Ostapenko, and P. Teselko, "Synthesis and characterization of nanocrystalline CrFeCoNi alloy by high energetic mechanical alloying," *Proc. 2017 IEEE 7th Int. Conf. Nanomater. Appl. Prop. N. 2017*, vol. 2017-Janua, pp. 7–10, 2017, doi: 10.1109/NAP.2017.8190394.

[213] F. Salemi, M. H. Abbasi, and F. Karimzadeh, "Synthesis and thermodynamic analysis of nanostructured CuNiCoZnAl high entropy alloy produced by mechanical alloying,"

J. Alloys Compd., vol. 685, pp. 278–286, 2016, doi: 10.1016/j.jallcom.2016.05.274.

[214] X. R. Tan, G. P. Zhang, Q. Zhi, and Z. X. Liu, "Effects of milling on the microstructure and hardness of Al2NbTi3V2Zr high-entropy alloy," *Mater. Des.*, vol. 109, pp. 27–36, 2016, doi: 10.1016/j.matdes.2016.07.066.

[215] A. Fourmont *et al.*, "Effects of planetary ball milling on AlCoCrFeNi high entropy alloys prepared by Spark Plasma Sintering : Experiments and molecular dynamics study To cite this version : HAL Id : hal-02995067 Effects of Planetary Ball Milling on AlCoCrFeNi High Entropy All," 2020.

[216] P. Akhlaghi, M. Amirjan, and N. Parvin, "The effect of processing parameters and heat-treatment on the microstructure and mechanical properties of PM CoCrFeMnNiTi 0 . 1 high-entropy alloy," *Mater. Chem. Phys.*, vol. 257, no. September 2020, p. 123722, 2021, doi: 10.1016/j.matchemphys.2020.123722.

[217] K. R. Cardoso, S. Izaias, and L. D. S. Vieira, "Mechanical alloying and spark plasma sintering of AlCrCuFeZn high entropy alloy," 2020, doi: 10.1080/02670836.2020.1839195.

[218] F. J. Baldenebro-Lopez, J. M. Herrera-Ramírez, S. P. Arredondo-Rea, C. D. Gómez-Esparza, and R. Martínez-Sánchez, "Simultaneous effect of mechanical alloying and arc-melting processes in the microstructure and hardness of an AlCoFeMoNiTi high-entropy alloy," *J. Alloys Compd.*, vol. 643, no. S1, pp. S250–S255, 2015, doi: 10.1016/j.jallcom.2014.12.059.

[219] A. Parakh, M. Vaidya, N. Kumar, R. Chetty, and B. S. Murty, "Effect of crystal structure and grain size on corrosion properties of AlCoCrFeNi high entropy alloy," *J. Alloys Compd.*, vol. 863, p. 158056, 2021, doi: 10.1016/j.jallcom.2020.158056.

[220] L. Guirong *et al.*, "Effects of boron on microstructure and properties of microwave sintered FeCoNi1.5CuY0.2 high-entropy alloy," *J. Alloys Compd.*, vol. 866, p. 157848, 2021, doi: 10.1016/j.jallcom.2020.157848.

[221] A. Fourmont, S. Le Gallet, O. Politano, C. Desgranges, and F. Baras, "Effects of

planetary ball milling on AlCoCrFeNi high entropy alloys prepared by Spark Plasma Sintering: Experiments and molecular dynamics study," *J. Alloys Compd.*, vol. 820, p. 153448, 2020, doi: 10.1016/j.jallcom.2019.153448.

[222] Y. Geng *et al.*, "Microstructure, mechanical and vacuum high temperature tribological properties of AlCoCrFeNi high entropy alloy based solid-lubricating composites," *Tribol. Int.*, vol. 151, no. March, p. 106444, 2020, doi: 10.1016/j.triboint.2020.106444.

[223] Y. Duan, X. Wen, B. Zhang, G. Ma, and T. Wang, "Optimizing the electromagnetic properties of the FeCoNiAlCrx high entropy alloy powders by composition adjustment and annealing treatment," *J. Magn. Magn. Mater.*, vol. 497, no. July 2019, p. 165947, 2020, doi: 10.1016/j.jmmm.2019.165947.

[224] C. Suryanarayana, "Mechanical alloying and milling," *Prog. Mater. Sci.*, vol. 46, no. 1–2, pp. 1–184, 2001, doi: 10.1016/S0079-6425(99)00010-9.

[225] M. A. Ruiz-Esparza-Rodríguez *et al.*, "Influence of process control agent and Al concentration on synthesis and phase stability of a mechanically alloyed AlxCoCrFeMnNi high-entropy alloy," *J. Alloys Compd.*, vol. 882, 2021, doi: 10.1016/j.jallcom.2021.160770.

[226] W. Lee and S. I. Kwun, "The effects of process control agents on mechanical alloying mechanisms in the Ti-Al system," *J. Alloys Compd.*, vol. 6, no. 96, pp. 193–199, 1996.

[227] L. Lu and Y. F. Zhang, "Influence of process control agent on interdiffusion between Al and Mg during mechanical alloying," vol. 290, pp. 279–283, 1999.

[228] R. Ju, J. J. Su, R. Berlanga, J. Bonastre, and L. Escoda, "The effects of process control agents on mechanical alloying behavior of a Fe – Zr based alloy," vol. 435, pp. 472–476, 2007, doi: 10.1016/j.jallcom.2006.08.108.

[229] S. Yadav, A. Kumar, and K. Biswas, "Wear behavior of high entropy alloys containing soft dispersoids (Pb , Bi)," *Mater. Chem. Phys.*, vol. 210, pp. 222–232, 2018, doi: 10.1016/j.matchemphys.2017.06.020.

[230] G. Jin *et al.*, "Applied Surface Science High temperature wear performance of laser-cladded FeNiCoAlCu high- entropy alloy coating," *Appl. Surf. Sci.*, vol. 445, pp. 113–122, 2018, doi: 10.1016/j.apsusc.2018.03.135.

[231] B. Li, B. Qian, Y. Xu, Z. Liu, and F. Xuan, "Fine-structured CoCrFeNiMn high-entropy alloy matrix composite with 12 wt % TiN particle reinforcements via selective laser melting assisted additive manufacturing," vol. 252, pp. 88–91, 2019, doi: 10.1016/j.matlet.2019.05.108.

[232] H. E. A. D. Composite, "Effect of Binding and Dispersion Behavior of High-Entropy Alloy (HEA) Powders on the Microstructure and Mechanical Properties in a Novel," 2018, doi: 10.3390/e20120924.

[233] Y. Long, J. Che, Z. Wu, H. T. Lin, and F. Zhang, "High entropy alloy borides prepared by powder metallurgy process and the enhanced fracture toughness by addition of yttrium," *Mater. Chem. Phys.*, vol. 257, no. June 2020, p. 123715, 2021, doi: 10.1016/j.matchemphys.2020.123715.

[234] J. Wang, T. Guo, J. Li, W. Jia, and H. Kou, "Microstructure and mechanical properties of non-equilibrium solidified CoCrFeNi high entropy alloy," *Mater. Chem. Phys.*, vol. 210, pp. 192–196, 2018, doi: 10.1016/j.matchemphys.2017.06.037.

[235] S. Mohanty *et al.*, "Powder metallurgical processing of equiatomic AlCoCrFeNi high entropy alloy: Microstructure and mechanical properties," *Mater. Sci. Eng. A*, vol. 679, no. July 2016, pp. 299–313, 2017, doi: 10.1016/j.msea.2016.09.062.

[236] J. M. Zhu, H. M. Fu, H. F. Zhang, A. M. Wang, H. Li, and Z. Q. Hu, "Microstructures and compressive properties of multicomponent AlCoCrFeNiMox alloys," *Mater. Sci. Eng. A*, vol. 527, no. 26, pp. 6975–6979, 2010, doi: 10.1016/j.msea.2010.07.028.

[237] B. Kang, J. Lee, H. J. Ryu, and S. H. Hong, "Ultra-high strength WNbMoTaV high-entropy alloys with fine grain structure fabricated by powder metallurgical process," *Mater. Sci. Eng. A*, vol. 712, no. September 2017, pp. 616–624, 2018, doi: 10.1016/j.msea.2017.12.021.

[238] Z. Fu *et al.*, “Microstructure and mechanical behavior of a novel Co20Ni20Fe20Al20Ti20 alloy fabricated by mechanical alloying and spark plasma sintering,” *Mater. Sci. Eng. A*, vol. 644, pp. 10–16, 2015, doi: 10.1016/j.msea.2015.07.052.

[239] I. Moravcik *et al.*, “Synergic strengthening by oxide and coherent precipitate dispersions in high-entropy alloy prepared by powder metallurgy,” *Scr. Mater.*, vol. 157, pp. 24–29, 2018, doi: 10.1016/j.scriptamat.2018.07.034.

[240] Z. Fu *et al.*, “Microstructure and strengthening mechanisms in an FCC structured single-phase nanocrystalline Co25Ni25Fe25Al7.5Cu17.5 high-entropy alloy,” *Acta Mater.*, vol. 107, pp. 59–71, 2016, doi: 10.1016/j.actamat.2016.01.050.

[241] Y. Liu, J. Wang, Q. Fang, B. Liu, Y. Wu, and S. Chen, “Intermetallics Preparation of super fi ne-grained high entropy alloy by spark plasma sintering gas atomized powder,” *Intermetallics*, vol. 68, pp. 16–22, 2016, doi: 10.1016/j.intermet.2015.08.012.

[242] Ł. Rogal, D. Kalita, A. Tarasek, P. Bobrowski, and F. Czerwinski, “Effect of SiC nano-particles on microstructure and mechanical properties of the CoCrFeMnNi high entropy alloy,” *J. Alloys Compd.*, vol. 708, pp. 344–352, 2017, doi: 10.1016/j.jallcom.2017.02.274.

[243] W. Ji *et al.*, “Mechanical alloying synthesis and spark plasma sintering consolidation of CoCrFeNiAl high-entropy alloy,” *J. Alloys Compd.*, vol. 589, pp. 61–66, 2014, doi: 10.1016/j.jallcom.2013.11.146.

[244] Q. C. Fan, B. S. Li, and Y. Zhang, “The microstructure and properties of (FeCrNiCo)AlxCuy high-entropy alloys and their TiC-reinforced composites,” *Mater. Sci. Eng. A*, vol. 598, pp. 244–250, 2014, doi: 10.1016/j.msea.2014.01.044.

[245] C. Tsai, M. Tsai, J. Yeh, and C. Yang, “Effect of temperature on mechanical properties of Al 0 . 5 CoCrCuFeNi wrought alloy,” vol. 490, pp. 160–165, 2010, doi: 10.1016/j.jallcom.2009.10.088.

[246] J. Hou, M. Zhang, S. Ma, P. K. Liaw, Y. Zhang, and J. Qiao, "Materials Science & Engineering A Strengthening in Al 0 . 25 CoCrFeNi high-entropy alloys by cold rolling," *Mater. Sci. Eng. A*, vol. 707, no. September, pp. 593–601, 2017, doi: 10.1016/j.msea.2017.09.089.

[247] W. Chen, Z. Fu, S. Fang, H. Xiao, and D. Zhu, "Alloying behavior, microstructure and mechanical properties in a FeNiCrCo0.3Al0.7 high entropy alloy," *Mater. Des.*, vol. 51, pp. 854–860, 2013, doi: 10.1016/j.matdes.2013.04.061.

[248] Y. P. Wang, B. S. Li, M. X. Ren, C. Yang, and H. Z. Fu, "Microstructure and compressive properties of AlCrFeCoNi high entropy alloy," *Mater. Sci. Eng. A*, vol. 491, no. 1–2, pp. 154–158, 2008, doi: 10.1016/j.msea.2008.01.064.

[249] Bin Liu, Jingshi Wang, Yong Liu, Qihong Fang, Yuan Wu, Shiqi Chen, C.T. Liu, "Intermetallics Microstructure and mechanical properties of equimolar FeCoCrNi high entropy alloy prepared via powder extrusion," *Intermetallics*, vol. 75, pp. 25–30, 2016, doi: 10.1016/j.intermet.2016.05.006.

[250] Weiping Chen, Zixuan Li, Tiwen Lu, Tianbing He, Ruikai Li, Bing Li, Bingbing Wan, Zhiqiang Fu, Sergio Scudino, "Effect of ball milling on microstructure and mechanical properties of 6061Al matrix composites reinforced with high-entropy alloy particles," *Mater. Sci. Eng. A*, vol. 762, no. July, p. 138116, 2019, doi: 10.1016/j.msea.2019.138116.

[251] J. Y. Ko and S. I. Hong, "Microstructural evolution and mechanical performance of carbon-containing CoCrFeMnNi-C high entropy alloys," *J. Alloys Compd.*, vol. 743, pp. 115–125, 2018, doi: 10.1016/j.jallcom.2018.01.348.

[252] Y. X. Zhuang, X. L. Zhang, and X. Y. Gu, "Effect of molybdenum on phases , microstructure and mechanical properties of Al 0 . 5 CoCrFeMo x Ni high entropy alloys," vol. 743, pp. 514–522, 2018, doi: 10.1016/j.jallcom.2018.02.003.

[253] "Effects of milling time, sintering temperature, Al content on the chemical nature, microhardness and microstructure of mechanochemically synthesized FeCoNiCrMn

high entropy alloy - ScienceDirect.” https://www.sciencedirect.com/science/article/abs/pii/S0925838818312350 (accessed Jun. 12, 2021).

[254] J. Pan, T. Dai, T. Lu, X. Ni, J. Dai, and M. Li, “Microstructure and mechanical properties of Nb25Mo25Ta25W25 and Ti8Nb23Mo23Ta23W23 high entropy alloys prepared by mechanical alloying and spark plasma sintering,” *Mater. Sci. Eng. A*, vol. 738, no. September, pp. 362–366, 2018, doi: 10.1016/j.msea.2018.09.089.

[255] M. J. R. Haché, C. Cheng, and Y. Zou, “Nanostructured high-entropy materials,” *J. Mater. Res.*, vol. 35, no. 8, pp. 1051–1075, 2020, doi: 10.1557/jmr.2020.33.

[256] L. Gao, W. Liao, H. Zhang, J. U. Surjadi, D. Sun, and Y. Lu, “Microstructure, mechanical and corrosion behaviors of CoCrFeNiAl 0.3 High Entropy Alloy (HEA) films,” *Coatings*, vol. 7, no. 10, pp. 1–7, 2017, doi: 10.3390/coatings7100156.

[257] C. Dang, J. U. Surjadi, L. Gao, and Y. Lu, “Mechanical properties of nanostructured CoCrFeNiMn high-entropy alloy (HEA) coating,” *Front. Mater.*, vol. 5, no. August, pp. 1–6, 2018, doi: 10.3389/fmats.2018.00041.

[258] Z. Fu, W. Chen, S. Fang, D. Zhang, H. Xiao, and D. Zhu, “Alloying behavior and deformation twinning in a CoNiFeCrAl 0.6Ti0.4 high entropy alloy processed by spark plasma sintering,” *J. Alloys Compd.*, vol. 553, pp. 316–323, 2013, doi: 10.1016/j.jallcom.2012.11.146.

[259] W. Ji *et al.*, “Alloying behavior and novel properties of CoCrFeNiMn high-entropy alloy fabricated by mechanical alloying and spark plasma sintering,” *Intermetallics*, vol. 56, no. August 2018, pp. 24–27, 2015, doi: 10.1016/j.intermet.2014.08.008.

[260] Y. Geng *et al.*, “Sliding wear-induced chemical nanolayering in Cu–Ag, and its implications for high wear resistance,” *Tribol. Int.*, vol. 151, no. May, 2020, doi: 10.1016/j.triboint.2020.106444.

[261] A. Ostovari, M. N. Samodurova, K. Pashkeev, M. Doubenskaia, A. Sova, and E. A. Trofimov, “A novel intermediate temperature self-lubricating CoCrCu1-xFeNix high

entropy alloy fabricated by direct laser cladding," *Tribol. Int.*, vol. 156, no. December 2020, p. 106857, 2021, doi: 10.1016/j.triboint.2021.106857.

[262] S. Yadav, S. Sarkar, A. Aggarwal, A. Kumar, and K. Biswas, "Wear and mechanical properties of novel (CuCrFeTiZn)100-xPbx high entropy alloy composite via mechanical alloying and spark plasma sintering," *Wear*, vol. 410–411, no. May, pp. 93–109, 2018, doi: 10.1016/j.wear.2018.05.023.

[263] C. Nagarjuna *et al.*, "Applied Surface Science Worn surface and subsurface layer structure formation behavior on wear mechanism of CoCrFeMnNi high entropy alloy in different sliding conditions," *Appl. Surf. Sci.*, vol. 549, no. February, p. 149202, 2021, doi: 10.1016/j.apsusc.2021.149202.

[264] S. Kumar, A. Patnaik, A. Kumar, and P. Vinod, "Dry Sliding Wear Behavior of Al0.4FeCrNiCox(x = 0, 0.25, 0.5, 1.0 mol) High‐Entropy Alloys Saurav," *Metallogr. Microstruct. Anal.*, vol. 8, no. 0123456789, pp. 545–557, 2019, doi: 10.1007/s13632-019-00551-2.

[265] A. Dollmann, A. Kauffmann, M. Heilmaier, C. Haug, and C. Greiner, "Microstructural changes in CoCrFeMnNi under mild tribological load," *J. Mater. Sci.*, vol. 55, no. 26, pp. 12353–12372, 2020, doi: 10.1007/s10853-020-04806-0.

[266] P. F. Jiang, C. H. Zhang, S. Zhang, J. B. Zhang, J. Chen, and Y. Liu, "Fabrication and wear behavior of TiC reinforced FeCoCrAlCu-based high entropy alloy coatings by laser surface alloying," *Mater. Chem. Phys.*, vol. 255, no. July, p. 123571, 2020, doi: 10.1016/j.matchemphys.2020.123571.

[267] X. Guo *et al.*, "A comparison of the dry sliding wear of single-phase f.c.c. carbon-doped Fe40.4Ni11.3Mn34.8Al7.5Cr6 and CoCrFeMnNi high entropy alloys with 316 stainless stee," *Mater. Charact.*, vol. 170, no. September, p. 110693, 2020, doi: 10.1016/j.matchar.2020.110693.

[268] Y. Cai *et al.*, "Fracture and wear mechanisms of FeMnCrNiCo + x(TiC) composite high-entropy alloy cladding layers," vol. 543, no. December 2020, 2021.

[269] A. Verma, P. Tarate, A. C. Abhyankar, M. R. Mohape, and D. S. Gowtam, "High temperature wear in CoCrFeNiCux high entropy alloys: The role of Cu," *Scr. Mater.*, vol. 161, pp. 28–31, 2019, doi: 10.1016/j.scriptamat.2018.10.007.

[270] S. Kumar, A. Patnaik, A. K. Pradhan, and V. Kumar, "Room temperature wear study of Al 0.4 FeCrNiCo x (x = 0, 0.25, 0.5, 1.0 mol) high-entropy alloys under oil lubricating conditions," *J. Mater. Res.*, vol. 34, no. 5, pp. 841–853, 2019, doi: 10.1557/jmr.2018.499.

[271] A. P. Saurav Kumar, Pooja Rani and and V. K. ,* Ajaya Kumar Pradhan1, "Effect of cobalt content on wear behaviour of Al0.4FeCrNiCox (x=0, 0.25, 0.5, 1.0 mol) high entropy alloys tested under demineralised water with and without 3.5 % NaCl solution," *Mater. Res. Express*, vol. 6, no. 8, p. 0865b3, 2019.

[272] Z. Y. Lv, X. J. Liu, B. Jia, H. Wang, Y. Wu, and Z. P. Lu, "Development of a novel high- entropy alloy with eminent efficiency of degrading azo dye solutions," no. November 2015, pp. 1–11, 2016, doi: 10.1038/srep34213.

[273] S. Wu, W. Gao, T. Lu, and Y. Pan, "Co‐Free High‐Entropy Alloys Powders Immobilized by Electrospray and Microfluidics for Decolorization of Azo Dye," *Acta Metall. Sin. (English Lett.*, vol. 33, no. 8, pp. 1103–1110, 2020, doi: 10.1007/s40195-019-00997-x.

[274] I. Kunce, M. Polanski, and J. Bystrzycki, "Structure and hydrogen storage properties of a high entropy ZrTiVCrFeNi alloy synthesized using Laser Engineered Net Shaping (LENS)," *Int. J. Hydrogen Energy*, vol. 38, no. 27, pp. 12180–12189, 2013, doi: 10.1016/j.ijhydene.2013.05.071.

[275] U. Ulmer *et al.*, "ScienceDirect Effect of oxygen on the microstructure and hydrogen storage properties of V e Ti e Cr e Fe quaternary solid solutions," vol. 9, no. 0, 2014, doi: 10.1016/j.ijhydene.2014.08.152.

[276] Y. Kao *et al.*, "Hydrogen storage properties of multi-principal-component CoFeMnTi x V y Zr z alloys," *Int. J. Hydrogen Energy*, vol. 35, no. 17, pp. 9046–9059, 2010, doi:

10.1016/j.ijhydene.2010.06.012.

[277] I. Kunce, M. Polanski, and J. Bystrzycki, "ScienceDirect Microstructure and hydrogen storage properties of a TiZrNbMoV high entropy alloy synthesized using Laser Engineered Net Shaping (LENS)," *Int. J. Hydrogen Energy*, vol. 39, no. 18, pp. 9904–9910, 2014, doi: 10.1016/j.ijhydene.2014.02.067.

[278] S. Q. Xia, X. Yang, T. F. Yang, S. Liu, and Y. Zhang, "Irradiation Resistance in Al x CoCrFeNi High Entropy Alloys," vol. 67, no. 10, pp. 2340–2344, 2015, doi: 10.1007/s11837-015-1568-4.

[279] T. Egami, W. Guo, P. D. Rack, and T. Nagase, "Irradiation Resistance of Multicomponent Alloys," vol. 45, no. January, pp. 180–183, 2014, doi: 10.1007/s11661-013-1994-2.

[280] L. Yang, H. Ge, J. Zhang, T. Xiong, Q. Jin, and Y. Zhou, "Journal of Materials Science & Technology High He-ion irradiation resistance of CrMnFeCoNi high-entropy alloy revealed by comparison study with Ni and 304SS," *J. Mater. Sci. Technol.*, vol. 35, no. 3, pp. 300–305, 2019, doi: 10.1016/j.jmst.2018.09.050.

[281] T. Zrhfv *et al.*, "Journal of Materials Science & Technology A promising new class of irradiation tolerant materials :," *J. Mater. Sci. Technol.*, vol. 35, no. 3, pp. 369–373, 2019, doi: 10.1016/j.jmst.2018.09.034.

[282] D. T. Crane and J. W. Lagrandeur, "Progress Report on BSST-Led US Department of Energy Automotive Waste Heat Recovery Program," vol. 39, no. 9, pp. 2142–2148, 2010, doi: 10.1007/s11664-009-0991-0.

[283] N. Cucrfeal, "Thermoelectric behaviour with high lattice thermal Thermoelectric behaviour with high lattice thermal conductivity of," pp. 0–16, 2020.

[284] P. K. L. 2 Wanqing Dong 1, Zheng Zhou 1, Lijun Zhang 1, Mengdi Zhang 1 and and R. L. Gong Li 1, "Effects of Y, GdCu, and Al Addition on the Thermoelectric Behavior of CoCrFeNi High Entropy Alloys Wanqing," *Metals (Basel).*, vol. 8, p. 781, 2018, doi: 10.3390/met8100781.

[285] E. Brück, O. Tegus, L. Zhang, X. W. Li, F. R. De Boer, and K. H. J. Buschow, "Magnetic refrigeration near room temperature with Fe 2 P-based compounds," vol. 383, pp. 32–36, 2004, doi: 10.1016/j.jallcom.2004.04.042.

[286] J. Huo, L. Huo, H. Men, X. Wang, and A. Inoue, "Intermetallics The magnetocaloric effect of Gd-Tb-Dy-Al-M (M ¼ Fe , Co and Ni) high-entropy bulk metallic glasses," vol. 58, pp. 31–35, 2015, doi: 10.1016/j.intermet.2014.11.004.

[287] K. Sarlar, A. Tekg, and I. Kucuk, "Electromagnetics Magnetocaloric Properties of Rare-Earth-Free Mn 27 Cr 7 Ni 33 Ge 25 Si 8 High-Entropy Alloy," vol. 10, pp. 8–12, 2019.

[288] P. Yang, Y. Liu, X. Zhao, J. Cheng, and H. Li, "Electromagnetic wave absorption properties of mechanically alloyed FeCoNiCrAl high entropy alloy powders," *Adv. Powder Technol.*, vol. 27, no. 4, pp. 1128–1133, 2016, doi: 10.1016/j.apt.2016.03.023.

[289] G. Zhang, K. Ming, J. Kang, Q. Huang, and Z. Zhang, "Electrochimica Acta High entropy alloy as a highly active and stable electrocatalyst for hydrogen evolution reaction," *Electrochim. Acta*, vol. 279, pp. 19–23, 2018, doi: 10.1016/j.electacta.2018.05.035.

[290] H. Search, C. Journals, A. Contact, M. Iopscience, and I. P. Address, "A search for pulses of fluorescence produced by supernovae in the upper atmosphere," vol. 773.

[291] P. Ko *et al.*, "Discovery of a Superconducting High-Entropy Alloy," vol. 107001, no. September, pp. 1–5, 2014, doi: 10.1103/PhysRevLett.113.107001.

[292] K. Jasiewicz, B. Wiendlocha, P. Korbe, S. Kaprzyk, and J. Tobola, "Superconductivity of Ta34 Nb33Hf8 Zr14Ti11 high entropy alloy from first principles calculations," vol. 419, no. 5, pp. 415–419, 2016, doi: 10.1002/pssr.201600056.

[293] N. Ishizu and J. Kitagawa, "Results in Physics New high-entropy alloy superconductor Hf 21 Nb 25 Ti 15 V 15 Zr 24," *Results Phys.*, vol. 13, no. March, p. 102275, 2019, doi: 10.1016/j.rinp.2019.102275.

[294] G. S. F. T. A. Kosorukova and Y. N. Koval, “Directions for High-Temperature Shape Memory Alloys ’ Improvement : Straight Way to High-Entropy Materials ?,” *Shape Mem. Superelasticity*, vol. 1, no. 4, pp. 400–407, 2015, doi: 10.1007/s40830-015-0039-7.

[295] D. V. Ravi Kumar, Seenappa, V. Ravi Kumar, and C. R. Prakash Rao, “Influence of T6-heat treatment on mechanical properties of Al7075 alloy reinforced with Cenosphere,” *Mater. Today Proc.*, vol. 5, no. 11, pp. 25036–25044, 2018, doi: 10.1016/j.matpr.2018.10.304.

[296] T. Elmer, M. Worall, S. Wu, and S. Riffat, “An experimental study of a novel integrated desiccant air conditioning system for building applications,” *Energy Build.*, vol. 111, pp. 434–445, 2016, doi: 10.1016/j.enbuild.2015.11.065.

[297] Q. Shi, Y. Y. Tse, and R. L. Higginson, “Solid consolidation recycling of metastable beta titanium alloy Ti- 15V-3Cr-3Al-3Sn from machining chips,” pp. 1–20.

[298] J. Dai, J. Zhu, C. Chen, and F. Weng, “High temperature oxidation behavior and research status of modi fi cations on improving high temperature oxidation resistance of titanium alloys and titanium aluminides : A review,” *J. Alloys Compd.*, vol. 685, pp. 784–798, 2016, doi: 10.1016/j.jallcom.2016.06.212.

[299] G. Quan, W. Lv, J. Liang, and S. Pu, “Evaluation of the hot workability corresponding to complex deformation mechanism evolution for Ti–10V–2Fe–3Al alloy in a wide condition range,” *J. Mater. Process. Tech.*, vol. 221, pp. 66–79, 2015, doi: 10.1016/j.jmatprotec.2015.02.002.

[300] O. N. Senkov, S. V Senkova, D. M. Dimiduk, C. Woodward, and D. B. Miracle, “Oxidation behavior of a refractory NbCrMo 0.5 Ta 0.5 TiZr alloy,” pp. 6522–6534, 2012, doi: 10.1007/s10853-012-6582-0.

[301] C. M. Liu, H. M. Wang, S. Q. Zhang, H. B. Tang, and A. L. Zhang, “Microstructure and oxidation behavior of new refractory high entropy alloys,” *J. Alloys Compd.*, vol. 583, pp. 162–169, 2014, doi: 10.1016/j.jallcom.2013.08.102.

[302] Y. Liu, C. Cheng, J. Shang, R. Wang, P. Li, and J. Zhao, "Oxidation behavior of high-entropy alloys AlxCoCrFeNi (x=0.15, 0.4) in supercritical water and comparison with HR3C steel," *Trans. Nonferrous Met. Soc. China*, vol. 25, no. 4, pp. 1341–1351, 2015, doi: 10.1016/S1003-6326(15)63733-5.

[303] Y. Yu, N. Xu, S. Zhu, Z. Qiao, and J. Zhang, "Journal of Materials Science & Technology A novel Cu-doped high entropy alloy with excellent comprehensive performances for marine application," *J. Mater. Sci. Technol.*, vol. 69, pp. 48–59, 2021, doi: 10.1016/j.jmst.2020.08.016.

[304] E. Zhou *et al.*, "A novel Cu-bearing high-entropy alloy with significant antibacterial behavior against corrosive marine biofilms," *J. Mater. Sci. Technol.*, vol. 46, pp. 201–210, 2020, doi: 10.1016/j.jmst.2020.01.039.

[305] A. Verma, P. Tarate, A. C. Abhyankar, M. R. Mohape, and D. S. Gowtam, "High temperature wear in CoCrFeNiCu x high entropy alloys : The role of Cu," *Scr. Mater.*, vol. 161, pp. 28–31, 2019, doi: 10.1016/j.scriptamat.2018.10.007.

[306] Y. Zou, H. Ma, and R. Spolenak, "Ultrastrong ductile and stable high-entropy alloys at small scales," *Nat. Commun.*, vol. 6, 2015, doi: 10.1038/ncomms8748.

[307] Y. Zou, J. M. Wheeler, H. Ma, P. Okle, and R. Spolenak, "Nanocrystalline High-Entropy Alloys: A New Paradigm in High-Temperature Strength and Stability," *Nano Lett.*, vol. 17, no. 3, pp. 1569–1574, 2017, doi: 10.1021/acs.nanolett.6b04716.

[308] S. K. Chen and Y. F. Kao, "Near-constant resistivity in 4.2-360 K in a B2 Al2.08CoCrFeNi," *AIP Adv.*, vol. 2, no. 1, pp. 4–9, 2012, doi: 10.1063/1.3679072.

[309] P. Xie *et al.*, "Highly efficient decomposition of ammonia using high-entropy alloy catalysts," *Nat. Commun.*, vol. 10, no. 1, pp. 1–12, 2019, doi: 10.1038/s41467-019-11848-9.

[310] Y. Yao *et al.*, "Computationally aided, entropy-driven synthesis of highly efficient and durable multi-elemental alloy catalysts," *Sci. Adv.*, vol. 6, no. 11, pp. 1–12, 2020, doi: 10.1126/sciadv.aaz0510.

[311] T. Li *et al.*, "Denary oxide nanoparticles as highly stable catalysts for methane combustion (Nature Catalysis, (2021), 4, 1, (62-70), 10.1038/s41929-020-00554-1)," *Nat. Catal.*, vol. 4, no. 5, p. 439, 2021, doi: 10.1038/s41929-021-00613-1.

[312] Y. L. Chen, Y. H. Hu, C. A. Hsieh, J. W. Yeh, and S. K. Chen, "Competition between elements during mechanical alloying in an octonary multi-principal-element alloy system," *J. Alloys Compd.*, vol. 481, no. 1–2, pp. 768–775, 2009, doi: 10.1016/j.jallcom.2009.03.087.

[313] Y. L. Liu, S. B. Kang, and H. W. Kim, "Complex microstructures in an as-cast Al-Mg-Si alloy," *Mater. Lett.*, vol. 41, no. 6, pp. 267–272, 1999, doi: 10.1016/S0167-577X(99)00141-X.

[314] M. Warmuzek, K. Rabczak, and J. Sieniawski, "The course of the peritectic transformation in the Al-rich Al-Fe-Mn-Si alloys," *J. Mater. Process. Technol.*, vol. 162–163, no. SPEC. ISS., pp. 422–428, 2005, doi: 10.1016/j.jmatprotec.2005.02.030.

[315] M. Warmuzek, J. Sieniawski, K. Wicher, and G. Mrówka, "The study of the distribution of the transition metals and Si during primary precipitation of the intermetallic phases in Al-Mn-Si alloys," *J. Mater. Process. Technol.*, vol. 175, no. 1–3, pp. 421–426, 2006, doi: 10.1016/j.jmatprotec.2005.04.005.

[316] X. Jiang, M. Galano, and F. Audebert, "Extrusion textures in Al, 6061 alloy and 6061/SiCp nanocomposites," *Mater. Charact.*, vol. 88, pp. 111–118, 2014, doi: 10.1016/j.matchar.2013.11.009.

[317] K. Huang, K. Marthinsen, Q. Zhao, and R. E. Logé, "The double-edge effect of second-phase particles on the recrystallization behaviour and associated mechanical properties of metallic materials," *Prog. Mater. Sci.*, vol. 92, pp. 284–359, 2018, doi: 10.1016/j.pmatsci.2017.10.004.

[318] W. Guo *et al.*, "Influence of elastic tensile stress on aging process in an Al-Zn-Mg-Cu alloy," *Mater. Lett.*, vol. 106, pp. 14–17, 2013, doi: 10.1016/j.matlet.2013.04.095.

[319] J. Liu *et al.*, "Improved structural homogeneity and mechanical properties of

nanoparticles reinforced Al composites after orthogonal thermomechanical processes," vol. 767, pp. 293–301, 2018, doi: 10.1016/j.jallcom.2018.07.083.

[320] J. Liu *et al.*, "Simultaneously increasing strength and ductility of nanoparticles reinforced Al composites via accumulative orthogonal extrusion process," vol. 3831, 2018, doi: 10.1080/21663831.2018.1471421.

[321] Y. Sun, L. Fu, Z. Fu, A. Shan, and E. J. Lavernia, "Enhanced thermal stability and ductility in a nanostructured Ni-based alloy," *Scr. Mater.*, vol. 141, pp. 1–5, 2017, doi: 10.1016/j.scriptamat.2017.07.013.

[322] X. Wu *et al.*, "Heterogeneous lamella structure unites ultrafine-grain strength with coarse-grain ductility," vol. 112, no. 47, 2015, doi: 10.1073/pnas.1517193112.

[323] Y. Zhao, X. Ma, H. Chen, X. Zhao, and X. Liu, "Preferred orientation and interfacial structure in extruded nano-Al 3 BC / 6061 Al," *Mater. Des.*, vol. 131, no. March, pp. 23–31, 2017, doi: 10.1016/j.matdes.2017.05.088.

[324] J. George E, Dieter, "Mechanical_metallurgy." McGRAW-HILL BOOK COMPANY, inc, pp. 3–609, 1961.

[325] K. B. Nie, X. J. Wang, K. Wu, X. S. Hu, and M. Y. Zheng, "Development of SiCp/AZ91 magnesium matrix nanocomposites using ultrasonic vibration," *Mater. Sci. Eng. A*, vol. 540, pp. 123–129, 2012, doi: 10.1016/j.msea.2012.01.112.

[326] S. F. Hassan and M. Gupta, "Effect of particulate size of Al2O3 reinforcement on microstructure and mechanical behavior of solidification processed elemental Mg," *J. Alloys Compd.*, vol. 419, no. 1–2, pp. 84–90, 2006, doi: 10.1016/j.jallcom.2005.10.005.

[327] T. Hasegawa and K. Okazaki, "Uniform tensile elongation obtained from experiment and its estimation using dislocation dynamics parameters," *Mater. Sci. Eng. A*, vol. 297, no. 1–2, pp. 266–271, 2001, doi: 10.1016/S0921-5093(00)01267-3.

[328] A. R. Miedema, "On the heat of formation of solid alloys. II," *J. Less-Common Met.*,

vol. 46, no. 1, pp. 67–83, 1976, doi: 10.1016/0022-5088(76)90180-6.

[329] X. Yang and Y. Zhang, "Prediction of high-entropy stabilized solid-solution in multi-component alloys," *Mater. Chem. Phys.*, vol. 132, no. 2–3, pp. 233–238, 2012, doi: 10.1016/j.matchemphys.2011.11.021.

[330] W. W. Zhang *et al.*, "A novel high-strength Al-based nanocomposite reinforced with Ti-based metallic glass nanoparticles produced by powder metallurgy," *Mater. Sci. Eng. A*, vol. 734, no. July, pp. 34–41, 2018, doi: 10.1016/j.msea.2018.07.082.

[331] R. N. Shahid and S. Scudino, "Strengthening of Al-Fe3Al composites by the generation of harmonic structures," *Sci. Rep.*, vol. 8, no. 1, pp. 1–12, 2018, doi: 10.1038/s41598-018-24824-y.

[332] H. Yang, T. D. Topping, K. Wehage, L. Jiang, E. J. Lavernia, and J. M. Schoenung, "Tensile behavior and strengthening mechanisms in a submicron B4C-reinforced Al trimodal composite," *Mater. Sci. Eng. A*, vol. 616, pp. 35–43, 2014, doi: 10.1016/j.msea.2014.07.079.

[333] M. Yang, D. Yan, F. Yuan, P. Jiang, E. Ma, and X. Wu, "Dynamically reinforced heterogeneous grain structure prolongs ductility in a medium-entropy alloy with gigapascal yield strength," *Proc. Natl. Acad. Sci. U. S. A.*, vol. 115, no. 28, pp. 7224–7229, 2018, doi: 10.1073/pnas.1807817115.

[334] N. Chawla, J. J. Williams, and R. Saha, "Mechanical behavior and microstructure characterization of sinter-forged SiC particle reinforced aluminum matrix composites," *J. Light Met.*, vol. 2, no. 4, pp. 215–227, 2002, doi: 10.1016/S1471-5317(03)00005-1.

[335] G. E. Dieter, "Mechanical metallurgy.," *Mech. Metall.*, 2011, doi: 10.5962/bhl.title.35895.

[336] H. Yang, L. Jiang, M. Balog, P. Krizik, and J. M. Schoenung, "Reinforcement Size Dependence of Load Bearing Capacity in Ultrafine-Grained Metal Matrix Composites," *Metall. Mater. Trans. A Phys. Metall. Mater. Sci.*, vol. 48, no. 9, pp.

4385–4392, 2017, doi: 10.1007/s11661-017-4186-7.

[337] L. Zhao, H. Lu, and Z. Gao, "Microstructure and Mechanical Properties of Al/Graphene Composite Produced by High-Pressure Torsion," *Adv. Eng. Mater.*, vol. 17, no. 7, pp. 976–981, 2015, doi: 10.1002/adem.201400375.

[338] L. Jiang *et al.*, "Toughening of aluminum matrix nanocomposites via spatial arrays of boron carbide spherical nanoparticles," *Acta Mater.*, vol. 103, pp. 128–140, 2016, doi: 10.1016/j.actamat.2015.09.057.

[339] Z. Zhang *et al.*, "Mechanical behavior of ultrafine-grained Al composites reinforced with B4C nanoparticles," *Scr. Mater.*, vol. 65, no. 8, pp. 652–655, 2011, doi: 10.1016/j.scriptamat.2011.06.037.

[340] S. Abbaszadeh, A. Pakseresht, H. Omidvar, and A. Shafiei, "Investigation of the High-Temperature Oxidation Behavior of the Al0.5CoCrFeNi High Entropy Alloy," *Surfaces and Interfaces*, vol. 21, p. 100724, 2020, doi: 10.1016/j.surfin.2020.100724.

[341] S. Son *et al.*, "Superior antifouling properties of a CoCrFeMnNi high-entropy alloy," *Mater. Lett.*, vol. 300, no. May, p. 130130, 2021, doi: 10.1016/j.matlet.2021.130130.

[342] S. Yin *et al.*, "Deposition of FeCoNiCrMn high entropy alloy (HEA) coating via cold spraying," *J. Mater. Sci. Technol.*, vol. 35, no. 6, pp. 1003–1007, 2019, doi: 10.1016/j.jmst.2018.12.015.

[343] K. Kuwabara, H. Shiratori, T. Fujieda, K. Yamanaka, Y. Koizumi, and A. Chiba, "Mechanical and corrosion properties of AlCoCrFeNi high-entropy alloy fabricated with selective electron beam melting," *Addit. Manuf.*, vol. 23, no. April 2017, pp. 264–271, 2018, doi: 10.1016/j.addma.2018.06.006.

[344] J. Li *et al.*, "Additive manufacturing of high-strength CrMnFeCoNi high-entropy alloys-based composites with WC addition," *J. Mater. Sci. Technol.*, vol. 35, no. 11, pp. 2430–2434, 2019, doi: 10.1016/j.jmst.2019.05.062.

[345] Z. Gu, P. Mao, Y. Gou, Y. Chao, and S. Xi, "Microstructure and properties of

MgMoNbFeTi2Yx high entropy alloy coatings by laser cladding," *Surf. Coatings Technol.*, vol. 402, no. August, p. 126303, 2020, doi: 10.1016/j.surfcoat.2020.126303.

[346] Y. Geng *et al.*, "Nano-coupled heterostructure induced excellent mechanical and tribological properties in AlCoCrFeNi high entropy alloy," *Tribol. Int.*, vol. 154, no. July 2020, p. 106662, 2021, doi: 10.1016/j.triboint.2020.106662.

[347] M. A. Haq, N. S. A. Eom, N. Su, H. Lee, T. S. Kim, and B. S. Kim, "Powder interface modification for synthesis of core-shell structured CoCrFeNiTi high entropy alloy composite," *Appl. Surf. Sci.*, vol. 506, no. November 2019, p. 144925, 2020, doi: 10.1016/j.apsusc.2019.144925.

[348] A. Zhang, J. Han, B. Su, P. Li, and J. Meng, "Microstructure, mechanical properties and tribological performance of CoCrFeNi high entropy alloy matrix self-lubricating composite," *Mater. Des.*, vol. 114, pp. 253–263, 2017, doi: 10.1016/j.matdes.2016.11.072.

[349] C. Shang, E. Axinte, W. Ge, Z. Zhang, and Y. Wang, "High-entropy alloy coatings with excellent mechanical, corrosion resistance and magnetic properties prepared by mechanical alloying and hot pressing sintering," *Surfaces and Interfaces*, vol. 9, no. June, pp. 36–43, 2017, doi: 10.1016/j.surfin.2017.06.012.

[350] Z. Gu, S. Xi, P. Mao, and C. Wang, "Microstructure and wear behavior of mechanically alloyed powder AlxMo0.5NbFeTiMn2 high entropy alloy coating formed by laser cladding," *Surf. Coatings Technol.*, vol. 401, no. July, 2020, doi: 10.1016/j.surfcoat.2020.126244.

[351] H. Figiel, O. Zogał, and V. Yartys, "Effect of Iron content on the microstructure evolution, mechanical properties and wear resistance of FeXCoCrNi high-entropy alloy system produced via MA-SPS Parisa," *J. Alloys Compd.*, vol. 404–406, no. SPEC. ISS., p. 1, 2005, doi: 10.1016/j.jallcom.2005.05.002.

[352] C. Shang, E. Axinte, W. Ge, Z. Zhang, and Y. Wang, "CoCrFeNi(W1 − xMox) high-entropy alloy coatings with excellent mechanical properties and corrosion resistance

prepared by mechanical alloying and hot pressing sintering," *Surfaces and Interfaces*, vol. 9, pp. 36–43, 2017, doi: 10.1016/j.surfin.2017.06.012.

[353] P. Moazzen, M. R. Toroghinejad, T. Zargar, and P. Cavaliere, "Investigation of hardness, wear and magnetic properties of NiCoCrFeZrx HEA prepared through mechanical alloying and spark plasma sintering," *J. Alloys Compd.*, vol. 892, p. 161924, 2022, doi: 10.1016/j.jallcom.2021.161924.

[354] R. Ravi and S. R. Bakshi, "Microstructural evolution and wear behavior of carbon added CoCrFeMnNi multi-component alloy fabricated by mechanical alloying and spark plasma sintering," *J. Alloys Compd.*, vol. 883, p. 160879, 2021, doi: 10.1016/j.jallcom.2021.160879.

[355] J. Xu, S. Wang, C. Shang, S. Huang, and Y. Wang, "Microstructure and properties of CoCrFeNi(WC) high-entropy alloy coatings prepared using mechanical alloying and hot pressing sintering," *Coatings*, vol. 9, no. 1, 2019, doi: 10.3390/coatings9010016.

[356] G. Deng *et al.*, "Effects of normal load and velocity on the dry sliding tribological behaviour of CoCrFeNiMo0.2 high entropy alloy," *Tribol. Int.*, vol. 144, no. October 2019, p. 106116, 2020, doi: 10.1016/j.triboint.2019.106116.

[357] Y. Huang, Z. Wang, Z. Xu, X. Zang, and X. Chen, "Microstructure and properties of TiNbZrMo high entropy alloy coating," *Mater. Lett.*, vol. 285, pp. 3–6, 2021, doi: 10.1016/j.matlet.2020.129004.

[358] Q. Yang, Y. Tang, Y. Wen, Q. Zhang, D. Deng, and X. Nai, "Microstructures and properties of CoCrCuFeNiMox high-entropy alloys fabricated by mechanical alloying and spark plasma sintering," *Powder Metall.*, vol. 61, no. 2, pp. 115–122, 2018, doi: 10.1080/00325899.2017.1415248.

[359] M. L. Liang *et al.*, "Microstructure and sliding wear behavior of FeCoNiCr0.8Al0.2 high-entropy alloy for different durations," *Int. J. Refract. Met. Hard Mater.*, vol. 103, no. November 2021, p. 105767, 2022, doi: 10.1016/j.ijrmhm.2021.105767.

[360] M. Pole, M. Sadeghilaridjani, J. Shittu, A. Ayyagari, and S. Mukherjee, "High

temperature wear behavior of refractory high entropy alloys based on 4-5-6 elemental palette," vol. 843, 2020.

[361] N. Malatji, A. P. I. Popoola, T. Lengopeng, and S. Pityana, "Materials Today : Proceedings Tribological and corrosion properties of laser additive manufactured AlCrFeNiCu high entropy alloy," vol. 28, pp. 944–948, 2020.

Document Information

Analyzed document	Akshay_Thesis_Final_copy.pdf (D167102251)
Submitted	5/16/2023 8:21:00 AM
Submitted by	Dr. Mohammad Taufik
Submitter email	mohammad.taufik@manit.ac.in
Similarity	7%
Analysis address	mohammad.taufik.manitb@analysis.urkund.com

Sources included in the report

SA	**Rahul Singh M.Tech Thesis 01-07.pdf** Document Rahul Singh M.Tech Thesis 01-07.pdf (D110044320)	2
W	URL: https://www.researchgate.net/publication/317061347_High-entropy_alloy_CoCrFeMnNi_produced_by_p... Fetched: 2/8/2023 11:17:54 AM	3
SA	**HIGH ENTROPY ALLOYS.docx** Document HIGH ENTROPY ALLOYS.docx (D142464095)	6
SA	**project report 10-05-2022docx - Google Docs.pdf** Document project report 10-05-2022docx - Google Docs.pdf (D166487293)	8
W	URL: https://vdoc.pub/documents/high-entropy-alloys-fundamentals-and-applications-1v57o0at3j8o Fetched: 9/22/2021 3:03:23 PM	20
W	URL: https://www.sciencedirect.com/science/article/abs/pii/S0925838818312350 Fetched: 5/16/2023 8:43:00 AM	7
W	URL: https://www.researchgate.net/publication/324681604_The_influence_of_nanocrystalline_CoNiFeAl_0... Fetched: 1/13/2023 7:57:35 PM	7
SA	**Manuscript-Al Can-Gr-B4C MMC-(Feb 22, 2023) (AutoRecovered) (AutoRecovered) 2.docx** Document Manuscript-Al Can-Gr-B4C MMC-(Feb 22, 2023) (AutoRecovered) (AutoRecovered) 2.docx (D159320434)	5
SA	**20117201002-TS(J JEBEEN MOSES).pdf** Document 20117201002-TS(J JEBEEN MOSES).pdf (D28740479)	1
SA	**full thesis-1.docx** Document full thesis-1.docx (D21301883)	3
W	URL: https://www.degruyter.com/document/doi/10.1515/ntrev-2021-0071/html?lang=en Fetched: 5/30/2022 3:22:37 PM	12

PhD Thesis

ORIGINALITY REPORT

9%	5%	7%	%
SIMILARITY INDEX	INTERNET SOURCES	PUBLICATIONS	STUDENT PAPERS

PRIMARY SOURCES

1	ir.amu.ac.in Internet Source	1%
2	idoc.pub Internet Source	<1%
3	Mikhail Slobodyan, Evgeniy Pesterev, Alexey Markov. "Recent advances and outstanding challenges for implementation of high entropy alloys as structural materials", Materials Today Communications, 2023 Publication	<1%
4	link.springer.com Internet Source	<1%
5	Ambuj Pateriya, Mohan Kumar Pradhan. "Dry Sliding Wear Response of Aluminium Matrix Composites (AMCs): A Critical Review", Materials Research Express, 2023 Publication	<1%
6	ouci.dntb.gov.ua Internet Source	<1%

7	Henry, Ononiwu Ndudim. "Machinability Studies and Charaterization of Aluminium Matrix Reinforced with Fly-Ash and Carbonized Eggshells", University of Johannesburg (South Africa), 2022 Publication	<1 %
8	psasir.upm.edu.my Internet Source	<1 %
9	Nandini Singh, Yagnesh Shadangi, Vikas Shivam, Nilay Krishna Mukhopadhyay. "MgAlSiCrFeNi low-density high entropy alloy processed by mechanical alloying and spark plasma sintering: Effect on phase evolution and thermal stability", Journal of Alloys and Compounds, 2021 Publication	<1 %
10	Liqiang Zhan, Jiabin Hou, Guofeng Wang, Yuqing Chen, Shuyi Luo, Qingxin Kang, Zhenlun Li, Xunhu Xu. "Study on mechanical alloying behavior and thermal stability of HfMoNbTaTi refractory high-entropy alloy", Materials Characterization, 2023 Publication	<1 %
11	journals.nnc.kz Internet Source	<1 %
12	kupdf.net Internet Source	<1 %